NEUTRON & X-RAY SCATTERING STUDIES OF Fe-BASED MATERIALS

by

STAVROS SAMOTHRAKITIS

A thesis submitted to
The University of Birmingham
for the degree of
DOCTOR OF PHILOSOPHY

School of Metallurgy and Materials
College of Engineering and Physical Sciences
The University of Birmingham
February 2018

Abstract

Small-angle scattering technique uses the scattering of radiation (e.g. neutrons or X-rays) at small angles to probe large-scale structures within matter, up to thousands of Ångstroms. It is proven a valuable tool for investigating precipitation in reactor pressure vessel (RPV) steels and Fe-Ga alloys offering a statistical average over a large volume of samples.

RPV steels, being of crucial importance for the longevity of a nuclear reactor, have been a long-standing theme for investigations. The main topics of such investigations are the effects of irradiation upon the steels and the consequent implications on their macroscopic properties. In this thesis, small-angle neutron scattering is employed to investigate irradiation induced precipitates in low- and high-Cu RPV steels. After irradiations with protons to low damage levels, precipitates could be clearly observed only in the high-Cu RPV steels. Stable pre-irradiation formed features are attributed to precipitation of carbides.

Fe-Ga binary alloys have attracted much attention due to the still unexplained high magnetostriction they exhibit. To investigate the composition of nanoheterogeneities in a Fe-Ga sample, anomalous small-angle X-ray scattering is employed exploiting the energy dependence of the Fe and Ga atoms near their respective absorption edges. The nano-precipitates are found to have a Fe_3Ga stoichiometry.

ACKNOWLEDGEMENTS

This thesis epitomizes three years of work, where I have immersed myself in the area of neutron and X-ray scattering. As such, I would like to express my gratitude to my supervisor, Dr. Mark Laver, for introducing me to this exciting science as well as for his help and patience during the entire period of my PhD. I thank him for his guidance and support during long, arduous experiments, and for his general day-to-day insights and advice in data analysis and theoretical discussions.

Special thanks to my good friends and colleagues Camilla B. Larsen, Robert Arnold, Jonathan and Ellie Young for their support and help as well as all the beautiful and fun times during experiments. Without their help and advice, in different aspects of my work, I could not have reached the end. I hope one way or the other we will keep collaborating and share even more unique moments. I would also like to thank all my fellow students and friends, Will, Joe, Aimee, Shervin and all the rest, from the 1B20 office for all the amazing times we had.

Additionally, I would like to acknowledge the help and advice of Dr. Brian Connolly and Dr. Christopher Cooper from the University of Birmingham as well as all local contacts from neutron and X-ray scattering facilities, in Europe and the USA, of whom the support allowed for the completion of the experimental work. Also a big thank you to Professor Andrea Bianchi from the University of Montreal for the training he provided on crystal growth techniques and Dr. Yeshpal Singh from the University of Birmingham for all his advice regarding my thesis and PhD defence.

Finally and most importantly, I would like to thank my family and friends for their continued understanding and support during the entire period of my PhD. My parents for

all their sacrifices and for always believing in my dreams. My beautiful wife and daughter, for their patience and support through both easy and difficult times as well as for the incredible cooking that kept me going. My brother, his wife, and my amazing nephew who through their own struggles taught me to never give up. All my friends and extended family back in Greece who never forgot me and never ever gave up on me.

I love you all!

Της παιδείας αι μεν ρίζαι πικραί, οι δε καρποί γλυκείς.

CONTENTS

INTRODUCTION & OVERVIEW

Iron (Fe) is the fourth most abudant element found on Earth's crust (after oxygen, silicon, and aluminium) with a 5.6 % abudance[1], and the most abundant among metals. It is solid at ambient temperature with a melting point of 1535 ^{o}C[1]. It is metallic and part of the first transition series of the periodic table. At atmospheric pressure, it can be found in two main crystal structures, body centred cubic (BCC) and face centred cubic (FCC), with the former being the ground state (at room temperature) and the latter appearing at elevated temperatures with a transformation temperature of 911 ^{o}C[1]. At higher pressures it can also be found with a hexagonal closed packed (HCP) crystal structure[1]. This property of iron, i.e. the variety of the crystal structures in which it can be found, is called polymorphism and the different phases are called allotropes. Despite the fact that polymorphism is quite common among crystalline materials, it is a property that makes iron unique due to its immediate connection to the metal's magnetic properties; depending on its crystal structure and temperature, iron exhibits paramagnetic, ferromagnetic as well as antiferromagnetic behaviour[1].

The use of iron can be traced back thousands of years, at the beginning of the so-called Iron Age. At around 1500 B.C.E. people in the European peninsula came to understand its importance as a material since it was proven to be more favourable than bronze, an alloy of copper, tin and other elements, which was the most widely used material up to that point in history. Cast iron replaced bronze as the main material in tool and weapon manufacturing and the so-called Bronze Age gradually came to an end. Ever since iron is one of the most used metals and even today, due to its low cost and high

strength (mainly in the form of steel) in combination with its magnetic properties, it is irreplaceable. Iron forms a variety of compounds and alloys including steel, cast iron, iron oxides and numerous other alloys (e.g. binary Fe-Ga alloys) that find applications in numerous fields including industry, construction and manufacturing, magnetism as well as health and environment. The investigation of two of such alloys, steels used in nuclear industry and magnetostrictive binary Fe-Ga alloys, sets the scope for this thesis.

For the last few decades steel has been used in nuclear industry mainly for the manufacturing of different parts of a nuclear reactor with the most important being the reactor's pressure vessel (RPV) that contains the reactor's core and fuel and typically operates under high pressure and temperature. Due to the harsh environment of a nuclear reactor the steel alloys, most commonly referred to as RPV steels, are often subject to irradiation damage. This is mainly caused by particles (i.e. neutrons) of high kinetic energy, produced during the fission reaction, that interact with the RPV steels resulting in their embrittlement and failure[2]. One of the main embrittlement causing mechanisms is irradiation induced or enhanced precipitation, leading to an increase in hardness and a shift of the ductile-to-brittle transition temperature of the steels[3]. After years of investigations it was understood that precipitation of clusters enriched in copper was of major concern[3–5]. Copper is an impurity element that was introduced in the steel alloys mainly through the welding process due to the use of copper-coated welding rods[6]. Over the years copper levels were well controlled and reduced but it was found that precipitation of solute elements, such as manganese and nickel that are added in the alloy to improve its useful properties, could also lead to hardening and consequently embrittlement[7–10].

The first part of the experimental work conducted in this thesis is focused on probing, by means of small-angle neutron scattering, the formation of copper-rich or manganese-nickel-rich clusters during proton irradiation of RPV steels. Irradiated steels have been extensively studied and there are numerous publications on the topic. Even if the formation and the nature of such clusters seem to be well understood, in this thesis a slightly different approach is taken towards the interpretation of the results by discussing the

possible magnetic nature of the precipitates. Most neutron scattering results from RPV steels investigation are interpreted under the assumption that irradiation induced or pre-irradiation formed precipitates are non-magnetic. In this thesis both approaches are discussed and the differences in the calculated composition are evaluated and compared with results provided by other experimental techniques, such as atom probe tomography. The effect of overall proton fluence and damage level within the steels is also discussed seemingly playing a crucial role in the formation of precipitates mainly in low-copper containing alloys.

The alloys of iron with rare earth elements such as terbium and dysprosium as well as other elements such as aluminium and gallium have been found to exhibit quite significant magnetostrictive behaviour[11], which is the change of dimensionality (shape and/or size) of ferromagnetic materials during the process of magnetisation, i.e. under the influence of an applied magnetic field. Magnetostrictive materials are quite important since they find applications as torque micro-sensors, mass actuators, electro-hydraulic actuators, sonar transducers and many other[11]. The alloy that exhibits the highest reported magnetostriction, about 2000 $\mu\epsilon$, at room temperature is the ternary alloy of iron, terbium, and dysprosium also known by its commercial name, Terfenol-D[12]. The drawback of Terfenol-D is that it is brittle and cannot withstand high tensile loads making it non-ideal for practical use. A possible alternative to Terfenol-D is the binary alloy of Fe-Ga that exhibits significant magnetostriction, about 400 $\mu\epsilon$ for 19 at. % Ga, and has good mechanical and magnetic properties[13,14]. Magnetostriction in most magnetostrictive materials is well understood but its occurrence in Fe-Ga alloys still lacks a full explanation with the content of gallium as well as the thermal history of the alloy seemingly being of high significance. Theories have been proposed trying to explain the phenomenon[15–17] but decisive experimental proof has not been brought to light solidly supporting any of them. One of these theories argues that the manifestation of magnetostriction in Fe-Ga is due to Ga-rich nano-clusters, different in structure and composition than the phase of the matrix[16,17]. The precipitates are magnetically coupled to the matrix and an applied

magnetic field leads to their spatial reorientation and magnetostriction[16,17].

The second experimental topic of this thesis is focused on Fe-Ga trying to resolve the existence of precipitates in the nanoscale. By means of anomalous small-angle X-ray scattering their nature, i.e. structure and composition, is investigated. For interpretation of the results various approaches are taken. One of the initial objectives is to find the optimal model to describe any features within the specimen. The analysis of the experimental findings though is proven to be difficult and far from robust since the chosen experimental technique is novel for investigating such alloys. Direct comparison with literature and results from different studies is also performed to substantiate the results.

In Chapter 1 the theoretical foundations of the two main experimental techniques, small-angle neutron scattering and small-angle X-ray scattering, used for the scope of this thesis are laid out. In Chapter 2 the literature on Fe-Ga system and its magnetostriction is reviewed with introductory information on magnetism and magnetic anisotropy. Then, in Chapter 3 a revision of the basics of irradiation damage in matter is provided with focus on irradiation induced embrittlement of RPV steels. Chapter 4 and 5 introduce the experimental work performed on high- and low-Cu proton irradiated RPV steels. Chapter 6 is the final chapter of the main body of the thesis providing the last part of the experimental work. In it, the investigation of a Fe-Ga sample by means of anomalous small-angle X-ray scattering is reported. An overall conclusions section is also given highlighting the main points and findings of the research and finally a future work chapter is provided with suggestions for further investigation on the topics of the thesis and possible improvements on the current research work.

References

[1] W. Pepperhoff and M. Acet. *Constitution and Magnetism of Iron and its Alloys*. Springer Science & Business Media, 2013.

[2] G. S. Was. *Fundamentals of Radiation Materials Science: Metals and Alloys*. Springer, 2016.

[3] G. R. Odette. On the dominant mechanism of irradiation embrittlement of reactor pressure vessel steels. *Scripta Metallurgica*, 17(10):1183–1188, 1983.

[4] G. R. Odette and G. E. Lucas. Embrittlement of nuclear reactor pressure vessels. *JOM*, 53(7):18, 2001.

[5] E. Meslin, B. Radiguet, and M. Loyer-Prost. Radiation-induced precipitation in a ferritic model alloy: An experimental and theoretical study. *Acta Materialia*, 61(16):6246–6254, 2013.

[6] M. Tomimatsu and T. Hirota. *Embrittlement of reactor pressure vessels (RPVs) in pressurized water reactors (PWRs)*, pages 57–106. Irradiation Embrittlement of Reactor Pressure Vessels (RPVs) in Nuclear Power Plants, Woodhead Publishing Series in Energy: Number 26. Elsevier Ltd., 2015.

[7] M. K. Miller, M. A. Sokolov, R. K. Nanstad, and K. F. Russell. APT characterization of high nickel RPV steels. *Journal of Nuclear Materials*, 351(1):187–196, 2006.

[8] P. D. Edmondson, M. K. Miller, K. A. Powers, and R. K. Nanstad. Atom probe tomography characterization of neutron irradiated surveillance samples from the R. E. Ginna reactor pressure vessel. *Journal of Nuclear Materials*, 470:147–154, 2016.

[9] E. Meslin, M. Lambrecht, M. Hernández-Mayoral, F. Bergner, L. Malerba, P. Pareige, B. Radiguet, A. Barbu, D. Gómez-Briceño, A. Ulbricht, et al. Characterization of neutron-irradiated ferritic model alloys and a RPV steel from combined APT, SANS, TEM and PAS analyses. *Journal of Nuclear Materials*, 406(1):73–83, 2010.

[10] N. Soneda, K. Dohi, K. Nishida, A. Nomoto, M. Tomimatsu, and H. Matsuzawa. Microstructural characterization of RPV materials irradiated to high fluences at high flux. *Journal of ASTM International*, 6(7):1–16, 2009.

[11] E. Goran. Handbook of Giant Magnetostrictive Materials, 2000.

[12] A. Clark and D. Crowder. High temperature magnetostriction of $TbFe_2$ and $Tb_{27}Dy_{73}Fe_2$. *IEEE Transactions on Magnetics*, 21(5):1945–1947, 1985.

[13] A. E. Clark, J. B. Restorff, M. Wun-Fogle, T. A. Lograsso, and D. L. Schlagel. Magnetostrictive properties of body-centered cubic Fe-Ga and Fe-Ga-Al alloys. *IEEE Transactions on Magnetics*, 36(5):3238–3240, 2000.

[14] A. E. Clark, K. B. Hathaway, M. Wun-Fogle, J. B. Restorff, T. A. Lograsso, V. M. Keppens, G. Petculescu, and R. A. Taylor. Extraordinary magnetoelasticity and lattice softening in bcc Fe-Ga alloys. *Journal of Applied Physics*, 93(10):8621–8623, 2003.

[15] M. Wuttig, L. Dai, and J. Cullen. Elasticity and magnetoelasticity of Fe-Ga solid solutions. *Applied Physics Letters*, 80(7):1135–1137, 2002.

[16] A. G. Khachaturyan and D. Viehland. Structurally heterogeneous model of extrinsic magnetostriction for Fe-Ga and similar magnetic alloys: Part i. decomposition and confined displacive transformation. *Metallurgical and Materials Transactions A*, 38(13):2308–2316, 2007.

[17] A. G. Khachaturyan and D. Viehland. Structurally heterogeneous model of extrinsic magnetostriction for Fe-Ga and similar magnetic alloys: Part ii. giant magnetostriction and elastic softening. *Metallurgical and Materials Transactions A*, 38(13):2317–2328, 2007.

CHAPTER 1

NEUTRON & X-RAY SCATTERING

1.1 Introduction

During the past decades, the far-reaching utility of neutrons and X-rays as investigative probes has been demonstrated in scientific fields as diverse as physics, materials science, and biology. Both probes share many properties that make them invaluable tools in condensed matter research.

Neutron and X-ray wavelengths are in the order of a few Ångstroms, thus matching atomic distances in materials. Consequently, both can be used in diffraction and scattering experiments to extract structural information, such as atomic arrangements, and material composition. Neutrons and X-rays are also used to probe dynamics, because their energy can match the fundamental energy scales of excitations in materials. They both penetrate matter easily with neutrons being more penetrating as they do not interact strongly with electrons (i.e. they are electrically neutral). As a result, these probes are widely used for bulk measurements as well as surface and interface measurements, whereas probes such as electrons are mainly used for studying surfaces and interfaces alone. Electrons are much less penetrating due to the Coulomb interaction with the electron cloud of the investigated atoms.

X-rays and neutrons also have a range of dissimilarities. Photons, being the carriers of electromagnetic force, carry no mass and always travel at constant velocity, the speed of light. On the other hand, neutrons have a mass and travel at finite speeds (e.g. 2.2 km/s

corresponding to a neutron energy of about 0.025 eV). The fundamental nature of the two particles is therefore described by different equations; neutrons obey the Schrödinger equation, while the behaviour of photons is governed by Maxwell's equations. Despite possessing wavelengths in roughly the same range, the two probes can have quite a difference in energy, with X-rays having orders of magnitude higher energy, e.g. 0.08 eV neutron energy versus 12400 eV X-ray energy for a wavelength $\lambda = 1$ Å.

In this chapter the main properties of neutrons and X-rays are presented and the similarities and differences in their scattering interactions with matter are analysed. Some general information on their production is also given. Thereafter the main scattering techniques (small-angle scattering of neutrons and X-rays) used for the scope of the thesis, are described.

1.2 Neutrons Versus X-Rays

Because of the wave-particle duality neutrons possess a wavelength which can be calculated using:

$$\lambda_n[\text{Å}] = \frac{h}{\sqrt{2m_n E_n}} = \sqrt{\frac{81.8047}{E_n[meV]}} \tag{1.1}$$

where h is the Planck constant, m_n is the mass of the neutron and E_n its energy. Depending on a neutron's kinetic energy, its wavelength can be comparable with interatomic distances[1]. As an example, a neutron with energy E = 2.3 meV has a wavelength of λ = 6 Å. Similarly, X-rays have wavelengths comparable to interatomic scales. They are a form of electromagnetic radiation (the term X-ray radiation and X-ray photons are used interchangeably in this thesis for describing X-rays since photons are the carrier particles of electromagnetic radiation) with energies ranging from 100 eV to 100 KeV corresponding to wavelengths of 10 to 0.01 nm. The high energies of X-rays make them less appropriate for studying low-energy excitations and introduce the possibility of damaging samples.

A schematic comparing the interaction of neutrons and other forms of radiation (e.g. X-rays or electrons) with matter can be seen in Fig. 1.1. Neutrons interact with atomic nuclei through short-range nuclear interactions. Because they possess a magnetic dipole moment μ_n ($\sim$0.001μ_B), they also interact with magnetic fields from unpaired electrons (Fig. 1.1) and can be manipulated by external magnetic fields[2]. For that reason, neutrons are sensitive to the magnetic properties of materials.

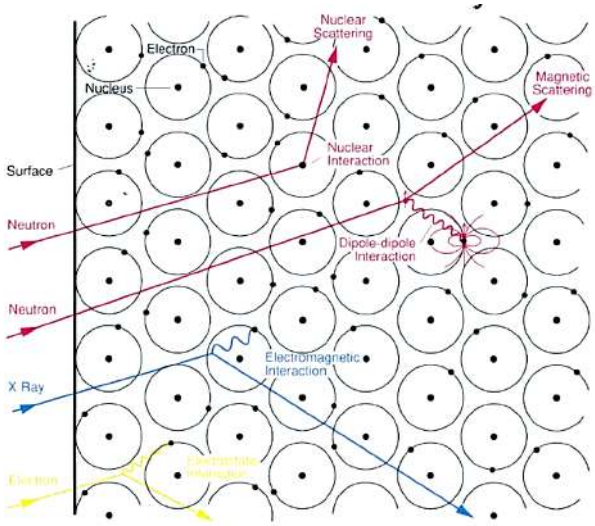

Figure 1.1: Comparison of neutron (red), x-rays (blue), and electron (yellow) interaction with matter[3]. Electrons and X-rays mainly interact with the electron cloud in the material, while neutrons interact with both nuclear potentials as well as magnetic structures.

Additionally, neutrons hold no electric charge thus they penetrate matter easily and do not destroy the samples under investigation[2]. X-rays are charge-less like neutrons, but are less penetrating and more damaging due to their interactions with the electron cloud. Consequently, neutrons can be used with a variety of different sample environment equipment in the path of the beam, such as cryomagnets, cryostats, and furnaces.

Neutrons appear superior to X-rays due to their adaptability to many different measurement methods. A major drawback of neutrons is that neutron sources generally have low flux[2]. As a result, the experimental time can be longer than in other techniques and samples need to be relatively large (e.g. 100 mm^2 surface area and at least 0.1 mm in thickness). Comparatively, a major advantage of using X-rays is that they are relatively easy to produce, because the production doesn't require nuclear processes. X-ray sources

such as synchrotrons, have high brilliance, e.g. 10^{21} $\frac{\text{photons/s}}{\text{mrad}^2 \cdot \text{mm}^2 \cdot 0.1\%\text{BW}}$ for PETRA III, DESY, Germany. As a result, experimental time can be quite short, and investigations can be performed with smaller volume or quantity of samples.

Another problem occurring with the use of neutrons is that during an experiment, samples of specific compositions can become activated. For that reason it is very important that their compositions are well known prior to any measurement. Also, as shown in Fig. 1.2, some elements such as Cd, Sm, or B absorb neutrons massively. Probing samples containing these elements can therefore be quite challenging.

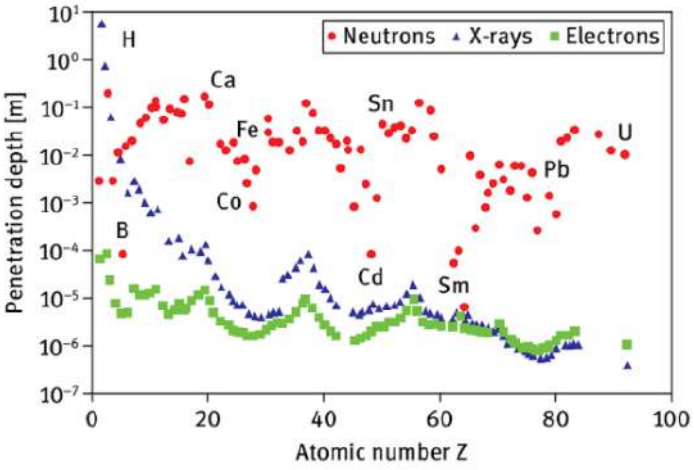

Figure 1.2: Graph showing the dependency of the penetration depth of different forms of radiation on the atomic number of elements[3,4]. The penetration depths of X-rays and electrons display an overall decreasing trend with increasing atomic number, while the penetration depth with respect to neutrons appear more randomly scattered. Here neutrons with a wavelength of 1.4 Å are used[3,4].

Because of long neutron measurement times originating from a combination of low flux and possible high absorption of neutrons, X-rays are usually preferred for purely structural studies. One exception is samples with a high amount of light elements such as hydrogen. Since the interaction of X-rays with atoms is due to the electrons in the atomic shells, X-rays are insensitive to light elements and the interaction gets stronger with increasing atomic number. Furthermore, because neutron interactions with hydrogen and deuterium are widely different, deuterium labelling method, also referred to as deuteration, is one key advantage of neutron scattering that can be used for the enhancement of contrast in

samples containing hydrogen[5].

1.3 Neutron & X-Ray Production

1.3.1 Production of Neutrons

Since the very beginning of research with neutron scattering, there has been an increasing demand for higher neutron fluxes. Neutrons can be produced via many different processes, which usually involve the use of heavy nuclei such as U or Pb. Neutrons are one of the fundamental building blocks of matter that can be released through (i) the fission process by splitting atoms in a nuclear reactor or (ii) the spallation process by bombarding heavy metal atoms with energetic protons. Fission reactors are continuous neutron sources generating a relatively constant stream of neutrons whereas spallation sources generate neutrons with a pulse.

Nowadays, the highest neutron flux of a continuous source is around 10^{15} n/cm^2 s right after neutrons exit the core of the reactor with a thermal power of around 58 MW (ILL, Grenoble, France). Due to heat removal restrictions of continuous-mode reactors, the neutron flux is unlikely to increase. Because of the nature of their operation, spallation sources can reach even higher neutron fluxes; the pulsed-mode operation makes heat removal easier than it is for fission reactors[6]. A schematic comparing thermal neutron fluxes of fission reactors and spallation sources, over the years, can be seen in Fig. 1.3.

1.3.1.1 Nuclear Fission

Nuclear fission is the process of heavy nuclei, such as U-235 or Pu-239, splitting into lighter ones after their bombardment with energetic particles. The fission reaction and its products can be seen in Fig. 1.4. During a nuclear fission reaction substantial amounts of energy (∼200MeV) are produced mainly in the form of kinetic energy of the fission-produced nuclei (fragments) as well as gamma radiation and fast neutrons[8]. The fission

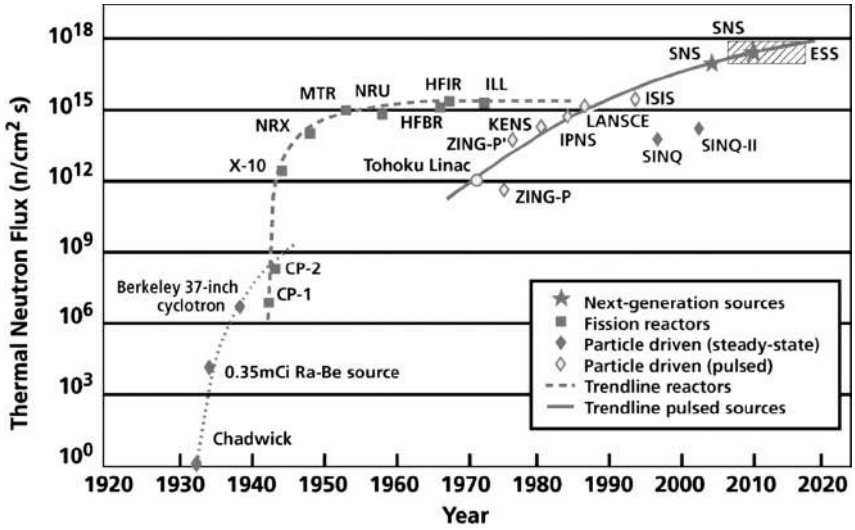

Figure 1.3: Comparison of the neutron flux of several neutron sources, both continuous and pulsed. As evidenced by the trend lines, massive further improvement of the flux of continuous sources is unlikely to occur. Hence, all of the next generation sources, such as the soon to be built European Spallation Source (ESS), are pulsed[7].

fragments since they are massive particles remain inside the reactor's core, but neutrons and gamma radiation penetrate matter easily and need to be properly shielded. For neutron scattering experiments, fast neutrons (and energetic gammas) are not desirable and are not permitted to reach the experimental hall and detectors. In order to be used for any measurements, fast neutrons are first slowed down using a moderator, such as H_2O or heavy water[1]. The neutrons are then guided within special designed tubes to be used for thermal and cold neutron scattering; cold and thermal neutrons have kinetic energies below 1 eV[8] (cold neutron energy is 0 – 0.025 eV and thermal neutron energy is about 0.025 eV)[9].

1.3.1.2 Spallation

Spallation describes a nuclear process where a target is hit by high-energy particles and thus induced to eject fragments of itself such as neutrons. In a spallation source, protons are produced and guided into a synchrotron ring, where they are accelerated and typically reach energies in the range of 500 – 800 MeV[10]. When their energy is sufficiently high

they are guided onto a neutron rich target of high Z such as W-183. From the collision of the energetic protons with the target material 10–30 neutrons/proton are produced with their kinetic energy being around 1 MeV[10]. Afterwards, the produced neutrons are processed and manipulated in the same manner as for fission reactors to be used for neutron scattering experiments. A schematic of the spallation process and its products is shown in Fig. 1.4.

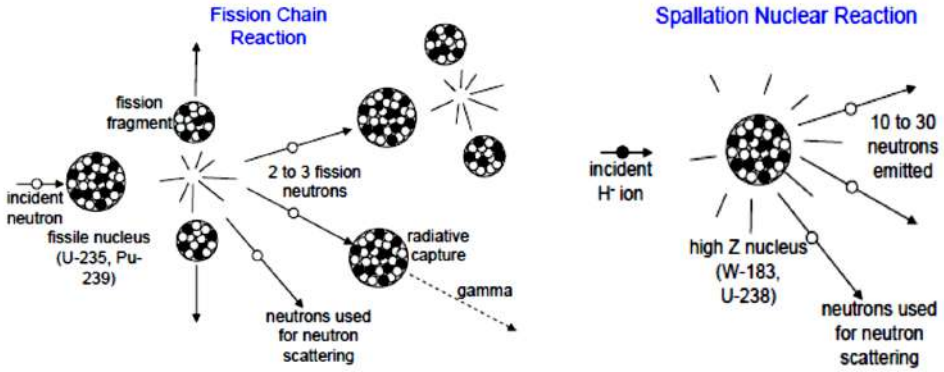

Figure 1.4: Depiction of the fission (*right*) and spallation (*left*) processes. As part of the fission chain reaction, the target nucleus is fragmented into smaller nuclei also producing neutrons and gamma radiation, while the spallation nuclear reaction results in the emission of neutrons alone. More neutrons are created per reaction event during the spallation process[6].

1.3.2 X-Ray Production & Synchrotron Radiation

X-rays are produced when energetic charged particles, such as electrons, interact with matter. In laboratory-based sources, the electrons are produced by heating up a filament (cathode) and then accelerated within vacuum by applying a high voltage towards a metal target (anode).

The generation of X-rays can happen in two different ways, one being the so-called characteristic X-ray generation and the other bremsstrahlung or "braking" X-ray generation[11]. The first occurs when an electron of high energy, shot at an atom, collides with an inner shell electron ejecting it from the atom producing a "hole" within the shell. An outer shell electron the fills the gap with the transition generating an X-ray photon. The

second is the process when an accelerating electron passes near a nucleus of an atom, decelerates and has its trajectory alternated. The energy lost during this process is emitted as an X-ray photon.

For obtaining faster, more detailed and accurate results from X-ray diffraction/scattering experiments, synchrotron radiation and not lab-based X-rays are used. The main difference is in the source's brilliance; a synchrotron source is $\sim 10^9$ times brighter than a laboratory X-ray source. Synchrotron radiation is generated in accelerators when charged particles, such as positrons or electrons, are accelerated to velocities approaching the speed of light and their trajectory is changed in magnetic fields to keep them in circular orbit.

The main parts of a synchrotron are the electron gun, the linear accelerator (LINAC), the booster synchrotron, the storage ring, and the beamlines[12,13]. After the electrons are produced in the electron gun they are first accelerated by the LINAC and guided into the booster synchrotron. The booster synchrotron plays the role of a pre-accelerator where the electrons are accelerated into higher speeds before injected into the storage ring. The

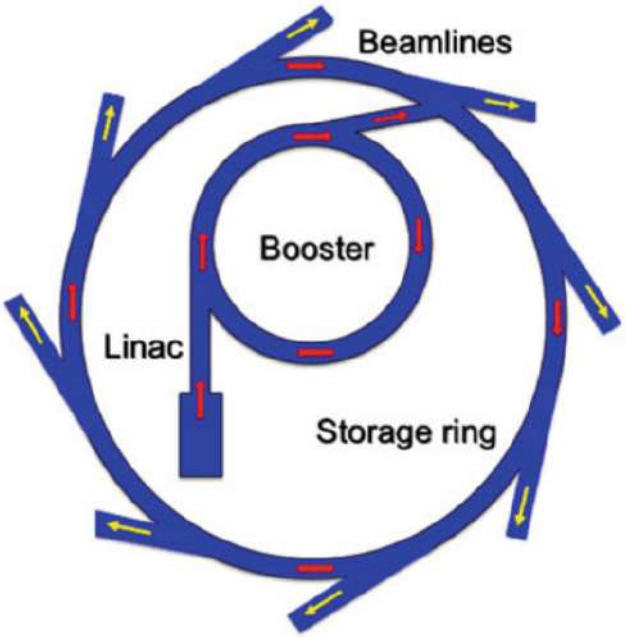

Figure 1.5: Schematic representation of a synchrotron that consists of the linear accelerator (LINAC), the booster, the storage ring as well as the various beamlines[13].

booster synchrotron only operates a few times within a day, as long as needed for the storage ring to be refilled. The storage ring is where the electrons are kept in circular orbit, at a constant energy, close to the velocity of light. A schematic of a synchrotron and the storage ring is depicted in Fig. 1.5. The generated radiation is then guided towards the so-called beamlines, positioned by the accelerator pointing radially outwards, to be used by scientists. Each beamline is designed to be used for a specific technique and for different areas of research.

1.4 Main Types of Scattering

Just like electromagnetic waves or electrons, once a neutron beam interacts with a sample, four phenomena may occur: transmission, absorption, scattering, or reflection. The scattering could be either elastic or inelastic: within the first case we refer to diffraction, whereas within the second case we refer to spectroscopic analysis[6].

In elastic scattering, as the term elastic denotes, there is no energy transfer to or from the atoms in the sample studied. In an elastic scattering experiment all the information about the scatter exists in the neutron intensity measured as a function of the momentum transfer $\vec{q} = \vec{k_f} - \vec{k_i}$, $|\vec{q}| = 4\pi/\lambda \cdot \sin(\theta)$, where $\vec{k_i}$ and $\vec{k_f}$ are the incident and final (scattered) neutron wave vectors respectively, λ is the neutron wavelength and 2θ the scattering angle[14]. The vector $\vec{q}$ is typically referred to as the scattering vector. The structure of materials can be studied using diffraction techniques which include small-angle scattering. Surfaces and interfaces can be analysed using techniques such as reflectometry.

During scattering, neutrons as well as X-rays can exchange energy with the atoms with which they interact. This phenomenon, called inelastic scattering (or quasielastic for nearly zero energy transfer) will set the atoms in motion, and can therefore reveal information regarding the system's dynamics. The spectroscopical techniques mostly used are time of flight, spin echo and three-axis spectroscopy.

1.5 Scattering Basics

A scattering event can be either elastic or inelastic. The distinction between the two types of scattering lies on whether the interaction between the neutron or photon and the sample involves just a momentum transfer or both a momentum and energy transfer. In either case, the momentum change, $\vec{p}$, is expressed by

$$\vec{p} = \hbar\vec{k}_i - \hbar\vec{k}_f \tag{1.2}$$

with $\vec{k}_i$ being the wave vector corresponding to the incident neutron or photon and $\vec{k}_f$ corresponding to the wave vector of the scattered particle. The constant $\hbar$ is the reduced Planck constant. The difference between the two defines the scattering vector $\vec{q}$. In the case of inelastic scattering, the energy change is given by

$$E = \hbar\omega, \quad \omega = \omega_i - \omega_f \tag{1.3}$$

with ω_i and ω_f being the angular frequency of the incoming and scattered particle respectively.

The discussion will be focused on elastic scattering so we take $E = 0 \Longleftrightarrow \omega = 0$ and $|\vec{k_i}| = |\vec{k_f}| = 2\pi/\lambda$. The modulus of the scattering vector is $|\vec{q}| = \frac{4\pi}{\lambda}\sin\theta$. Let us now consider an atom with its nucleus resting at the origin of the coordinate system as depicted in Fig. 1.6. An incoming beam of neutrons or X-rays with wave vector along the z-axis will have a wavefunction given by

$$\Psi_i = e^{ik_i z} \tag{1.4}$$

After interacting with the nucleus, the scattered wave function can be described as

$$\Psi_f = f(\lambda, \theta)\frac{e^{ik_f r}}{r} \tag{1.5}$$

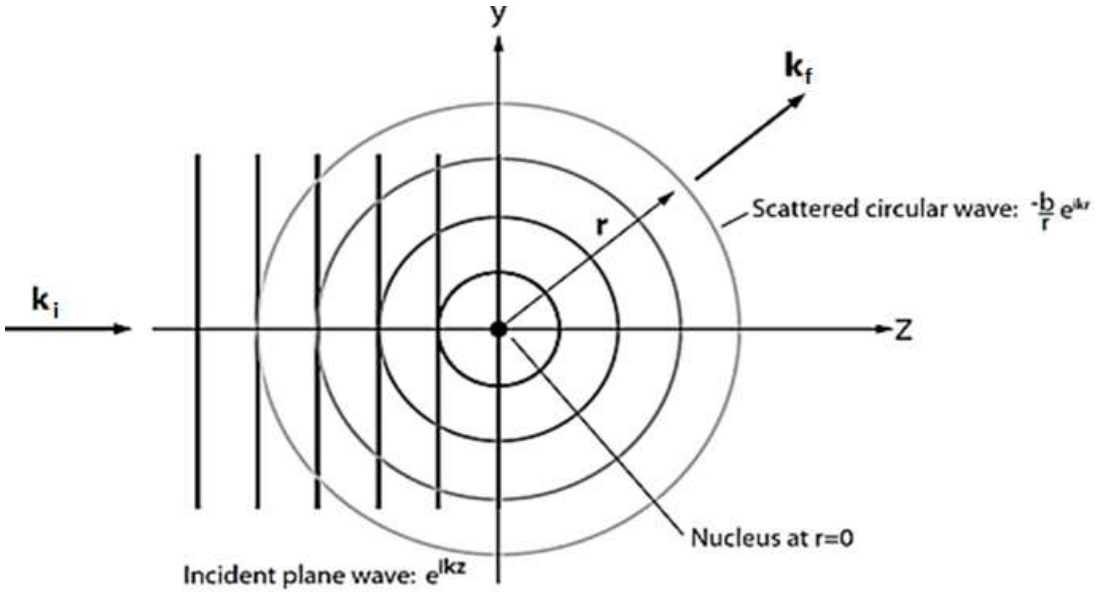

Figure 1.6: Illustration of an elastic scattering event. A fixed nucleus is placed at the centre of the coordinate system, with which the incoming neutron, described as a plane wave with wave vector $\vec{k}_i$, interacts. The resulting scattered wave is approximated as a circular wave with wave vector $\vec{k}_f$.[3].

where the function $f(\lambda, \theta)$ gives the probability of a particle of a given λ to be deflected in a direction θ. On account of the fundamentally different nature of neutrons and X-rays and how they interact with matter, the formulation of $f(\lambda, \theta)$ will vary between the two.

Let us first consider the interaction of neutrons with the nucleus of an atom. As an approximation, the Fermi pseudopotential is used to describe the interaction[15]. This effective potential is defined as:

$$V(\vec{r}) = b_j \delta(\vec{r} - \vec{r_j}) \tag{1.6}$$

where δ corresponds to the Dirac delta function and b corressponds to the so-called nuclear scattering length. The nuclear scattering length is a measure of the interaction between the neutron and the nucleus[6,15,16]. The use of the Dirac delta function implies that the nucleus is approximated to be a point scatterer[17]. This approximation is accurate due

the range of the nuclear forces (10^{-14} to 10^{-15} m) that cause the scattering being much shorter than the wavelength of the neutrons (10^{-10} m), which further implies that the scattering wave is spherically symmetric[3,14,17]. The scattering length b is connected to the function $f(\lambda, \theta)$ by $f(\lambda, \theta) = -b$. Consequently, following equation 1.5 the scattered neutron wave will have a wave function given by

$$\Psi_f = -\frac{b}{r} e^{ik_f r} \tag{1.7}$$

Moving to a more realistic setting, where scattering happens from a three-dimensional arrangement of nuclei, the Fermi pseudopotential is formulated as:

$$V(\vec{r}) = \sum_j b_j \delta(\vec{r} - \vec{r_j}) \tag{1.8}$$

The above potential gives rise to a scattered wave, which is written as a superposition of the scattering waves from each individual nuclei:

$$\Psi_f = -\sum_j \left(\frac{b_j}{r}\right) e^{i\vec{q}\cdot\vec{r_j}} \tag{1.9}$$

with $\vec{q} = \vec{k_f} - \vec{k_i}$ being the scattering vector.

It is necessary to mention that the negative sign in equations 1.7 and 1.9 is a matter of convention; if one assumes a positive value of b the negative sign denotes a repulsive interaction potential. It needs to be pointed out that b is complex and its imaginary part corresponds to absorption[15,18]. Materials such as Cd or V that have quite large imaginary part of their scattering length, are high neutron absorbers[14,18] with Cd commonly used for blocking neutrons.

X-ray radiation, being part of the electromagnetic spectrum, consists of oscillating magnetic and electric fields. As a result they interact with the electric charge of the electronic cloud of atoms[17] but not as strongly as fixed-charge particles such as electrons. The elastic scattering of X-rays is also referred to as Thomson scattering. As was done for

neutrons, an electron's capacity for scattering an incoming X-ray beam can be quantified by the corresponding scattering length. The X-ray scattering length of a free electron is given by[11,17]

$$r_e = \frac{e^2}{4\pi\epsilon_o m_e c^2} = 2.82 \quad \times 10^{-15} \text{ m} \tag{1.10}$$

with e, m_e, and c corresponding to the charge of the electron, the mass of the electron, and the speed of light respectively and ϵ_o to the permittivity of free space. The scattering length is also referred to as Thomson scattering length or as the classical radius of the electron[11,17] and it is proportional to the function $f(\lambda, \theta)$ ($f(\lambda, \theta) \sim f_o r_e$). The term f_o is known as the *atomic form factor* and so the scattered X-ray wave will have a wave function

$$\Psi_f \sim f_o r_e \tag{1.11}$$

We can now generalise the aforementioned discussion for an assembly of electrons in an atom. The incoming X-ray beam will hit the atom and interact with its collection of electrons in its atomic shells as depicted in figure 1.7. In order to consider the total scattering from the electronic cloud an integration over all contributions of the electrons residing within different shells should be performed. The atomic form factor is then given by the integral[11,19]

$$f_o = \int \rho_e(\vec{r}) e^{i\vec{q}\cdot\vec{r}} d\vec{r} \tag{1.12}$$

where ρ_e is the electron density. In the limit of a vanishing scattering vector, $q \to 0$, the nuclei scatter in phase so that $f_o(q = 0) = Z$, where Z is the atomic number of the element.

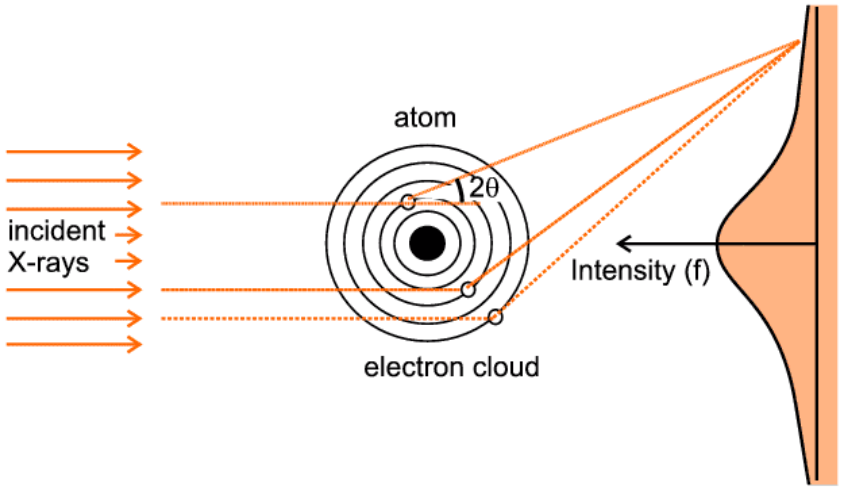

Figure 1.7: Schematic illustration showing the scattering of X-rays by the electronic cloud of an atom and the resulting intensity profile. X-rays scatter elastically from the electron cloud (Thomson scattering) with a scattering angle of 2θ as given by Bragg's law, $2d{\cdot}\sin(\theta) = n\lambda$. The intensity peak at the centre of the scattering profile is caused by intensity contributions from unscattered X-rays.[20].

1.5.1 Differential Scattering Cross Section

With the term differential scattering cross section we refer to the area of the atom that effectively scatters incident particles and is what is being measured during a scattering experiment. The differential scattering cross-section by definition is given as

$$\frac{d\sigma}{d\Omega} = \frac{\text{number of particles scattered per second into } d\Omega}{\Phi d\sigma} \tag{1.13}$$

with Φ being the incident beam flux where scattered particles are measured at a solid angle $d\Omega$ along a direction θ,ϕ (see Fig. 1.8).

The total scattering cross-section is found from integrating equation 1.13 over all solid angles

$$\sigma_{tot} = \int_{allsolidangles} \frac{d\sigma}{d\Omega} d\Omega \tag{1.14}$$

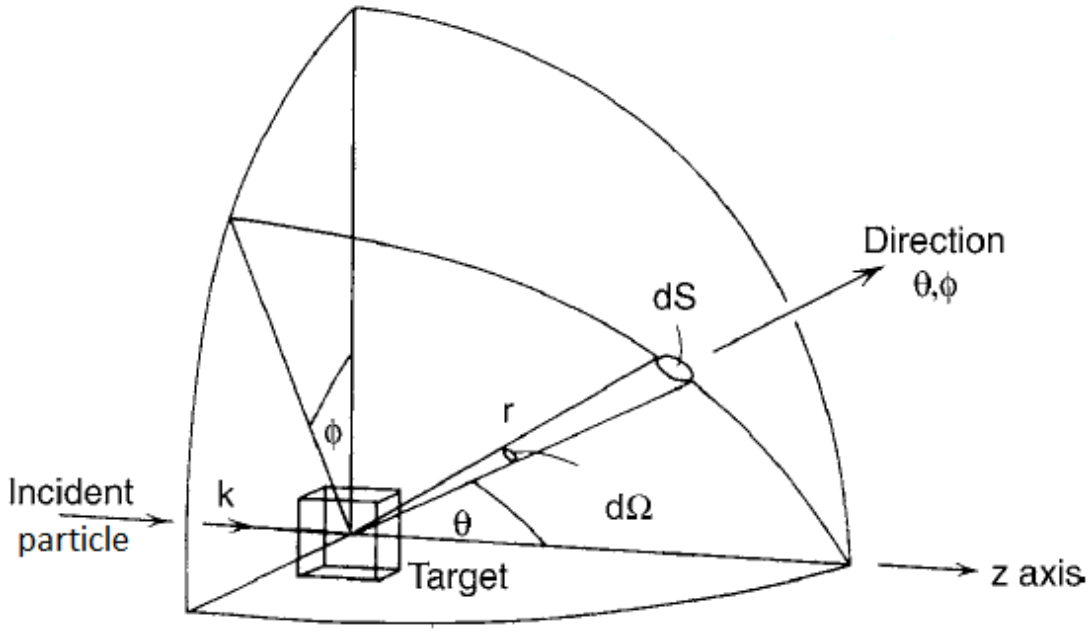

Figure 1.8: Geometry of a scattering experiment[16]. An incoming particle interacts with the target material and is scattered into the solid angle $d\Omega$, as quantified by the scattering cross section.

Taking the relations mentioned above under consideration one could calculate the differential scattering cross section $d\sigma/d\Omega$. Considering the velocity of particles to be v one can calculate the number of particles penetrating a surface area dS by

$$v dS \left|\psi_f\right|^2 \tag{1.15}$$

and the particle flux is given as

$$\Phi = v \left|\psi_i\right|^2 = v \tag{1.16}$$

If one first considers neutrons, the differential scattering cross section for neutrons can be derived by introducing equations 1.15 and 1.16 into equation 1.13 and considering equations 1.8 and 1.9[21]

$$\frac{d\sigma}{d\Omega}(\vec{q}) = \frac{1}{N}\left|\sum_{j}^{N} b_j e^{i\vec{q}\cdot\vec{r_j}}\right|^2 \tag{1.17}$$

where we normalise with the number of scattering bodies, N.

Following a similar process for X-rays, by taking into account equations 1.11 and 1.12 the differential scattering cross section for X-rays is[11,19]:

$$\frac{d\sigma}{d\Omega}(\vec{q}) \sim \left|\int \rho_e(\vec{r}) e^{i\vec{q}\vec{r}} d\vec{r}\right|^2 \tag{1.18}$$

When a beam is incident on a sample the scattering signal consists of coherent scattering, incoherent scattering, and absorption[22] thus the total scattering cross section σ_{tot} is:

$$\sigma_{tot} = \sigma_{coh} + \sigma_{inc} + \sigma_{abs} \tag{1.19}$$

Naturally occurring elements will typically consist of several different isotopes, each of which have their own neutron scattering length. The coherent scattering cross-section of a specific material is found by squaring the average of the included scattering lengths:

$$\sigma_{coh} = 4\pi\left(\frac{1}{N}\sum_{i=1}^{N} b_i\right)^2 = 4\pi\langle b\rangle^2 \tag{1.20}$$

Bragg scattering, which involves correlations between the positions of the atoms, is an example of a coherent scattering process. Likewise, inelastic scattering from phonons and magnons are coherent scattering processes that inform about the dynamic and magnetic properties of the material[18]. Incoherent scattering does not depend on any spatial correlation and the incoherent scattering cross section is instead caused by disorder in the scattering lengths:

$$\sigma_{inc} = 4\pi\left(\left\langle b^2\right\rangle - \langle b\rangle^2\right) \tag{1.21}$$

Incoherent scattering is therefore $\vec{q}$-independent and involves the correlation of a sin-

gle atom at different times. This also means that incoherent scattering doesn't affect the shape of the scattering signal. Examples of incoherent contribution are Stoner and crystal-field excitations as well as diffusions and nuclear excitations due to hyperfine field splitting[18].

For both neutrons and X-rays, σ_{abs}, gives the rate of absorption and varies with the wavelength, λ. Absorption (or transmission) depends on the sample's properties, such as thickness, density, and atomic number as well as on the the energy of the X-rays. Experimentally it can be calculated by

$$A = \frac{1}{T} = \frac{I_o}{I_t} \tag{1.22}$$

where A and T stand for absorption and transmission respectively. I_o denotes the intensity of the incoming beam and I_t the intensity of the beam transmitted through the sample. Considering a sample of thickness D, I_t is given by

$$I_t = I_o e^{-n\sigma_{abs}D} \tag{1.23}$$

where n is the number of atoms per unit volume and can be calculated using

$$n = \rho_{mac} \sum_i \frac{1}{m_i} \tag{1.24}$$

with ρ_{mac} being the sample's macroscopic density, and $\mathrm{m_i}$ the atomic mass of the $\mathrm{i^{th}}$ element within the sample. The product $n\sigma_{\mathrm{abs}}$ is the so-called *absorption coefficient* with its reciprocal giving the *absorption length* representing the average distance travelled by a particle in the sample before being absorbed.

1.5.2 Magnetic Scattering

In addition to nuclei, neutrons can also be scattered by unpaired electrons within atoms due to neutron's inherent magnetic moment. The theory for magnetic scattering is

very similar to nuclear scattering except that magnetic scattering occurs via a magnetic dipole interaction. Such interaction can take place either due to the magnetic moment corresponding to the intrinsic spin of the electron or due to magnetic fields produced by the orbital motion of the electrons. During a scattering experiment the two contributions cannot be separated so the total scattering signal contains information of the total magnetic moment within the specimen. Also taking into account that the electrons, with which the neutrons interact during magnetic scattering, are located in ranges greater than those of the nucleus size and that these ranges are in the same order of magnitude as the neutron's wavelength, the scattered wave cannot be considered to be a spherical wave as for nuclear scattering.

In order to describe the magnetic scattering of neutrons an expression for the interaction potential is necessary. The magnetic dipole moment for neutrons is $\vec{\mu_n} = -\gamma\mu_N\vec{\sigma}$ and that for electrons is $\vec{\mu_e} = -2\mu_B\vec{s}$, where $\gamma = 1.913$ and is known as the gyromagnetic operator and μ_N and μ_B are the nuclear and Bohr's magneton respectively. The term $\vec{\sigma}$ represents the operator of the neutron spin as given by the Pauli matrices and $\vec{s}$ is the spin angular momentum of the electrons[18]. The magnetic interaction potential is given by[18]

$$V_M(\vec{r}) = -\gamma\mu_N 2\mu_B\vec{\sigma}\cdot\left\{\nabla\times\left(\frac{\vec{s}\times\widehat{r}}{r^2}\right)+\frac{1}{\hbar}\frac{\vec{p}\times\widehat{r}}{r^2}\right\} \tag{1.25}$$

where $\vec{p}$ is the momentum of the orbiting electrons. The first term of 1.25 is due to spin and the second term represents the orbital motion of electrons. The resulting differential scattering cross section arising from the magnetic interaction of neutrons with electrons is proportional to the magnetic interaction potential.

It is important to point out that since the spins of a system have a direction the magnetic dipole interaction is also vectorial[18,23]. We define $\vec{M}_\perp$ to be

$$\vec{M}_\perp = \hat{q}\times\left(\vec{M}\times\hat{q}\right) = \vec{M}-\left(\vec{M}\cdot\hat{q}\right)\hat{q} \tag{1.26}$$

also known as the Halpern-Johnson vector, $\vec{A}$. $\vec{M}_{\perp}$ is the component of the magnetisation, $\vec{M}$, perpendicular to $\vec{q}$ (see Fig. 1.9). The above equation incorporates the interaction of neutrons with magnetic moments in the sample. Due to the dipolar nature of such interaction neutrons can only be scattered by the component of the magnetic moment (i.e. magnetisation) perpendicular to $\vec{q}$[18,23]. Detailed derivations of the above equation can be found in Ref. 18.

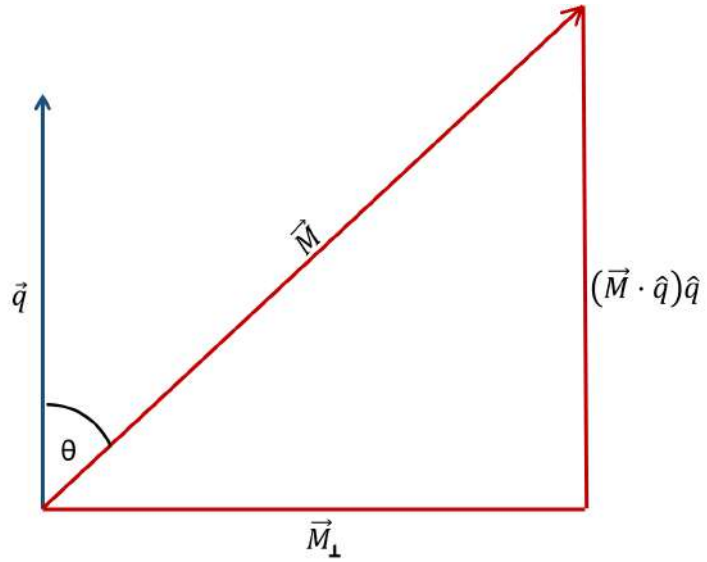

Figure 1.9: Schematic showing the component of magnetisation, $\vec{M}$, perpendicular to $\vec{q}$.

Magnetic neutron scattering can be used to investigate a variety of magnetic phases and phenomena from simple ferromagnetic phase transition and antifferomagnetism to superconductivity, skyrmions, and frustrated magnetism.

1.6 Small-Angle Scattering

With the term small-angle scattering (SAS) we refer to the coherent, elastic scattering of neutrons or X-rays at small angles, close to the incoming beam. The typical angle range for SAS is 0.2°-20°[6]. By using the definition of the scattering vector $|\vec{q}|$ and within the small-angle approximation, we have

$$|\vec{q}| = \frac{4\pi}{\lambda}\sin(\theta) \approx \frac{4\pi}{\lambda}\theta \tag{1.27}$$

and

$$d = \frac{2\pi}{|\vec{q}|} \approx \frac{\lambda}{2\theta} \tag{1.28}$$

meaning that for small angles, or equivalently small $|\vec{q}|$, the d-spacing is large. A typical $\vec{q}$-range, for example in Small-Angle Neutron Scattering (SANS), is between 0.001 Å^{-1} and 0.45 Å^{-1}, corresponding to d-spacings from 630 nm down to 14 Å but depending on the neutrons' wavelength and the neutron beam collimation during an experiment the size ranges probed can be between 1 nm and 10,000 nm[6].

The earlier discussion on neutron scattering involved atomic properties, for both nuclear and magnetic scattering. Due to the large size scales involved in SANS though, it is not convenient to employ the atomic properties but rather the material properties of samples. As a result, we introduce the nuclear scattering length density (SLD) defined as[21]

$$\rho_{nucl}(\vec{r}) = \frac{1}{V}\sum_{j}^{N} b_j \delta(\vec{r} - \vec{r_j}) \tag{1.29}$$

where $\vec{r}$ is the position vector within the sample, $\vec{r_j}$ is the position vector of the j^{th} atom, V is the volume of the sample, and b_j is the scattering length. When more than one phase is present within a sample one needs to account for all of them when calculating the scattering cross section. The SLD can then be calculated by

$$\rho_{nucl} = \frac{1}{V}\sum_{i} \chi_i b_i = \frac{d_{mac}}{M_{mol}}\sum_{i} \chi_i b_i \tag{1.30}$$

where χ_{i} is the atomic fraction of the element i in the phase, d_{mac} is the phase's macroscopic density, and M_{mol} is the molar mass of the system given by $M_{\mathrm{mol}} = \sum_i \chi_i M_i$ with M_i being the molar mass of the i^{th} element. Revisiting equation 1.17 one can now introduce the scattering length density into the differential scattering cross section formula

and replace the sum with an integral over the entire sample by normalising by the sample volume.

$$\frac{N}{V}\frac{d\sigma}{d\Omega}(\vec{q}) = \frac{1}{V}\left|\int \rho(\vec{r})e^{i\vec{q}\cdot\vec{r}}d\vec{r}\right|^2 \tag{1.31}$$

The nuclear scattering length density difference, also referred to as *nuclear contrast* corresponding to different phases is $\Delta\rho^2_{nucl} = (\rho_1 - \rho_2)^2$. The corresponding magnetic scattering length density for neutrons is given by

$$\rho_{magn} = \frac{d_{mac}\mu}{M_{mol}}\sum \chi_i \vec{M}_i \tag{1.32}$$

where $\vec{M}$ is the magnetisation of the phase in Bohr magnetons (not to be confused with the molar mass M) and $\mu = 0.27 \times 10^{-12}$ cm. The magnetic contrast factor in a sample is given as the difference between the magnetisation of different phases

$$\Delta\rho_{magn} \propto \mu_N \left[\frac{\vec{q}\times(\vec{M}\times\vec{q})}{q^2}\right] \propto (\vec{M}_i - \vec{M}_j) \tag{1.33}$$

where i, j here denote different phases within the sample (e.g. matrix and scatterers). For X-rays instead of the scattering length density we use the electron density (as presented in the previous section) and is given by

$$\rho_{elec} = \frac{d_{mac}}{M_{mol}}\sum_i \chi_i Z_i \tag{1.34}$$

where Z_i is the atomic number of element i. In this case the contrast factor is the averaged electron density fluctuation squared, $\Delta\rho^2_{elec}(E) = (\rho_1 - \rho_2)^2$, of different phases, with E being the X-ray energy.

Assuming a simple two-phase system, e.g. spherically isotropic particles embedded in a matrix (i.e. solvent). The macroscopic scattering cross section received by SAS is given by[6,24]

$$\frac{d\Sigma(\vec{q})}{d\Omega} \sim N_o V_p^2 \Delta\rho^2 \left|F(\vec{q})\right|^2 S(\vec{q}) \tag{1.35}$$

where N_o is number density of the scatterers within the specimen, V_p is average volume of the particles, $\Delta\rho^2$ corresponds to the contrast factor of neutrons or X-rays, and $F(\vec{q})$ is the form factor of the scattering bodies that for spherical objects of radius R is given by[24]

$$|F(\vec{q}, R)| = 3\frac{sin(\vec{q}R) - \vec{q}R \cdot cos(\vec{q}R)}{(\vec{q}R)^3} \tag{1.36}$$

The term $S(\vec{q})$ is the inter-particle structure factor given by

$$S(\vec{q}) = \left|\sum_j^N e^{i\vec{q}\cdot\vec{r}_j}\right| \tag{1.37}$$

and for randomly-oriented dilute systems it is $S(\vec{q}) = 1$[6,21].

Since the contrast factor, $\Delta\rho^2$, is the scattering length density (or electron density) difference squared, $(\rho_1 - \rho_2)^2$, one can see that during a scattering measurement only $\Delta\rho^2$ can be determined and is not possible to know if $\rho_1 > \rho_2$ or the other way around. This is the so called "phase problem" meaning that one cannot retrieve information on the phase of the system[6]. The scattering measurements take place in reciprocal space (also referred to as Fourier space) as can be seen by equation 1.37 and in order to retrieve real space size information either a Fourier transformation or fitting of known models is required.

In Fig. 1.10 examples of scattering curves for different scattering objects are provided. From the figure it is seen that the scattering curves for monodispersed spheres and cylinders (Fig. 1.10(a) and 1.10(b)) are very similar while the curve of polydispersed spheres (Fig. 1.10(c)) is smeared out due to the size distribution. The defining parameters in all three cases are the volume fraction of the scattering objects, their size (or size distribution), and the contrast between the scattering objects and the matrix (given as the square of the difference between the scattering length or electron densities). All these parameters can be used as fitting parameters during model fitting processes. Regarding the size of

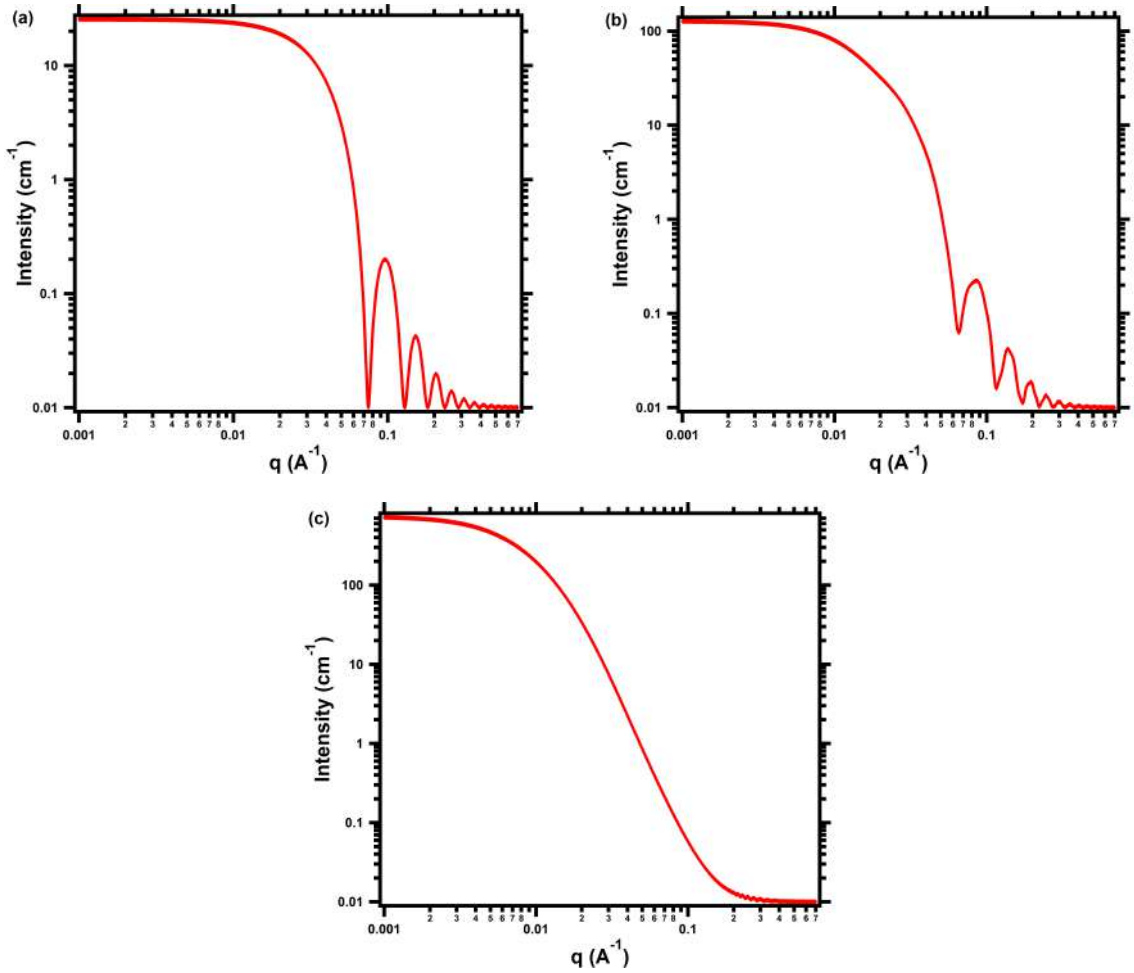

Figure 1.10: Theoretical scattering curves of (a) monodispersed spheres, (b) monodispersed cylinders, and (c) polydispersed spheres with a log-normal size distribution. For the monodispersed spheres a radius of 60 Åwas chosen. The corresponding bump on the scattering curve if found at $\vec{q} = 0.017$ Å^{-1}. A median radius of 60 Åwas also chosen for the log-normal distribution of the polydispersed spheres. The radius of the cylindrical objects is also 60 Åwhile their length was kept at 400 Å. For all three models a volume fraction of 0.01 and a scattering contrast of 5×10^{-6} was chosen.

the scattering objects (e.g. radius of spheres) the shape of the scattering curve gives an indication; the radius (or median radius in the case of a lognormal distribution) is given as $R = 2\pi/|\vec{q}|$ (or $R = 1/|\vec{q}|$ by approximation as is the case in the figures above). The

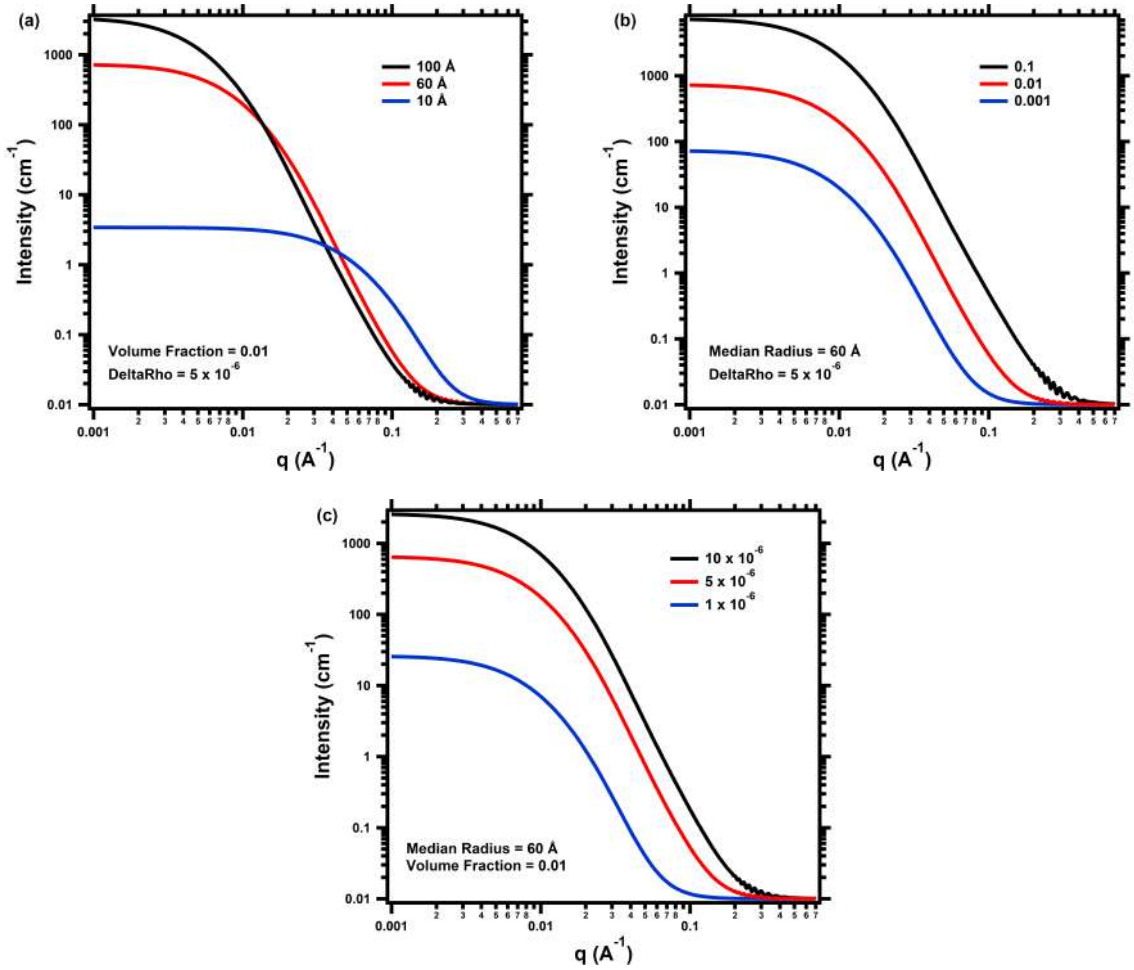

Figure 1.11: Theoretical scattering curves of spherical objects with a log-normal size distribution of varying (a) median radius, (b) volume fraction, and (c) scattering contrast. Decreasing the volume fraction or the scattering contrast results in a decrease of the scattering intensity while decreasing the median radius reveals a more complex behaviour by a simultaneous shift of the scattering curve in $\vec{q}$. This is expected since the scattering vector in reciprocal space and the real space size are connected as seen in equation 1.28.

volume fraction and the contrast factor are multiplicative factors and they are directly proportional to the scattering intensity. Their values cannot be known or indicated directly by the scattering curve or its shape but by having prior knowledge of the sample and the scattering bodies within it (i.e. composition and/or magnetic properties). Since all three aforementioned parameters contribute to the scattering intensity changing one

would affect the others, that would increase or decrease accordingly trying to fit the experimental scattering intensity. The way the fitting curve is affected by varying the fitting parameters is shown in Fig. 1.11. It is clear that changing the volume fraction or the scattering contrast will affect the intensity of the curve but changing the radius of the scattering objects will also result in a shift of the curve in $\vec{q}$. Overall a good (statistically) fit does not necessarily mean a realistic fit. The success of any fitting process also lies in the critical evaluation of the researcher. Regarding the aforementioned models (and similar models) it is safe to get a good starting value for the size of the scattering objects by looking at the position of any bump on the scattering curve and then try to fit the other parameters accordingly.

Regarding the scattering of an object by neutrons or X-rays, in both cases the scattering intensity would be given by equation 1.35. The main difference lies in the contrast factor that is calculated differently for the two probes and contains different information, as seen in equations 1.30 and 1.34. The information on the volume fraction and size of the scattering object should be the same whether that was probed with X-rays or neutrons.

1.6.1 Anomalous Small-Angle X-Ray Scattering

Anomalous small-angle X-ray scattering (ASAXS) is the term used for when, during a SAXS measurement, the scanning energies are in proximity to an element's X-ray absorption edge. This method utilizes the contrast differences of the scattering features that occur near the absorption edges of the elements within the sample due to the dependence of their scattering factor upon X-ray energy[25]. As a result, this technique allows the isolation of the scattering of a particular element and its contribution to the total SAXS profile with respect to the rest of the matrix, thus enabling the calculation of its spatial distribution.

The technique is called *anomalous* SAXS because one makes use of the anomalous properties of the atomic scattering factor, f. The atomic scattering factor is given as

the ratio between the amplitude of the wave scattered by an atom (more specifically by its electron distribution) and that scattered by a free classical electron[26]. The scattering factor, f, is given by

$$f(E) = f_o + f'(E) + if''(E) \tag{1.38}$$

where $f_o = Z$, with Z being the atomic number of the element, and E is the energy of the X-rays. The second and third term on the right hand side of 1.38 are anomalous dispersion corrections of the scattering factor in the vicinity of the X-ray absorption edge and depend on both the X-rays' energy and the atomic number, Z, of the element. The corrected atomic scattering factor is a complex number. As depicted in Fig. 1.12 the scattering factors change significantly close to the absorption edge. This change is due to

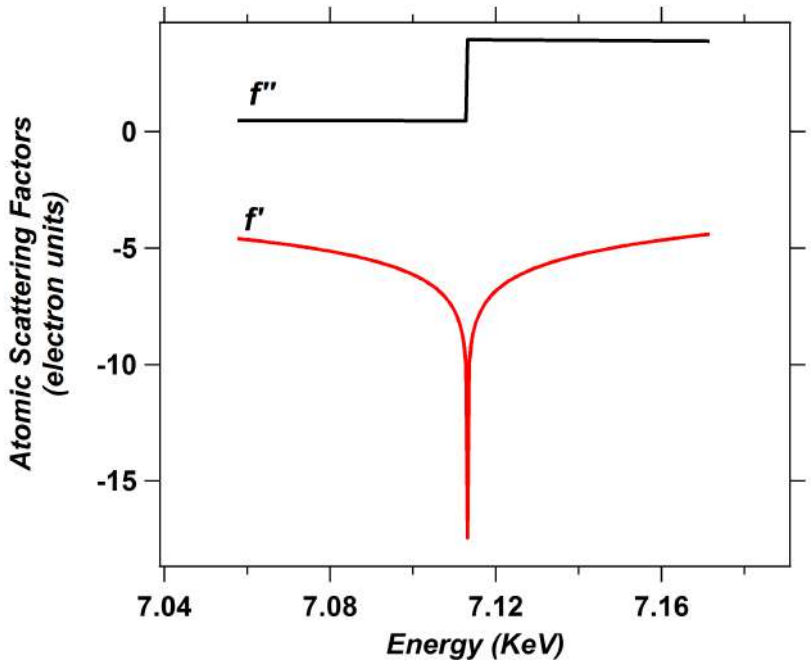

Figure 1.12: Atomic form factors of Fe as a function of X-ray energy, given close to the Fe K absorption edge. In the vicinity of the edge, f' decreases dramatically while the imaginary form factor f" increases. Values for both form factors have been extracted from the tabulated values by Cromer and Liberman[27].

resonant absorption by the bound electrons because of frequency matching. In order to calculate f' and f'' one can refer to the results of D.T. Cromer and D. Liberman (1970)[27]

where f'' is derived to be

$$f'' = \frac{m_e c \epsilon_o E \mu_a}{e\hbar} \tag{1.39}$$

where m_e represents the mass of the electron, c is the velocity of light in vacuum, e is the electron's charge, $\hbar$ is the reduced Planck's constant, and μ_a denotes the so-called attenuation coefficient. Consequently, equation 1.39 provides a relation between f'' and the attenuation coefficient, indicating that an increase of absorption translates to an increase of the imaginary part of the scattering factor and *vice versa*. A relation between f' and f'' is given by the Kramers-Kronig relation[27]

$$f'(E_o) = \frac{2}{\pi} \int_0^\infty \frac{E f''(E)}{E_o^2 - E^2} dE \tag{1.40}$$

Tabulated values for f' and f'', calculated theoretically, are given by Cromer and Liberman[27]. During a small-angle X-ray scattering investigation one also needs to take into account fluorescence. Fluorescence is the effect occurring due to the energy of the X-rays exceeding the electron bounding energy resulting in an increase of the background scattering signal. Therefore, during an ASAXS measurement, in order to avoid fluorescence, it is ideal to keep the X-ray energy below the absorption edges of the elements being present in the sample. If there is fluorescence adding to the measured background, its contribution can be removed from the SAXS measurements by measuring at wide angles.

Performing ASAXS on a system containing scattering features enriched with an anomalous element, allows the isolation of the scattering of that particular element from the total scattering and can be done both qualitatively and quantitatively. SAXS is a technique based in contrast variation between the electron density of scatterers and the electron density of the matrix.

The difference of the two electron densities squared, i.e. the contrast, is proportional to the square modulus of f(E) and is given by

$$(\Delta\rho(E))^2 \propto f^*(E)f(E) = f_o^2 + 2f_o f'(E) + f''(E)^2 \tag{1.41}$$

where again $\Delta\rho$ denotes the difference in electron density and it is energy dependent. Using this anomalous effect one can separate the resonant atom's contribution from the total scattering signal using the Stuhrmann method[28,29] following

$$I(\vec{q}, E) = i_o(\vec{q}) + f'(E)i_{oR}(\vec{q}) + (f'(E)^2 + f''(E)^2)i_R(\vec{q}) \tag{1.42}$$

where i_o is the SAXS term far from the absorption edge, i_{oR} is the scattering cross term that includes the amplitudes of both normal and resonant SAXS terms of the anomalous atoms, and i_R is the resonant term that originates from the absorbing atoms alone. By performing the experiment for three or four energies close to the absorption edge and solving the equation 1.42 one can isolate the resonant part containing information on the resonant scattering elements alone.

1.7 $\vec{q}$-Resolution of Small-Angle Scattering

During small-angle scattering measurements it is important that the $\vec{q}$-resolution is known. This can provide with an idea on what features the technique can resolve in $\vec{q}$-space. Resolution functions due to wavelength spread of the velocity selector or monochromator, collimation, as well as detector spatial resolution can all contribute to the overall resolution function[30].

It is apparent that the resolution of SANS and SAXS will differ; apart from the differences that the experimental set-ups might have and the different detectors used, the wavelength spread of the two probing beams is quite different as well. A typical wavelength resolution for SANS is $\Delta\lambda/\lambda = 0.1$ and that for SAXS is in the order of 10^{-3} or smaller. Calculations for $\vec{q}$-resolution usually take into account resolutions along the $\vec{q}$-vector and perpendicular to it separately. J. S. Pedersen *et al.*[30] via analytical treatment

of a resolution function were able to calculate all contributions under the assumption that all functions can be approximated as Gaussian distributions. Their results showed that along the nominal $\vec{q}$-vector, resolution due to the detector as well as collimation was independent of $\vec{q}$ and only changes due to wavelength spread were found, with the width increasing with increasing q. Calculations for direction perpendicular to the scattering vector showed that the width is independent of $\vec{q}$ for all contributions.

The above results indicate that even if all three contributions can be taken into account the one that makes the most difference is the contribution due to wavelength spread. Since the wavelength resolution of synchrotron X-rays is at least two orders of magnitude greater than that of neutrons it is apparent that the q-resolution will also be greater. Consequently, using X-rays will resolve narrower features in $\vec{q}$-space.

1.8 Concluding Remarks

In this chapter neutrons and X-rays were presented and it was established that both can serve as valuable probes for the investigation of matter and its properties. The specific technique of small-angle scattering can be used to provide information regarding features in the nano-scale (e.g. nano-precipitates) within a sample, such as volume fraction and size distribution as well as composition, offering at the same time a statistical average over a large volume of material. In the experimental part of the thesis the technique is employed to investigate precipitation in reactor pressure vessel steels and a binary Fe-Ga alloy, where neutrons and X-rays are used respectively.

References

[1] B. T. M. Willis and C. J. Carlile. *Experimental Neutron Scattering*. Oxford University Press, 2009.

[2] J. M. Carpenter and C. K. Loong. *Elements of Slow-Neutron Scattering*. Cambridge University Press, 2015.

[3] R. Pynn. *Neutron Scattering: A Primer*. Los Alamos Science. 1990.

[4] A. Braun. *X-ray Studies on Electrochemical Systems: Synchrotron Methods for Energy Materials*. Walter de Gruyter GmbH & Co KG, 2017.

[5] Y. B. Melnichenko and G. D. Wignall. Small-angle neutron scattering in materials science: Recent practical applications. *Journal of Applied Physics*, 102(021101), 2007.

[6] B. Hammouda. *Probing Nanoscale Structures - The SANS Toolbox*. 2016.

[7] M. Arai, T. E. Mason and K. N. Clausen. Next-generation neutron sources. *MRS Bulletin*, 28(12):923–928, 2003.

[8] S. C. Vogel and H. G. Priesmayer. *Neutron Production, Neutron Facilities and Neutron Instrumentation*, Volume 63 of *Reviews in Minerology and Geochemistry: Neutron Scattering in Earth Sciences*. 2006.

[9] N. J. Carron. An Introduction to The Passage of Energetic Particles Through Matter, CRC Press, Taylor and Francis Group. 2007.

[10] H. Conrad. *Spallation-Neutrons Beyond Nuclear Fission*, pages 721–757. Handbook of Particle Detection and Imaging. Springer-Verlag, Berlin-Heidelberg, 2012.

[11] J. Als-Nielsen and D. McMorrow. *Elements of Modern X-ray Physics*. Wiley, 2011.

[12] R. Treusch. *Radiation Sources: Production and Properties of Synchrotron Radiation*, pages 97–112. Neutrons and Synchrotronn Radiation in Engineering Material Science. Wiley-VCH, 2008.

[13] A. Balerna and S. Mobilio. *Introduction to Synchrotron Radiation*, pages 3–28. Springer Berlin Heidelberg, 2015.

[14] D. S. Sivia. *Elementary Scattering Theory For X-ray and Neutron Users*. Oxford University Press, 2011.

[15] H. Rauch and W. Waschkowski. *Neutron Properties-Neutron Scattering Lengths*. Neutron Data Booklet. OCP Science, 2003.

[16] G. L. Squires. *Introduction to the Theory of Thermal Neutron Scattering*. Cambridge University Press, 2011.

[17] A. Schreyer. *Physical Properties of Photons and Neutrons*, pages 79–90. Neutrons and Synchrotron Radiation in Engineering Material Science. Wiley-VCH, 2008.

[18] T. Chatterji. *Magnetic Neutron Scattering*. Neutron Scattering from Magnetic Materials. Elsevier, 2006.

[19] G. Porod. *General Theory*, pages 17–51. Small Angle X-Ray Scatteiring. Wiley-VCH, 2008.

[20] S. Jacques, P. Barnes and M. Vickers. *Scattering of X-rays by a Collection of Electrons as in an Atom*. http://pd.chem.ucl.ac.uk/pdnn/diff1/scaten.htm. Accessed: 27-01-2017.

[21] M. Laver. *Small-Angle Scattering of Nanostructures and Nanomaterials.* Encyclopedia of Nanotechnology. Springer, 2012.

[22] E. H. Kisi and C. J. Howard. *Applications of Neutron Powder Diffraction.* Oxford University Press, 2008.

[23] G. Kostorz. X-ray and neutron scattering. *Physical Metallurgy*, 2:1227–1316, 2014.

[24] R. P. May. *Small-Angle Scattering.* Neutron Data Booklet. OCP Science, 2003.

[25] R. W. James. *Optical Principles of the Diffraction of X-Rays.* Cornell University Press, 1965.

[26] C. Kittel. *Introduction to Solid State Physics.* Wiley, 1966.

[27] D. T. Cromer and D. Liberman. Relativistic calculation of anomalous scattering factors for X-rays. *The Journal of Chemical Physics*, 53:1891–1898, 1970.

[28] H. B. Sturhmann. Resonance scattering in macromolecular structure research. *Advances in Polymer Science*, 67:123–163, 1985.

[29] A. Hoell, D. Tatchev, S. Haas, J. Haug and P. Boesecke. On the determination of partial structure functions in small-angle scattering exemplified by $Al_{89}Ni_6La_5$ alloy. *Advances in Polymer Science*, 42:323–325, 2009.

[30] J. S. Pedersen, D. Posselt, and K. Mortensen. Analytical treatment of the resolution function for small-angle scattering. *Journal of Applied Crystallography*, 23(4):321–333, 1990.

CHAPTER 2

MAGNETOSTRICTION & MAGNETOSTRICTIVE MATERIALS: THE SPECIFIC CASE OF GALFENOL

2.1 Introduction

Magnetostriction is a phenomenon appearing, to some extent, in all ferromagnetic materials. It describes the change in size and/or shape of a material in response to a change in its magnetisation when an external magnetic field is applied. After the discovery of the phenomenon in Fe, by J. P. Joule in 1842[1], there was an extensive effort in exploring a variety of magnetostricive materials as well as their prospect applications as actuators, sensors, sonar systems and many others.

The highest value of magnetostriction exhibited by a material at room temperature is that of Terfenol-D, the commercial name of TbDyFe compounds. Terfenol-D exhibits a magnetostriction of about 2000 $\mu\epsilon$[2] but its poor mechanical properties, such as low tensile strength and brittleness, as well as the high cost of rare earth elements, render it non-ideal for practical use, especially in harsh environments.

An alternative to Terfenol-D is Galfenol. Galfenol is the commercial name of Fe-Ga binary alloys. Galfenol exhibits magnetostriction of up to 400 $\mu\epsilon$. This value is one order

[2]The S.I. unit for strain, $\delta l/l$, is 1 m/m = 1 ϵ. Most commonly strain is some orders of magnitude smaller, typically in the order of 1 μm/m and therefore the unit $\mu\epsilon$ (microstrain) is used.

of magnitude smaller than that of Terfenol-D but Fe-Ga alloys have very good mechanical properties, need low magnetic fields to reach saturation, and have low hysteresis. All these, along with the low cost for its production, make Galfenol a potential alternative to Terfenol-D.

Even if the resulting magnetostriction in Fe-Ga is known and exploited, its origin still lacks explanation. Two main theories have been proposed and experimental data have been brought forward supporting one or the other, yet to date conclusive evidence is missing. Despite this, it is generally acknowledged that magnetostriction in Fe-Ga is tightly connected to the Ga content and the thermal history of the alloys giving rise to a mixture of structural phases that seem to play an essential part in the manifestation of the phenomenon. A deep understanding of the various structural transitions is thus necessary to make a direct connection with magnetostriction in Galfenol.

In this chapter an overview of magnetostriction and its manifestation in Fe-Ga alloys is given. First a discussion on the basics of magnetism and magnetic states is provided with a focus on magnetism of 3d transition elements and more specifically Fe. The fundamentals of magnetic anisotropy and magnetostriction in cubic systems are presented next leading to a discussion on magnetostrictive materials focusing on Fe-Ga and the connection of magnetostriction with its microstructure.

2.2 Fundamentals of Magnetism

Magnetism, at the atomic level, originates from the magnetic dipole moments of atoms. Magnetic moments arise from unpaired electrons within the atoms, i.e. from partially filled atomic shells, due to orbital angular momentum and spin angular momentum. The former is the effect of the motion of the electrons orbiting the nucleus, while the latter is an intrinsic angular momentum, purely quantum-mechanical, acting as an extra degree of freedom and has no classical counterpart. Let us first consider an electron moving around a nucleus in a Bohr orbit of radius r having a velocity v, as depicted in Fig. 2.1.

The electron has a mass m_e and a charge -e. From classical physics, a circulating charge will generate a current $i = \mathrm{e}/T = \mathrm{e}v/2\pi r$, where T is the period of circulation within the loop (orbit). Such a current loop will generate a magnetic field which is the same as if a magnetic dipole were positioned at the centre of the loop of surface area A[2]. The magnetic dipole would be oriented perpendicular to A and would have a magnetic dipole moment, $\vec{\mu_l}$. Its magnitude is $\mu_l = iA$. Due to the circular motion the orbiting electron also has an orbital angular momentum, $\vec{L}$ with magnitude $L = mvr$. The ratio of μ_l with L is constant and in terms of fundamental constants is given by

$$\frac{\mu_l}{L} = \frac{\mu_B}{\hbar} \tag{2.1}$$

where μ_B is the Bohr magneton and is given by

$$\mu_\mathrm{B} = \frac{e\hbar}{2m} = 0.927 \times 10^{-23}\ \mathrm{A \cdot m^2} \tag{2.2}$$

and $\hbar = 1.054571800(13) \times 10^{-34}$ J·s is the reduced Planck's constant.

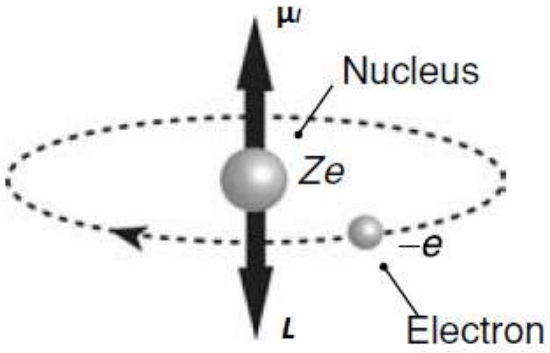

Figure 2.1: Simplified model of an atom with a nucleus in the middle and a single electron orbiting around it. A magnetic moment, $\vec{\mu_l}$, is generated due the orbital motion. The magnetic moment is antiparallel to its orbital angular momentum, $\vec{L}$[3].

Equation 2.1 can be written in a vector form giving both the magnitude of the magnetic dipole moment and its orientation relative to $\vec{L}$

$$\vec{\mu_l} = -\frac{\mu_B}{\hbar}\vec{L} \tag{2.3}$$

Quantum-mechanically, the magnitude of the orbital angular momentum is given by

$$L = \hbar\sqrt{l(l+1)} \tag{2.4}$$

where l is the so-called orbital angular momentum quantum number and takes integer values between 0 and n-1. The number n determines the size of the electron's orbit and defines its energy and it is known as the principal quantum number. The magnetic dipole moment is then given by

$$\mu_l = \mu_B\sqrt{l(l+1)} \tag{2.5}$$

and its z-component is given by

$$\mu_{l_z} = -\mu_B m_l \tag{2.6}$$

where m_l is the so-called orbital magnetic quantum number and takes integer values between -l and l. The negative sign indicates that the moment is antiparallel to the orbital angular momentum due to the negative electron charge, as seen in Fig. 2.1.

Experiments by O. Stern and W. Gerlach in 1922[4] led to the conclusion that electrons also have an intrinsic angular momentum, $\vec{S}$, called spin. The quantum-mechanical expression for the magnitude of spin is

$$S = \hbar\sqrt{s(s+1)} \tag{2.7}$$

with its z-component being

$$S_z = m_s\hbar \tag{2.8}$$

where s is the spin quantum number and m_s is the spin projection quantum number. The magnetic moment generated by the spin angular momentum, in vector form, is given by

$$\vec{\mu_s} = -g_e \mu_B \vec{S} \tag{2.9}$$

where g_e is the so-called spectroscopic splitting factor with a value of $2.002290716(10) \approx 2$[5]. For a free electron it is also referred to as the g-factor. The z-component of $\vec{\mu_s}$ is given by

$$\mu_{s_z} = -g_e \mu_B m_s \tag{2.10}$$

The experimental observation that the electron is deflected in only two directions, when sent through a non-uniform magnetic field, leads to the conclusion that μs_z can take only two values. If we consider that m_s takes values between -s and s, then for an electron with $s = 1/2$, $m_s = \pm 1/2$, corresponding to "spin up" and "spin down states".

The orbital angular momentum and the spin angular momentum are coupled via spin-orbit interaction. This spin-orbit coupling, also referred to as Russel – Saunders coupling, gives rise to a total angular momentum, $\vec{J} = \vec{L} + \vec{S}$, with $\vec{L}$ and $\vec{S}$ precessing around $\vec{J}$ (see Fig. 2.2).

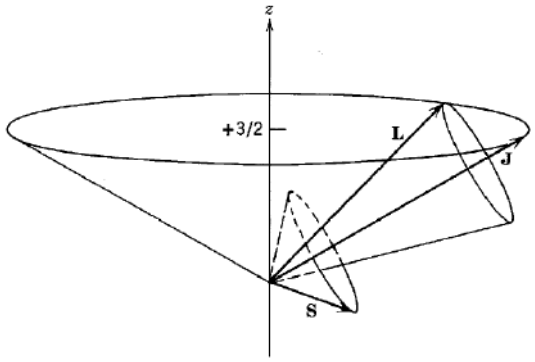

Figure 2.2: The total angular momentum $\vec{J}$ emerges from the spin-orbit coupling and is composed of a vectorial sum of the orbital angular momentum, $\vec{J}$, and the intrinsic angular momentum, $\vec{S}$. Both are precessing around $\vec{J}$[2].

Following a similar approach as for the orbital and spin angular momenta, the magnitude of the total angular momentum is given by

$$J = \hbar\sqrt{j(j+1)} \tag{2.11}$$

with j being the total angular momentum quantum number. To determine the values of j we make use of the inequality

$$|\vec{J}| = |\vec{L} + \vec{S}| \geqslant ||\vec{L}| - |\vec{S}|| \tag{2.12}$$

or equivalently

$$|\sqrt{j(j+1)}\hbar| \geqslant |\sqrt{l(l+1)}\hbar - \sqrt{s(s+1)}\hbar| \tag{2.13}$$

and for an electron with $s = 1/2$, the above relation is satisfied for $j = l + 1/2$, l - $1/2$. The z-component of J is given by

$$J_z = m_j\hbar \tag{2.14}$$

with m_j taking values between -j and +j. The total magnetic moment, in terms of the orbital and spin magnetic moments, will be given by

$$\vec{\mu} = -\mu_{\mathrm{B}}(\vec{L} + 2\vec{S}) \tag{2.15}$$

For a free atom in its ground state, $\vec{L}$, $\vec{S}$, and $\vec{J}$ can be determined by employing the so-called Hund's rules[5]. These are as follows:

- The electrons are arranged so as the value of S takes the maximum value without violating Pauli's exclusion principle. This results in electrons occupying different orbitals before starting pairing up thus minimizing the Coulomb energy due to repulsion. The spin-spin interaction within the atom dictates that when occupying different orbitals the electron's are arranged in a spin-parallel configuration.

- The orbital angular momentum L also takes its largest possible value as long as it

does not violate the exclusion principle and the first Hund's rule.

- If a shell is less than half full, J takes its possible minimum value with the ground-state assuming a value of $J = L$ - S, but if the shell contains more electrons J takes its maximum possible value hence the ground-state has a J equal to $L + S$.

The Russel-Saunders coupling (L-S coupling), discussed above, generally applies to light atoms (typically $Z < 30$) where the total spin $\vec{S}$ of a group of electrons is coupled with the total orbital angular momentum $\vec{L}$ of that same group resulting in the total angular momentum $\vec{J}$. In contrast, in heavier atoms, e.g. atoms of rare earth elements, the spin $\vec{s_i}$ and orbital angular momentum $\vec{l_i}$ of an individual electron are coupled to give the individual total angular momentum, $\vec{j_i}$, for that electron alone. Then all the individual total angular momenta are coupled resulting in the total angular momentum $\vec{J}$ of the system.

2.2.1 Magnetic States

All materials exhibit some sort of magnetic behaviour according to which they can generally be classified into six main categories: diamagnetic, paramagnetic, ferromagnetic, antiferromagnetic, ferrimagnetic, and magnetic glass[6]. Most of the elements in the periodic table are either paramagnetic or diamagnetic at room temperature with only four (iron, nickel, cobalt, and gadolinium) being ferromagnetic and only one (chromium) being antiferomagnetic.

2.2.1.1 Diamagnetism

Materials containing atoms with no unpaired electrons exhibit diamagnetic behaviour having a zero net magnetic moment when no external magnetic field is applied. Applying an external field results in acceleration and precession of the orbital electrons due to electromagnetic induction. Lenz's law dictates that application of an external magnetic field

induces an oppositely aligned magnetic flux in the sample. Consequently, the susceptibility of diamagnetic elements is negative and small, typically $\chi \approx -10^{-6}$ (dimensionless in SI units), with only bismuth having a susceptibility in the order of negative 10^{-4}. The orbitally induced magnetisation of diamagnetic materials is opposite to the applied field hence they are repelled by a magnetic field.

More or less all materials have diamagnetic properties always contributing to a material's response to a magnetic field but in non-diamagnetic materials the weak diamagnetic force is overcome by other stronger effects. Superconductors when in the Meissner regime are considered to be perfect diamagnets since they repel the magnetic field entirely and have the largest negative susceptibility of χ = -1.

2.2.1.2 Paramagnetism

Paramagnetism is a non-ordered magnetic state appearing in materials with unpaired electrons. The magnetic moments within paramagnetic materials orientate randomly because of thermal fluctuations. Under the influence of an externally applied magnetic field the moments slightly follow the direction of the field resulting in a net magnetic moment with the material weakly attracted by the field. A small magnetic field though is not sufficient to overcome the thermal agitation and large fields are required to induce a magnetically ordered state.

P. Curie was the first one to observe the temperature dependence of paramagnetic materials in 1895[7]. This dependence can be expressed by the so-called Curie law indicating that in paramagnetic materials the susceptibility, χ, decreases with increasing temperature. This is expressed by

$$\chi = \frac{C}{T} \tag{2.16}$$

where C is the so-called Curie constant, which is material-specific, and T is the temperature measured in K. As the temperature is lowered paramagnetic materials have higher

susceptibility. Later, in 1906, P. -E. Weiss[8] extended Curie's law into what is known as the Curie-Weiss law given by

$$\chi = \frac{C}{T - \theta_C}, \qquad (T > \theta_C > 0) \tag{2.17}$$

where θ_C is the paramagnetic Curie temperature and is a "transition boundary" below which there is a transition from the paramagnetic state to ordered magnetic states.

Some compounds and most chemical elements are paramagnetic and exhibit a magnetic susceptibility in the order of $\chi = 10^{-5} - 10^{0}$.

2.2.1.3 Ferromagnetism

Ferromagnetism is an ordered magnetic state exhibiting strong magnetic behaviour. The susceptibility of ferromagnetic materials is typically $\chi = 10 - 10^{7}$. As a result the induced magnetisation of such materials is very large. The reason of such strong magnetic behaviour is the strong atomic moments due to unpaired electrons, as discussed earlier, as well as the spontaneous magnetisation resulting from the alignment of magnetic moments parallel to each other facing the same direction creating magnetic domains each magnetised to saturation even in the absence of a magnetic field. The magnetic domains are separated by the so-called domain walls and do not necessarily have the same magnetisation direction although there might be a certain crystallographic axis, called the easy axis, with preferred moment orientation. If a magnetic field is applied all the magnetic domains start to align toward the field direction. This occurs by volume variation of the domains and domain wall movement as the magnetisation vector coherently rotates toward the direction of the applied magnetic field. P. -E. Weiss in 1906[8] was the first to explain the spontaneous magnetisation and proposed the mechanism of formation of magnetic domains (also referred to as Weiss regions) by introducing an effective molecular field, the Weiss mean-field. Originally the Weiss theory proposed that the molecular field was proportional to the bulk magnetisation but it failed to apply to ferromagnets

since the magnetisation varies from domain to domain. In this case the molecular field is proportional to the saturation magnetisation at T = 0 K.

W. K. Heisenberg, in 1928[9], introduced the exchange interaction between neighbouring spins, S_i and S_j, explaining the origin of the large molecular fields acting in ferromagnetic substances. The exchange interaction energy, E_{ex}, is the eigenvalue of the Hamiltonian

$$\mathcal{H}_{ex} = \mathcal{H}_{ij} = -2J\vec{S}_i \cdot \vec{S}_j \tag{2.18}$$

J expresses the so-called exchange integral (not to be confused with the total angular momentum). The exchange integral gives information on the lowest energy state, determining if it is spin parallel or spin anti-parallel. By convention it is spin parallel for positive J (resulting in ferromagnetic state) and spin anti-parallel for negative J (resulting in antiferomagnetic state).

Temperature is a decisive parameter in whether and how magnetism is expressed in any type of material. Spontaneous magnetization can only occur at sufficiently low temperatures, where thermal fluctuations are low and a long range order can emerge. In ferromagnetic materials, the critical temperature point at which a paramagnetic-to-ferromagnetic order transition occurs is known as the Curie temperature, T_c. The susceptibility of a ferromagnetic material behaves as according to the Curie-Weiss law

$$\chi = \frac{C}{T - T_C} \tag{2.19}$$

One observes that for T = $\mathrm{T_C}$ the susceptibility diverges meaning that there might be a non-zero magnetisation even at the absence of a magnetic field. This defines the Curie temperature as being the limit for emerging spontaneous magnetisation.

2.2.1.4 Antiferromagnetism & Ferrimagnetism

Antiferromagnetism is an ordered state where neighbouring spins are aligned anti-parallel so that the corresponding magnetic moments cancel each other. An antiferro-

magnetic material has a zero net magnetic moment and produces no spontaneous magnetisation, though in some cases a magnetic moment could appear due to canted antiferromagnetism. The small antiferromagnetic susceptibility is $\chi = 10^{-5} - 10^{-2}$, similar to that of paramagnetism. The difference between the two states is that in antiferomagnetism there is an ordered spin configuration. The susceptibility of an antiferomagnet increases with increasing temperature reaching a maximum value at a transition temperature, the Néel temperature, T_N. Above T_N the ordered state disappears completely and the material passes into the paramagnetic regime, following the Curie-Weiss law. In the antiferromagnetic regime the magnetic moments form two (or more) magnetic sublattices. In the vicinity of one sublattice the magnetic moments are the same, both in size and direction. As in antiferromagnetism, ferrimagnetic materials have at least two

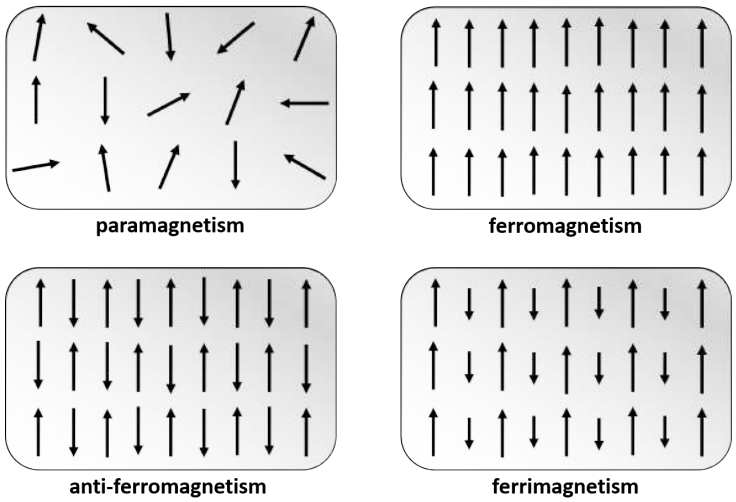

Figure 2.3: Summary of the spin arrangements corresponding to the magnetic states described in sections 2.2.1.2-2.2.1.4. Spins in the paramagnetic state are randomly oriented, while spins in the ferromagnetic state are all oriented along one directions. Antiferromagnetic and ferrimagnetic states are both constructed from two sublattices with oppositely aligned spins. The spins on the two sublattices all have the same magnetic moment in the antiferromagnetic state, but have differing values in the ferrimagnetic state. As a consequence, only the ferromagnetic and ferrimagnetic states have a finite net magnetization.

magnetic sublattices with anti-parallel configuration but in contrast to antiferomagnetism the magnetic moments do not entirely cancel each other. This is because the moments of different sublattices do not have the same magnitude. As a result a ferrimagnet has a spontaneous magnetisation but naturally its exchange integral, J, is smaller than that of a

ferromagnet. Above the Néel temperature, T_N, ferrimagnetic materials become paramagnetic. In Fig. 2.3 the spin orientation of paramagnetic, ferromagnetic, anti-ferromagnetic and ferrimagnetic materials can be seen.

2.2.2 3d Transition Metals and Magnetism of Fe

Fe is quite a significant element due to its magnetic properties. It is one of the three elements in the periodic table, along with Co and Ni, that are ferromagnetic at room temperature. It is part of the so-called 3d transition metals series. These 3d elements, from Sc to Ni, and all d-block (transition) elements are considered "special" because they have an "out of sequence" filling of atomic orbitals. Hund's rules, along with Pauli's exclusion principle, dictate that orbitals should be filled from inner to outer shells with increasing principal quantum number, n, i.e increasing energy. In the case of the 3d transition metals though, the 4s orbital is partially or fully occupied before the 3d orbital starts to get filled. 4d and 5d orbitals follow the same trend.

Following Hund's first rule, the most energetically favourable configuration in unfilled orbitals is a parallel spin configuration. Of course electrons due to Coulomb interaction repel each other and due to Heisenberg's exchange interaction being repulsive for parallel spins they repel each other further. As a result the separation for electrons with parallel spins is larger than for those with antiparallel spin configuration and the maximum separation is achieved when an equilibrium is reached with Coulomb repulsion decreasing. Unfilled orbitals with parallel spin configuration result in a net magnetic moment. For example, the Fe free atom with 5 spin-up electrons and one spin-down electron in the 3d orbital has a magnetic moment of 4 μ_B[10]. Despite the fact though that quite a few atoms have partially filled orbitals, i.e. unpaired electrons, most solids are non-magnetic (i.e. not magnetically ordered). This is due to the fact that when atoms come together to form bonds the electrons of the outer shells taking part in the bonding process are shared and their moments cancel. Consequently, solids retain the magnetic properties of their

corresponding atoms only when they have unpaired electrons in inner shells that do not participate in bonds. This is the case for transition metals (among a few other cases, e.g. rare earth elements).

Even if the magnetic moment of free Fe atom is in the order of 4 μ_B, the case is different for bulk bcc Fe of which magnetic moment is about 2.2 μ_B/atom[10]. This indicates that the magnetic properties of transition metals must be dependent on crystal structure. This cannot be more apparent than the case of Fe. Fe at atmospheric pressure can be in two structural phases, α-Fe with a bcc structure as the ground state at ambient temperature and γ-Fe with a fcc structure at higher temperatures. The bcc Fe structure is usually referred to as ferrite and the fcc as austenite. Ferrite is known to be ferromagnetic with a Curie temperature of 768 °C[11] over which it undergoes a second order transition into the paramagnetic phase. When γ-Fe is in its stable condition it is paramagnetic but studies have shown that it orders antiferromangetically at low temperatures[11,12].

Studies performed by V. L. Moruzzi *et al.*[13] in 1986, showed that in fcc γ-Fe a non-magnetic phase is energetically more favourable than a ferromagnetic ordering but they did not investigate the possibility of antiferromagnetism. More recently, D. Lee and S. Hong[12] by applying the full-potential linearized augmented plane wave method within the generalized gradient approximation showed that indeed for bcc Fe the ground state is ferromagnetic with a moment of 2.240 μ_B/atom, but for fcc Fe an antiferromagnetic state is more stable than both non-magnetic and ferromagnetic phases accompanied by a tetragonal distortion.

It is apparent that the bulk structure of Fe is quite significant for its magnetic properties and needs to be taken into account when investigating phenomena such as magnetostriction which is common in Fe-bearing compounds.

2.3 Magnetic Domains

It is established that a characteristic of ferromagnetism is the occurrence of spontaneous magnetisation due to the exchange interaction energy resulting in a spin-parallel configuration. The net magnetisation of the entire system though is not necessarily saturated. The reason for this is that if a sample's magnetisation is in the same direction throughout (i.e. magnetised to saturation), magnetic "free poles" appear on the surface of the material due to a discontinuous change in the component of the magnetisation normal to the surface. This produces a large demagnetising field and a large magnetostatic energy. The formation of magnetic domains is a direct consequence of the demagnetising field. Domains form so as to minimise the energy cost due to the demagnetising field by balancing the exchange energy with the magnetostatic energy. The magnetic moments within each individual domain are aligned parallel pointing in the same direction but the magnetisation of different domains is not necessarily collinear.

To understand how the above mechanism works one can have a look in Fig. 2.4. A material consisting of a single magnetic domain results in high magnetostatic energy. If the material is divided into two magnetic domains the magnetostatic energy is halved. Following the same principle, dividing a material into N domains results in a reduction of the magnetostatic energy by a multiplicative factor of $1/N$. Concurrently however, the formation of domain walls will increase the overall exchange energy due to the interaction of differently aligned spins between domains. The final number and orientation of domains is dictated by the balance between the overall magnetostatic energy and domain wall exchange energy. Generally, the most energetically favourable domain configuration is the so-called ring configuration (or closure domains), as given in the last part of Fig. 2.4, ideally resulting in zero magnetostatic energy.

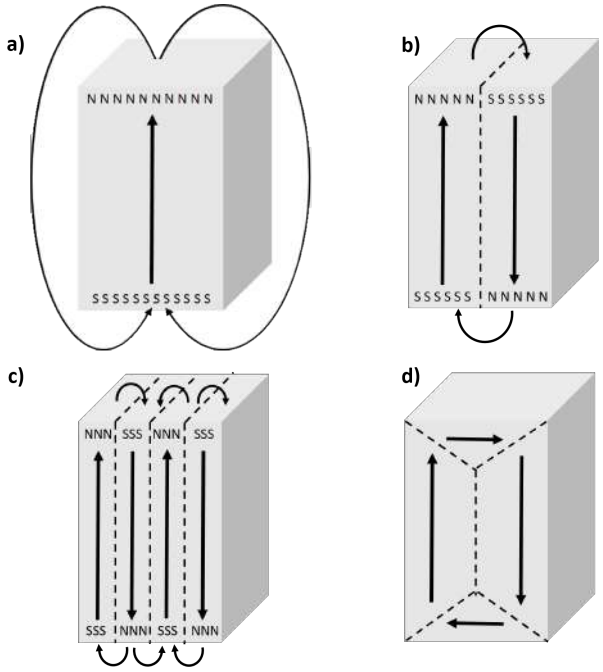

Figure 2.4: Illustration of how the formation of magnetic domains reduces the magnetostatic energy. In (d) the demagnetising field has vanished entirely due to the formation and orientation of magnetic domains. In an actual sample, domains will form to the extent that the magnetostatic energy is in equilibrium with the domain wall exchange energy.

2.4 Magnetic Anisotropy

Spontaneous magnetization is caused by the exchange interaction between spins. Assuming no other additional interactions, spins can freely align themselves along any direction within a crystal without changing the internal energy. Ferromagnetic materials exhibit a preferred crystallographic axis, better known as the easy axis, along which the overall magnetization tends to orientate. Deviation from the easy axis leads to an increase of the internal energy of the system. Thus, it is only by applying an external field that the average spin orientation can be forced away from the easy axis direction. The anisotropy induced by the presence of the easy axis is theoretically described by including the magnetic anisotropy energy in the description of a system. In the magnetocrystalline

anisotropy description, each crystal direction is associated with an energy value in such a way that spin alignment along the easy axis minimizes the energy term. For cubic crystal structures the anisotropic energy is given by[14,15]

$$E_K = K_o + K_1(\gamma_1^2\gamma_2^2 + \gamma_2^2\gamma_3^2 + \gamma_3^2\gamma_1^2) + K_2(\gamma_1^2\gamma_2^2\gamma_3^2) + ... \tag{2.20}$$

with constants K_o, K_1 and K_2 being the cubic anisotropy constants and $\gamma_{1,2,3}$ being the direction cosines. Higher terms are usually not needed. K_o is angle independent and is ignored because in most cases one is interested only in changes in the energy when the saturation magnetisation vector rotates from one direction to another. Sometimes the term involving K_2 is also neglected because K_2 itself is very small.

Insight into how the magnetic anisotropy term arises from the exchange coupling between spin pairs can be gained by looking back into equation 2.18, which is the isotropic description of the exchange energy. As a result, to describe magnetic anisotropy, additional terms need to be added that are dependent on the orientation of the magnetic moments with respect to the crystal axes. An expression for the interaction energy between a pair of spins can be derived by assuming that neighbouring spins make an angle ϕ with the bond axis. Following the work from Ref. 14 the expression is expanded in Legendre polynomials resulting in

$$\varepsilon_{ij} = g + l(\cos^2\phi - \frac{1}{3}) + q(\cos^4\phi - \frac{6}{7}\cos^2\phi + \frac{3}{35}) + ... \tag{2.21}$$

with g, l, and q being expansion coefficients.

The first term of the above equation is independent of the angle ϕ so it corresponds to the exchange interaction (i.e. $g = E_{ex}$). The second term corresponds to the dipole-dipole interaction. The third term of the equation is a higher order term corresponding to the so-called quadrupolar interaction[14,16]. One can then calculate the magnetic anisotropy for all spin-pairs in a crystal by summing up the energy given by equation 2.21. Assuming a simple cubic crystal, as shown in Fig. 2.5, one has

$$E_K = \sum_{\langle i,j \rangle} \varepsilon_{ij} \tag{2.22}$$

where $\langle i, j \rangle$ corresponds to pairing spins.

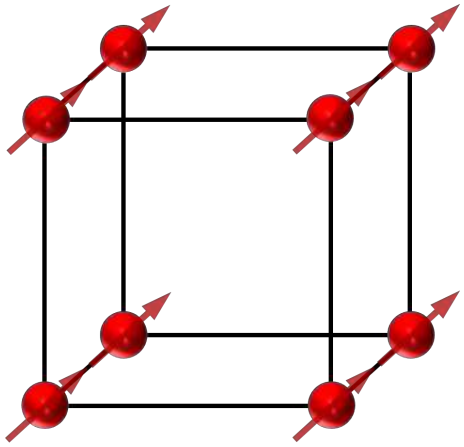

Figure 2.5: Spins arranged ferromagnetically on a simple cubic unit cell.

Considering nearest-neighbours interactions alone the above equation becomes

$$E_K = N \sum_n \left\{ l \left(\gamma_i^2 - \frac{1}{3} \right) + q \left(\gamma_i^4 - \frac{6}{7}\gamma_i^2 + \frac{3}{35} \right) \right\} \tag{2.23}$$

with index n = 1,2,3 and γ_n corresponding to the direction cosines of parallel spins. For example, for spin bonding parallel to the x-axis the cosine is equal to γ_1 and similarly γ_2 for y-axis and γ_3 for z-axis.

If we use the identity $\gamma_1^2 + \gamma_2^2 + \gamma_3^2 = 1$[14] the above equation becomes

$$E_K = -2Nq \left(\gamma_1^2\gamma_2^2 + \gamma_2^2\gamma_3^2 + \gamma_3^2\gamma_1^2 \right) + const. \tag{2.24}$$

where N represents the total number of atoms in a unit volume. If one compares the above equation with equation 2.20 one gets $K_1 = -2Nq$. Similar calculations for a BCC and an FCC crystal structure give $K_1 = -(16/9)Nq$ and $K_1 = -Nq$ respectively[14]. In the above calculations only K_1 was derived, because higher order terms of the magnetic anisotropy energy can be ignored when distant spin-pair interactions are neglected.

2.5 Magnetostriction

2.5.1 Magnetostrictive Phenomena

Broadly speaking, magnetostriction is the isotropic (volume) or anisotropic (shape) deformation of magnetic materials when they get magnetised. Magnetostriction occurs due to magnetoelastic coupling exhibited, to some extend, by all magnetic materials, but most importantly ferromagnetic materials. The deformation due to magnetostriction is defined as $\lambda = \delta l/l_o$, where l_o is the length of the material along a specific direction in its unstrained (un-magnetised) state and δl is the resulting dimensional change. In general, λ is quite small (e.g. 10^{-5} – 10^{-6}), it can be measured using the strain-gauge technique and it can be either positive or negative corresponding to expansive or compressive deformation respectively.

Macroscopically, the phenomenon of magnetostriction manifests in various forms and can generally be distinguished in two main groups; the so-called direct effects (e.g. Joule magnetostriction, Wiedemman effect etc.) and the inverse effects (e.g. Villari effect, Matteucci effect etc.).

Joule magnetostriction refers to changes in length of a magnetic material when there is a change in its magnetisation induced by an externally applied magnetic field. It is also known as linear magnetostriction. This type of magnetostriction is characterized by a change in length following the same direction as the applied field assuming a constant overall volume. Joule magnetostriction gets it name from J. P. Joule, who first observed the effect in iron wires in 1842[17].

An inverse effect to Joule magneostriction is the Villari effect, which was first described in 1865[18]. It describes changes in magnetisation of a material due to applied mechanical stresses. If application of an increasing stress (e.g. a tensile stress) to a material leads to an increase of magnetisation, the material is said to have a net positive magnetostriction. An example of a material displaying positive Villari magnetostriction is iron. On the

other hand, materials, such as nickel, display a negative Villari magnetostriction, because the overall magnetisation of the material increases with compressive stress.

The Wiedemann effect (1859)[19] describes a material's rotational deformation due to helical anisotropy induced when a current passes through it (e.g. current through a wire) and a moving magnetic field of constant magnitude, e.g. a bar magnet, is applied on the surface of the material. The Matteucci effect is the inverse to the Wiedemann effect and describes the induction of helical anisotropy and electromagnetic force when a ferromagnetic material is twisted (e.g. applied torque).

W. F. Barrett in 1882[20] realised that when in a magnetic field ferromagnetic material undergo a volumetric change. He named the effect volume magnetostriction (also referred to as magnetovolume effect). The effect is more evident close to the Curie temperature of the materials. The inverse effect is called the Nagaoka-Honda effect[21] and describes a change in the magnetic state of a ferromagnetic material due to a change in its volume.

2.5.2 Fundamentals of Magnetostriction

The aforementioned magnetostrictive effects, despite being macroscopic, originate from atomic scales. At the atomic level, magnetostriction, as magnetocrystalline anisotropy, is dependent on the process of magnetisation and it is the result of the magnetoelastic coupling. Application-wise, an ideal magnetostrictive material should have a small magnetocrystalline anisotropy, such that only small external fields are needed to distort the lattice. Additionally, such a lattice distortion should be as large as possible, which is realized by having a strong magnetoelastic coupling between spins.

Let us model the dipole-dipole interaction energy between two interacting neighbouring dipoles by revisiting equation 2.21. Let the domain magnetisation direction cosines be γ $(\gamma_1, \gamma_2, \gamma_3)$, as given in equation 2.20, and ω $(\omega_1, \omega_2, \omega_3)$ the bond direction cosines. The interaction energy[14,16] between the two dipoles as a function of the bond length r and the magnetisation direction cosines is given by

$$\varepsilon(\vec{r},\gamma) = l(\vec{r})\left((\gamma\cdot\omega)^2 - \frac{1}{3}\right) + q(\vec{r})\left((\gamma\cdot\omega)^4 - \frac{6}{7}(\gamma\cdot\omega)^2 + \frac{3}{35}\right) \tag{2.25}$$

The first term represents the dipole-dipole interaction, as discussed in the previous section, and depends on the magnetisation direction. The second and higher order terms also contribute to magnetostriction but the contribution is very small and is ignored. The interaction energy for an unstrained state is then given by

$$\varepsilon(\vec{r},\gamma) = l(\vec{r_o})\left((\gamma\cdot\omega)^2 - \frac{1}{3}\right) \tag{2.26}$$

where $\vec{r_o}$ is the equilibrium bond length.

When the crystal is under strain, each pair will change its bond direction and length and the interaction energy will also change. Assuming a strain in the crystal given by the tensor

$$\tilde{\epsilon} = \begin{Bmatrix} \epsilon_{xx} \\ \epsilon_{yy} \\ \epsilon_{zz} \\ \epsilon_{xy} \\ \epsilon_{yz} \\ \epsilon_{zx} \end{Bmatrix} \tag{2.27}$$

the bond length changes from $\vec{r_o}$ to $\vec{r_o}(1+\tilde{\epsilon})$. This leads to a change of $\Delta\varepsilon$ in the interaction energy of each spin-spin bond in the lattice. The interaction energy of a simple cubic lattice can therefore be derived by summing up $\Delta\varepsilon$ for all the spin pairs, leading to[14,15]

$$E_{\text{magel}} = b_1\left\{\epsilon_{xx}(\gamma_1^2 - \frac{1}{3}) + \epsilon_{yy}(\gamma_2^2 - \frac{1}{3}) + \epsilon_{zz}(\gamma_3^2 - \frac{1}{3})\right\} + b_2\left\{\epsilon_{xy}\gamma_1\gamma_2 + \epsilon_{yz}\gamma_2\gamma_3 + \epsilon_{zx}\gamma_3\gamma_1\right\} \tag{2.28}$$

where b_1 and b_2 are the so-called magnetoelastic coupling coefficients[22,23]. Their values for a given ferromagnetic material depends on the materials magnetostriction coefficient and elastic constant values. The energy term is also known as the magnetoelastic energy. Microscopically the magnetoelastic coupling coefficients depend on the coordination number of the material, the unstrained bond length as well as on the function $l(\vec{r})$ and its spatial gradient[14].

From equation 2.28 one observes that E_{magel} is linearly dependent on the strain tensor components. Consequently, the crystal can be deformed without limit and for that reason it is counterbalanced by the so-called elastic energy given by[6]

$$E_{\text{el}} = \frac{1}{2}\epsilon^T \tilde{C} \epsilon \tag{2.29}$$

where $\tilde{C}$ is the stiffness matrix[6], also referred to as the elastic module tensor, and ϵ^T is the transpose of the tensor ϵ. For cubic systems, due to cubic symmetry, the elastic module tensor gets symmetrical with $\mathrm{C_{ij}} = \mathrm{C_{ji}}$ and the number of independent elements is reduced to only three ($\mathrm{c_{12}}$, $\mathrm{c_{11}}$, $\mathrm{c_{44}}$). The tensor is then given by[6]

$$\tilde{C} = \begin{bmatrix} c_{11} & c_{12} & c_{12} & 0 & 0 & 0 \\ c_{12} & c_{11} & c_{12} & 0 & 0 & 0 \\ c_{12} & c_{12} & c_{11} & 0 & 0 & 0 \\ 0 & 0 & 0 & c_{44} & 0 & 0 \\ 0 & 0 & 0 & 0 & c_{44} & 0 \\ 0 & 0 & 0 & 0 & 0 & c_{44} \end{bmatrix} \tag{2.30}$$

where c_{11}, c_{12}, and c_{44} are the elastic moduli. The condition for equilibrium between the magnetoelastic and elastic energies is reached by minimizing the total energy

$$E = E_{\text{magel}} + E_{\text{el}} \tag{2.31}$$

Solving for the above condition we obtain the equilibrium strain, also referred to as

magnetostrictive strain

$$\lambda = \begin{Bmatrix} \lambda_{xx} \\ \lambda_{yy} \\ \lambda_{zz} \\ \lambda_{xy} \\ \lambda_{yz} \\ \lambda_{zx} \end{Bmatrix} = \begin{Bmatrix} \frac{b_1}{c_{12}-c_{11}}(\alpha_1^2 - \frac{1}{3}) \\ \frac{b_1}{c_{12}-c_{11}}(\alpha_2^2 - \frac{1}{3}) \\ \frac{b_1}{c_{12}-c_{11}}(\alpha_3^2 - \frac{1}{3}) \\ -\frac{b_2}{c_{44}}\alpha_1\alpha_2 \\ -\frac{b_2}{c_{44}}\alpha_2\alpha_3 \\ -\frac{b_2}{c_{44}}\alpha_3\alpha_1 \end{Bmatrix} \tag{2.32}$$

For detailed calculations the reader is referred to Refs. 6 and 14.

The expansion observed along any direction $(\omega_1, \omega_2, \omega_3)$ is given by

$$\frac{\delta l}{l} = \lambda_{xx}\omega_1^2 + \lambda_{yy}\omega_2^2 + \lambda_{zz}\omega_3^2 + \lambda_{xy}\omega_1\omega_2 + \lambda_{yz}\omega_2\omega_3 + \lambda_{zx}\omega_3\omega_1 \tag{2.33}$$

and by substituting the values of λ from equation 2.32 it becomes

$$\frac{\delta l}{l} = \frac{b_1}{c_{12} - c_{11}}\left(\gamma_1^2\omega_1^2 + \gamma_2^2\omega_2^2 + \gamma_3^2\omega_3^2 - \frac{1}{3}\right) - \frac{b_2}{c_{44}}\left(\gamma_1\gamma_2\omega_1\omega_2 + \gamma_2\gamma_3\omega_2\omega_3 + \gamma_3\gamma_1\omega_3\omega_1\right) \tag{2.34}$$

Assuming that the domain magnetisation is along the [100] crystallographic direction, the elongation in the same direction is obtained by setting $\gamma_1 = \omega_1 = 1$ and $\gamma_2 = \gamma_3 = \omega_2 = \omega_3 = 0$, and is given by

$$\lambda_{100} = \frac{2}{3}\frac{b_1}{c_{12} - c_{11}} \tag{2.35}$$

In a similar way any expansion along the [111] crystallographic direction is given by

$$\lambda_{111} = -\frac{1}{3}\frac{b_2}{c_{44}} \tag{2.36}$$

by setting $\gamma_i = \omega_i = 1/\sqrt{3}$ (i = 1, 2, 3). By using the above equations for λ_{100} and λ_{111} equation 2.34 then becomes

$$\frac{\delta l}{l} = \frac{3}{2}\lambda_{100}\left(\gamma_1^2\omega_1^2 + \gamma_2^2\omega_2^2 + \gamma_3^2\omega_3^2 - \frac{1}{3}\right) + 3\lambda_{111}\left(\gamma_1\gamma_2\omega_1\omega_2 + \gamma_2\gamma_3\omega_2\omega_3 + \gamma_3\gamma_1\omega_3\omega_1\right) \tag{2.37}$$

As a result the magnetostriction of a cubic system can be expressed in terms of λ_{100} and λ_{111}. If the magnetisation is along [110], the corresponding elongation is related to λ_{100} and λ_{111} by[14]

$$\lambda_{110} = \frac{1}{4}\lambda_{100} + \frac{3}{4}\lambda_{111} \tag{2.38}$$

From the above analysis one can easily observe that volume change due to the magnetostriction, $\delta u/u = \lambda_{xx} + \lambda_{yy} + \lambda_{zz}$, is zero[14].

2.6 Magnetostrictive Materials & Applications

In the previous section the various magnetostrictive phenomena as well as the fundamentals of the mechanism of magnetostriction were discussed. J. P. Joules was the first to observe magnetostriction in iron wires. Since then systematic studies were performed and most of ferromagnetic elements (e.g. Fe, Co, Ni) were found to exhibit magnetostriction up to a few decades of $\mu\epsilon$[24] but with limited practical applications. Classical magnetostrictive materials shaped into wires, tapes, and bulk alloys usually include alloys rich in Fe, Co, or Ni but most of them show magnetostriction with values still less than 100 $\mu\epsilon$[24]. Rare earth materials, such as Tb and Dy, were found to exhibit magnetostriction of up to 10,000 $\mu\epsilon$. However, values of such high magnitude, within these elements, are limited to extremely low temperatures, while exhibiting insignificant values at ambient temperature. In order to increase the T_C limit, there were attempts of alloying rare earth elements with 3d or 4d transition metals, having higher Curie temperatures, so as to get significant magnetostriction at room temperature. For example, alloys such as $TbFe_2$ and $DyFe_2$, at room temperature, exhibit magnetostrictions of 2630 $\mu\epsilon$ and

650 με respectively[10]. The drawback though is that both these compounds require large magnetic fields to reach saturation due to their large magnetocrystalline anisotropy. By mixing both Tb and Dy in proper amounts with Fe leads to reduced magnetocrystalline anisotropy and consequently to lower saturation magnetic fields. The resulting alloy is $Tb_xDy_{1-x}Fe$, commercially known as Terfenol-D, and exhibits magnetostriction values of up to 2000 με at room temperature[25]. One major problem with Terfenol-D is that it exhibits low tensile strength, a value of about 30 MPa, as well as brittleness. This makes it less capable of enduring shock loads and mechanical tensions. Consequently, the useful applications of Terfenol-D are highly limited.

A significant change came with the development of Fe-Ga alloys, commercially known as Galfenol, after the pioneering work of A. E. Clark *et al.* in the early 2000s[26,27]. Galfenol exhibits magnetostriction of up to 400 με at room temperature[26,27], requires low magnetic fields to reach saturation (100 Oe) and has very low hysteresis[28]. Fe-Ga alloys also have ductile-like behaviour and demonstrate high tensile strength, about 500 MPa[28]. They can withstand shock loads and operate in harsh environments and in a temperature range of -20 to 80 °C they show little variation in their magnetic and mechanical properties. Adding their high Curie temperature, $T_C > 650$°C, high permeability, $\mu_r > 100$, as well as the fact that they are corrosion resistant makes Fe-Ga alloys ideal for prospective applications such as smart microelectromechanical systems.

Binary alloys of Fe and elements such as Al or Be have also been investigated[29–31]. Although Fe-Al exhibits similar behaviour as that of Fe-Ga for up to 25 % Al or Ga respectively, magnetostriction of Galfenol is more than twice than that of Fe-Al[30] (especially at 19 % Ga - see next section). Fe-Be binary alloys, studied for up to 11 % Be, exhibit similar magnetostriction as Galfenol. However, Be is a highly toxic material, making its use as well as attainability laborious. Additional studies on ternary alloys of Fe, Ga and elements such as Al, Ni, Mo, Co, and Sn showed insignificant improvement to Galfenol's magnetostriction[32,33].

After the development of highly magnetostrictive materials extensive studies on their

applications were performed. One of the very first applications was their use as generators of motion and force for underwater sound sources with the U.S. Navy carrying extensive research in this field[10]. After Terfenol-D became commercially available it paved the way for the development of new electromechanical devices and many potential applications were proposed, including sound and vibration sources, active vibration control systems, sonar systems, actuators, sensors and others[10].

2.7 Fe-Ga (Galfenol) Alloys & Magnetostriction

In the previous section a small overview of magnetostrictive materials and their prospective applications was provided. It was discussed that Fe-Ga alloys exhibit large magnetostriction with significant increase upon addition of Ga in α-Fe. It has been pointed out that the relative high magnetostriction of Galfenol along with its ductile-like behaviour, low saturation fields and high tensile strength makes it quite promising for practical use especially as an alternative to Terfenol-D that shows poor mechanical properties.

Magnetostriction in Fe-Ga, apart from being highly dependent on the addition of Ga into Fe, is also dependent on the heat treatment and heat treatment history of the alloys. A variety of structures, such as ordered FCC $L1_2$, ordered BCC B2 or $D0_3$, and disordered A2, can be obtained and as such, to be able to evaluate and fully understand the complex relationship of Galfenol and the magnetostriction it exhibits, one first needs to comprehend the metallurgical properties of the alloys. In Fig. 2.6 the equilibrium phase diagram of Fe-Ga is provided. At room temperature Fe exists as α-Fe with a BCC crystal structure (disordered A2 structure). At the same temperature, upon addition of Ga, the A2 phase is maintained for up to 12 at. % of Ga. Beyond this level and up to around 25 at. % the resulting structure is a mixture of the A2 and the ordered $L1_2$ (αFe_3Ga) phases. For Ga content over 25 at. % and up to 30 at. % the $L1_2$ phase dominates. At higher temperatures structural transitions into the $D0_3$, B2, and $D0_{19}$ (βFe_3Ga) also occur. Work by Ikeda *et al.*[34] on Galfenol samples, with previous studies conducted by

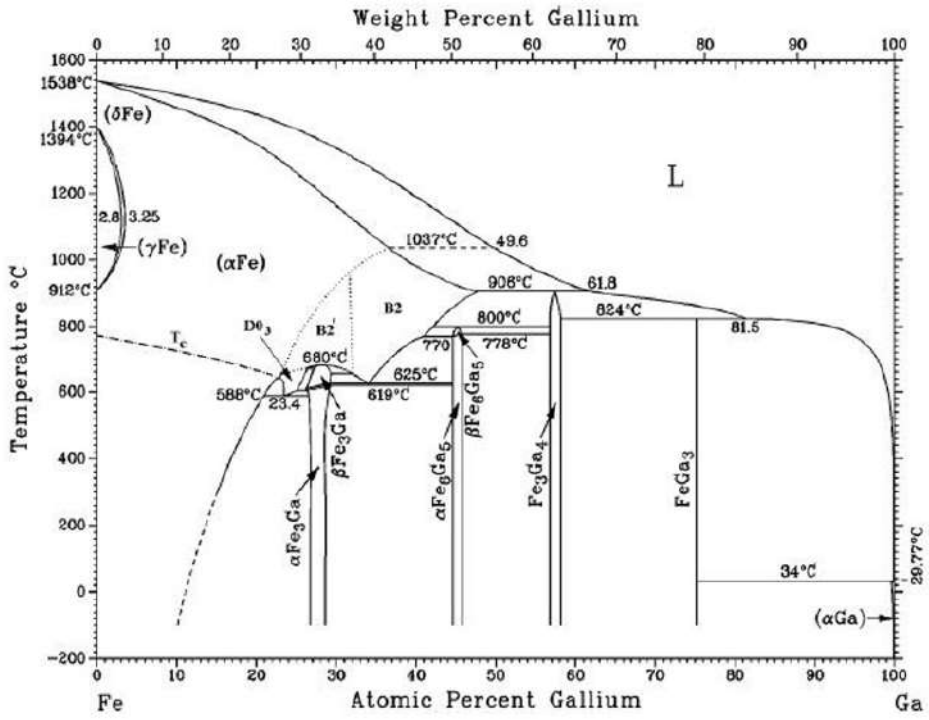

Figure 2.6: Equilibrium phase diagram of Fe-Ga[36].

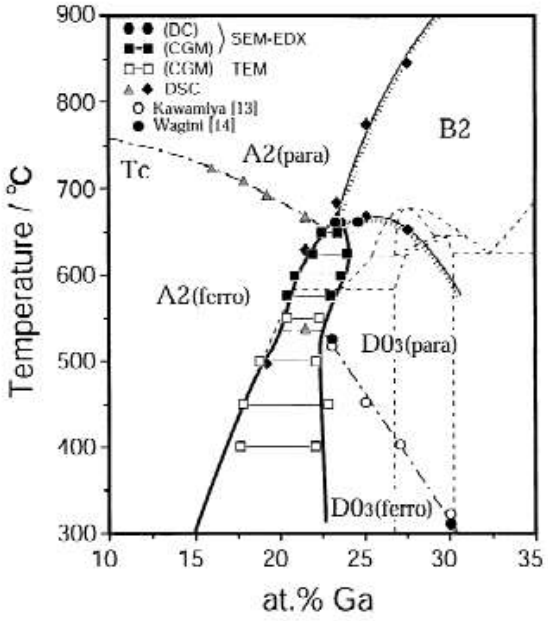

Figure 2.7: The metastable phase diagram of Fe-Ga[34].

Kawamiya *et al.*[35], showed quite a strong dependence of the phase transitions within the system upon cooling rates; formation of phases such as the $D0_{19}$ and the $L1_2$ could be avoided when the system is cooled down at slow rates and the formation of phases such as the $D0_3$ can be avoided if the system is quenched. Their work led to the development of the so-called metastable phase diagram as shown in Fig. 2.7.

In Galfenol magnetostriction reaches values of about 400 $\mu\epsilon$ for a Ga content of 19 at. %, being almost tenfold to that of α-Fe ($3/2\lambda_{100} = 32$ $\mu\epsilon$). The magnetostriction constant $3/2\lambda_{100}$ measured with respect to the Ga content (provided in Fig. 2.8), indicates that this increase is indeed dependent upon the cooling rate of the system.

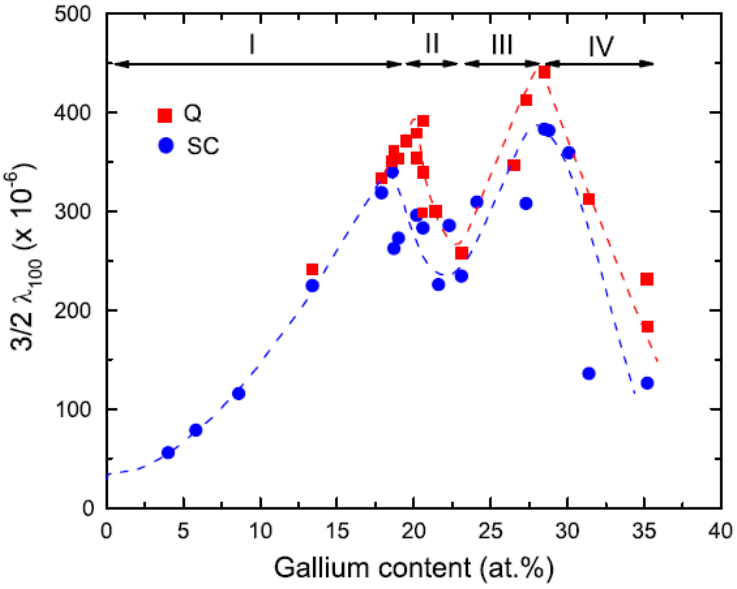

Figure 2.8: $3/2\lambda_{100}$ magnetostriction constant as a function of Ga content. The graph is divided in four regions; (I) increasing magnetostriction up to 17 at. % Ga for slow-cooled samples or 20 at. % Ga for quenched samples, (II) decreasing magnetostriction for up to 23 at. % Ga, (III) increasing magnetostriction peaking up again for Ga content of about 27 at. % and (IV) a fourth region where the magnetostriction decreases again.[37]

The $3/2\lambda_{100}$ magnetostriction constant keeps increasing for up to 19 at. % Ga, reaching values of $\sim$ 400 $\mu\epsilon$, when the alloys are quenched but when the samples are cooled at nominal rates they exhibit a decrease in magnetostriction after exceeding 17 at. % of Ga with a local minimum ($\sim$ 225 $\mu\epsilon$) appearing at around 24 at. % Ga and the

magnetostriction increasing again with a second peak appearing at around 28 at. %. This shows a connection between structural transitions and the properties of Fe-Ga with the $D0_3$ and $L1_2$ phases certainly playing a key role in the enhancement of the system's functional properties[38].

The large magnetostriction observed is exceptional taking into account that it is enhanced with the addition of Ga, being a non-magnetic element. In α-Fe magnetostriction is generated in two steps; first the magnetic domain walls are spatially shifted and then the magnetisation is coherently rotated away from the easy axis[39]. Magnetostriction in Fe-Ga though still remains a puzzle and the mechanism generating it still lacks solid explanation. Extensive studies have been performed[27,29,37,39–57] and a few theories have been proposed trying to explain the phenomenon. One of the leading theories proposes that this large increase in magnetostriction is due to Ga-Ga pairs randomly distributed throughout the solid solution matrix[40] changing the strain locally and consequently the magnetic anisotropy with the atomic bond being deformed due to spin-orbit coupling. Another one argues that the magnetostriction originates from structural reorientation of Ga-rich local $D0_{22}$ tetragonal nanoprecipitates[41,42].

In 2001 J. Cullen *et al.*[29] showed that enhancement of magnetostriction in Galfenol arises from a decrease of the $\frac{1}{2}(C_{11}-C_{12})$ shear elastic constant, since $\lambda_{100} \propto \frac{2}{(C_{11}-C_{12})}$, via a transition from the disordered αFe BCC to a B2-like phase. The same year M. Wuttig *et al.*[40] demonstrated the same decrease of $\frac{1}{2}(C_{11}-C_{12})$ and argued that this as well as the consequent increase of magnetostriction is attributed to next-nearest Ga pairs creating a local stress. To support this they used a model showing a quadratic relationship between the value of Ga content and the magnetostriction constant λ_{100} leading to the first peak (see Fig. 2.9), with the second peak believed to be due to softening of the shear modulus. Similar results were found by A. E. Clark *et al.* in 2003[27].

Work from R. Wu *et al.*[43,44], using first principle calculations, supports this hypothesis showing that the magnetostriction is highly dependent on the atomic arrangements within the unit cell with a B2-like structure playing an important role; they found that a B2-

like phase results in a positive value of λ_{100} magnetostriction of about + 380 $\mu\epsilon$ and they argue that a large portion of this phase with Ga atoms along the [100] direction is required for high positive magnetostriction. Experimental data supporting this model were also provided by T. A. Lograsso *et al.*[45] using X-Ray diffraction on both slow-cooled and quenched Fe-Ga single crystals containing 19 at. % of Ga. They first verified the connection between cooling rates and structural transitions showing the suppression of long-range ordering upon quenching. Observed anomalous diffraction reflections were attributed to a tetragonal structure with short-range ordering of Ga pairs along the [100] direction.

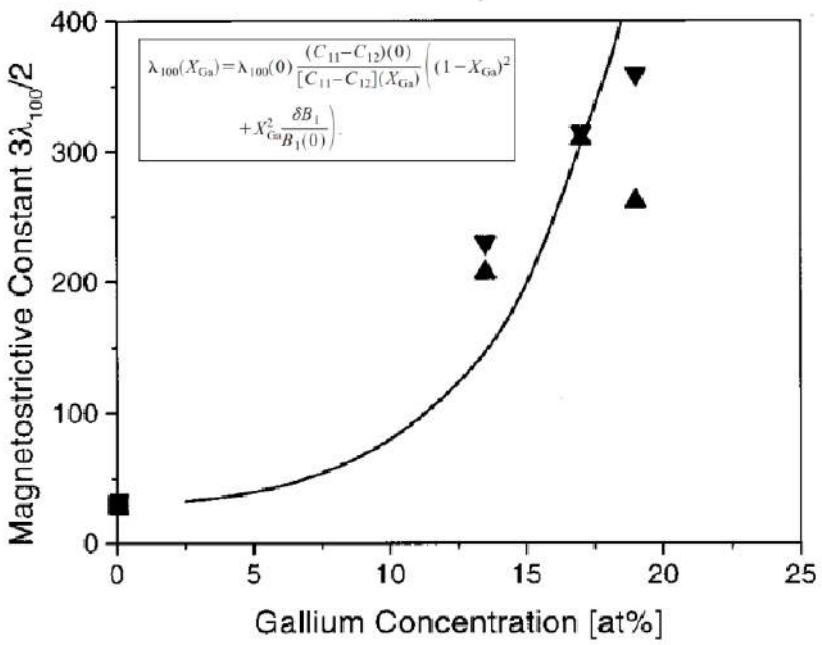

Figure 2.9: Measurements of the $3/2\lambda_{100}$ magnetostriction constant leading to the first peak at 19 at. % Ga. The solid line is the fit of the equation given in the inset of the figure showing that the magnetostriction constant depends quadratically on the Ga content. Adapted from Ref. 40.

In 2007, J. Cullen *et al.*[46] re-tackled the problem by following the studies of M. Wuttig and R. Wu. They used a "model of the anisotropy in crystalline ferromagnetic alloys containing defect clusters", based on micro magnetic theory and they concluded that local [100]-type Ga pairs are indeed responsible for local magnetic anisotropy. Due to the

defects' low mobility at room temperature, strain due to local magnetisation rotation and not reorientation of the defects themselves is responsible for the induced magnetostriction.

The competing idea of reorientation of $D0_{22}$ nanoprecipitates was first introduced by A. G. Khachaturyan and D. Viehland in 2007[41,42]. In this model, it is thought that $D0_{22}$ tetragonal distortions and the A2 bcc matrix are connected via a magnetic coupling. It is theorised that the magnetostriction is the product of these tetragonal phases reorienting and not an intrinsic property connected with a homogeneous ferromagnetic matrix. Their model is based on the following assumptions; Fe-Ga alloys with a disordered bcc A2 structure (and alloys with same structure and similar properties) are generally heterogeneous in the nanoscale; precipitation of the ordered $D0_3$ phase out of the A2 bcc matrix is the cause of the heterogeneities. This is expressed by the transformation bcc $\rightarrow$ bcc' + $D0_3$ decomposition; the $D0_3$ precipitates undergo a diffusionless Bain strain transformation into a face centred tetragonal (FCT) $D0_{22}$ phase. This is thought to bring the structure closer to an ordered fcc-based $L1_2$ phase. It needs to be pointed out that the phases included in the transformation series are all ferromagnetic.

A few studies performed over the last ten years have provided evidence of the existence of heterogeneities but none so far shows a conclusive connection with the generation of magnetostriction. A year after the model was first proposed, S. Bhattacharyya *et al.*[48], by means of TEM and HRTEM, observed $D0_3$ nanoprecipitates within the A2 matrix and in 2009 H. Cao *et al.*[49] reported studies on Fe-Ga by means of neutron diffuse scattering. Their results show that the $D0_3$ precipitates should undergo a cubic-to-tetragonal transformation; a local structural distortion with the (300) peak splitting indicate that the precipitates are highly distorted from cubic to tetragonal or even lower symmetry. They argue that since for 19 at. % Ga content (where magnetostriction has its highest value) the diffuse scattering intensity is stronger, magnetostriction is directly connected to the tetragonally distorted heterogeneities. In 2010, C. Mudivarthi *et al.*[52], investigated a quenched $Fe_{81}Ga_{19}$ single crystal by means of small-angle neutron scattering (SANS). Their results show the presence of nano-sized heterogeneities that have different mag-

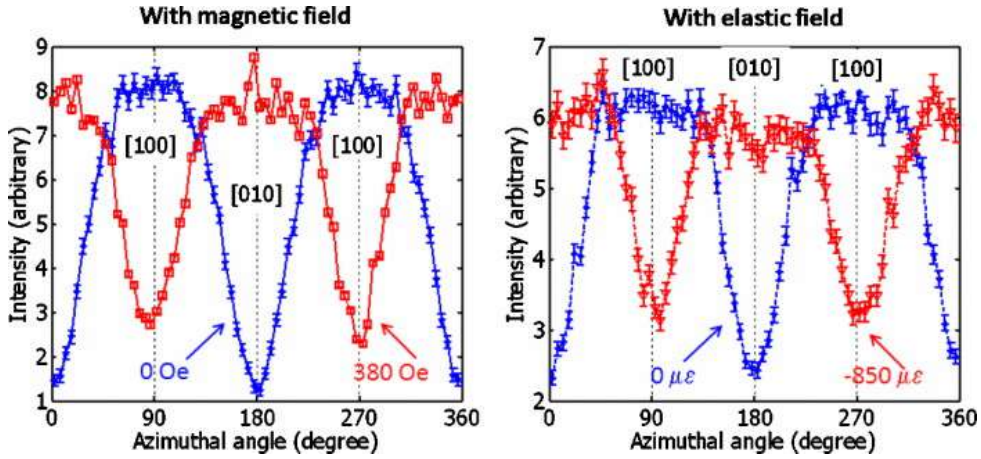

Figure 2.10: Plots of small-angle neutron scattering intensities with respect the azimuthal angle. A reorientation of nano-heterogeneities is apparent with applying magnetic (left) and elastic (right) fields.

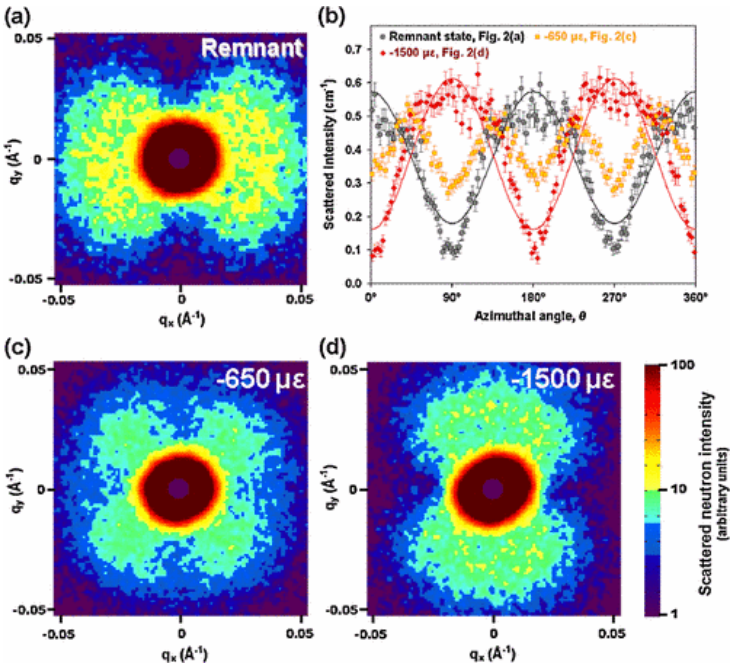

Figure 2.11: Small-angle neutron scattering measuremnts of Fe-Ga single crystal with 19 at. % Ga content. In (a) no strain nor magnetic field is applied but the signal is anisotropic in one direction due to remnant magnetisation. Reorientation of the signal is observed with increasing strain (c)(d). In (b) the scattering intensity with respect to the azimuthal angle is plotted clearly showing the anisotropic signal and the reorientation with applied strain[39].

netisation from that of the A2 matrix. The nanoclusters correspond similarly in applied magnetic and elastic fields as shown in Fig. 2.10. They argue that the nano-features are directly connected to magnetostriction but SANS fails to provide with information about their structure and composition. A similar study by M. Laver *et al.*[39], using polarised SANS on a similar sample, gave similar results; heterogeneities were present in the sample of which magnetisation was different than that of the matrix. The reorientation of the clusters with applied magnetic or elastic field was apparent but again there was not a conclusion on the exact nature of the precipitates. Fig. 2.11 depicts the reorientation of the magnetic signal of the heterogeneities with an applied strain field of up to 1600 $\mu\epsilon$.

2.8 Concluding Remarks

In this chapter after introducing basic information on magnetism and magnetic states, the concept of magnetic anisotropy and magnetostriction was discussed. Magnetostrictive materials and their prospective applications were also briefly introduced. The most important part of the chapter was the subsequent discussion on Fe-Ga alloys that exhibit relatively high values of magnetostriction ($\sim$ 400 $\mu\epsilon$). The occurrence of magnetostriction in these alloys though has yet to be fully explained with one proposed theory arguing that the spatial reorientation of nano-heterogeneities precipitating out of the matrix of the material is responsible for the manifestation of magnetostriction. In one part of the experimental sections of this thesis the concept of precipitation in a Fe-Ga sample is investigated. The experimental work is mainly focused on detecting such precipitates and analysing their composition by means of anomalous small-angle X-ray scattering (presented in the previous chapter). Such information will be valuable for future investigations regarding the connection of the precipitates with magnetostriction in Fe-Ga.

References

[1] J. P. Joule. On the effects of magnetism upon the dimensions of iron and steel bars. *Philosophical Magazine Series 3*, 30(199):76–87, 1847.

[2] R. M. Eisberg and R. Resnick. *Quantum physics of atoms, molecules, solids, nuclei and particles; 2nd ed.* Wiley, New York, NY, 1985.

[3] J. M. D. Coey *Magnetism and Magnetic Materials*. Cambridge University Press, Cambridge, 2009.

[4] W. Gerlach and O. Stern. Der experimentelle Nachweis der Richtungsquantelung im Magnetfeld. In *Walther Gerlach (1889–1979)*, pages 26–29. Springer, 1989.

[5] K. H. J. Buschow, F. R. Boer, et al. *Physics of magnetism and magnetic materials*, volume 92. Springer, 2003.

[6] T. Miyazaki and H. Jin. *The Physics of Ferromagnetism*, volume 158. Springer Science & Business Media, 2012.

[7] J. Sólyom. *Fundamentals of the Physics of Solids: Volume 1: Structure and Dynamics*, Volume 1. Springer Science & Business Media, 2007.

[8] P. Weiss. L'hypothèse du champ moléculaire et la propriété ferromagnétique. *J. Phys. Theor. Appl.*, 6(1):661–690, 1907.

[9] W. Heisenberg. Zur Theorie des Ferromagnetismus. *Zeitschrift für Physik*, 49(9):619–636, Sep 1928.

[10] E. Goran. *Handbook of Giant Magnetostrictive Materials*. Academic Press: Los Angeles, CA, USA, 2000.

[11] W. Pepperhoff and M. Acet. *Constitution and Magnetism of Iron and its Alloys*. Springer Science & Business Media, 2013.

[12] D.-K. Lee and S.-C. Hong. Correlation between structures and magnetism in iron: Ferromagnetism and antiferromagnetism. *Journal of Magnetics*, 12(2):68–71, 2007.

[13] V. L. Moruzzi, P. M. Marcus, K. Schwarz, and P. Mohn. Ferromagnetic phases of bcc and fcc Fe, Co, and Ni. *Physical Review B*, 34(3):1784, 1986.

[14] S. Chikazumi and C. D. Graham. *Physics of Ferromagnetism*, volume 94. Oxford University Press on Demand, 2009.

[15] E. Kneller, A. Seeger, and H. Kronmüller. *Ferromagnetismus*. Springer, 1962.

[16] L. Néel. Anisotropie magnétique superficielle et surstructures d'orientation. *J. Phys. Radium*, 15(4):225–239, 1954.

[17] J. P. Joule. On a new class of magnetic forces. *Ann. Electr. Magn. Chem*, 8(1842):219–224, 1842.

[18] E. Villari. Ueber die Aenderungen des magnetischen Moments, welche der zug und das hindurchleiten eines galvanischen Stroms in einem Stabe von Stahl oder Eisen hervorbringen. *Annalen der Physik*, 202(9):87–122, 1865.

[19] G. Wiedemann. Ueber die Torsion und die Beziehungen derselben zum Magnetismus. *Annalen der Physik*, 182(2):161–201, 1859.

[20] W. F. Barrett. On the alterations in the dimensions of the magnetic metals by the act of magnetisation. *Nature*, 26:585–586, 1882.

[21] H. Nagaoka and K. Honda. Sur l'aimantation et la magnétostriction des aciers au nickel. *Journal de Physique Théorique et Appliquée*, 3(1):613–620, 1904.

[22] C. Kittel. Physical theory of ferromagnetic domains. *Reviews of Modern Physics*, 21(4):541, 1949.

[23] E. W. Lee. Magnetostriction and magnetomechanical effects. *Reports on Progress in Physics*, 18(1):184, 1955.

[24] R. Hasegawa. Glassy Metals: Magnetic, Chemical and Structural properties. *Boca Raton: CRC Press, 1983, edited by Hasegawa, Ryusuke*, 1983.

[25] A. Clark and D. Crowder. High temperature magnetostriction of $TbFe_2$ and $Tb_{27}Dy_{73}Fe_2$. *IEEE Transactions on Magnetics*, 21(5):1945–1947, 1985.

[26] A. E. Clark, J. B. Restorff, M. Wun-Fogle, T. A. Lograsso, and D. L. Schlagel. Magnetostrictive properties of body-centered cubic Fe-Ga and Fe-Ga-Al alloys. *IEEE Transactions on Magnetics*, 36(5):3238–3240, 2000.

[27] A. E. Clark, K. B. Hathaway, M. Wun-Fogle, J. B. Restorff, T. A. Lograsso, V. M. Keppens, G. Petculescu, and R. A. Taylor. Extraordinary magnetoelasticity and lattice softening in bcc Fe-Ga alloys. *Journal of Applied Physics*, 93(10):8621–8623, 2003.

[28] R. A. Kellogg, A. M. Russell, T. A. Lograsso, A. B. Flatau, A. E. Clark, and M. Wun-Fogle. Tensile properties of magnetostrictive iron–gallium alloys. *Acta Materialia*, 52(17):5043–5050, 2004.

[29] J. R. Cullen, A. E. Clark, M. Wun-Fogle, J. B. Restorff, and T. A. Lograsso. Magnetoelasticity of Fe-Ga and Fe-Al alloys. *Journal of Magnetism and Magnetic Materials*, 226:948–949, 2001.

[30] R. C. Hall. Magnetostriction of aluminum-iron single crystals in the region of 6 to 30 atomic percent aluminum. *Journal of Applied Physics*, 28(6):707–713, 1957.

[31] A. E. Clark, M. Wun-Fogle, J. B. Restorff, T. A. Lograsso, and G. Petculescu. Magnetostriction and elasticity of body centered cubic Fe $100_{1-x}Be_x$ alloys. *Journal of applied physics*, 95(11):6942–6944, 2004.

[32] L. Dai, J. Cullen, M. Wuttig, T. Lograsso, and E. Quandt. Magnetism, elasticity, and magnetostriction of FeCoGa alloys. *Journal of Applied Physics*, 93(10):8627–8629, 2003.

[33] J. B. Restorff, M. Wun-Fogle, A. E. Clark, T. A. Lograsso, A. R. Ross, and D. L. Schlagel. Magnetostriction of ternary Fe-Ga-x alloys (x = Ni, Mo, Sn, Al). *Journal of Applied Physics*, 91(10):8225–8227, 2002.

[34] O. Ikeda, R. Kainuma, I. Ohnuma, K. Fukamichi, and K. Ishida. Phase equilibria and stability of ordered bcc phases in the fe-rich portion of the Fe-Ga system. *Journal of Alloys and Compounds*, 347(1):198–205, 2002.

[35] N. Kawamiya, K. Adachi, and Y. Nakamura. Magnetic properties and mössabauer investigations of Fe–Ga alloys. *Journal of the Physical Society of Japan*, 33(5):1318–1327, 1972.

[36] T. B. Massalski, H. Okamoto, P. R. Subramanian, L. Kacprzak, and W. W. Scott. *Binary Alloy Phase Diagrams*, Volume 1. American Society for Metals, Metals Park, OH, 1986.

[37] Q. Xing, Y. Du, R. J. McQueeney, and T. A. Lograsso. Structural investigations of Fe-Ga alloys: Phase relations and magnetostrictive behavior. *Acta Materialia*, 56(16):4536–4546, 2008.

[38] V. V. Palacheva, A. Emdadi, F. Emeis, I. A. Bobrikov, A. M. Balagurov, S. V. Divinski, G. Wilde, and I. S. Golovin. Phase transitions as a tool for tailoring magnetostriction in intrinsic Fe-Ga composites. *Acta Materialia*, 130:229–239, 2017.

[39] M. Laver, C. Mudivarthi, J. R. Cullen, A. B. Flatau, W.-C. Chen, S. M. Watson, and M. Wuttig. Magnetostriction and magnetic heterogeneities in iron-gallium. *Physical review letters*, 105(2):027202, 2010.

[40] M. Wuttig, L. Dai, and J. Cullen. Elasticity and magnetoelasticity of Fe-Ga solid solutions. *Applied Physics Letters*, 80(7):1135–1137, 2002.

[41] A. G. Khachaturyan and D. Viehland. Structurally heterogeneous model of extrinsic magnetostriction for Fe-Ga and similar magnetic alloys: Part i. decomposition and confined displacive transformation. *Metallurgical and Materials Transactions A*, 38(13):2308–2316, 2007.

[42] A. G. Khachaturyan and D. Viehland. Structurally heterogeneous model of extrinsic magnetostriction for Fe-Ga and similar magnetic alloys: Part ii. giant magnetostriction and elastic softening. *Metallurgical and Materials Transactions A*, 38(13):2317–2328, 2007.

[43] R. Wu. Origin of large magnetostriction in FeGa alloys. *Journal of Applied Physics*, 91(10):7358–7360, 2002.

[44] R. Wu, Z. Yang, and J. Hong. First-principles determination of magnetic properties. *Journal of Physics: Condensed Matter*, 15(5):S587, 2003.

[45] T. A. Lograsso, A. R. Ross, D. L. Schlagel, A. E. Clark, and M. Wun-Fogle. Structural transformations in quenched Fe-Ga alloys. *Journal of Alloys and Compounds*, 350(1):95–101, 2003.

[46] J. Cullen, P. Zhao, and M. Wuttig. Anisotropy of crystalline ferromagnets with defects. *Journal of Applied Physics*, 101(12):123922, 2007.

[47] S. Pascarelli, M. P Ruffoni, R. Sato Turtelli, F. Kubel, and R. Grössinger. Local structure in magnetostrictive melt-spun Fe_{80} Ga_{20} alloys. *Physical Review B*, 77(18):184406, 2008.

[48] S. Bhattacharyya, J. R. Jinschek, A. Khachaturyan, H. Cao, J. F. Li, and D. Viehland. Nanodispersed $D0_3$-phase nanostructures observed in magnetostrictive Fe-19% Ga Galfenol alloys. *Physical Review B*, 77(10):104107, 2008.

[49] H. Cao, P. M. Gehring, C. P. Devreugd, J. A. Rodriguez-Rivera, J. Li, and D. Viehland. Role of nanoscale precipitates on the enhanced magnetostriction of heat-treated Galfenol ($Fe_{1-x}Ga_x$) alloys. *Physical Review Letters*, 102(12):127201, 2009.

[50] F. Bai, H. Zhang, J. Li, and D. Viehland. Magnetic force microscopy investigation of the static magnetic domain structure and domain rotation in Fe-x at.% Ga alloys. *Applied Physics Letters*, 95(15):152511, 2009.

[51] C. Mudivarthi, S.-M. Na, R. Schaefer, M. Laver, M. Wuttig, and A. B. Flatau. Magnetic domain observations in Fe-Ga alloys. *Journal of Magnetism and Magnetic Materials*, 322(14):2023–2026, 2010.

[52] C. Mudivarthi, M. Laver, J. Cullen, A. B. Flatau, and M. Wuttig. Origin of magnetostriction in Fe-Ga. *Journal of Applied Physics*, 107(9):09A957, 2010.

[53] Y. Du, M. Huang, S. Chang, D. L. Schlagel, T. A. Lograsso, and R. J. McQueeney. Relation between Ga ordering and magnetostriction of Fe-Ga alloys studied by X-ray diffuse scattering. *Physical Review B*, 81(5):054432, 2010.

[54] C. Paduani and C. Bormio-Nunes. Density functional theory study of Fe_3Ga. *Journal of Applied Physics*, 109(3):033705, 2011.

[55] H. D. Chopra and M. Wuttig. Non-joulian magnetostriction. *Nature*, 521(7552):340–343, 2015.

[56] X. Liu, M. Li, J. Gou, Q. Li, Y. Lu, T. Ma, and X. Ren. Evidence for lattice softening of the Fe-Ga magnetostrictive alloy: Stress-induced local martensites. *Materials & Design*, 2017.

[57] Y. Ke, C. Jiang, J. Tao, and H. Duan. Local inhomogeneous structural origin of giant magnetostriction in Fe-Ga alloys. *Journal of Alloys and Compounds*, 2017.

CHAPTER 3

RADIATION DAMAGE IN REACTOR PRESSURE VESSEL STEEL ALLOYS: A REVIEW

3.1 Introduction

A reactor pressure vessel (RPV) is considered to be the most important component of a nuclear reactor; it is the main containment of the reactor's core as well as its coolant and a fracture of the vessel could lead to serious damage of the core with radioactive substances escaping. A schematic example of an RPV is shown in Fig. 3.1. RPVs, surrounding the harsh environment of the reactor's core, are made of high-strength low-alloy (HSLA) ferritic steel forgings capable of withstanding the energy and heat, coming from the fuel of the reactor. Despite the RPV steels' inherent high toughness, damage is common and is attributed to energetic particles, i.e. neutrons, bombarding the material thus interacting with and transferring momentum to its atoms. When the kinetic energy of particles, such as neutrons, is sufficiently high the possibility of ionization or displacement of atoms is also increased. As a result, defects and clusters appear in the material, giving rise to changes of mechanical properties (e.g. hardness) that could be crucial for its effectiveness.

Hardening and consequently embrittlement of alloys used for nuclear applications are thought to be due to grain boundary segregation, matrix defect hardening and precipitation events within the material. All three will be discussed in the sections to follow with precipitation being the main subject of debate. Over the course of numerous in-

vestigations copper was found to be one of the major contributors in embrittlement of RPV alloys with Cu-rich precipitates (CRPs) being present in specimens with high copper content. On the contrary, steels having sufficiently low copper, were found to contain precipitates enriched in elements such as manganese, nickel, or silicon always depending on their content within the alloys. In literature such precipitates are most commonly referred to as Mn-Ni precipitates (MNPs).

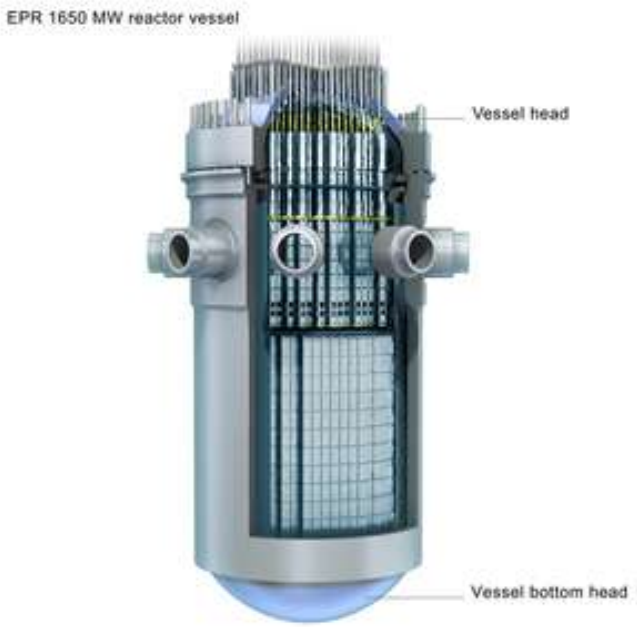

Figure 3.1: Schematic of the Reactor Pressure Vessel (RPV) of the Flamanville 3 EPR 1650 MW reactor that is under construction in Normandy, France[1].

Due to the importance of RPVs and because of the high cost for replacing them, investigations of precipitation events and their role in embrittlement are of high importance. Techniques such as small-angle neutron scattering (SANS), atom probe tomography (APT), positron annihilation spectroscopy (PAS) and others, in combination with micromechanical testing, have been used over the last decades in order to provide a full understanding on the nature of precipitates, giving both structural and compositional information. In this chapter some of these microstructural probing techniques along with reported results will be presented and discussed.

3.2 Alloys for Reactor Pressure Vessel Fabrication

3.2.1 Basics of Steel Metallurgy

Steel is defined as being the alloy of iron and carbon. In its simplest form it contains no more than about 2 wt. % of carbon. It finds applications in various fields, mainly in construction and industry, due to its low cost and high tensile strength. Pure iron, the base metal of steel, can naturally be found in three crystalline phases, body centred cubic (BCC), face centred cubic (FCC), and hexagonal close packed (HCP). Due to its crystal structure allowing the easy movement of its atoms, iron is soft and ductile thus not ideal for practical use. The addition of even small amounts of carbon prevents dislocation movement resulting in the increased hardness of the alloy. Tuning the amount of carbon controls the steel's useful properties as well as adding other alloying elements, such as manganese, nickel, and phosphorous that exist in the iron matrix, either as precipitate phases or solute elements.

The phase diagram of steel (Fe - C) is given in Fig. 3.2. Due to its high complexity, information for carbon up to about 7 wt. % is provided. As seen in the figure, depending on the carbon content and temperature, steel can be found in different phases[2] (a phase is a distinct, homogeneous part of a material, i.e. homogeneous in crystal structure as well as composition) with the main being α-ferrite, γ-austenite, and δ-ferrite. α-ferrite is a solid solution of carbon in BCC iron matrix, with the carbon content not exceeding 0.022 wt. %. This phase is magnetic due to BCC iron being magnetic. It is stable at room temperature but at 912 °C it transforms into γ-austenite. Austenite is the solid solution of carbon in FCC iron with the maximum solubility of carbon being 2.14 wt. %. In contrast to α-ferrite, γ-austenite is a non-ferromagnetic phase. It is easily work-hardened and is both ductile and strong. At 1395 °C it undergoes a phase transition into δ-ferrite; δ-ferrite has the same structure as α-ferrite but is only stable at temperatures above 1395 °C with its melting temperature at 1538 °C. Another phase, cementite (Fe_3C), is

actually a metastable intermetallic compound. At temperatures between 650 and 700 °C it slowly decomposes into α-Fe and C (graphite) but it is stable at room temperature. Cementite contains 6.67 wt. % carbon and 93.33 wt. % iron.

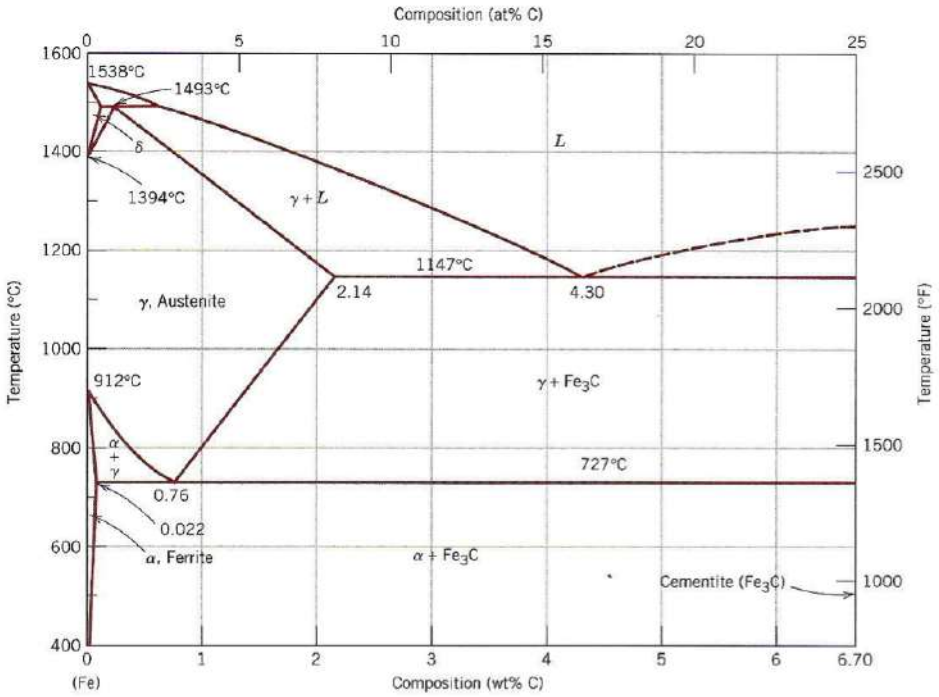

Figure 3.2: Phase diagram of steel showing the different phases as a function of carbon content and temperature[3].

Apart from the aforementioned phases, steel can be of a variety of constituents resulting from mixed phases. Most common of these are the pearlitic, martensitic, and bainitic constituents (though martensite can be thought of as another phase)[4].

Pearlite is a structure containing alternating layers (lamellar structure) of cementite and α-ferrite[4]. It can be created by slowly cooling down from the austenitic phase through the so-called eutectoid (solid-solid) reaction[4]. It contains 0.76 wt.% of carbon (eutectoid composition) and usually makes steel ductile. Steels containing less carbon are often referred to as hypoeutectoid and steels containing over 0.76 wt.% of carbon are called hypereutectoid. The austenite-to-pearlite transformation is dependent upon carbon diffusion, i.e. movement of carbon atoms within the iron lattice[4].

Martensite is produced when austenite is quenched forming a body-centered tetragonal

(BCT) structure[4]. Due to quenching the carbon atoms do not have sufficient time to precipitate out of the iron matrix and thus martensite is supersaturated with carbon[4]. For this reason the martensitic transformation is a diffusionless transformation. Typically, for a steel with a eutectoid composition an amount of austenite, called retained austenite, will remain after the martensitic transformation. When the content of carbon is lower or higher than the eutectoid composition, the retained austenite will be decreased or increased respectively[4]. Overall martensite is quite hard and brittle thus making it difficult to be used in industry and construction as commercial steel but tempering can restore ductility, while keeping strength at high levels.

Bainite contains carbon needles in a ferritic matrix and it is hard with low ductility. As in martensite, tempering can restore its ductility. Bainitic transition occurs at a slower cooling rate than that of martensitic transformation but at a higher rate than that for pearlite formation[4]. The cooling rates involved in the bainitic transformation allow for carbide precipitation due to diffusion of carbon, in contrast to diffusionless martensitic transformation. Bainite is typically distinguished between upper and lower. Upper bainite forms at temperatures between 400 and 550 °C and contains carbides aligned along the lath boundaries of ferrite[4]. Lower bainite forms at temperatures between 250 and 400 °C containing carbides within the ferritic laths and not at the boundaries[4].

The phase diagram in Fig. 3.2 is the equilibrium Fe - C phase diagram but typically in steel processing equilibrium is rarely achieved. As it was discussed a variety of constituents can exist depending on cooling rates as well as composition, i.e. carbon content. For this reason such structures are not included in the equilibrium phase diagram. To better describe the transformation kinetics a time temperature transformation (TTT) diagram, also known as isothermal transformation (IT) diagram, or a continuous cooling transformation (CCT) diagram might be more useful[4]. The difference between the two lies in the way of cooling. In a TTT diagram after a transformation temperature is reached the temperature of the system is kept constant until the transformation is complete and then the system is cooled down at room temperature. In contrast, a CCT diagram de-

scribes the process of a continuous cooling of the system, i.e. varying or constant cooling rates but not zero. Examples of a TTT and a CCT diagram are given in Fig. 3.3.

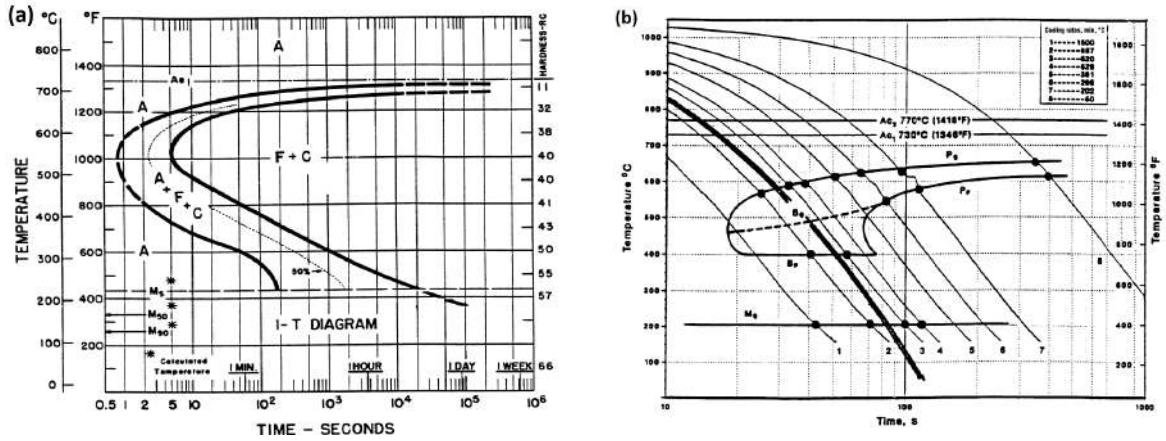

Figure 3.3: (a) TTT diagram of AISI/SAE 1080 steel. In the diagram austenite, ferrite, and cementite are denoted as A, F, and C respectively. Ae_1 denotes the equilibrium eutectoid temperature while M_s the martensite transformation start temperature[4]. (b) CCT diagram of AISI/SAE 1080 steel where eight different cooling rates are given. The points on the diagram denote phase transormtion temperatures[4].

More specifically, on the TTT diagram one can see different phases (or mixture of them) and how they form, with respect to temperature and time, isothermally. On the diagram, austenite is marked as A, ferrite as F, and cementite as C. The temperature above which austenite is stable is given as Ae_1 (also referred to as equilibrium eutectoid temperature). The austenite that exists below that temperature is unstable and is called subcritical austenite. The martensitic transormation start temperature is denoted as M_s. To receive such a diagram, samples (typically thin specimens) are heated above the Ae_1 temperature and then are placed in a salt or lead pot having constant temperature, below Ae_1[4]. The specimens are held under constant temperature for an amount of time (holding time) to allow for the phase transformation to advance. Then the specimens are quenched so as to stop the transformation. Example of such a process is the so-called austempering during which austenite is isothermally transformed into bainite.

The TTT diagram discussed above was developed to study the time progression of phase transformations under constant temperature but most commonly heat treatments of steels are performed under various heating and cooling rates. The CCT diagram given in

Fig. 3.3(b) describes such processes. To construct the diagram specimens are cooled down at different cooling rates (simulating oil and air cooling, quenching etc.) while tracking the start and finish temperature of each phase transformation[4]. Such temperatures are

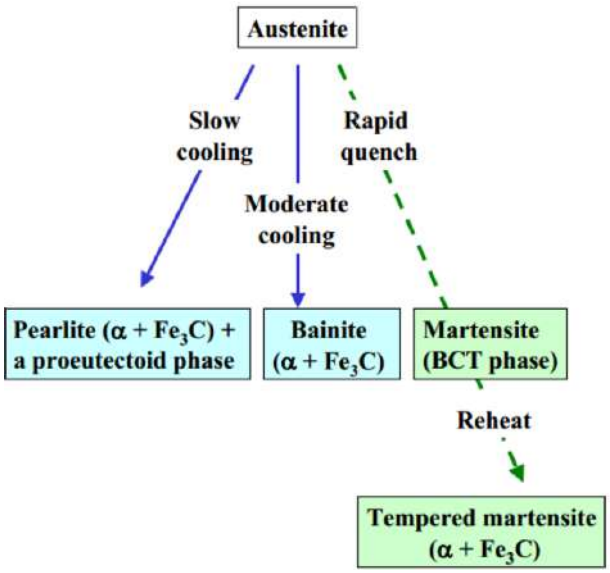

Figure 3.4: Schematic illustration of different constituents resulting from the parent austenitic phase upon different cooling rates. The dashed green line following the martensitic transformation corresponds to a diffusionless tranformation.

denoted in the diagram with the subscript s and f respectively (e.g. B_s and B_f for bainite). It is indeed seen that for different cooling rates different constituents prevail. For example to form bainite an intermediate cooling rate, between those for pearlite (slow cooling) and martensite (quenching), is required. The different structures and the corresponding cooling rates are summarized and illustrated in Fig. 3.4. It is noteworthy that, in contrast to the Fe - C diagram, there are not single TTT or CCT diagrams but, depending on the type and composition, different steels will have different diagrams.

Following the TTT or most commonly the CCT diagram of a steel one can perform a variety of heat treatment processes. In general heat treatment can be defined as a process or series of processes involving heating and cooling of an alloy in order to control its properties receiving desirable results. Different heat treatments control different properties. For example, to produce microstructural uniformity normalising or homogenising is typically performed[4]. For increasing hardness quenching of the alloys is performed whereas

for decreasing hardness and improve ductility one performs annealing, or tempering[4]. Of course the main difference between different heat treatments lies in the heating or cooling rates as well as the temperature ranges. For example during annealing a steel is heated above the Ae_1 temperature forming austenite and then slowly cooled in a controlled way, inside a furnace. Normalising is similar to annealing; a steel is heated above the critical Ae_1 temperature fully and homogeneously being austenitised but, after some time, the steel is air cooled instead of furnace cooled. For this reason the cooling rate of the steel is faster than that after annealing. Normalising is typically cheaper than annealing. Tempering is the process during which a quenched alloy is reheated below the transformation temperature for a specific amount of time and then cooled down to room temperature. Tempering is often performed to restore ductility in hard martensite. Of course these are just some typical examples of heat treatments. For more detailed information about the different heat treatments and their results as well as an overall detailed overview of the metallurgy of steels the reader is referred to Ref. 4.

3.2.2 Brittle and Ductile Fracture

Fracture of a material is defined as its separation into pieces when a stress is applied[5]. The two distinct steps of fracture are (i) the crack formation and (ii) the crack propagation[5]. Depending on the ability of a material to deform plastically or not before it is fractured, fracture can be distinguished into ductile or brittle respectively[5].

More specifically, ductile materials exhibit extensive plastic deformation and energy absorption before fracture. The plastic deformation results in necking of the material prior to fracture. Micro-voids are formed and coalesce to form the initial crack which then propagates by shear deformation. Finally fracture (separation) occurs[5].

In contrast, in the case of brittle fracture there is no significant plastic deformation. The crack propagation is very fast and almost perpendicular to the direction of the applied stress. The crack typically propagates due to atomic bonds breaking (cleavage) in the

direction of a crystallographic direction (cleavage plane)[5]. Depending on the way the crack propagates, brittle fracture can be distinguished in transgranular and intergranular. In the former case the cracks move through the grains while in the latter the fracture crack propagates through grain boundaries[5].

Upon cooling a ductile material can become brittle. This is known as the ductile-to-brittle transition and the temperature at which the transition occurs is known as the ductile-to-brittle transition temperature (DBTT)[5]. In general steels become brittle at low temperatures causing serious embrittlement, but alloying elements or impurities can increase the DBTT causing fracture even at high temperatures. This for example is a major problem for steels used in nuclear industry where operation temperatures are in the order of about 300 °C and impurities or solute clustering increase the DBTT (the reader is referred to the following sections for more information).

3.2.3 Types of Steels Used for the Fabrication of Reactor Pressure Vessels

This section is focused on the different materials used for the fabrication of reactor pressure vessels (RPV) that contain the core and coolant of nuclear reactors. Nuclear reactors, generally, can be categorised based on a variety of different aspects such as the type of reaction taking place, their commercial purpose, the coolant used, or the type of construction. Focusing on the coolant type, most of reactors in operation today are the so-called light water reactors (LWR). The LWR can be further distinguished into pressurised water reactors (PWR) and boiling water reactors (BWR). Their difference lies in the way they generate steam for power production. A PWR uses a secondary steam generating circuit, separated from the primary heating and transfer unit where water is held under high pressure at a temperature of about 300 °C. On the other hand, a BWR generates steam in the pressure vessel itself, in the space above the core. Since the vast field of nuclear technology and the specifics of the operation of nuclear reactors

are outside the scope of this thesis the reader is referred to Refs. 6 and 7. PWRs are the most common reactors in use today with BWRs being the second most common. The RPVs used in PWRs can be distinguished in western-type RPVs and WWER RPVs (WWER stands for water-water energetic reactor), with WWER being PWRs mainly used in eastern Europe[8]. The materials under investigation in this thesis are model alloys resembling steels used for the fabrication of western-type RPVs thus the discussion will be focused on this type.

Generally, different components of a western-type RPV, such as nozzles, shells, studs, flanges etc., are fabricated using different materials that have changed and evolved following the evolution of the PWRs products. For example the shell plates of earlier vessels, according to the Westinghouse designers, were made out of ASME SA 302 Grade B steel but those of later vessels were manufactured by using ASME SA 533 alloys[9]. Other types of alloys used in RPVs include ASME SA 508 Class 2, 22NiMoCr37 or 20MnMoNi55, and 16MnD5 in USA, Germany, and France respectively. Information on the various alloys used for the beltline region of the RPVs are given in Fig. 3.5 and the compositions of the different steel types are provided in Fig. 3.6.

Country	Shells	Austenitic cladding
USA	SA302 GR B SA533 GR B, Class 1 SA 508 Class 2 SA 508 Class 3	TYPE 308L, 309L TYPE 304
France	16MnD5	
Germany	20MnMoNi55 22NiMoCr3 7	
WWER-440	15Kh2MFA(A)	Sv 07Kh25N13 — 1st layer Sv 08Kh19N10G2B — 2nd layer
WWER-1000	15Kh2NMFA(A)	

Figure 3.5: Table showing the different types and code names of steel alloys emploued for the manufacturing of beltline of the RPVs built in USA, France and Germany as well as WWER eastern type reactors[8].

The SA 302, Grade B alloy (20MnMo55 in Germany) is a Mn-Mo plate steel that was used for RPVs manufactured mostly in the 1960s. Over the years the need for commercial

Designation	Elements (mass %)													
	C	Si	Mn	P	S	Cr	Mo	Ni	V	Cu	Al	Sn	N	As
ASTM A 302B	max	0.15	1.15	max	max		0.45							
	0.25	0.30	1.50	0.035	0.040		0.60							
ASTM A 336, Code Case 1236	0.19	0.15	1.10	max	max	max	0.50	0.40						
	0.25	0.35	1.30	0.035	0.035	0.35	0.60	0.50						
ASME A 508 Cl 2 (1971)	max	0.15	0.50	max	max	0.25	0.55	0.50	max					
	0.27	0.35	0.90	0.025	0.025	0.45	0.70	0.90	0.05					
ASME A 533 GR B (1971)	max	0.15	1.15	max	max		0.45	0.40						
	0.25	0.30	1.50	0.035	0.040		0.60	0.70						
ASME A 508 Cl 2 (1989)[a]	max	0.15	0.50	max	max	0.25	0.55	0.50	max	max				
	0.27	0.40	1.00	0..015	0.015	0.45	0.70	1.00	0.05	0.15				
ASME A 508 Cl 3 (1989)[a]	max	0.15	1.20	max	max	max	0.45	0.40	max					
	0.25	0.40	1.50	0.015	0.015	0.25	0.60	1.00	0.05					
ASME A 533Gr B (1989)	max	0.15	1.15	max	max		0.45	0.40						
	0.25	0.40	1.50	0.035	0.040		0.60	0.70						
16 MnD5 RCC-M 2111[b]	max	0.10	1.15	max	max	max	0.43	0.50	max	max	max			
	0.22	0.30	1.60	0.02	0.012	0.25	0.57	0.80	0.01	0.20	0.040			
18 MnD5 RCC-M 2112 (1988)	max	0.10	1.15	max	max	max	0.45	0.50	max	max	max			
	0.20	0.30	1.55	0.015	0.012	0.25	0.55	0.80	0.01	0.20	0.040			
20 Mn Mo Ni 5 5 (1983, 1990)[c,d]	0.17	0.15	1.20	max	max	max	0.40	0.50	max	max	0.010	max	max	max
	0.23	0.30	1.50	0.012	0.008	0.20	0.55	0.80	0.02	0.12[e]	0.040	0.011	0.013	0.036
22 Ni Mo Cr 3 7 (1991)[f]	0.17	0.15	0.50	max	max	0.25	max	0.60	max	max	0.010	max	max	max
	0.23	0.35	1.00	0.012	0.008	0.50	0.60	1.20[g]	0.02	0.12[e]	0.050	0.011	0.013	0.036

[a] Supplementary Requirement S 9.1(2) and S 9.2 for A 508 Cl 2 and A 508 Cl 3.
[b] Forgings for reactor shells outside core region. Restrictions for core region (RCC-M 2111): S ≤ 0.008, P ≤ 0.008, Cu ≤ 0.08.
[c] VdTÜV Material Specification 401, Issue 1983.
[d] KTA 3201.1 Appendix A, Issue 6/90.
[e] Cu-Content for RPV (core region) shall be ≤0.10%.
[f] According to Siemens/KWU under consideration of SR 10 (MPA Stuttgart).
[g] For flanges and tube sheets the Ni content shall be ≤1.40%.

Figure 3.6: Table showing the compositional requirements and main ferritic materials used for western-type RPVs[8].

power increased and so did the size of the vessels. Steel alloys with higher hardenability were required due to the increased thickness of the vessel wall. This was achieved by adding nickel, with content between 0.4 and 0.7 wt.%, in the SA 302, Grade B having as a result the increase of the high fracture toughness and yield strength across the entire vessel's wall. A few other alloys used around the same time, mostly for nozzles and flanges, are the SA–182 F1 and SA–336 F1 that are a modified Mn-Mo-Ni forging steel and a C-Mn-Mo steel respectively. The drawback of using this kind of forging steels lies in their processing; expensive and time consuming heat treatment was necessary for reducing hydrogen blistering. To overcome this problem a newer version of steels was used to replace the alloys that did not require such extensive thermal treatment. The alloy is the SA–508 Class 2[10] (originally described to be an ASTM A366 Code Case 1236 steel) and is widely used in flanges, nozzles as well as ring forgings and other components. In Germany it was introduced as 22NiMoCr36 or 22NiMoCr37 steel and it became one of the most common and important materials for the manufacturing of German reactors. A modified version, known as SA-508 Class 3, is mainly used today in the manufacturing of RPVs of western type.

3.3 Fundamentals of Material Irradiation

3.3.1 Radiation Damage & Defects

During irradiation of matter by energetic particles, interactions between the incident projectiles and the atoms within the material can lead to alternation of regular ordering of the lattice resulting in microstructural defects. The defects, being the result of radiation damage, can cause changes of mechanical and structural properties of materials with serious implications on safety and productivity of nuclear equipment. In the specific case of fission reactions most of the radiation damage is caused by neutrons because of their high kinetic energy. The binding energy of atoms within a lattice varies but it is generally

low, in the range of about 10 to 60 eV[11]. The kinetic energy of neutrons can be in excess of 0.1 MeV thus more than sufficient to knock off atoms from their lattice position.

The mechanism of radiation damage is initiated by energy transfer from the incident particles to the atoms of the irradiated solid. The process can be characterised by a few distinct steps[12]; the incoming particles interact with the atoms transferring energy to them, in the form of kinetic energy, leading to the formation of primary knock-on atom (PKA). The PKA is displaced by its normal position and due to usually having high kinetic energy it creates higher order knock-on atoms. The resulting effect is the so-called displacement cascade. Finally the original PKA stops at an interstitial site denoting the conclusion of the radiation damage event.

The space originally occupied by a displaced atom becomes a vacancy (i.e. vacant space) and the vacancy-interstitial pair is referred to as Frenkel pair. If an interstitial atom is in close proximity to a vacancy there is possibility of recombination. Thermal effects also need to be taken into account during irradiation due to diffusion of vacancies-interstitials[13]. This might result in Frenkel pairs collapsing. The low temperature recovery of irradiated materials is attributed to this process. An atom occupying an interstitial site is normally the same as the atoms of the matrix of the irradiated material and it is called a self-interstitial. A self-interstitial might induce higher strain in the lattice of the

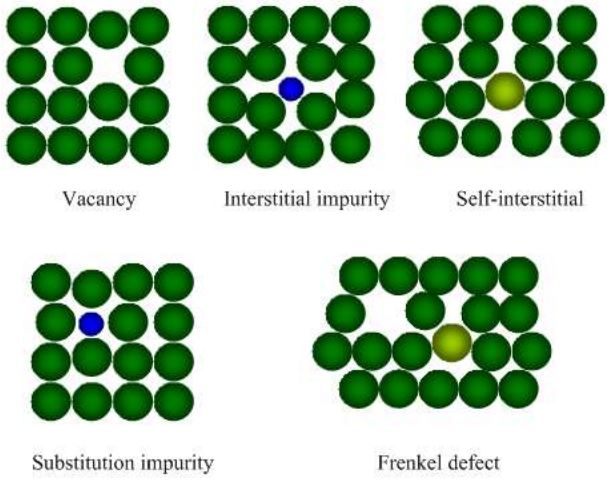

Figure 3.7: Schematic depicting the various point defects within a material[14].

material, being as large as the atoms of the lattice, in contrast to an interstitial impurity

that might be of smaller size. This is clearly seen in Fig. 3.7.

The self-interstitial atom and the atom pushed from its original position, at the interstitial site, create a pair with the shape of a dumbbell[15]. The centre of mass of the system of these two atoms lies in the original site location. The so-called dumbbell interstitial, depending on the crystal structure, can cause serious changes to the lattice of the material. For example a BCC lattice would undergo a shape and volume change, as can be seen in Fig. 3.8.

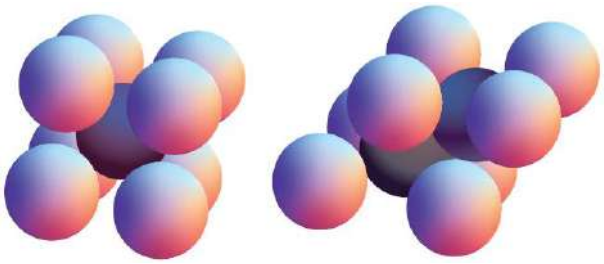

Figure 3.8: Volumetric change of a BCC unit cell due to a self-interstitial[15].

In contrast, if the lattice is FCC then it would undergo a volumetric expansion. For more information on the various volume changes due to self-interstitials the reader is encouraged to read the work of W. G. Wolfer[15], providing a mathematical approach on the topic.

Radiation damage itself can be distinguished into three main groups[16]:

- Displacement damage; lattice atoms displaced and shifted from their original position creating vacancies and interstitials, existing as Frenkel pairs.
- Ion implantation or transmutation by stopping of incoming particles or capturing by the nucleus respectively, resulting in changes in chemical composition.
- Ionization of atoms via orbital electron excitation.

For quantifying radiation damage the term displacement per atom (dpa) is used. As atoms are displaced from their original position within the lattice, upon a collision with an incident particle of sufficient kinetic energy, the dpa value gives a measure of, as its name

indicates, the number of displacements of an atom from its initial site. It is dependent on the incident particle's type, energy, flux and fluence, as well as on the irradiated material's properties. The most widely used model for describing radiation damage and providing a dpa value is the model developed by Kinchin and Pease[12,16], normally just referred to as the K-P model. It is the simplest radiation damage model. Its main assumption is that a PKA will create a collision cascade via an elastic collision with another atom only if the original energy transferred to the PKA is greater than a threshold energy. This also known as the displacement threshold, which is the minimum energy needed to displace an atom from its original position. If the transferred energy is less than the threshold energy then the atom will not be displaced but rather vibrate about its equilibrium position. In such a case the vibration will be transmitted to the neighbouring atoms and the energy will be released as heat. The collision of a PKA with an atom is based on the hard sphere approximation denoting that the interaction between atoms vanishes when their separation distance is greater than their radius. Other assumptions of the model are the randomness of the atomic arrangement, i.e. crystal structure effects are neglected, and the assumption of non-annihilation of defects.

3.3.2 Simulating Neutron Irradiation Damage

Neutron irradiation is the main cause of irradiation damage and embrittlement of RPV functional materials. When exposed in the irradiation environment of a nuclear reactor the RPV steels will age and degrade through accumulated irradiation damage over years of exposure.

Experiments performed on RPV materials using neutrons are both time consuming and of high cost. In order to reach appreciable fluence level matching the accumulated radiation damage from a nuclear reactor during its operating time, several years are required. On top of that, specimens irradiated with neutrons become radioactive making their study quite challenging; special requirements for handling, characterising as well as

shipping are needed.

Research on irradiated fission-reactor materials and the resulting effects of neutron exposure started in the years between 1940 and 1945 during the Second World War[17] and after the appearance of the first nuclear reactors with increasing efforts over the following years. Researchers of North American Aviation at Downey California were probably the first to realise that the use of heavy or light charged particles could be an alternative to the use of neutrons with apparent advantages[18]. The first use of heavy ions started in c.a. 1970 because a damage rate $\sim 10^4$ higher than that received with neutrons could be available[19].

Irradiation induced damage tests using heavy or light charged particles are quite appealing for several reasons. Ions having similar mass to that of the target material can be easily produced in MeV accelerators at high current having as a result shorter irradiation time, low cost, and almost no residual radioactivity[20]. Precise control and variation of temperature, dose rate, as well as overall dose along with the extended damage levels is another factor making the use of charged particles over neutrons beneficial.

At this point it is important to introduce the concept of the Bragg curve. Charged particles moving through a sample gradually lose energy due to collisions and ionisation. A Bragg curve is the plot providing information on the particle's energy loss with respect to the depth reached into the material (distance travelled)[21]. The curve has a characteristic peak, the so-called Bragg peak, appearing just before the particles stop. The peak is the result of large amount of energy being released by the particles. Consequently, the density of vacancies at this point in the sample is higher[21].

3.3.2.1 Protons for Simulating Neutron Irradiation Damage

Using protons for simulating neutron irradiation is quite advantageous because of the accelerated dose rates provided. Protons have a high displacement cross section. As a result their mean free path is reduced; being positively charged particles, protons, interact with the screened Coulomb potential posed by the electronic cloud of the atoms.

Consequently, a proton will have a mean free path of $\sim 10^6$ times shorter[22] than that of a neutron interacting with the nucleus when the velocities of the two particles are similar. This results in much shorter irradiation time with appreciable damage levels, up to 10 dpa[12], reached in hours rather than years. Additionally, the screened Coulomb potential is considered to be a good approximation for describing the interaction of protons with target materials leading to low residual radioactivity; proton collisions within this approximation create multiple PKAs with low energy whereas neutron collisions, within the hard-sphere approximation, create a significantly smaller number of PKAs but with substantially higher energy thus causing sample activation.

Another feature that makes protons valuable for irradiation testing is the relatively good penetration depth compared to ions of heavier elements (e.g. Ni); it is reported that protons generate penetration depths that could easily exceed 40 μm[12], always depending on the target material and the energy of the proton beam, resulting in reduced variations in dose and dose rates. Also, compared to heavy ions, such as Ni^{++} (see Fig. 3.9), their larger penetration depth results in larger analysis volume. From Fig. 3.9 one can see that

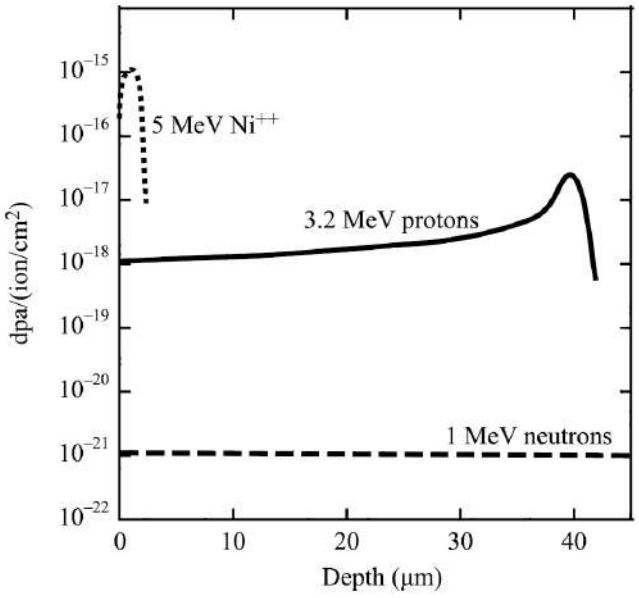

Figure 3.9: Damage profile of stainless steel irradiated with 1 MeV neutrons, 3.2 MeV protons and 5 MeV Ni ions. The graph gives the displacement per atom with respect to the penetration depth for the three different particles. Adapted from Ref. 12.

protons have relatively flat damage profile resulting in the aforementioned low variation

in dose rates. This low variation allows for even distribution of induced damage.

In a study contacted by G. S. Was *et.al.* on "Emulation of neutron irradiation effects with protons: validation of principle"[20] it is shown that two high-Cr stainless steels, irradiated by both protons and neutrons at damage levels reaching 5 dpa, exhibited similar yield stress values resulting in similar hardness results (see Fig. 3.10(a) and 3.10(b)). Fig. 3.10(c) gives results of a similar study performed by P. Cohen *et.al.*[23] on RPV steels

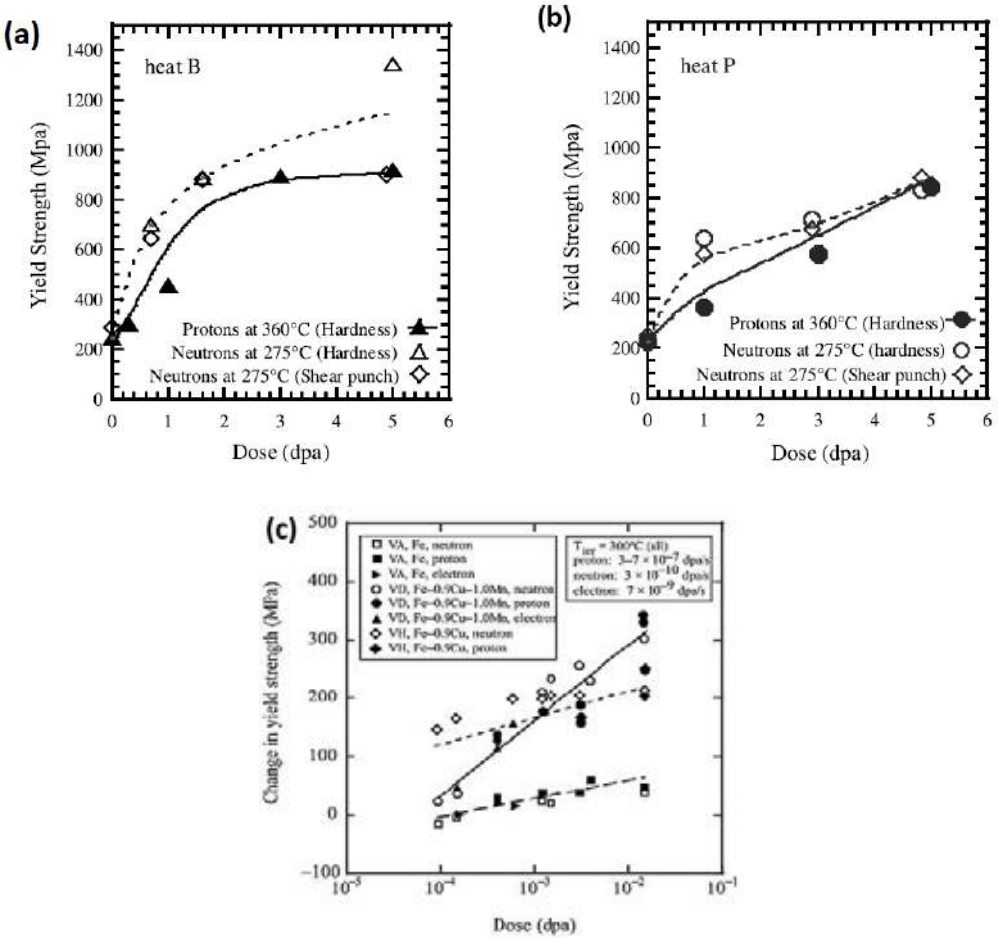

Figure 3.10: Plot (a) and (b) display how the yield strength of high-Cr stainless steels depends on the radiation dose. Heat B refers to 304 stainless steel and heat P to 316 stainless steel. Shear punch measurements were carried out on neutron-irradiated steels, while the hardness measurements were carried out on steels that had been irradiated with both neutrons and protons[20]. Plot (c) shows how the change in yield strength depends on the irradiation dose for a variety of different projectiles at about 300°C[23].

of varying composition irradiated at various damage levels by neutrons, protons, and electrons at 300 °C. As in the study of G. S. Was[20], the results here showed that despite

the varying damage rates and range of compositions, changes of yield stress and hardness were consistent.

In 2015 K. J. Stephenson and G. S. Was[24] conducted a study on austenitic stainless steels that were both neutron and proton irradiated in order to compare "microstructure, microchemistry, hardening, susceptibility to IASCC (irradiation assisted stress corrosion cracking) initiation, and deformation behaviour resulting from proton or reactor irradiation"[24]. The proton irradiations produced a damage level of 5.5 dpa and the neutron irradiations produced a damage level ranging between about 5 and 12 dpa. The specimens were investigated by means of TEM, energy-dispersive X-ray spectroscopy, microhardness measurements, and constant extension rate tensile testing. The results showed that protons could be used as surrogates to neutrons for irradiation-induced damage experiments. Despite differences in time scale and other parameters the damage effects were indeed comparable; the level of grain boundary segregation and changes in hardness and yield stress were similar and the relative susceptibility to irradiation assisted stress corrosion cracking was "nearly identical"[24].

The use of protons for the irradiation of test RPV alloys indeed offers many advantages, however potential activation of elements within the steels cannot be fully discarded. To achieve similar damage to that in a reactor, while operating within a reasonable time frame for the irradiations, it is important to use as high an energy as possible. However, this brings up two potential issues:

1. Transmutation – By bombarding the alloy with relatively high energy protons (on the order of MeV), there is a chance for transmutation of elements within the matrix. For example, Fe will transmute to Co at about 5.5 MeV and the produced Co will be extremely active. This will not only change the material to be studied, but also brings in issues with sample transport and handling.

2. Matrix damage – There is an argument that bombarding the matrix with particles that have such distinctly different energies (MeV as opposed to eV), may cause changes in the matrix that may affect the experimental results or material microstructure (in a

way not fully consistent with neutron irradiation effects).

3.3.3 Particle Accelerators for Irradiation Damage Testing

3.3.3.1 Cyclotron

A cyclotron is one of the earliest particle accelerators in which charged particles are accelerated within a semicircular path with increasing radius. The cyclotron's invention is attributed to Ernest O. Lawrence[25] in 1934 for which he received the 1939 Nobel prize in physics[26]. His 60-inch cyclotron is depicted in Fig. 3.11. Despite cyclotron's use being reduced in the 1950s due to the synchrotron's appearance they are still in use today, mainly as parts of multi-stage accelerators.

Cyclotrons make use of the magnetic field generated by charged particles in order to hold them in spiral trajectories with the help of an external static magnetic field, while a high-frequency oscillating electric field is used for accelerating them. A schematic representation of a cyclotron is depicted in Fig. 3.12. It consist of two D-shaped hollow metal chambers (electrodes), also known as "dees", positioned between the poles of an electromagnet which is kept under vacuum. The electromagnet produces a constant magnetic field perpendicular to the particle's trajectory. The alternating electric field used for the particles' acceleration is applied in the gap between the two electrodes and is induced by a high-frequency (radiofrequency) potential supplied directly to the electrodes. Protons that are to be accelerated are produced by hydrogen gas ionisation and then injected at the centre of the cyclotron in the gap between the two electrodes. They are then accelerated towards the electrode kept at negative potential where, due to the magnetic field, they travel in a semicircular trajectory until they reach the gap between the two electrodes again at which point the electric field is reversed so the protons travel through the second electrode. The entire process is continuous and repeated resulting in a spiral accelerating motion of the protons. Once they reach a desirable energy level they are released and guided via a beam-line towards the target material.

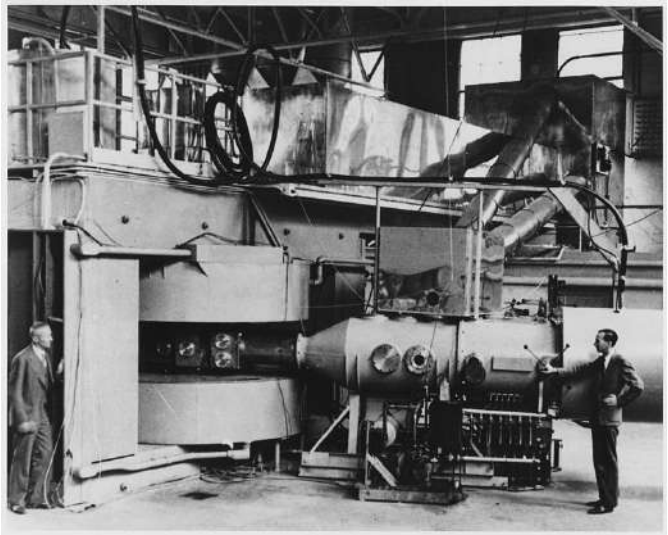

Figure 3.11: One of the earlier cyclotrons developed by Ernest Orlando Lawrence. The picture was taken at the Lawrence Radiation Laboratory, University of California in August 1939[27].

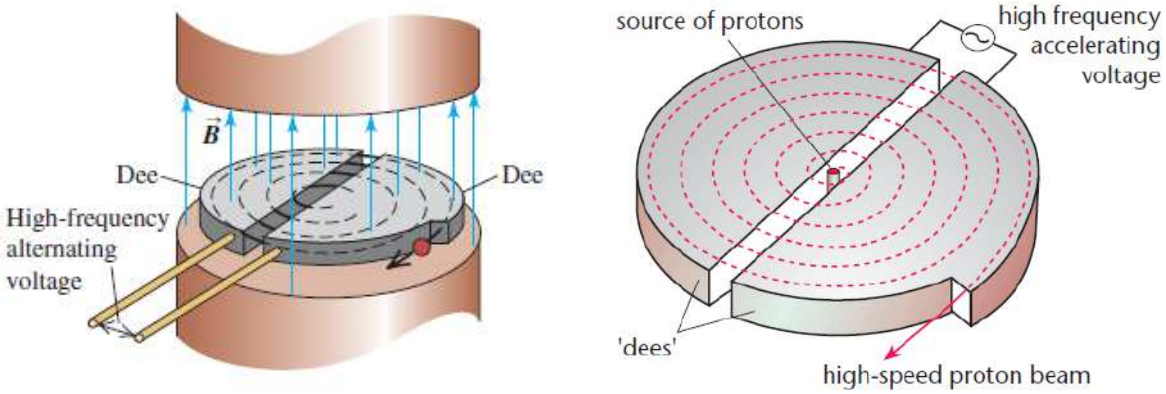

Figure 3.12: Schematic representations of a cyclotron, clearly showing the "dees", the gap across which the protons are accelerated, and the path taken by the protons. In the left figure, the magnetic field, which controls the trajectory of the particles, is depicted. The right figure gives a clearer picture of the semicircular proton path[28,29].

3.3.3.2 Dynamitron®

A Dynamitron® is a cascaded rectifier used as linear particle accelerator[30] and depending on its set up it can be used for accelerating either electrons or protons. It was patented in 1959[31] and then developed by Radiation Dynamics, Inc., currently part of IBA-Industrial, Inc. (see Fig. 3.13). A schematic representation of a Dynamitron® is depicted in Fig. 3.14 where one can see that the rectifiers are driven in parallel; two series of rectifier diodes are positioned opposite to each other connected to the high-voltage terminal and the earth terminal respectively. The so-called accelerator column is surrounded by large RF electrodes[32] that provide the rectifiers with the alternating radiofrequency potential, thus creating a high-frequency alternating electric field. The accelerator is also enclosed in corona half rings that provide the necessary capacitance coupling between the electrodes and the rectifiers[30,32].

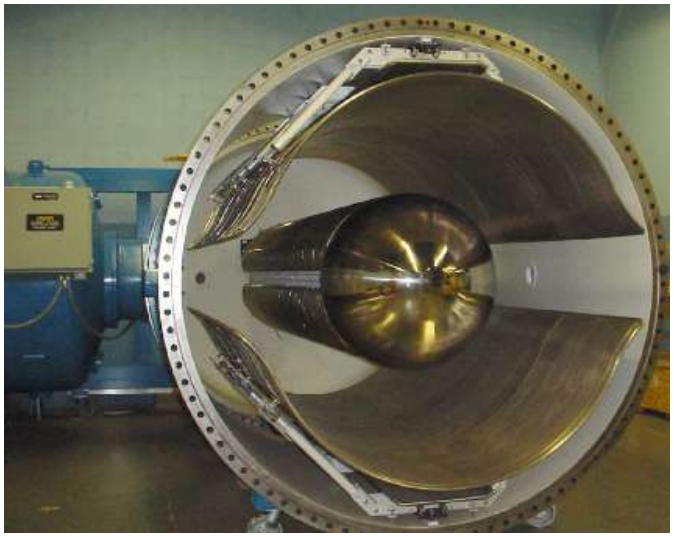

Figure 3.13: The Dynamitron® developed by Radiation Dynamics, Inc. in the 1960s[33].

The protons entering the accelerator column will be accelerated gradually by the electric field produced by the RF electrodes; the alternating potential results to the protons accelerating between rectifiers. The charged particles will be accelerated at a maximum velocity reaching the end of the tube where they are driven towards the target material.

Nowadays Dynamitrons® up to 5 MV are commercially available (provided by IBA).

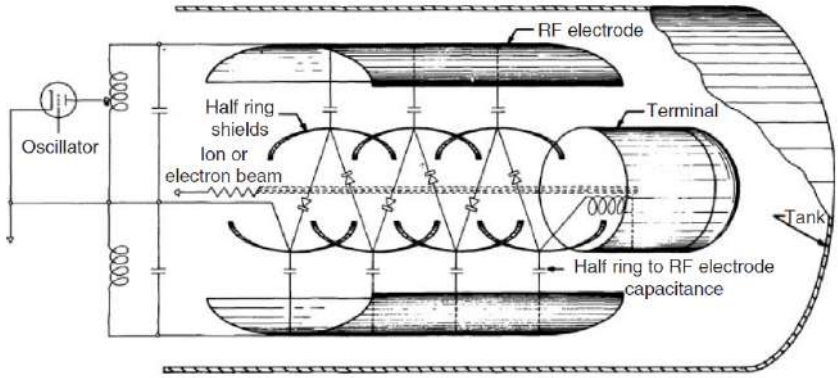

Figure 3.14: A schematic representation of a Dynamitron® particle accelerator[30].

Most of them are built to accelerate electrons for applications such as sterilization and industrial polymerization. Dynamitrons® built for proton acceleration are used, as in the context of the present work, in applications such as emulating neutron irradiation-induced damage in RPV steels.

3.4 Probing Techniques for the Microstructural Characterisation of RPV Steels

In order to probe changes occurring in RPV steels due to irradiation, microstructural techniques are required. Methods such as Small-Angle Neutron Scattering (SANS), Atom Probe Tomography (APT), and Positron Annihilation Spectroscopy (PAS) as well as complementary techniques such as SEM, TEM and Vickers microhardness measurements can provide structural and/or compositional information near or at the atomic scale giving valuable insight on the microstructure after irradiation. The embrittlement of the materials can then be understood and quantified by correlating micro-scale irradiation effects with macro-scale material properties such as hardness, yield strength and others.

3.4.1 Small-Angle Neutron Scattering

Small-angle neutron scattering is a technique that makes use of neutrons interacting with atomic nuclei as well as the magnetic moment of unpaired electrons thus providing both structural and magnetic order information. During a SANS measurement it is the intensity of elastically scattered neutrons that is being recorded and analysed. SANS is extensively used for probing irradiation-induced or enhanced precipitation events over a large volume (a few mm^3) of material providing information on their size distribution and number density as well as an estimate of their composition[34]. There are numerous studies published on SANS analysis of RPV steels and precipitation[35–41].

In 2006 A. Ulbricht *et al.*[40] reported a SANS study on post-irradiation annealed RPV steels. For their experiments they used two different steels, referred to as M1 and M2, of varying composition (see Fig. 3.15).

Composition of the materials (analysis) in wt% (balance Fe)

Code	C	Mn	Si	Cr	Ni	Mo	V	S	P	Cu
M1	0.20	1.42	0.23	0.13	0.80	0.52	0.008	0.005	0.020	0.15
M2	0.18	1.33	0.26	0.16	0.73	0.55	0.006	0.004	0.020	0.29

Figure 3.15: Table providing the composition of samples M1 and M2 in wt.% (balance Fe).[40]

The samples were irradiated under various neutron fluences and flux densities at 255 °C in the prototype VVER-2 reactor. Their SANS measurements were performed at the V4 instrument of Helmholtz Zentrum Berlin and D11 instrument of the Institute Laue-Langevin, Grenoble. The resulting SANS intensity curves are given in Fig. 3.16. From their results the effect of post-irradiation annealing was apparent and it is clearly seen in the scattering plots, with the as-irradiated samples having more distinct features.

A similar study is that of F. Bergner *et al.*[41] on the "Nature of defect clusters in neutron-irradiated iron-based alloys deduced from small-angle neutron scattering"[41]. The samples investigated in this study were low-Cu and high-Cu Fe-based model alloys denoted as alloy A and alloy B respectively. They were both irradiated at 270 °C under

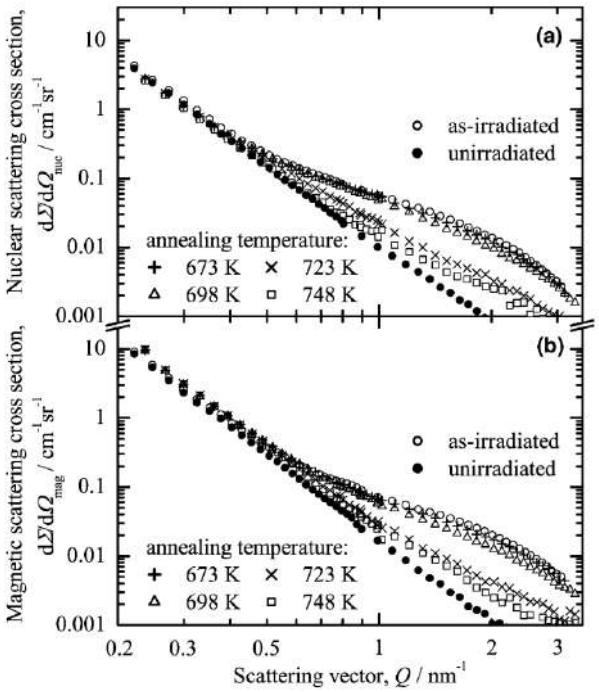

Figure 3.16: Nuclear and magnetic scattering curves for unirradiated, as-irradiated, and annealed samples.[40]

two different irradiation conditions. The SANS measurements were performed at the V4 instrument of Helmholtz Zentrum Berlin. The resulting scattering curves are depicted in Fig. 3.17(a). Any precipitation occurred within the materials after irradiation or heat treatment were easily detected by the SANS technique and can be seen as an increase in the SANS intensity at higher $\vec{q}$ values. Overall from the SANS results and by analysing A ratio values received for each sample the authors tried to estimate the possible composition of the irradiation induced features found in both sets of specimens. Overall, their work clearly demonstrated the capability of SANS in detecting precipitation events in the nanometre scale as well as in providing information on their size distribution but failed to provide a solid answer for their composition indicating that the technique has a deficiency in this area.

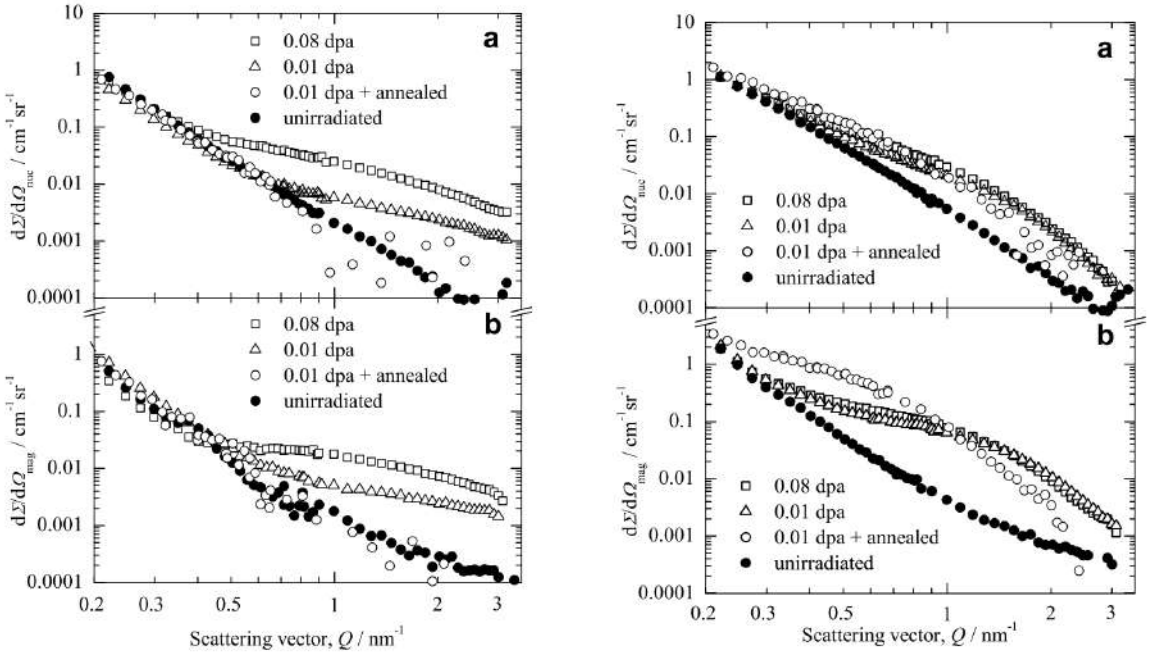

Figure 3.17: Nuclear (a) and magnetic (b) scattering curves for sample A (left) and sample B (right).[41]

3.4.2 Atom Probe Tomography

Atom Probe Tomography (or 3D Atomic Probe Tomography) is a technique that makes use of field evaporation, time-of-flight spectroscopy and position-sensitive detection[34]. The samples under investigation, after being properly shaped (needle shaped), are cooled down to cryogenic temperatures and then with the use of a high electric field, surface atoms are positively ionised resulting in their repulsion from the positively charged surface. The process can be described as a controlled evaporation. The removed ions are then detected and their behaviour after evaporation is analysed.

APT is used for destructively analysing the microstructure of materials and is shown to be quite effective in chemical analysis of solute clusters[34]. The samples analysed with APT are usually of small volume (e.g. 50 x 50 x 100–200 nm^3)[34]. The method has the advantage of being able to even probe just a few atoms. This makes APT a very useful method for mapping the atomic lattice in great detail making deviations from its normal

structure easy to detect. Careful analysis of the data provides information on composition of the overall examined area as well as size, composition, and number density of nano-features detected. APT, like SANS, has been employed in multiple occasions[42–46] for probing irradiation induced precipitation. In 2007 M.K. Miller *et al.*[44] reported an APT study of high-Ni and high-Cu RPV steel welds from the Midland and Palisades reactors. The specimens used were both unirradiated and neutron irradiated to a relative high fluence (up to 3.4 x 10^{23} m^{-2}). Their APT maps are given in Fig. 3.18.

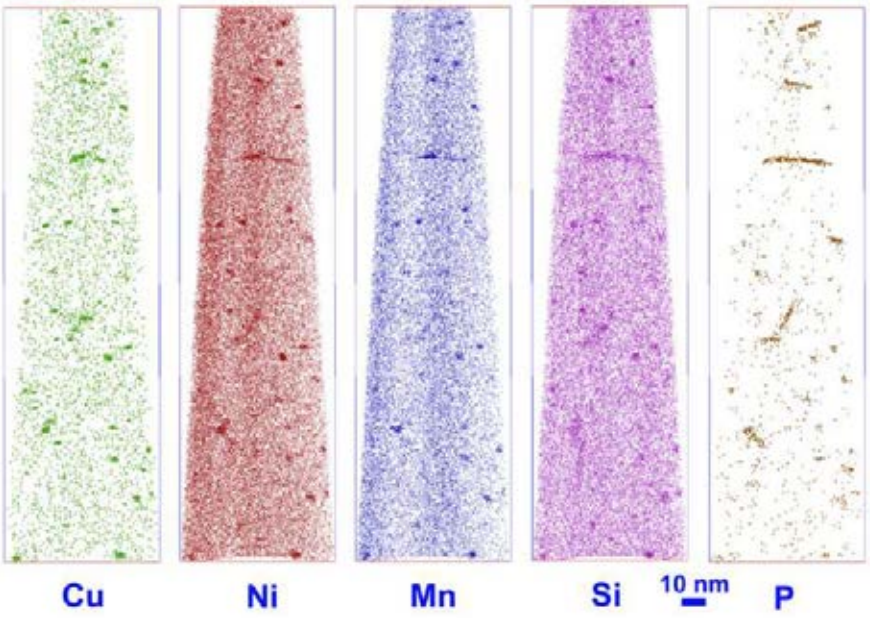

Figure 3.18: APT results of steel weld from the Midland reactor, as measured by M.K. Miller *et al.*[44]. The steel weld had prior to measurements been exposed to a neutron fluence of 3.4×10^{23} m^{-2}. Each box is an atom map of a specific element, clearly conveying the evidence for Cu-, Ni-, Mn-, and Si-enriched precipitates in the steel weld.

Their results indicated the presence of nanometre sized, about 2 nm, clusters enriched in Cu, Mn, Ni, and Si and there was no clear indication of other matrix elements, such as Fe, within the clusters. P was mainly found to segregate to dislocations. The composition of the precipitates was estimated using the the maximum separation envelope method.

More recently, P. D. Edmondson *et al.*[46] performed APT measurements on low-Cu forgings and high-Cu arc welds of surveillance specimens from the pressure vessel of the R. E. Ginna reactor. Their measurements yielded similar results as in Ref. 44 with precipitates enriched in Cu, Mn, Ni, Si and possibly P being present in the high-Cu specimens

but no significant precipitation having occurred in the low-Cu samples. The authors argue that local variation of Cu might play a key role in the formation of precipitates thus indicating the importance of materials composition.

3.5 Irradiation Induced Embrittlement of RPV Steels

In earlier discussion it was established that energetic particles, such as neutrons, protons or heavy nuclei, interacting with matter could cause damage and changes in the microstructure of materials. When their kinetic energy is sufficiently high, they displace atoms from their normal site in the lattice resulting in the creation of vacancies, interstitials, and other point defects. There are three main types of microstructural damage believed to occur due to the presence of micro-defects. These are[47]

- Matrix defects and damage due to dislocation loops and defect clusters. In low copper alloys it is sometimes considered to be the main damage event and is dependent on neutron dose.
- Induced or enhanced grain boundary segregation of elements such as phosphorous.
- Irradiation induced or enhanced precipitation; formation of clusters enriched in Cu, Mn, Ni, and other elements that is found to increase the yield strength of the alloys.

Matrix damage and precipitation cause embrittlement through an increase in hardness of the steels[47]. On the contrary, grain boundary segregation causes embrittlement without changing the hardness of the alloys[47].

3.5.1 Matrix Defect Hardening & Damage

Matrix damage has been characterized into two main components; unstable matrix features (UMF) and stable matrix features (SMF)[47]. The former is thought to be due

to clusters of vacancies or interstitial point defects at the sub-nanometer scale (< 1nm) created during the displacement cascade event. UMFs have a relatively short life span, $\sim 3 \times 10^5$ s, at a temperature of around 290 °C which is a common temperature inside the core of a nuclear reactor[48]. As a result they undergo thermal recovery and they are not considered as important for irradiation-induced damage, but sometimes they freeze in the matrix during cooling after the process of irradiation.

SMFs are considered to be defect cluster-solute complexes that are produced within the samples and depend on both irradiation conditions and properties of the irradiated materials[12,47]. They are believed to be one of the contributors of irradiation induced hardening and embrittlement in RPV steel alloys, and they are particularly important in low-Cu steels where the formation of Cu-enriched clusters is limited. Matrix damage has been found to increase the yield stress and the ductile-to-brittle transition temperature (DBTT) of the RPV steels[47].

3.5.2 Grain Boundary Segregation

With the term grain boundary segregation we refer to the process in which alloying elements, during irradiation, diffuse to the region of the grain boundaries of the alloy in order to reduce their free energy; within the matrix of the RPV steel there are more point defects than usual that become mobile during irradiation and migrate to regions of the material with lower energy, such as the boundaries of the grains. As a result, the grain boundaries become enriched in embrittling elements such as phosphorous, silicon, or carbon[49]. Consequently, over time, there will be regions that will have different mechanical properties from the rest of the material resulting in localized defects and embrittlement, and enhancement of the intergranular stress corrosion cracking process, which can lead to brittle fracture[47], thus causing major changes in macro-mechanical properties[12]. The resulting defects and damage will eventually reduce the productivity and life of an RPV and the nuclear reactor.

In contrast to matrix damage that causes embrittlement through hardening, grain boundary segregation leads to nonhardening embrittlement[47] and for that reason it has received relatively less attention than other irradiation-induced damage mechanisms.

3.5.3 Precipitation in RPV Steel Alloys

Irradiation induced or enhanced precipitation is considered to be one of the main and most important mechanisms for damage and embrittlement of materials used in nuclear applications for the fabrications of RPVs. It is due to radiation enhanced diffusion (RED) caused by the point defects produced during the initial damage cascade event. The increase in diffusion is attributed to the high concentration of point defects in the material and the formation of new defects during irradiation. If the solubility of the elements contained in the solute clusters is lower than their concentration, their enrichment leads to the formation of new phases at localised points distributed in the matrix. As a result, RED leads to solute enrichment or depletion at defect sinks, e.g. grain boundaries or pre-existing precipitates and clusters.

The three main phases of precipitation that are typically found in RPV steels are carbides, Cu-rich clusters, and Mn-Ni-Si clusters[50]. Elements such as Mn, Ni, and Si can stabilise the Cu phases but in low-Cu steels precipitates can be found to be enriched with these solutes and so, despite the fact that adding alloying elements helps to improve the properties of the materials, they can also cause major defect problems[50,51].

We can describe the main types of precipitation events as[50,51]:

- Radiation induced precipitates; precipitation events that are created due to non-equilibrium solute segregation. They are usually dissolved during post-irradiation heat treatment.

- Radiation enhanced precipitates; precipitates present in samples prior to irradiation with irradiation accelerating their growth accompanied by an increase in their size.

- Radiation modified precipitates; precipitates that have variation in composition from the thermodynamically stable phase.

The presence of precipitates can significantly increase the hardness of materials and consequently have serious effects on their toughness; changes in hardness due to the presence of precipitation events is because of impingement of glide dislocations by precipitates. The interaction of precipitates and dislocations is dependent on the size, number density, and distribution of the precipitates as well as their nature and their interaction with the matrix.

3.5.3.1 Carbides

Carbides typically form during the steels' heat treatment as part of their initial manufacturing process. Due to RPV steels' complex microstructures (e.g. bainitic, tempered martensitic, ferritic) they can contain distributions of various carbides including $M_{23}C_6$ and M_7C[51,52] (M standing for metal) or more commonly Mo_2C and Fe_3C[51,52], the latter also referred to as cementite. Such precipitates can have sizes ranging between about 10 nm and up to a few microns and they are generally stable during irradiation[51,52]. Depending on their size and number density, they can act as a hardness increasing mechanism by stopping dislocation free movement.

3.5.3.2 Cu-rich precipitates

CRPs are considered one of the leading mechanisms of embrittlement in alloys containing more than 0.1 wt.% Cu[50]. Cu is not typically an alloying element of RPV steels but it is introduced in the steels mainly as an impurity; older RPVs, mostly fabricated before the 1970's but still in use today, were made by welding a lot of preformed steel plates together to make the vessel's walls and components and several of these welds are located within the belt-line region. At the time of fabrication, Cu-coated welding rods were used in the welding process and as a result the Cu content of the welds was high

(about 0.4 wt.%)[53]. Over the years, as the importance of Cu and its contribution as an embrittling element became apparent, limitations for the content of Cu within the welds and the core belt-line were imposed and Cu-coated weld rods were excluded from the fabrication process. In Fig. 3.19 the reduction of Cu content in Japanese reactor pressure vessels over the years is provided. The reason for Cu posing such a major problem is its low solubility in the Fe matrix of the RPV steels. The exact solubility limit of Cu in Fe at reactor working temperatures (about 290 °C) is still a matter of debate but it is agreed that it is generally low (0.0003 wt. %[54], 0.007 wt. %[55], 0.05 wt. %[56]). This results in supersaturation of Cu in the matrix. Precipitation of Cu occurs in order to reduce the high strain energy associated with the supersaturation and is accelerated by radiation enhanced diffusion[57]. It has been observed that CRPs rapidly form at low neutron

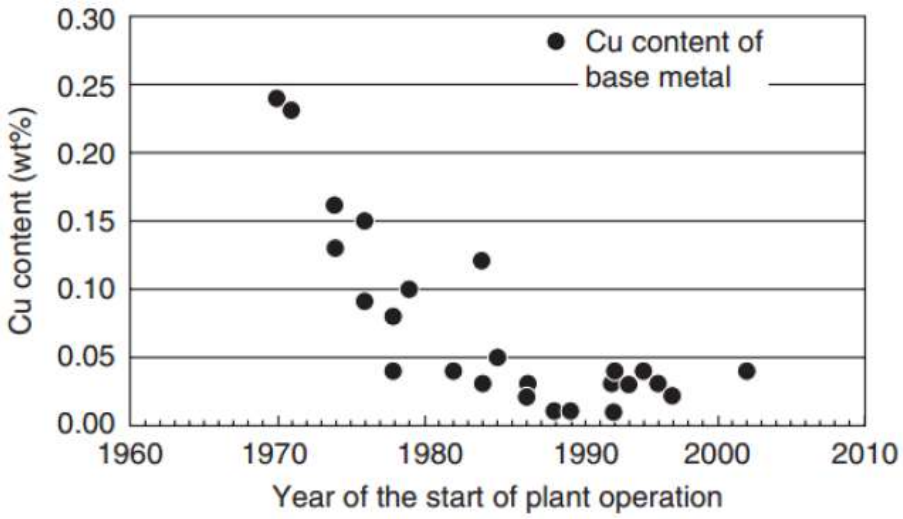

Figure 3.19: Copper content in Japanese RPVs in a period of around 35 years since the early 1970's until the mid-2000's[53].

fluences with their growth rate decreasing at higher fluences. Their size ranges between about 2 to 5 nm in diameter. Typically Cu acts as nucleation point and solutes such as Mn, Ni, and Si precipitate around it forming precipitates with a Cu-core Mn-Ni-(Si)-shell structure.

F. Bergner *et al.*[39] in 2010 performed experiments on a series of test alloys, including

Fe-0.1%Cu, Fe-0.3%Cu, and Fe-1.2%Mn-0.7%Ni-0.1%Cu, that were neutron irradiated at damage levels between 0.026 and 0.19 dpa with corresponding neutron fluence between 1.7 x 10^{23} n/cm^2 and 1.3 x 10^{24} n/cm^2. The irradiations were performed at a constant temperature of 300 °C. All specimens were investigated by means of SANS. The resulting scattering curves, provided in Fig. 3.20, clearly show the presence of irradiation induced precipitation in all three alloys. This is made clear by the increase in the scattering in-

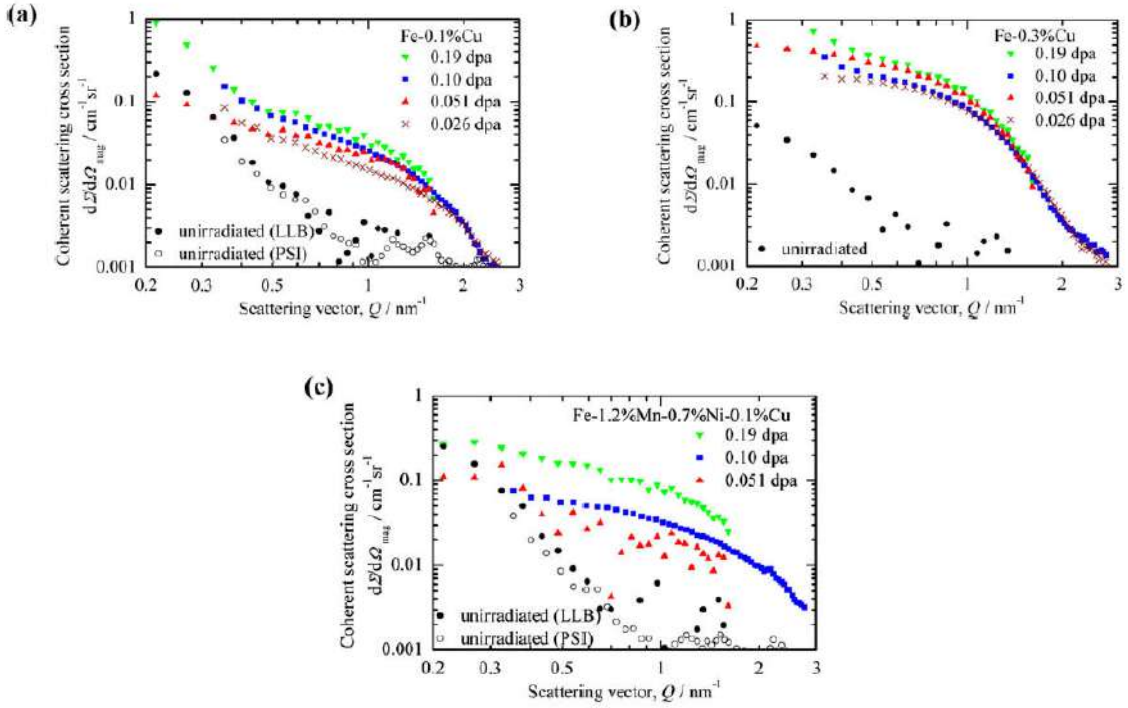

Figure 3.20: (a) (b) SANS measurements of two Fe-Cu binary alloys, which have been exposed to different levels of irradiation damage. (c) SANS measurements of a complex alloy, which has been exposed to the same damage levels as the binay alloys. All results have been obtained by Ref. 39.

tensity compared to that of the unirradiated control specimens. Further analysis revealed that the precipitates had a radius ranging between about 1 and 2.3 nm. Investigations on the possible composition of the scattering features indicated that the precipitates present in the Fe-Cu binary alloys were Cu-vacancies clusters with a core-shell structure. The precipitates found in the quaternary Fe-MnNiCu alloy was found to be enriched in Cu, Mn, and Ni with Cu possibly acting as a nucleation point.

Cu precipitation has been found to have a direct connection with hardness of RPV

steels and the variation in Cu content within the steels plays a key role in its increase. T. Takeuchi *et al.*[58] performed experiments by means of three-dimensional local electrode APT, PAS and Vickers microhardness to probe changes in hardness of two specimens of A533B-1 steel. The two samples were of low and high Cu content, 0.04 and 0.16 wt. % respectively, and were irradiated within a Japanese Material Testing Reactor with increasing neutron dose (values between 0.32 and 9.9 x 10^{19} n/cm^2) under a relatively constant neutron flux (1.7 x 10^{13} n cm^{-2} s^{-1}) and at constant temperature (290 °C). The Vickers micro-hardness testing was performed on both samples as a function of dose. The results are shown in Fig. 3.21. It is apparent that following the same dose rates the two samples have a profound difference in hardness values. The sample with higher Cu content (sample A) has constantly higher hardness than the sample with the low copper content (sample B). Their results also showed that the size of the produced clusters was roughly the same for both samples with corresponding dose rates but the volume fraction and the number density of the precipitates were higher for the high-Cu steel (see Fig. 3.22). It is apparent that due to the increase in number density of precipitates, especially for the high-Cu specimens, the separation distance between them is smaller, thus hindering the gliding of dislocations and consequently increasing hardness.

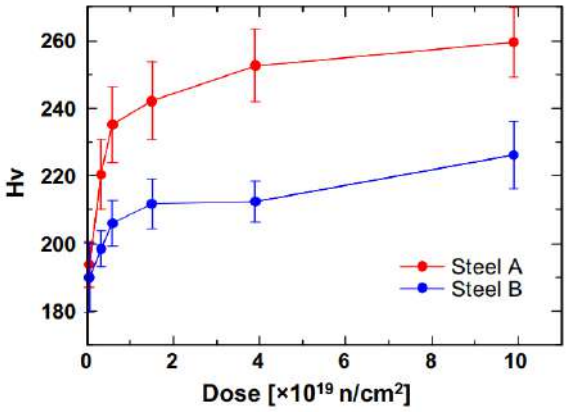

Figure 3.21: Hardness as a function of neutron irradiation dose for two steel samples, steel A and B, containing 0.16 wt. % Cu and 0.04 wt. % Cu respectively. Hardness values were obtained with Vickers microhardness test method. The plots clearly indicate higher hardness values with higher Cu content[58].

A study reported in a technical report for the International Atomic Energy Agency also

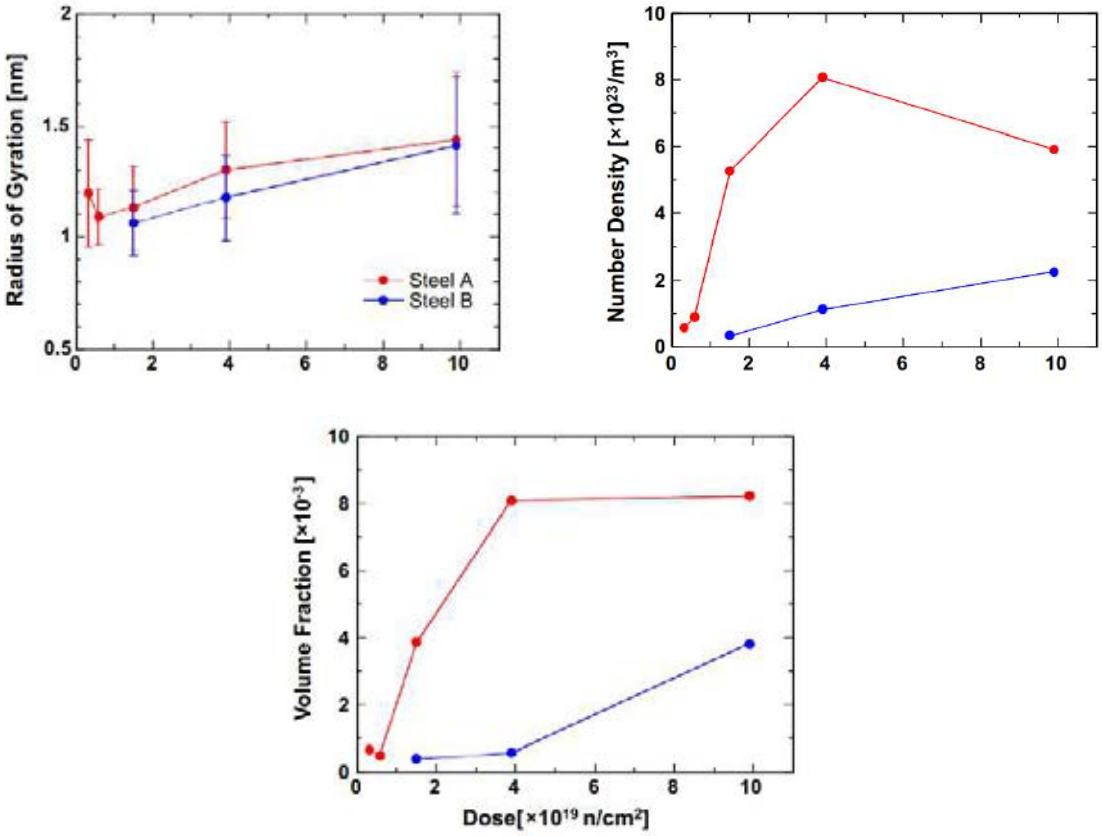

Figure 3.22: In addition to the hardness values presented in Fig. 3.20, several other parameters of steel A (0.16 Cu wt. %) and B (0.04 Cu wt. %) were measured and reported in Ref. 58. The top left plot shows measurements of the radius of gyration, the top right plot shows measurements of the number density and the bottom plot shows the volume fraction. All measurements have been performed as a function of the irradiation dose. Apart from the radius of gyration that is generally the same for the two different Cu levels the other two parameters show significant increase with increasing Cu content.

supports the idea of increased irradiation sensitivity of steels with increasing Cu content. The study was performed on two RPV weld specimens with different Cu content, 0.3 wt.% and 0.06 wt.% respectively, irradiated at a temperature of 288 °C with a neutron fluence of 1 x 10^{23} n/cm^2. The study was performed by looking at the Charpy impact toughness of the two samples. The results are shown in Fig. 3.23. It is apparent that the ductile-to-brittle behaviour is generally as expected but there is a profound effect with increasing Cu content. The unirradiated condition is used as a reference. The sample containing lower levels of Cu appears to have a slightly decreased upper shelf energy and increased transition temperature but overall the changes compared to the unirradiated specimen are small. For the high-Cu sample though the changes are more profound; the shift in transition temperature and the decrease of toughness are massive compared to both the unirradiated and the low-Cu samples. Even though irradiation changes the ductile-to-brittle transition temperature and the ductile toughness at both Cu levels the effect is clearly amplified for higher Cu content.

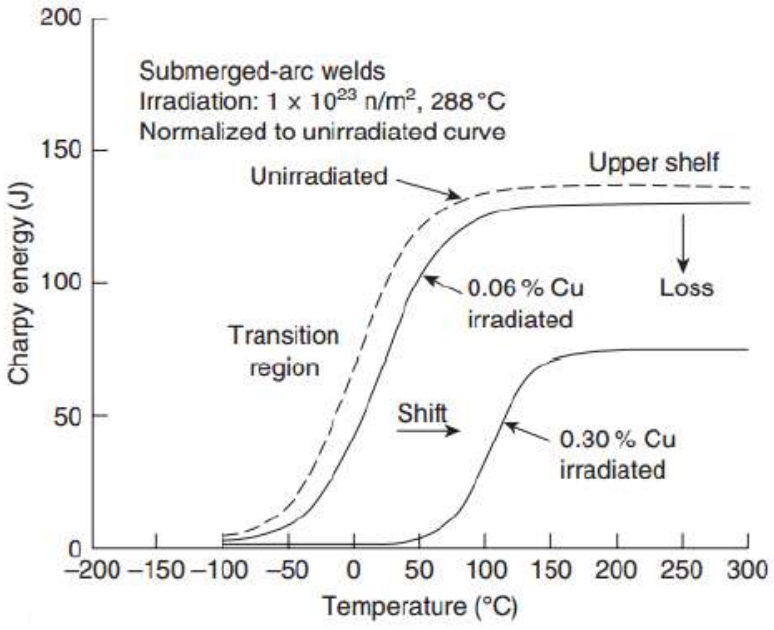

Figure 3.23: Charpy energy versus temperature showing the significant role of copper content.[8]

3.5.3.3 Mn-Ni-Si precipitates

Alloying elements such as Mn and Ni are added in RPV steels in order to improve the properties of the materials; Mn is mainly added for brittleness attenuation (reducing brittlness caused by S impuring through MnS formation[4]) and Ni for steel strengthening[4]. It is established that Mn, Ni, and Si precipitation is tightly connected with Cu precipitation in high-Cu RPV steels with Cu acting as nucleation point that drives solute precipitation with an impact on the embrittlement of the steels[57]. Due to the well-known effects of Cu and CRPs, modern RPVs are manufactured with alloys containing less than 0.1 wt. % of Cu. It has been observed though that irradiation can induce the precipitation of Mn-Ni-Si clusters even in the absence of Cu[43,46,59,60]. Despite Mn, Ni, and Si having a high solubility limit in the Fe matrix it is believed that these elements have a synergistic effect lowering their overall solubility thus precipitating out of the matrix forming thermodynamically stable phases with sizes in the order of a few nanometres.

MNPs were first predicted by G. R. Odette in 1995[61] who originally named them late-blooming-phases due to the belief that they start forming at high accumulated fluences ($> 10^{24}$ n/m^2[62]) though it has been reported that they can form even at lower fluences, in the order of 10^{23} or 10^{22} n/m^2[60,63]. In 2009, F. Bergner *et al.*[63] reported a study performed on two low-Cu (0.01 wt. % Cu) Japanese IAEA type A533B-cl.1 RPV specimens, denoted as JPB and JPC. The difference between the two was the level of P in the samples, 0.017 wt. % and 0.007 wt. % respectively. The steels were neutron irradiated at a temperature of 255 °C with fluences ranging between about 7 x 10^{22} n/m^2 and 90 x 10^{22} n/m^2 and were measured by means of SANS. The resulting differential scattering cross sections (Fig. 3.24) clearly indicate the formation of precipitates in both specimens seen as a distinct increase of the scattering intensity at higher $\vec{q}$ values. The precipitates had an average size of 1 nm. Further analysis indicated that in both cases and at any damage level the clusters contained Mn, Ni, and vacancies with possible dominance of Mn at lower fluences and Ni at higher. It is also clear that the difference in P levels has

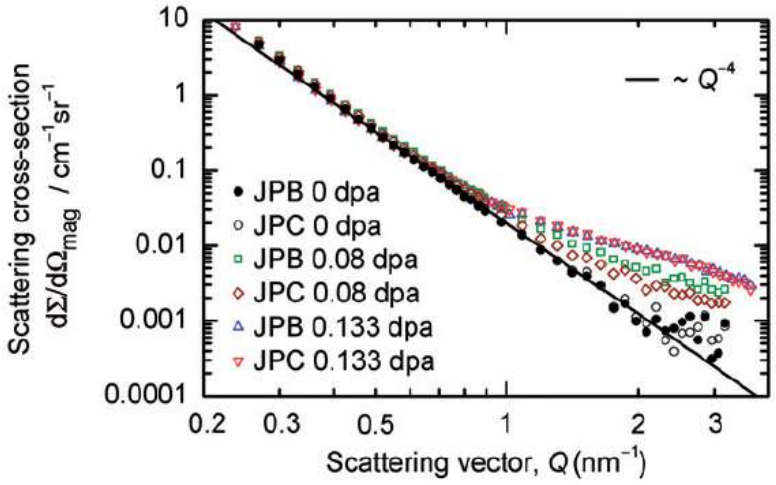

Figure 3.24: Magnetic scattering cross section of Japanese JPB (0.017 wt. % P) and JPC (0.007 wt. % P) RPV steels as given in Ref. 63. The steels have been exposed to different levels of irradiation before the neutron measurements with the effects of increasing damage levels being clear in the scattering signal.

no impact in the formation of the precipitates.

3.6 Concluding Remarks

In this chapter the concept of radiation damage in matter was covered with main focus given on neutron (and proton) irradiation effects on RPV steels and embrittling mechanisms (e.g. irradiation induced precipitation). Prior to this, an introduction on the basics of the metallurgy of steels was given with a subsequent short discussion on the main steel alloys used for the fabrication of an RPV. In the following experimental part of the thesis some of the discussed irradiation effects (of protons) on RPV test alloys are investigated. The content of Cu in the steels along with the synergistic effects of proton (instead of neutron) irradiation are examined and irradiation induced precipitates are probed by means of small-angle neutron scattering (presented in Chapter 1).

References

[1] Nuclear Engineering International. *Experts approve Areva's tests for Flamanville 3 RPV*. http://www.neimagazine.com/news/newsexperts-approve-arevas-tests-for-flamanville-3-rpv-4685045. Accessed: 18-02-2017.

[2] B. Capudean. Metallurgy matters: Phases, structures, and the influences of temperature. *Practical Welding Today*, 2003.

[3] Computational Thermodynamics Inc. *Computational Thermodynamics-Calculation of Phase Diagrams using the CALPHAD Method-Phase Diagrams*. http://www.calphad.com/iron-carbon.html. Accessed: 27-02-2017.

[4] B. L. Bramfitt and A. O. Benscoter. *Metallographer's guide: practice and procedures for irons and steels*. ASM International, 2001.

[5] F. C. Campbell. *Fatigue and fracture: understanding the basics*. ASM International, 2012.

[6] A. V. Nero. *A guidebook to nuclear reactors*. University of California Press, 1979.

[7] K. D. Kok. *Nuclear engineering handbook*. CRC Press, 2016.

[8] Nuclear Energy Series No. NP-T-3.11. Integrity of reactor pressure vessels in nuclear power plants: Assessment of irradiation embrittlement effects in reactor pressure vessel steels. Technical report, International Atomic Energy Agency, 2009.

[9] American Society for Testing and Materials. *Steel – Structural, Reinforcing, Pressure Vessel, Railway*. Annual Book of ASTM Standards, Section 1 – Iron and Steel Products. ASTM International, 1989.

[10] T. J. Griesbach. *Reactor Pressure Vessel Design and Fabrication*. Electric Power Research Inst., 1994.

[11] K. L. Murty and I. Charit. *An introduction to nuclear materials: fundamentals and applications*. John Wiley & Sons, 2013.

[12] G. Was. *Fundamentals of Radiation Materials Science*. Springer, 1994.

[13] C. L. Snead Jr. and T. Luhman. *Radiation Damage and Stress Effects in Superconductors: Materials for High-Field Applications*, pages 374–388. Physics of Radiation Effects in Crystals. North Holland, 1986.

[14] D. Kopeliovich. *Imperfections of crystal structure*. http://www.substech.com/dokuwiki/doku.php?id=imperfections_of_crystal_structure. Accessed: 19-02-2017.

[15] W. G. Wolfer. Fundamental properties of defects in metals. *Comprehensive Nuclear Materials*, 1:1–45, 2015.

[16] J. Koutsky and J. Kocik. *Radiation Damage of Structural Materials*. Elsevier Science Ltd., 1994.

[17] D. J. Mazey. Fundamental aspects of high-energy ion-beam simulation techniques and their relevance to fusion materials studies. *Journal of Nuclear Materials*, 174:196–209, 1990.

[18] A. K. Seeger. Some recollections of the radiation damage work of the 1950s. *Proceeding of The Royal Society A*, 371:165–172, 1980.

[19] S. Ishino and N. Sekimura. Role of charged particle irradiations in the study of radiation damage correlation. *Journal of Nuclear Materials*, 174:158–167, 1990.

[20] G.S. Was et.al. Emulation of neutron irradiation effects with protons: validation of principle. *Journal of Nuclear Materials*, 300:198–216, 2002.

[21] D. Schardt. *Tumor Therapy with High-energy Heavy-ion Beams*, pages 433–440. Fundamental & Applied Aspects of Modern Physics. World Scientific, 2001.

[22] H. Rosebaum. *Microstructures of Irradiated Material.* Academic Press, 1975.

[23] P. Cohen. *Water coolant technology of power reactors.* Gordon and Breach, 1969.

[24] K. J. Stephenson and G. S. Was. Comparison of the microstructure, deformation and crack initiation behavior of austenitic stainless steel irradiated in-reactor or with protons. *Journal of Nuclear Materials*, 456:85–98, 2015.

[25] E. O. Lawrence. Method and apparatus for the acceleration of ions, 02 1934.

[26] C. Sutton F. Close and M. Marten. *The Particle Odyssey: A Journey to the Heart of Matter.* Oxford University Press, 2004.

[27] Department of Energy. Office of Public Affairs. *60-inch cyclotron at the University of California Lawrence Radiation Laboratory, Berkeley.* https://catalog.archives.gov/id/558594. Accessed: 25-02-2017.

[28] Young and Freedman. *University Physics with Modern Physics.* Pearson Education, Inc., 2012.

[29] Revision World Networks Ltd. *Circular orbits.* https://revisionworld.com/a2-level-level-revision/physics/fields-0/circular-orbits. Accessed: 25-02-2017.

[30] D. C. Weisser. *Electrostatic Accelerators*, pages 93–122. Encyclopedia of Nuclear Physics ans its Applications. Wiley-VCH, 2013.

[31] M. R. Cleland. Voltage multiplication apparatus, February 24 1959. US Patent 2,875,394.

[32] M. R. Cleland and P. Farrell. Dynamitrons of the future. *NBS Accelerator Conference*, pages 227–234, 1965.

[33] M. R. Cleland. *Electron Beam Materials Irradiators*, pages 87–137. Industrial Accelerators and Their Applications. World Scientific, 2012.

[34] J. Hyde and C. English. *Microstructural characterisation techniques for the study of reactor pressure vessel (RPV) embrittlement*, pages 211–294. Irradiation Embrittlement of Reactor Pressure Vessels (RPVs) in Nuclear Power Plants, Woodhead Publishing Series in Energy: Number 26. Elsevier Ltd., 2015.

[35] R. G. Carter, N. Soneda, K. Dohi, J. M. Hyde, C. A. English and W. L. Server. Microstructural characterization of irradiation-induced Cu-enriched clusters in reactor pressure vessel steels. *Journal of Nuclear Materials*, 298:211–224, 2001.

[36] J. T. Buswell, W. J. Phythian, R. J. McElroy, S. Dumbill, P. H. N. Ray, J. Mace and R. N. Sinclair. Irradiation-induced microstructural changes and hardening mechanisms in model pwr reactor pressure vessel steels. *Journal of Nuclear Materials*, 225:196–214, 1995.

[37] B. D. Wirth, P. Asoka-Kumar, R. H. Howell, G. R. Odette and P. A. Sterne. Positron annihilation spectroscopy and small angle neutron scattering characterization of nanostructural features in irradiated Fe–Cu–Mn alloys. *MRS Proceedings*, 650:R6.5, 2001.

[38] P. Asoka-Kumar, R. H. Howell, B. D. Wirth, G. R. Odette and P. A. Sterne. Characterization of nanostructural features in irradiated reactor pressure vessel model alloys. *10th International Conference on Environmental Degradation of Materials in Nuclear Power Systems–Water Reactors, G.S. Was , ed., NACE International, Houston, TX*, 2002.

[39] F. Bergner, M. Lambrecht, A. Ulbricht and A. Almazouzi. Comparative small-angle neutron scattering study of neutron-irradiated Fe, Fe-based alloys and a pressure vessel steel. *Journal of Nuclear Materials*, 399:129–136, 2010.

[40] A. Ulbricht, F. Bergner, C. D. Dewhurst and A. Heinemann. Small-angle neutron scattering study of post-irradiation annealed neutron irradiated pressure vessel steels. *Journal of Nuclear Materials*, 353:27–34, 2006.

[41] F. Bergner, A. Ulbricht A. Gokhman and D. Erak. Nature of defect clusters in neutron-irradiated iron-based alloys deduced from small-angle neutron scattering. *Journal of Nuclear Materials*, 373:199–205, 2008.

[42] P. Pareige, R. E. Stoller, K. F. Russell and M. K. Miller. Atom probe characterization of the microstructure of nuclear pressure vessel surveillance materials after neutron irradiation and after annealing treatments. *Journal of Nuclear Materials*, 249(2-3):165–174, 1997.

[43] M. K. Miller, M. A. Sokolov, R. K. Nanstad, and K. F. Russell. APT characterization of high nickel RPV steels. *Journal of Nuclear Materials*, 351(1):187–196, 2006.

[44] M. K. Miller, K. F. Russell, M. A. Sokolov, and R. K. Nanstad. APT characterization of irradiated high nickel RPV steels. *Journal of Nuclear Materials*, 361(2):248–261, 2007.

[45] M. K. Miller, K. A. Powers, R. K. Nanstad, and P. Efsing. Atom probe tomography characterizations of high nickel, low copper surveillance RPV welds irradiated to high fluences. *Journal of Nuclear Materials*, 437(1):107–115, 2013.

[46] P. D. Edmondson, M. K. Miller, K. A. Powers, and R. K. Nanstad. Atom probe tomography characterization of neutron irradiated surveillance samples from the RE Ginna reactor pressure vessel. *Journal of Nuclear Materials*, 470:147–154, 2016.

[47] C. English and J. Hyde. *Radiation Damage of Reactor Pressure Vessel Steels*, pages 151–180. Comprehensive Nuclear Materials Vol. 4. World Scientific, 2012.

[48] G. R. Odette and G. E. Lucas. Embrittlement of nuclear reactor pressure vessels. *JOM*, 53:18–22, 2001.

[49] H.-H. Jina *et. al.* The formation of radiation-induced segregation at twin bands in ion-irradiated austenitic stainless steel. *Journal of Nuclear Materials*, 454, 1—3:28—-36, 2014.

[50] E. Meslin, B. Radiguet and M. Loyer-Prost. Radiation-induced precipitation in a ferritic model alloy: An experimental and theoretical study. *Acta Materialia*, 61:6246–6254, 2013.

[51] J. E. Zelenty. Understanding thermally induced embrittlement in low copper RPV steels utilising atom probe tomography. *Materials Science and Technology*, 38:981–988, 2015.

[52] M. K. Miller and K. F. Russell. Embrittlement of RPV steels: An atom probe tomography perspective. *Journal of Nuclear Materials*, 371:145–160, 2007.

[53] M. Tomimatsu and T. Hirota. *Embrittlement of reactor pressure vessels (RPVs) in pressurized water reactors (PWRs)*, pages 57–106. Irradiation Embrittlement of Reactor Pressure Vessels (RPVs) in Nuclear Power Plants, Woodhead Publishing Series in Energy: Number 26. Elsevier Ltd., 2015.

[54] G. Salje and M. Feller-Kniepmeier. The diffusion and solubility of copper in iron. *Journal of Applied Physics*, 48(5):1833–1839, 1977.

[55] S. Miloudi. *Etude du dommage d'irradiation dans les aciers de cuve des reacteurs a eau pressurisee.* PhD thesis, Paris 11, 1997.

[56] M. Perez, F. Perrard, Véronique Massardier, X. Kleber, A. Deschamps, H. De Monestrol, P. Pareige, and G. Covarel. Low-temperature solubility of copper in iron: experimental study using thermoelectric power, small angle X-ray scattering and tomographic atom probe. *Philosophical Magazine*, 85(20):2197–2210, 2005.

[57] E. D. Eason, G. R. Odette, R. K. Nanstad and T. Yamamoto. A physically based correlation of irradiation-induced transition temperature shifts for RPV steels. Technical report, Oak Ridge National Laboratory, 2006.

[58] T. Takeuchi, A. Kuramoto, J. Kameda, T. Toyama, Y. Nagai, M. Hasegawa, T. Ohkubo, T. Yoshiie, Y. Nishiyama and K. Onizawa. Effects of chemical composition and dose on microstructure evolution and hardening of neutron-irradiated reactor pressure vessel steels. *Journal of Nuclear Materials*, 402:93–101, 2010.

[59] E. Meslin, M. Lambrecht, M. Hernández-Mayoral, F. Bergner, L. Malerba, P. Pareige, B. Radiguet, A. Barbu, D. Gómez-Briceño, A. Ulbricht, et al. Characterization of neutron-irradiated ferritic model alloys and a RPV steel from combined APT, SANS, TEM and PAS analyses. *Journal of Nuclear Materials*, 406(1):73–83, 2010.

[60] N. Soneda, K. Dohi, K. Nishida, A. Nomoto, M. Tomimatsu, and H. Matsuzawa. Microstructural characterization of RPV materials irradiated to high fluences at high flux. *Journal of ASTM International*, 6(7):1–16, 2009.

[61] G. R. Odette. Radiation induced microstructural evolution in reactor pressure vessel steels. *MRS Online Proceedings Library Archive*, 373, 1994.

[62] P. B. Wells, T. Yamamoto, B. Miller, T. Milot, J. Cole, Y. Wu, and G. R. Odette. Evolution of manganese–nickel–silicon-dominated phases in highly irradiated reactor pressure vessel steels. *Acta Materialia*, 80:205–219, 2014.

[63] F. Bergner, A. Ulbricht, and H. -W. Viehrig. Acceleration of irradiation hardening of low-copper reactor pressure vessel steel observed by means of SANS and tensile testing. *Philosophical Magazine Letters*, 89(12):795–805, 2009.

CHAPTER 4

PROBING IRRADIATION INDUCED PRECIPITATION IN HIGH-COPPER REACTOR PRESSURE VESSEL STEEL ALLOYS

4.1 Introduction

In Chapter 3 it was discussed that damage in materials used for the fabrication of an RPV is quite common (for in-service reactors) and is mainly caused by neutrons of high energy interacting with the atoms in the material displacing them, thus resulting in the formation of defects and nano-particles within the lattice of the materials, making them less tough and less capable of withstanding the flaws that may be present. It was argued that one of the main factors contributing to embrittlement and hardening of RPV steels is irradiation-enhanced or irradiation-induced precipitation. The materials used for the manufacturing of RPVs are high-strength low-alloy ferritic steels and despite the fact that the weight percent of the alloying elements is low, the small amount of some of them could drastically change important macroscopic properties of the steels. It is well acknowledged that Cu is one of the major factors contributing to the embrittlement of RPV steels[1]. Cu-rich nano-scale precipitates (CRPs) are found in RPV steel alloys, containing Cu exceeding 0.1 wt.%[2,3], causing hardening and increasing the ductile-to-brittle transition temperature after irradiation. The reason for the high level of Cu in precipitates is mainly its low solubility in Fe (0.003 at. % $\sim$ 290 °C) in combination with irradiation enhanced

diffusion and nucleation. Due to the formation of CRPs and their effects, new generation RPVs are manufactured with alloys containing less than 0.1 wt.% of Cu[4]. Elements such as Mn, Ni, and Si though have also been found among precipitation events with Mn-Ni-Si precipitates forming even in the absence of Cu. These solute elements, among others, are added in order to improve the properties of the steels. For example, Mn is used for brittleness attenuation and Ni for steel strengthening[5]. Despite the fact that these solutes are important for improving the RPVs, solute clustering increases the embrittlement of the alloys and can be found in both high- and low-Cu RPV steels. The total solute available for precipitation from the matrix as well as the solubility levels of elements such as Mn, Ni, and Si should be taken into account.

In this chapter, SANS measurements on high-Cu RPV steels are reported and the effects of Cu content, in combination with the high levels of Mn and Ni, as well as temperature during irradiation or heat treatment of samples on the SANS results are discussed. The results provide information on the size distribution, number density and volume fraction of precipitates, as well as qualitative information of precipitation dependence on temperature. Information on the clusters' possible composition is also given by discussing the A ratio obtained from the SANS data analysis by considering both magnetic and non-magnetic scattering features.

4.2 Experimental Details

4.2.1 Materials & Sample Preparation

The samples investigated and reported in this chapter were high-Cu variants of RPV, 0.3 wt. % Cu model steel alloys, also containing high levels of Ni (3.5 wt. %) and Mn (1.5 wt. %). They were manufactured by vacuum induction melting. The steel plates were originally rolled and then heat treated at 920 °C for 1 h undergoing austenisation followed by an air cool. Next, they were tempered at 600 °C for 5 h followed by a final

air cool. The overall chemical composition of the alloy is given in Table 4.1.

Table 4.1: Composition of high-Cu model steel alloy (wt. %)

C	Mn	P	Si	Ni	Cr	Mo	Cu	Fe
0.21	1.48	0.008	0.20	3.47	0.1	0.52	0.31	93.702

A total number of six samples was studied. Four specimens were proton irradiated at 50 °C, 300 °C, and 400 °C respectively. Two non-irradiated samples were heat treated at 300 °C and 400 °C respectively for 2.5 h. An as-received control sample was measured as a reference. All samples were studied by means of SANS. Complementary SEM and Vickers microhardness were also performed.

Proton instead of neutron irradiation was used as experimental time is quicker and temperature control is more precise compared to neutron irradiation[6]. A typical neutron irradiation experiment, in a test reactor, would need years of exposure to reach appreciable fluence levels, comparable to that of a typical nuclear reactor during its entire operating time[7] with a typical damage rate of approximately 4×10^{-11} dpa/s for PWRs. While proton irradiation is more advantageous over neutron irradiation having high damage rates, good control of the irradiation conditions, low material activation, and low cost, it also has a few drawbacks such as differences in the primary knock-on atom (PKA) spectrum, accelerated damage rates, and small penetration depth leading to surface effects and consequently small analysis volume[8].

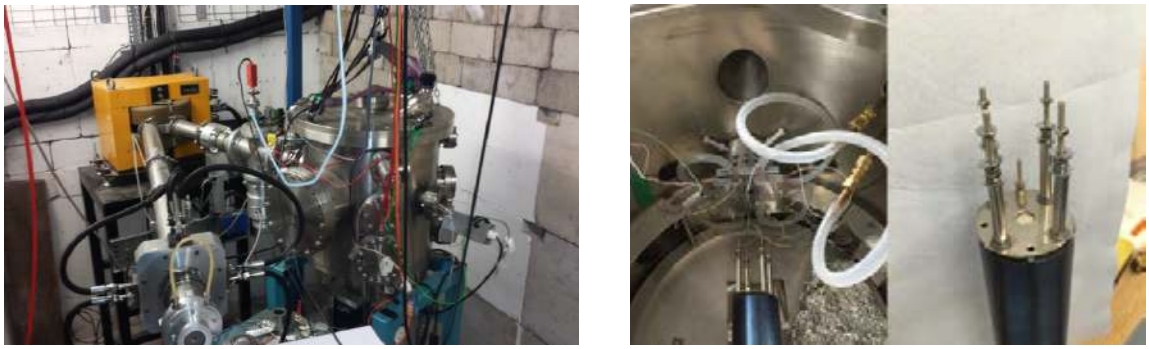

Figure 4.1: (a) Beam lines and vacuum chamber of the Scanditronix MC40 cyclotron used for the irradiation of specimens. (b) Picture of the vacuum chamber internals.

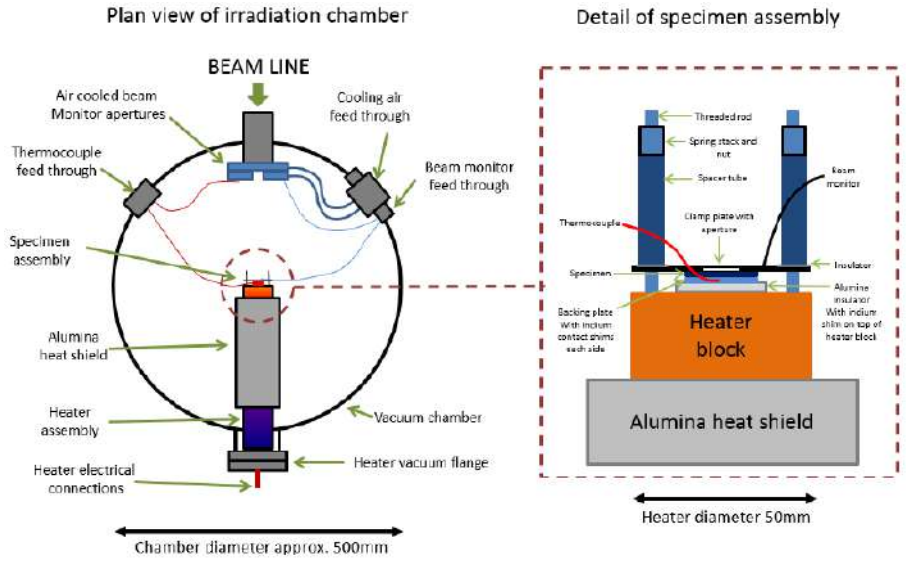

Figure 4.2: Schematic representation of the Scanditronix MC40 cyclotron's vacuum chamber and sample area (unpublished work of Dr Christopher Cooper, University of Birmingham).

The 5.4 MeV proton irradiations produced approximately 6 mdpa of damage by average and were performed using the Scanditronix MC40 cyclotron facility at the University of Birmingham, UK by Dr. Brian Connolly and Dr. Christopher Cooper. Detailed calculations of damage are provided in the next section. The induced damage was considered to be constant because the specimens were irradiated under the same conditions inside the cyclotron's vacuum chamber. Fig. 4.1 and 4.2 provide pictures and schematics of the cyclotron beam lines, vacuum chamber internals, and specimen area. In total, the proton irradiation facility provided an excellent control of temperature ($\pm$ 5 °C), which is crucial for controlled precipitation experiments as a function of total damage.

For the SANS measurements the specimens were polished down to about 200 μm and had a surface area of 10 $\times$ 10 mm^2. The thickness of the samples gave the ability to irradiate the specimens from both sides thus increasing total damage. The irradiation details and exact thickness of each sample can be seen in Table 4.2. For clarification the samples were labelled as samples HA to HF (where H stands for high-Cu) corresponding to the as-received sample, heat treated samples at 300 °C 2.5 h and 400 °C 2.5 h, and

irradiated samples at 50 °C, 300 °C, and 400 °C respectively.

Table 4.2: Summary of samples' thickness, irradiation conditions and heat treatment (where applicable). In the table AR stands for as-received, HT stands for heat treatment, and IR stands for irradiation.

Sample Code	Thickness (μm)	Damage Level (mdpa)	Temperature (°C)	Device	Energy (MeV)
HA	200	No Irradiation/AR	n/a	n/a	n/a
HB	175	No Irradiation/HT 2.5 h	300	n/a	n/a
HC	270	No Irradiation/HT 2.5 h	400	n/a	n/a
HD	180	6/IR 2.5 h	50	Cyclotron	5.4
HE	198	6/IR 2.5 h	300	Cyclotron	5.4
HF	198	6/IR 2.5 h	400	Cyclotron	5.4

4.2.1.1 Calculation of Damage Level - SRIM/TRIM

For the calculation of the total average damage, induced in the irradiated samples, the software SRIM[9] (**S**topping and **R**ange of **I**ons in **M**atter) was used. SRIM contains a group of programs that can be used to calculate the stopping of ions and their range into materials. It is a Monte Carlo code simulating the vacancies produced by ion collisions with matter. The produced vacancies are correlated with the displacement of the corresponding atoms from their original site in the matrix and a total dpa value can be calculated. The software runs based on the following assumptions

- During simulation the temperature of the system is 0 K thus not taking into account thermal effects. This can be somehow limiting for calculating actual damage in samples irradiated at high temperatures since annealing of specimens can have important effects.

- The target material is considered to be perfect and incoming ions will not be affected by previously implemented ions; there are no built-up effects in the material and each ion is considered independently.

- Collisions that cause negligible changes in the ion's trajectory (i.e. energy transfer is not sufficient) are not taken into account. A non-sufficient energy amount is

considered to be that which introduces less than a 0.1% changes in the final result. Under this assumption computing time is saved during the simulation.

For modelling of the damage, within the software, there are two main options; the "Ion Distribution and Quick Calculation of Damage", usually referred to as the K-P option because it utilises the simple Kinchin-Pease model, and the "Detailed Calculation with full Damage cascades", also referred to as F-C option, taking into account every single recoil until its energy drops below the displacement energy of the atoms in the sample. These two options are the ones most commonly chosen by SRIM users for damage calculation but there is a discrepancy between the two in the amount of the produced vacancies. To find the total vacancy number one uses the VACANCY.txt file produced after the termination of each simulation. In the file the vacancies by ions and by recoils are provided. These are summed and integrated through the entire thickness of the sample giving the total vacancies per ion fired. The number of vacancies produced using the F-C option though is almost double and there is a debate on which option is more accurate. Relatively recently, R.E. Stoller *et al.*[10] conducted a series of calculations comparing the results between the two different options. To do so they used two approaches. One was to use the VACANCY.txt file for calculating the displacements and the other one was to find the so-called damage energy and then calculate the number of vacancies based on the Norgett-Robinson-Torrens (NRT) model[11]. The latter is considered to be an accurate approach based on the fact that for a given damage energy the same amount of displacements should be produced. The damage energy is the portion of the initial primary knock-on atom energy lost due to collisions with the lattice atoms. The authors reported that the results received using the K-P option with both approaches were very close in contrast to using the F-C option. They added that the number of vacancies received using the F-C VACANCY.txt file was not in agreement with both MD calculations and irradiation experiments performed with neutrons at cryogenic conditions[12,13]. Hence, they conclude that the K-P option should be used and this is what was used for damage calculation in this study.

Originally, test simulations were performed by using both a simple Fe matrix and the full composition of the RPV alloy for comparison, using the same input parameters (incident particles and their energy, sample thickness, displacement energies etc.). The results showed that the differences in the resulting dpa values were minor thus Fe can be used as a good approximation to the entire sample. For the final simulations 100,000 incident protons (H ions) were simulated with an ion energy of 5.4 MeV, matching the cyclotron's beam energy during irradiations. The maximum penetration depth of hydrogen ions into Fe at this energy was calculated to be 91.35 μm, by using the "Ion Stopping and Range tables" option of SRIM. Following R.E. Stoller *et al.*[10] the displacement energy for Fe was set to be 40 eV instead of 25 eV that is the default value in SRIM.

To calculate the total damage in mdpa, after the completion of the simulations, the following process was used:

- A VACANCY.txt file was created after the termination of each simulation containing the number of vacancies by ions and by recoils. The vacancies were summed and integrated through the sample's entire thickness, taking into account that it is divided in 100 bins, giving the average number of displacements per ion (proton), x, within the material.

- Damage in mdpa was then calculated using

$$\text{dpa} = x\frac{\phi}{N_p} \tag{4.1}$$

  In the above equation ϕ gives the total number of protons per unit area, i.e the fluence (protons/cm^2). To calculate the fluence first one needs to calculate the total number of ions fired in the sample by dividing the overall charge from the cyclotron, 26432 μC per side, with the charge of one proton, 1.6 x 10^{-19} C. Then the total number of protons, 1.65 x 10^{17} per side, is divided with the irradiated surface area, 0.785 cm^2, to give the total fluence, 2.10 x 10^{17} protons/cm^2 per side. Since

the protons do not necessarily go through the entire specimen the overall atomic fraction needs to be scaled accordingly. This is expressed by N_p calculated by

$$N_p = N \times \text{depth to which ions penetrate (cm)} \tag{4.2}$$

where N is the atomic density of Fe, 8.481 x 10^{22} atoms/cm^3.

The resulting damage profile and the trajectories of the incoming protons can be seen in Fig. 4.3 and Fig. 4.4 respectively.

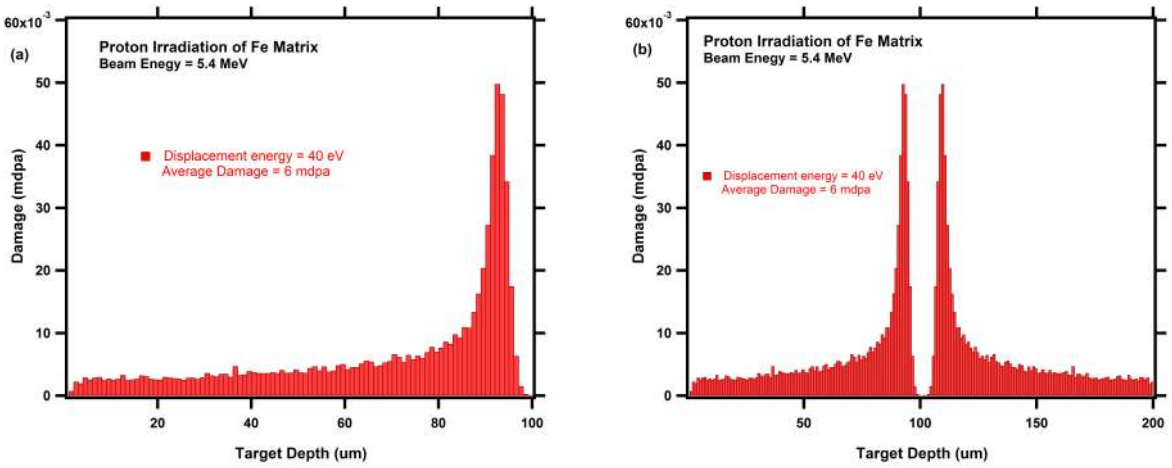

Figure 4.3: Damage profile of Fe matrix irradiated with a 5.4 MeV proton beam (a) from one side and (b) from both sides. The sample has a thickness of 200 μm and the total average damage calculated is about 6 mdpa. The displacement energy for Fe was kept at 40 eV.

As seen in Fig. 4.3, irradiations by ions do not produce a flat damage profile as neutrons would. Instead there is a Bragg peak appearing right before the ions stop travelling through the sample indicating a release of large amount of energy and a non-constant damage across the penetration depth within the sample. Because of that and due to the 200 μm thick samples been irradiated from both sides the damage was averaged over the entire thickness of the specimens giving an overall damage of about 6 mdpa (see Table 4.2). The damage profile of the sample irradiated from both sides is provided in Fig. 4.3(b).

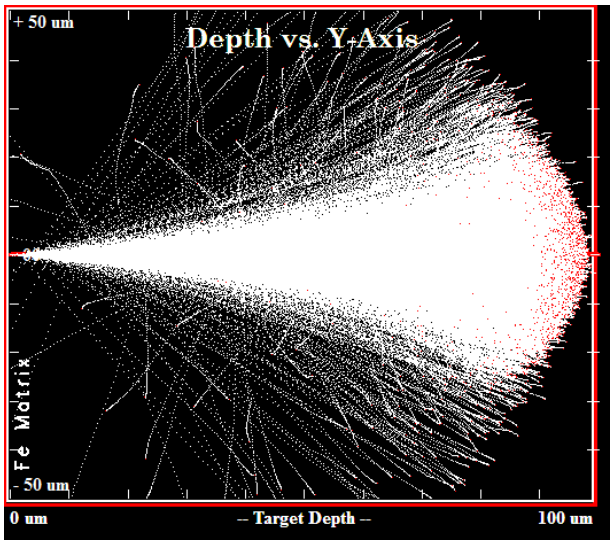

Figure 4.4: Trajectories and collisions of 100,000 protons of 5.4 MeV energy in Fe matrix as simulated by SRIM.

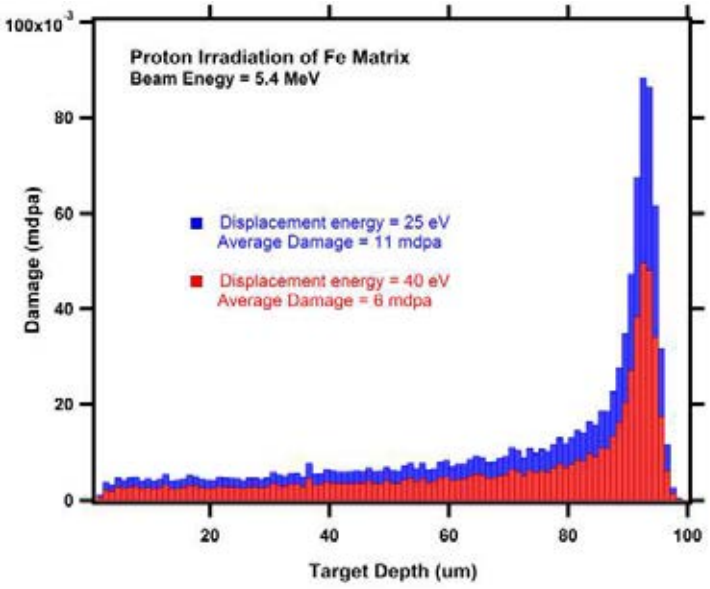

Figure 4.5: Comparison of damage profiles of Fe matrix irradiated with a proton beam of 5.4 MeV when the displacement energy for iron was kept at 25 eV (blue) and 40 eV (red). The resulting average damage was 11 and 6 mdpa respectively.

In Fig. 4.5 two different damage profiles, one for Fe displacement energy of 25 eV and one for Fe displacement energy of 40 eV, are plotted together for comparison. It is apparent that if the default displacement energy is chosen the average damage will be almost double. Consequently, it is important to use recommended values for displacement energies in order to keep the calculated damage values directly comparable with literature.

4.2.2 Vicker's Microhardness & SEM Imaging

Vicker's microhardness measurements were performed using the Mitutoyo MVK-H1 Hardness Testing Machine at the School of Metallurgy and Materials of the University of Birmingham, UK, on the as received specimen (sample HA). Due to radiation protection policies of the University of Birmingham it was not possible to measure irradiated samples.

Prior to any measurements the sample was mechanically ground and polished. For the grinding process abrasive SiC grit paper disks with grades 400, 600, and 1200 were used progressing from coarse to fine grit. The grade numbers correspond to the number of grains of SiC per square inch, with increasing number indicating finer grinding. For the polishing procedure soft cloth disks containing diamond particles were used. Disks of 9, 6, 3, and 1 micron were employed progressively. Diamond suspension was simultaneously used for reducing excess friction. The polishing process was performed with repeating steps when necessary resulting in the sample having a scratch-free mirror-like surface. The intermediate and final results were examined by means of optical microscopy.

The microhardness measurements were performed with the sample mounted on an aluminium stub ensuring that its surface was flat throughout the measurement for uniformity. Originally the edges of the sample were identified and a focus measurement was performed. Next, 9 - 13 equidistant indentations were performed forming a square matrix. The bulk hardness value was calculated by averaging over the values of the individual indentations.

SEM measurements were performed on the same sample. For the preparation of the

sample for the SEM the grinding and polishing procedures were again followed. Next, surface etching was performed so as to expose microstructural features, such as grain boundaries, and to chemically enhance contrast between different structural phases of the specimen. For the etching process 2% Nital was used as etchant. The sample was dipped in the etchant for a few seconds; sufficient time so as for the specimens not to be under- or over-etched. The end result was examined by means of optical microscopy after the sample was thoroughly cleaned using acetone. Next, the etched specimen was mounted on an aluminium stub using an adhesive conductive carbon disk. The SEM imaging was performed using the Hitachi S-4000 SEM facility of the School of Metallurgy and Materials of the University of Birmingham, UK. The SEM acceleration voltage used was 15 kV.

4.2.3 SANS - Configuration, Reduction & Analysis

Small-angle neutron scattering (SANS) measurements were performed on the SANS I instrument at SINQ-PSI, Switzerland[14] and at the D33 instrument at ILL[15], France, with preliminary measurements performed on the CG-2 instrument at HFIR-ORNL, USA. A schematic representation of a SANS instrument can be seen in Fig. 4.6. The typical SANS beam line consists of four main parts; the velocity selector, the collimation system, the sample area, and the detector.

After their production and moderation, neutrons are guided with specially designed, natural Ni or Ni-58 coated, neutron guides to the instruments through total internal reflection. A velocity selector, positioned after the neutron guides, is used for the selection of a single wavelength value, out of the full neutron wavelength distribution, as this is what is typically required by most SANS experiments. The selector, usually a rotating crystal, is consists of spinning absorbing blades that are tilted and the selection of the wavelength depends on the rotation speed. A typical wavelength resolution is $\Delta\lambda/\lambda = 10$ %.

The collimation system provides with the source-to-sample distance, guides the neu-

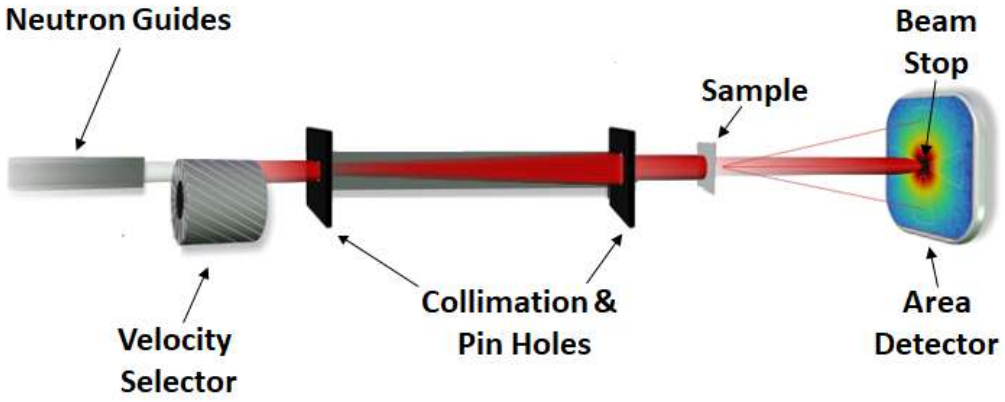

Figure 4.6: Schematic representation of a small-angle neutron scattering beam line depicting the neutron guides driving the neutron beam towards the instrument, the velocity selector, the collimation system along with the source and sample apertures, the sample area, and the 2D area detector along with the beam stop.

trons to the sample area and controls the beam's divergence. It consists of a set of neutron absorbing source and sample apertures (also defining the beam's size) and is contained within an evacuated path. The collimation length is adjustable with typical values ranging between 1 and 20 m.

The sample area and environment can be quite versatile. A sample holder that can take a single or multiple samples can be employed. A variety of sample environments, such as cryostats, electromagnets and cryomagnets, pressure cells and furnaces are often employed depending on the nature of the experiment.

For the detection of neutrons three main detector types are used; the gas-filled detectors, the scintillation detectors, and the semiconductor detectors. The type mostly used in SANS instruments is the position-sensitive proportional gas type detector. It is positioned in an evacuated tank for reducing air scattering and the sample-to-detector distance (SDD) is adjustable using motorised stages, with a typical minimum distance being about 1 m and the maximum ranging between 5 and 20 m depending on each instrument's configuration. Typically, for optimal set-up, the SDD is made to match the

collimation length.

In order to protect the detector from saturation or damage due to the strong direct neutron beam, a beam stop is employed. It is made of high neutron absorbing materials, such as Cd, and is positioned right before the detector in the path of the direct beam. As an extra protection measure, a monitor is also employed. Since the neutron source output varies from time to time, neutrons reaching the detector can exceed the saturation limit, thus using a monitor allows for counting of the incoming neutrons and electronically stopping their collection. Apart for safety reasons, a monitor is also useful for providing with the exact number of counts on the detector so as to adjust the counting time according to the requirements of a specific measurement.

For the experiments SDD of 3 to 18 m, with corresponding collimation, was chosen to measure a total scattering vector, $\vec{q}$, ranging from 0.0016 to 0.27 Å^{-1}. The neutron wavelength was $\lambda = 6 - 12$ Å. Different combinations of collimation, SDD, and wavelength allowed for the $\vec{q}$ - range to be covered, always depending on each instrument's limitations (samples HA, HD, HE, and HF were measured at a shorter $\vec{q}$-range due to instrumental configuration). For configuration details refer to Table 4.3. The counting time per sample varied for the different instruments depending on the statistics of the data received with higher $\vec{q}$ - ranges demanding longer measuring time because of coherent intensity decreasing with increasing $\vec{q}$, giving larger errors on the absolute intensity.

Table 4.3: Set-up details of SANS-I and D33 instruments used during the experiments.

Instrument	λ **(Å)**	**Collimation (m)**	$\mu_o\vec{H}$ **(T)**
SANS-I	6	3, 6, and 18	0.7
D33	6 and 13	2.8 and 12.8	1

For the detection of the scattered neutrons two-dimensional area detectors with 128x128 (SANS-I and D33) and 32x128 (D33) pixels were used and correction measurements for electronic noise and background scattering were performed. Saturating magnetic fields $\mu_o\vec{H} = 0.7 - 1$ T were applied perpendicular to the neutron beam to facilitate separation

of nuclear and magnetic contribution to the scattering. Circular and square Cd apertures were positioned in front of each sample to define the measured sample area. For raw-data reduction and their subsequent analysis the software GRASP[16] and the NCNR analysis pachage[17] were employed.

A systematic check for multiple scattering was also performed for all measurements. One way of ruling out multiple scattering is to investigate the ratio of integrated counts between a sample measurement and the corresponding direct beam measurement, after having been corrected with the appropriate attenuation coefficients. If the ratio is sufficiently small one can consider that the measurement is unaffected by multiple scattering. For example, the ratio for sample FD was calculated to be about 6×10^{-4}. This number is considered sufficiently small to exclude multiple scattering. Calculations for the rest of the samples through all $\vec{q}$-ranges yielded ratios of similar magnitudes. The differential scattering cross section $d\Sigma/d\Omega$ ($\equiv I(\vec{q})$) was finally derived after scaling of the scattered neutron beam intensity with transmission measurements and correcting for electronic noise and background scattering. Due to the applied saturating magnetic field, $\mu_o\vec{H}$, the scattering cross section is highly dependent on the field's orientation. When measuring the scattering vector, $\vec{q}$, perpendicular to $\mu_o\vec{H}$, the scattering intensity consists of both nuclear and magnetic scattering whereas for $\vec{q}$ parallel to the magnetic field only nuclear scattering contributes to the measured intensity. This can be seen in Fig. 4.7(b) where the integrated intensity versus the azimuthal angle is provided and a $\cos^2$ dependence is seen. If the scattering were consisted only of nuclear signal it would be isotropic and the integrated intensity constant for all angles. To isolate the nuclear and magnetic contributions a sector averaging, vertically and horizontally, on the 2D scattering image (Fig. 4.8) and subtraction of the horizontal from the vertical scattering intensity was performed. Sectors of $\Delta\theta = 35^o$ were chosen due to reduced signal-to-noise ratio.

As presented in Chapter 1, the scattering intensity, $I(\vec{q}) \equiv d\Sigma/d\Omega$, for a system of spherically isotropic particles with radially dependent properties can be calculated by

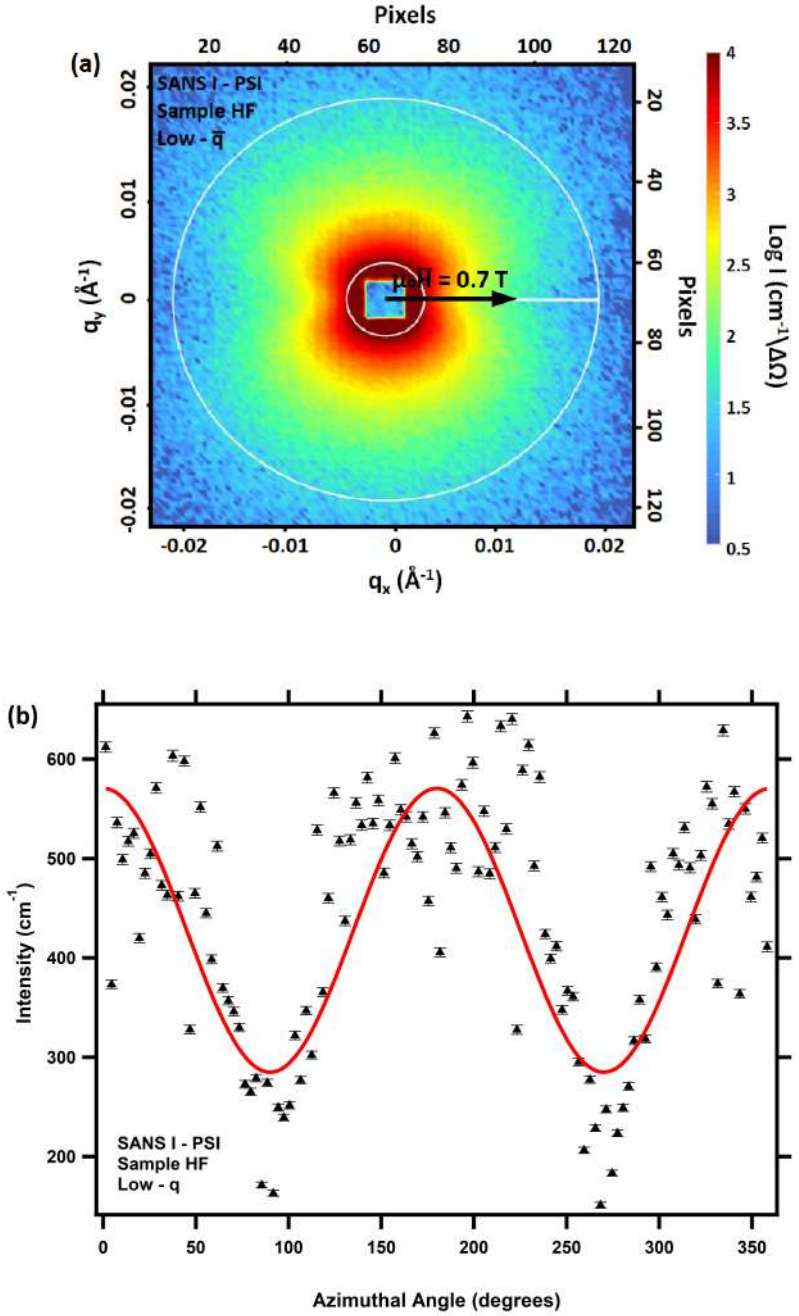

Figure 4.7: (a) Low-$\vec{q}$ 2D scattering image for sample HF with a 360° sector applied (excluding the beam centre) and (b) the corresponding 1D scattering signal with respect to the azimuthal angle of the 2D area detector. A $\cos^2$ dependence of the scattering signal is apparent indicated by the red fitted line.

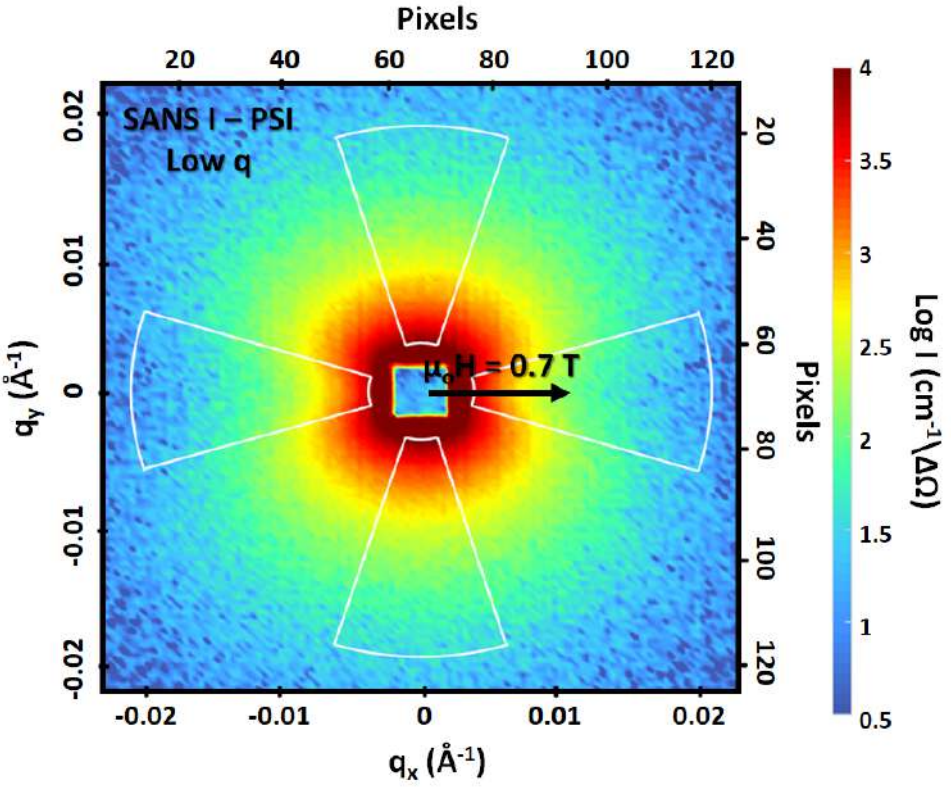

Figure 4.8: Low-$\vec{q}$ 2D scattering image for 0.3 wt. % Cu model RPV steel alloy irradiated at 400 °C (sample HF) to a total damage level of about 5 mdpa. The 0.7 T magnetic field was applied perpendicular to the incoming neutron beam as shown in the figure. The sectors seen in the figure are used for averaging purpose having a $\Delta\theta = 35^{o}$.

$$I(\vec{q}) = \Delta\rho^2 \int_0^\infty N(R) V_p^2(R) \left|F(\vec{q}, R)\right|^2 S(\vec{q}, R) dR \tag{4.3}$$

where R is the mean radius of the precipitates, $\Delta\rho$ is the scattering length density difference between the matrix and the scattering features, also referred to as the contrast factor, where ρ is defined as

$$\rho(\vec{r}) = \frac{1}{V} \sum_j^N b_j \delta(\vec{r} - \vec{R}_j) \tag{4.4}$$

with $\vec{r}$ being the position vector in the sample, $\vec{R}_j$ the position of the j^{th} scatterer, b_j the scattering length, and V is the volume of the sample. $N(R)$ gives the normalised number of particles (of radius R) per unit volume, $V_p(R)$ represents the volume of the scatterers, and $F(\vec{q}, R)$ is the so-called form factor. The form factor of spheres is given by:

$$|F(\vec{q}, R)| = 3 \frac{\sin(\vec{q}R) - \vec{q}R\cos(\vec{q}R)}{(\vec{q} \cdot R)^3} \tag{4.5}$$

$S(\vec{q}, R)$ is the so-called structure factor providing information on interparticle interactions and for dilute systems containing non-interacting randomly-oriented particles, it is $S(\vec{q}, R) = 1$.

$N(R)$ can be calculated using a size distribution such as a log-normal distribution for spheres, $P(R)$[18] and the number density, N_o of scatterers

$$N(R) = N_o P(R) = N_o \left(\frac{1}{\sigma \cdot R \cdot \sqrt{2\pi}} \cdot \exp\left[-\frac{1}{2\sigma^2} \cdot (\ln(R) - \mu)^2 \right] \right) \tag{4.6}$$

with $\mu = \ln(R_{med})$, where R_{med} is the precipitate median radius, and the polydispersity is given by σ. N_o can be calculated once the volume fraction and the mean volume of the

precipitates is known using

$$N_o = \frac{V_f}{\langle V_p \rangle} \tag{4.7}$$

where V_f is the volume fraction of precipitates and $\langle V_p \rangle$ is their mean volume.

The ratio between the magnetic and the nuclear scattering signal is encorporated in the so-called A-ratio. A-ratio is given as the ratio of the scattering signals received from the perpendicular and parallel averaging of the 2D scattering detector[19,20]. It is given by

$$A = \frac{(d\Sigma/d\Omega)_{\perp}}{(d\Sigma/d\Omega)_{\parallel}} = \frac{(d\Sigma/d\Omega)_{mag}}{(d\Sigma/d\Omega)_{nuc}} + 1 = \frac{\Delta\rho^2{}_{nuc} + \Delta\rho^2{}_{mag}}{\Delta\rho^2{}_{nuc}} \tag{4.8}$$

where in this case $\Delta\rho$ can be calculated by

$$\Delta\rho = \left(\sum_i x_i^C b_i^C - \sum_i x_i^M b_i^M \right) = \left(\sum_i x_i^C b_i^C - b_{Fe}^M \right) \tag{4.9}$$

where b_i is the nuclear or magnetic scattering length of element i, x_i is the fraction of element i, and C and M refer to cluster and matrix respectively.

4.3 Results

4.3.1 SEM & Hardness

Fig. 4.9 provides with the SEM image taken for the as-received specimen (sample HA). One can easily see that the sample seems to have a bainitic structure that is representative of steels found in service components. From the image it is also clear that there are features on the surface of the material, seen as white spherical particles. Such particles could be carbides, possible iron carbides (i.e. cementite). In steels cementite typically forms after

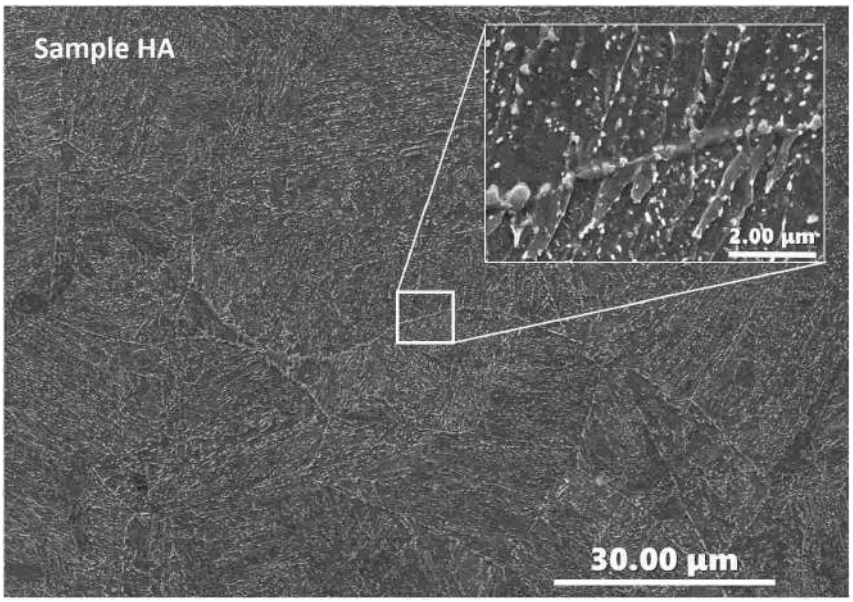

Figure 4.9: SEM image taken for the high-Cu RPV steel as-received sample. The inset is a zoomed-in area on the boundary region between grains. In the figure the presence of white spheroidal features is apparent. The features are probably cementite particles precipitating during cooling after the austenisation process of the steels.

the austenisation process, during cooling, or from the martensitic phase during tempering. By a rough estimation the average size of these spherical features is about 100 nm. Since the carbides seem to have precipitated within the ferritic laths it can be concluded that the bainitic structure is lower bainite.

The Vickers microhardness measurements gave a mean hardness value of 303.55 $\pm$11.67) HV. This value indicates that the microstructure of the still might indeed be bainitic since bainite has an intermediate hardness between that of pearlite, typically bellow 300 HV, and that of martensite, typically over 400 HV.

4.3.2 SANS

The resulting nuclear and magnetic differential scattering cross sections for all samples are plotted as a function of the total scattering vector, $\vec{q}$, and are given in Fig. 4.10. An offset has been applied to all curves for the sake of clearness. Since some of the samples

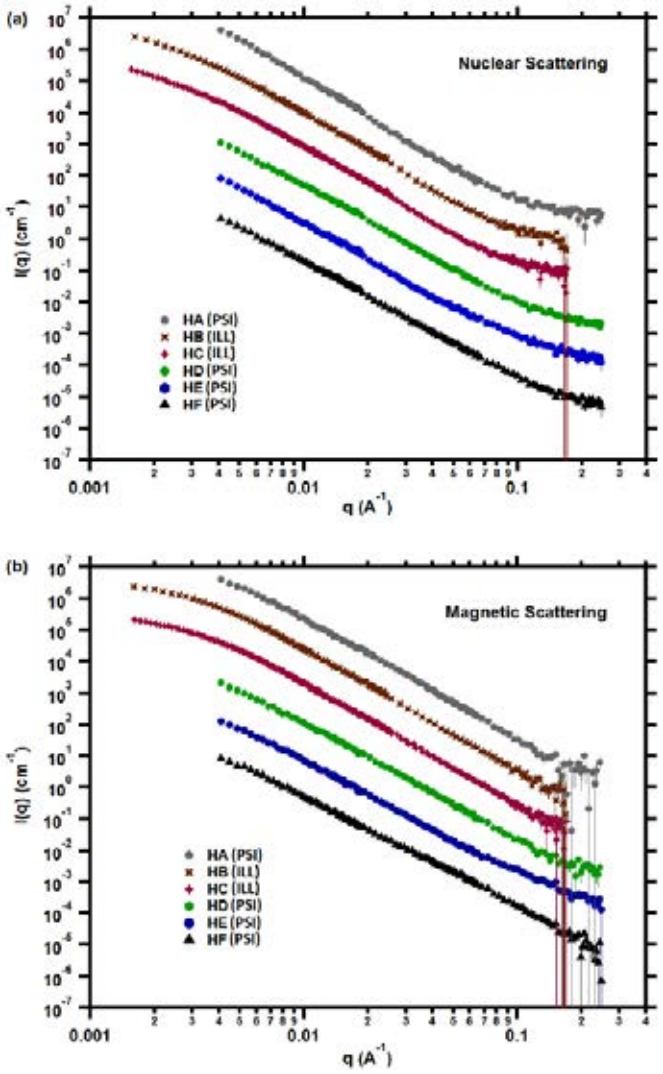

Figure 4.10: (a) Nuclear and (b) magnetic differential scattering cross section as a function of scattering vector, $\vec{q}$, for the high-Cu model RPV steel alloy irradiated to a total damage level of 6 mdpa.

were measured more than once, using different SANS instruments, here we present the data providing with the best statistics. As a first step a simple comparison between irradiated, heat treated, and as received scattering curves was performed. This was done to show any differences between the curves that might indicate irradiation induced features. In Fig. 4.11 and Fig. 4.12 the scattering curves of the as received, heat treated and irradiated samples are plotted together.

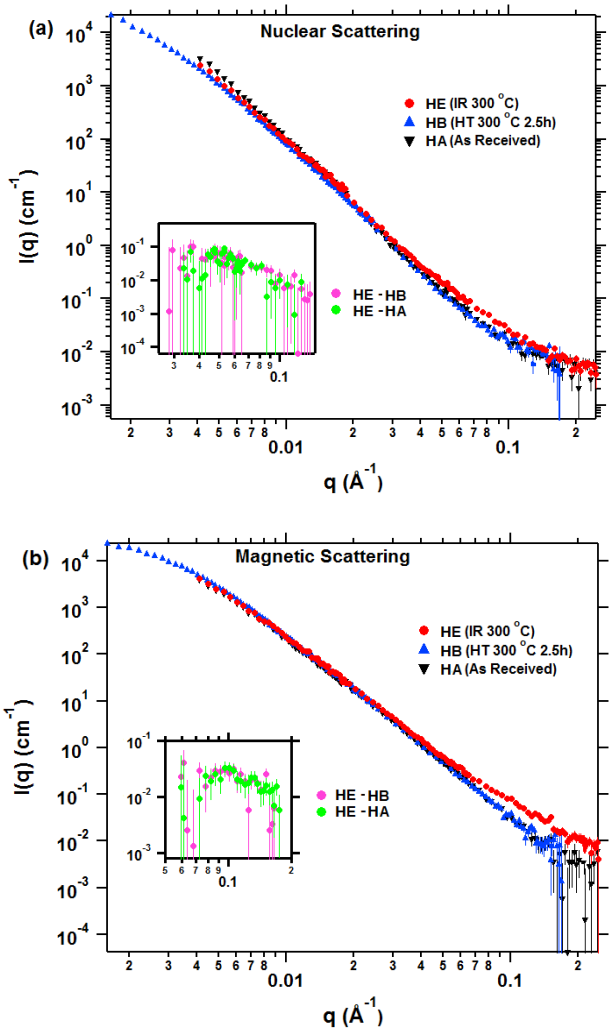

Figure 4.11: Comparison of the (a) nuclear and (b) magnetic scattering curves of as received, heat treated, and irradiated samples at a temperature of 300 °C. Both the nuclear and magnetic scattering curves of the irradiated sample have a bump at a $\vec{q}$ values roughly between 0.04 and 0.1 Å^{-1} indicating irradiation induced features that cannot be seen in the heat treated or as received samples. The inset at the bottom left is the resulting datasets after subtraction of the heat treated and as received scattering curves respectively.

From the figures it is apparent that the curves of the non-irradiated and irradiated

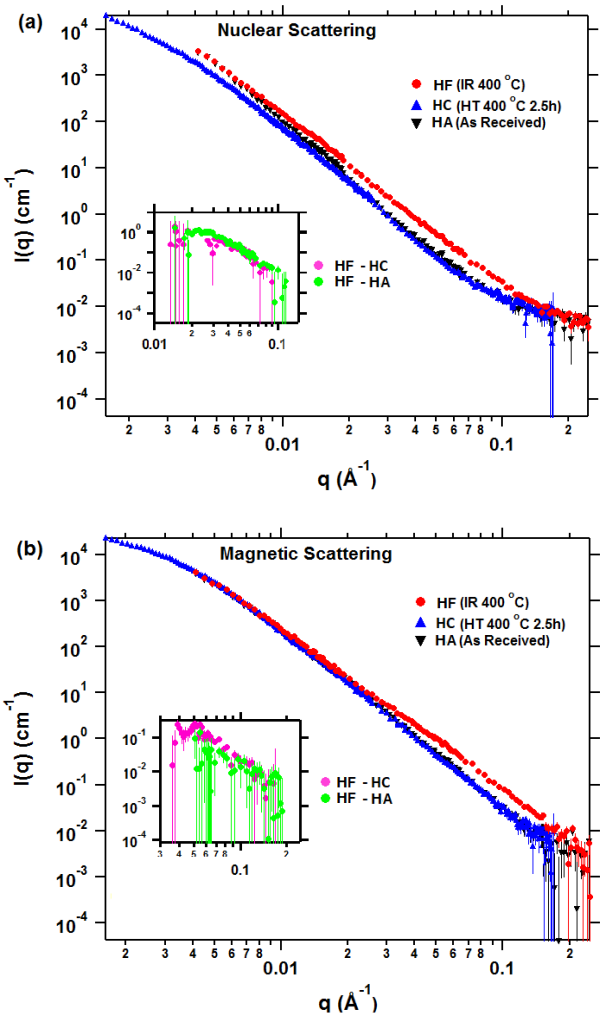

Figure 4.12: Comparison of the (a) nuclear and (b) magnetic scattering curves of as received, heat treated, and irradiated samples at a temperature of 400 °C. Both the nuclear and magnetic scattering curves of the irradiated sample have a bump at a $\vec{q}$ value roughly between 0.02 and 0.1 Å^{-1} indicating irradiation induced features that cannot be seen in the heat treated or as received samples. The inset at the bottom left is the resulting datasets after subtraction of the heat treated and as received scattering curves respectively.

samples are overlapping almost perfectly apart from a region in the higher $\vec{q}$-range. This indicates that there are scattering features that are induced after irradiation and are shown as a clear bump on the scattering curves of the irradiated samples. The corresponding real-space size is about 1.5 nm for the 300 °C irradiation and about 4 nm for the 400 °C irradiation. This is well in agreement with literature reported irradiation induced nano-precipitates. Additionally a simple observation of the scattering curves indicates that the scattering intensity of all samples follow a $\vec{q}^{-4}$ dependence (Porod law) that is typical of grain boundaries.

To investigate any scattering features the most common approach is to perform fitting processes with known models. The models most commonly used in literature are either a unimodal or a bimodal log-normal sphere distribution model. Before using one or the other a comparison with a single or double Guinier model was performed since this is one of the simplest models used to describe general scattering objects assuming no known specific model. In Fig. 4.13 an example of fitted Guinier or log-normal (both single and double) models is provided for sample HE. Since statistically the two models (Guinier or log-normal) do not deviate much, a unimodal and a bimodal log-normal sphere distribution model was chosen to be fitted onto the data-sets to get the best fitting results, and the resulting fitting curves, for each case, are plotted along with the corresponding scattering curves. The log-normal model was chosen to make comparison with literature easier.

In order to exclude Porod behaviour from the measured data so as to receive the signal due to precipitation alone, subtraction of a Porod model, $I(q) = Aq^{-m}$, (fitted to both nuclear and magnetic scattering data-sets) was performed. The modified scattering curves for the different samples can be seen in Fig. 4.14 - 4.16. By carefully looking at the modified scattering curves there is indication that a double precipitation event might be present for some of the samples.

From Fig. 4.14 - 4.16 it can be seen that a unimodal log-normal sphere model fits well only on the scattering curves of the as-received sample and the sample irradiated at 50 °C. This is not the case though for the the samples irradiated at higher temperatures, where

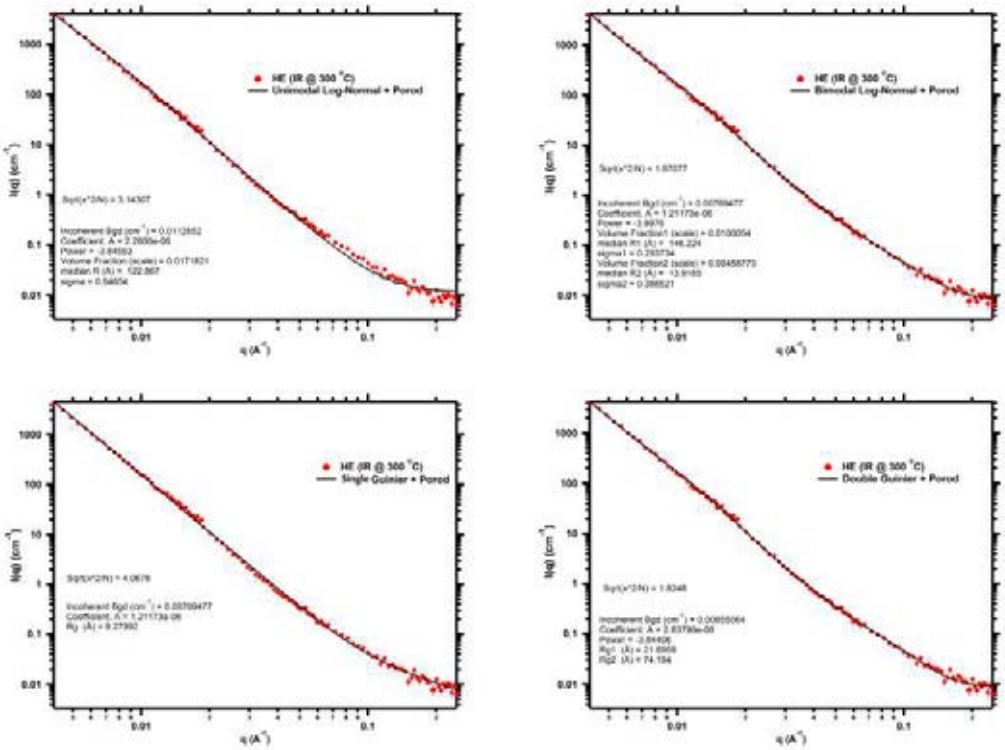

Figure 4.13: Comparison of fitting models for sample HE. From top left to bottom right: unimodal log-normal plus Porod, bimodal log-normal plus Porod, single Guinier plus Porod, double Guinier plus Porod. Both the Guinier and log-normal models behave similarly. For this specific sample a double Guinier or bimodal log-normal model seems to describe the scattering features better.

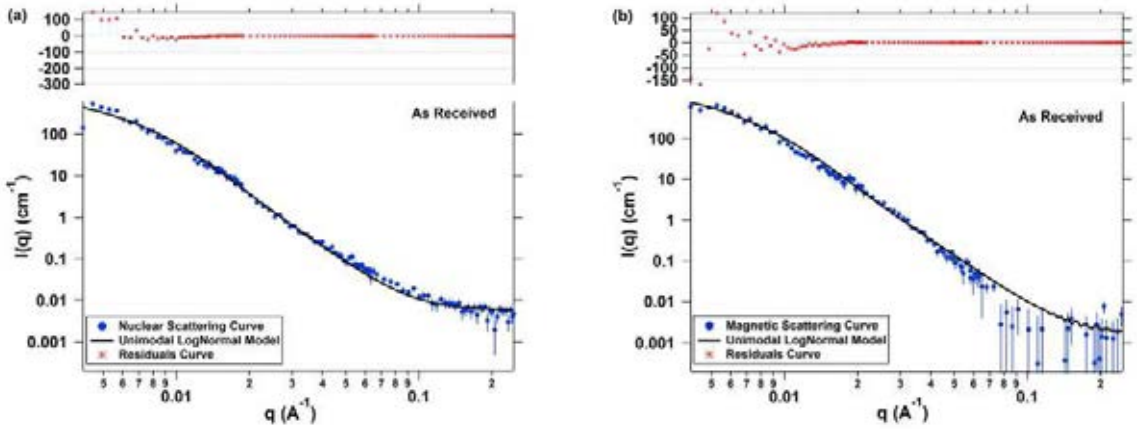

Figure 4.14: (a) Nuclear and (b) magnetic differential scattering cross section for sample HA after removal of the Porod law. The solid line is a unimodal log-normal sphere distribution model fit indicating a single scattering feature. The red markers are the residuals of the fit.

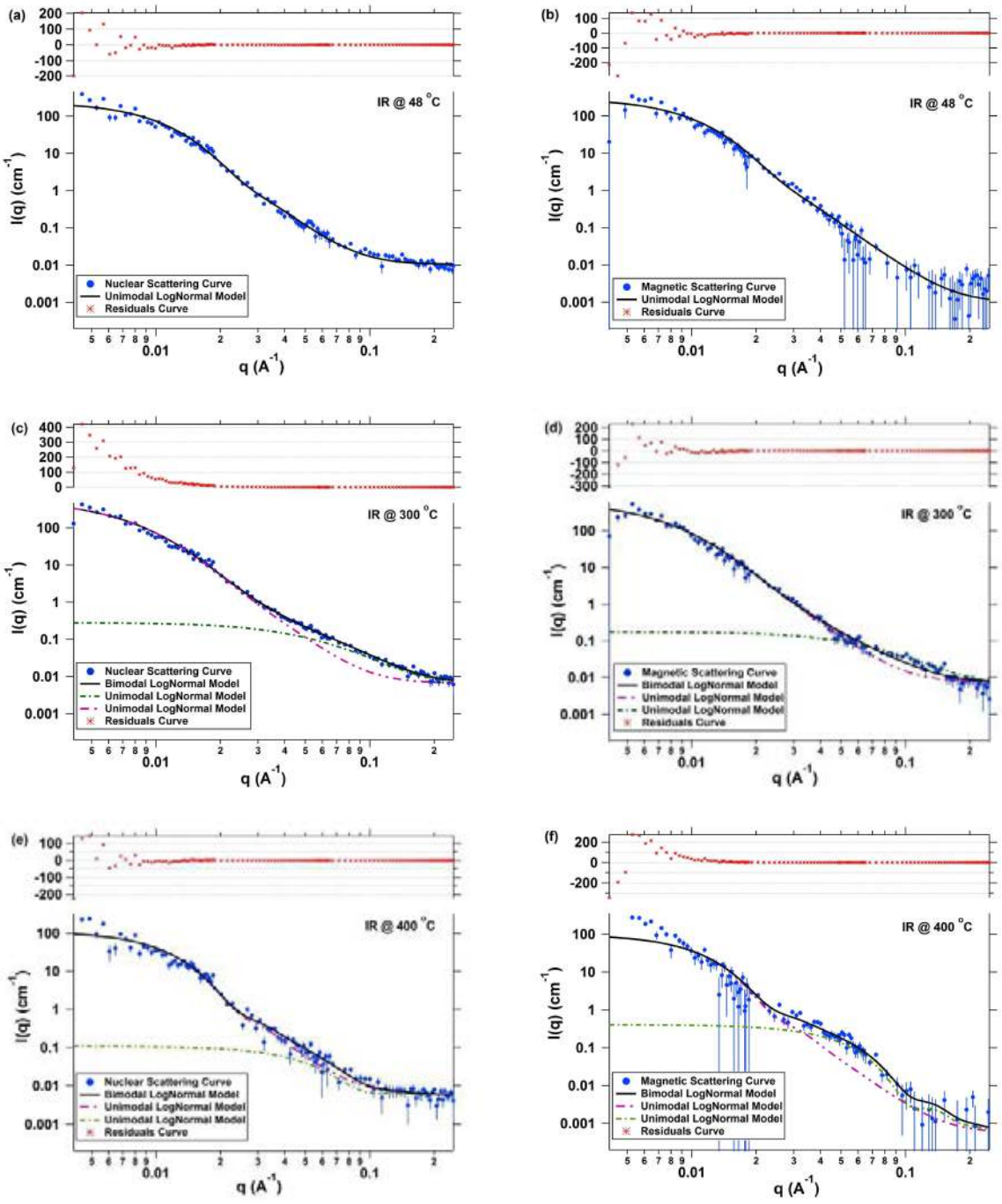

Figure 4.15: (a)(c)(e) Nuclear and (b)(d)(f) magnetic differential scattering cross section for samples HD, HE, and HF after removal of the Porod law. For sample HD the black solid line is a unimodal log-normal sphere distribution model fit indicating a single scattering feature. For samples HE and HF the black solid line is a a bimodal log-normal sphere distribution model fit indicating double scattering features. The individual unimodal models are also plotted (dashed lines) for reference. The red markers are the residuals of the fit.

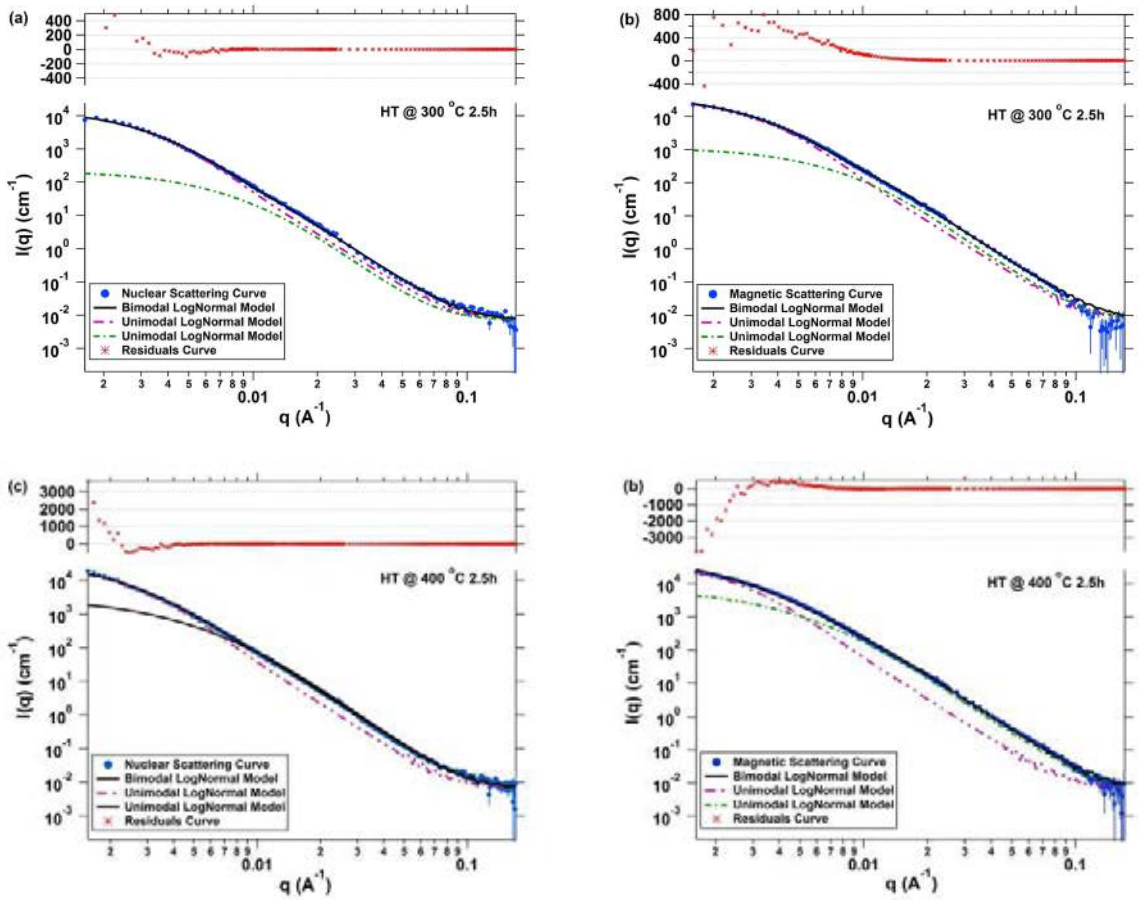

Figure 4.16: (a)(c) Nuclear and (b)(d) magnetic differential scattering cross section for samples HB, and HC after removal of the Porod law. The black solid line is a bimodal log-normal sphere distribution model fit indicating double scattering features. The individual unimodal models are also plotted (dashed lines) for reference. The red markers are the residuals of the fit.

the unimodal model fails to fit throughout the entire $\vec{q}$-range and the bimodal log-normal distribution seems to be more suitable for describing the scattering features. The two separate components of the bimodal models are included in the graphs showing clearly the two different precipitation events.

Using the fitting results of the log-normal sphere models we were able to obtain quantitative information of the scattering features, such as precipitation mean radius, R_{mean}, volume fraction, V_{f}, and number density, N_{o}. In order to calculate the absolute V_{f} the nuclear and magnetic contrast factors must be known. These factors depend on parameters such as cluster composition and their magnetic properties that are not known *a priori*, thus the absolute V_{f} cannot be calculated. During fitting the contrast factor was kept fixed at an arbitrary value of 4×10^{-12} Å^{-2} (scattering length density difference squared) and thus values of the relative instead of the absolute V_{f} are provided. The same applies for N_{o}.

Using equation 4.7 and combining with equations 4.3 and 4.6 we also received experimental values of the A ratio thus having an insight on the precipitates' possible composition. During fitting the coefficients corresponding to the radius of the precipitates, for both the magnetic and nuclear curves, were linked together to provide a single value assuming that the size of the scatterers should be the same for both signals. Since, the scattering contrast was fixed and was kept constant, the A ratio was calculated considering differences in number density and consequently volume fraction alone. Hence, the A ratio equation was modified accordingly and is given by

$$A = \frac{V_f^M}{V_f^N} + 1 \tag{4.10}$$

where M and N correspond to magnetic and nuclear signal respectively. Due to the averaging being performed using a 35° sector instead of a 90° one, that would contain the full contribution of the magnetic signal, the A ratio was scaled accordingly with the use of a scaling factor calculated as

$$C = \frac{\int_{-0.3}^{0.3} \cos x^2 dx}{\int_{-\pi/2}^{\pi/2} \cos x^2 dx} \tag{4.11}$$

This resulted in a value of 0.37 with which the first term of the right-hand side of equation 4.10 is multiplied. This was performed for all A ratio calculations, and their errors. A ratio values between 1.2 and 3 were calculated. The implemented log-normal distributions are plotted as a function of radius and are given in Fig. 6.12 with the as-received distribution plotted as a reference. All the calculated quantities and results are given in Table 4.4. First thoughts denote that the calculated size distributions along with the fact

Table 4.4: Characteristics of precipitates calculated from unimodal or bimodal log-normal distribution

Sample	$\mathbf{R_{mean}}$ **(Å)**	σ	**Rel.** $\mathbf{V_f}$	**Rel.** $\mathbf{N_o}$ **(** $\times\mathbf{10^{20}}$ $\mathbf{m^{-3}}$**)**	**A Ratio**
HA	144.3 ± 2.1	0.45 ± 0.01	0.016 ± 0.001	5.7 ± 0.4	1.70 ± 0.01
HB	322.8 ± 3.1	0.44 ± 0.01	0.027 ± 0.001	1.1 ± 0.1	1.94 ± 0.01
	94.0 ± 1.6	0.52 ± 0.01	0.0057 ± 0.0001	7.2 ± 0.6	2.93 ± 0.09
HC	378.8 ± 3.1	0.47 ± 0.01	0.027 ± 0.001	0.61 ± 0.02	1.57 ± 0.01
	94.4 ± 0.9	0.62 ± 0.01	0.0099 ± 0.0001	9.0 ± 0.4	2.89 ± 0.03
HD	146.6 ± 1.7	0.31 ± 0.01	0.016 ± 0.001	9.0 ± 0.5	1.43 ± 0.01
HE	134.9 ± 2.6	0.42 ± 0.01	0.016 ± 0.001	9.5 ± 0.8	1.43 ± 0.01
	10.5 ± 3.9	0.51 ± 0.08	0.006 ± 0.001	6140 ± 10	1.21 ± 0.04
HF	169.7 ± 2.2	0.21 ± 0.01	0.008 ± 0.001	3.4 ± 0.2	1.32 ± 0.02
	40.7 ± 2.5	0.14 ± 0.06	0.0007 ± 0.0001	240 ± 7	2.48 ± 0.19

that some of the scattering features are present in the samples prior to irradiation, also being relatively stable during irradiation, indicates that there exist two overall groups of scattering features different in nature. The smaller features (1 – 5 nm), appear only in the samples that were irradiated at 300°C and 400°C. Their size is well in agreement with the average sizes of irradiation-induced precipitates reported in literature[21,22]. In contrast, the larger scattering features, with sizes ranging between 10 and 40 nm (radii

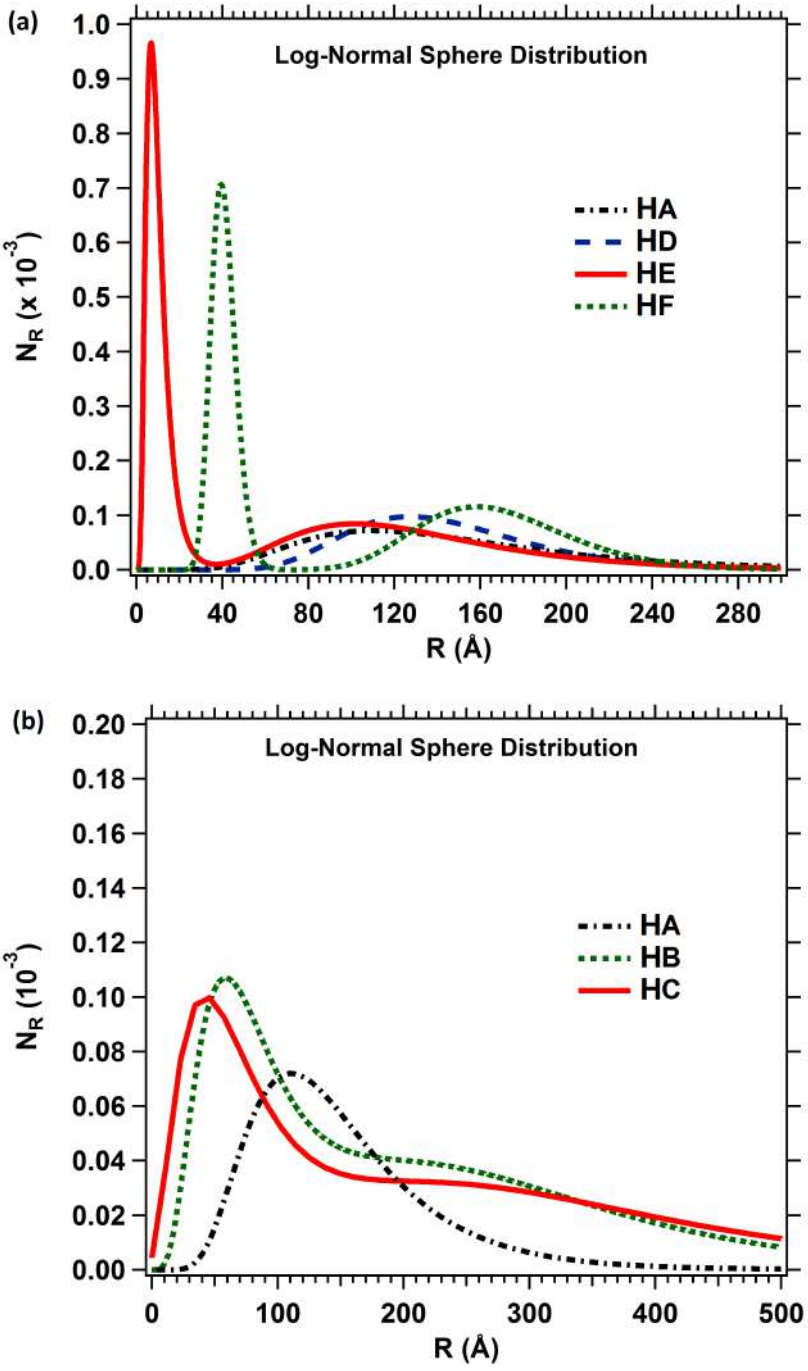

Figure 4.17: Log-normal sphere model size distribution for high-Cu steel alloy specimens. The distributions of irradiated (a) and heat treated (b) samples are plotted separately with the distribution of the as received specimen (HA) plotted in both as reference.

over 30 nm corresponding to samples HB and HC), are not commonly found among irradiation induced (fine) precipitates. These larger features are present in the samples prior to irradiation and they are rather stable during irradiation. This indicates that these features might be microstructural features, such as carbides[23], formed during the original service process of the steels, after austenisation. This is also supported by TEM and APT studies denoting that M_3C (M for metal) are the most common carbides found in both low- and high-Cu steels with the dominant metallic element being Fe[23], i.e. cementite. The fact that in samples HB and HC we were able to detect features of larger average size ($>$ 300 Å) is due to the extended $\vec{q}$-range of their corresponding scattering curves to lower values.

To check these fitting results an evaluation of the received values for the different parameters, i.e. average radius and volume fraction, is necessary. First we compare the SEM with the SANS results. Looking back at the SEM image provided in Fig. 4.9 it is seen that there is a general mismatch between the average sizes of the scattering bodies as given by the SEM and SANS. It is apparent that SANS provides a somewhat smaller average radius of the alleged carbides than that observed in the SEM image. This disagreement is clearly due to limitations during the SANS measurements; the lowest limit of the $\vec{q}$-range limits the highest average radius measured. One needs to recall from Chapter 1 that SANS provides an average over a large volume of sample but it is always limited by the $\vec{q}$-range probed. Subsequently, one can think that the average radii (for the larger features) given by the SANS measurements in our study correspond to the edge of a size distribution with a mean radius shifted at higher values that is out of detection limits. Of course extending the measured $\vec{q}$-range to lower values would allow for a better estimation of the size distribution of the carbides.

The fitting processes were also repeated for different starting parameters, including volume fraction (values between 0.001 and 0.1), radius (values between 10 and 700 Å), as well as scattering length densities (contrast values between 1×10^{-12} Å^{-2} and 100×10^{-12} Å^{-2}) to check the stability of the results. It was observed that for most of the fits the resulting

radius was almost the same each time (within error values) except when the starting parameters were forced to have unrealistic values (e.g. extremely large radius or extremely low volume fraction and vice versa) thus producing a singular matrix error, or returning negative values. As discussed in Chapter 1, the shape of the scattering curve can reveal a good estimation for the average size of the scattering object. For example, looking back in Fig. 4.14 (sample HA), one sees that there is an apparent bump for $\vec{q}$ values between 0.005 and 0.01 $Å^{-1}$ that gives a radius value between 100 and 200 Å in real space. This makes clear that the starting fitting value for radius should be chosen to be within these values. The returned value indicates that such a choice is correct. Similar approach is followed for all samples.

Still referring to sample HA, when the starting value for the radius was chosen to be below 70 Å, and especially at really low values (e.g. 10-20 Å), the fits resulted in either singular matrix error or negative volume fractions. With a starting radius over 70 Å and up to 200 Å the fits converged normally with the resulting average radius being around 150 Å and the volume fraction between 0.015 and 0.020. When the starting contrast was changed it was seen that realistic fitting parameters were received for low contrast values ($< 10 \times 10^{-12}$ $Å^{-2}$) while for large values the resulting volume fraction was unrealistically small and vice versa. Similar checking processes were performed for all samples with the returned fitting values behaving in a similar way. Overall it was observed that the starting fitting parameters do affect the resulting fitting values but in such a way that one is in position to evaluate their validity. As in any fitting process good knowledge of the system as well as careful critical evaluation of the results is crucial.

To further check the validity of the results and be able to receive more specific information regarding the samples (e.g. to find out whether precipitation of cementite takes place) the CALPHAD method of the software Thermocalc[24] (version 4.0, 2014) was employed. The software takes as input a variety of parameters, such as the bulk composition of the sample and the temperature of the system (or temperature range) and by describing the thermodynamics of the system through the Gibbs free energy it returns the possible

Table 4.5: Composition of cementite phase precipitating out of the matrix of the high-Cu RPV alloys as calculated using the CALPHAD method of Thermocalc[24] with the TCFe7 database. The precipitation of cementite occurs after the temperature of the systems drops below 650 °C.

Cementite Volume Fraction: 0.017		
Element	**Mole Fraction**	**Mass fraction**
Fe	0.64492	0.80341
Mn	0.07210	0.08836
C	0.25000	0.06698
Cr	0.02650	0.03074
Ni	0.00404	0.00529
Mo	0.00244	0.00522

phases based on phase equilibria. For the calculation the database TCFe7 was used. The temperature upper value was chosen to be 920 °C to match the processing temperature during fabrication of the steel. After the calculations were complete it was seen that cementite starts precipitating after the temperature of the system drops to about 650 °C with a phase volume fraction of about 0.17. The detailed results for the cementite phase are given in Table 4.5.

Using the composition given in the table above it was made possible to calculate the scattering length density of cementite. The scattering length density of the overall sample (i.e. matrix) was also calculated using the composition given in Table 4.1. These values along with the volume fraction of cementite, given by Thermocalc, where used as starting fitting parameters and using once again the model of polydispersed spheres with log-normal size distribution the fitting processes were repeated. In Table 4.6 the fitting results and parameters for sample HA, prior to and after Thermocalc calculations, are provided as an example for comparison.

By comparing the results it is made clear that the mean radii, as taken by the original fits and the fits using Thermocalc information, are very close and the volume fractions are

Table 4.6: Fitting parameters for sample HA before and after using Thermocalc

	Original Fitting Results	**Fitting Results With Thermocalc Input**
Volume Fraction	0.016 ± 0.001	0.017 ± 0.002
Average Radius (Å)	144.3 ± 2.1	152.9 ± 2.0
σ	0.45 ± 0.01	0.38 ± 0.01
SLD sphere ($Å^{-2}$)	2.0×10^{-6}	6.3×10^{-6}
SLD matrix ($Å^{-2}$)	0	7.8×10^{-6}
sqrt(X^2/N)	2.42	2.36

almost the same, within error values. Additionally, the arbitrarily chosen contrast value is not far from the calculated one, making the results even more solid. Consequently it can be deducted that the original fitting process and the resulting mean radius values along with the calculated A ratios can be overall trusted.

Unfortunately, Thermocalc cannot be used to predict irradiation induced precipitates and thus their possible composition still remains unknown. Based on the verification of the results regarding the cementite particles though, one can safely assume that the resulted fitting parameters and values that correspond to the smaller precipitates (seen in samples HE and HF) can also be trusted. Further discussion on the possible composition of the precipitates, analysing the A ratio values, is provided in the following sections.

4.4 Discussion

Research on RPV embrittlement has established the existence of a complex relationship between features occuring due to irradiation and changes to material's properties such as hardness. SANS, along side other techniques, e.g. APT, can be used to provide information on features such as mean precipitate radius, size distribution and number density, volume fraction, as well as possible composition[25].

For SANS, to calculate the absolute V_f the mean contrast factor between the scat-

tering features and the matrix must be known. The contrast factor is a function of the composition of the precipitates and the vacancy content, as well as the magnetic properties of the precipitates[25]. Values of these parameters must be chosen so as to agree with the experimentally calculated A ratio. Given the number of parameters involved, many solutions might exist. Consequently, assumptions are often made in the interpretation of SANS data. Some of these assumptions are explored below.

4.4.1 Non-magnetic clusters

Often in the SANS analysis of RPV steels, an assumption that the scattering features are non-magnetic (i.e., the scattering features are considered to be non-magnetic holes in a saturated magnetic α-Fe matrix) is made. Studies peformed by means of positron annihilation spectroscopy using a spin-polarized element-specific method have shown that clusters found in irradiated FeCuMn model alloys, being Cu-rich, carry no magnetic mament and contain 10 % Fe or less[26]. This is not entirely in agreement with some APT results, however APT can overestimate the amount of Fe[27,28]. Regarding alloys containing precipitates enriched in Mn and Ni, the assumption of non-magnetic precipitates is also an approximation. Consequently the magnetic contrast can be held constant and equal to the magnetic scattering length of the Fe in the matrix squared. As a result one has to only take into account variations in the nuclear contrast. As such, increasing the content of Cu, Ni, Si, and/or Fe in the precipitates results in increased A ratio values whereas increasing the Mn content (due to its negative nuclear scattering length) or vacancy content will decrease the A ratio.

Using equations 4.8 and 4.9, and under the assumption of non-magnetic clusters, A ratio values for various combinations of composition of the scattering features were calculated and compared with the experimental values. The A ratio equation was modified by assuming a combination of Cu, Mn, and Ni in the clusters and by using the corresponding nuclear scattering lengths along with the magnetic and nuclear scattering length of Fe[20]:

$$A = \left[\frac{0 - (6.0x_{Fe})_M}{(10.3x_{Ni} + 7.72x_{cu} - 3.73x_{Mn})_C - (9.45x_{Fe})_M}\right]^2 + 1 \tag{4.12}$$

where x is the fraction of the elements within the phases. The numbers multiplied with the fractions in the denominator correspond to the nuclear scattering lengths of Ni, Mn, Cu, and Fe respectively and that in the numerator gives the magnetic scattering length of Fe. The magnetic scattering length density for the scatterers is kept at zero. All the scattering lengths are given in fm. The indices M and C correspond to matrix and clusters respectively. The results are provided in Fig. 4.18 as a ternary plot providing all possible compositions for the calculated A ratios. One can easily see that there is a variety of Cu, Mn, and Ni contents giving the same A ratio values. Given the complexity in bulk composition of the samples studied here, a deeper and more precise investigation on the possible composition of the precipitates is required.

Examining the calculated A ratio values in combination with the wt. % of Cu, Mn, and Ni in the specimens the presence of a single element in the precipitation events is excluded, and in any case this would be in contrast with reported literature. Studies performed by means of SANS[21,22], PAS[29,30], as well as molecular dynamics[31] have shown that binary FeCu alloys contain clusters of Cu and vacancies with a core-shell formation and ternary FeMnNi alloys contain mixed Mn-Ni clusters. It is also reported that in contrast to clusters enriched in Cu, Mn-Ni precipitates do not contain vacancies. This is due to Ni and Mn atoms segregating on self-interstitial solute clusters thus forming clusters[32].

From Fig. 4.18 one can see that small A ratio values, about 1.4 or smaller, indicate high content of Mn in the clusters; Mn is the only element that can reduce the A ratio because of its negative scattering length. Values of about 1.5 can be derived by having a varying combination of Cu, Mn, and Ni with Mn dominating and Cu along with Ni being present in lower amounts, seemingly being inversely proportional since their nuclear scattering lengths are relatively close and increasing the amount of one would decrease the amount of

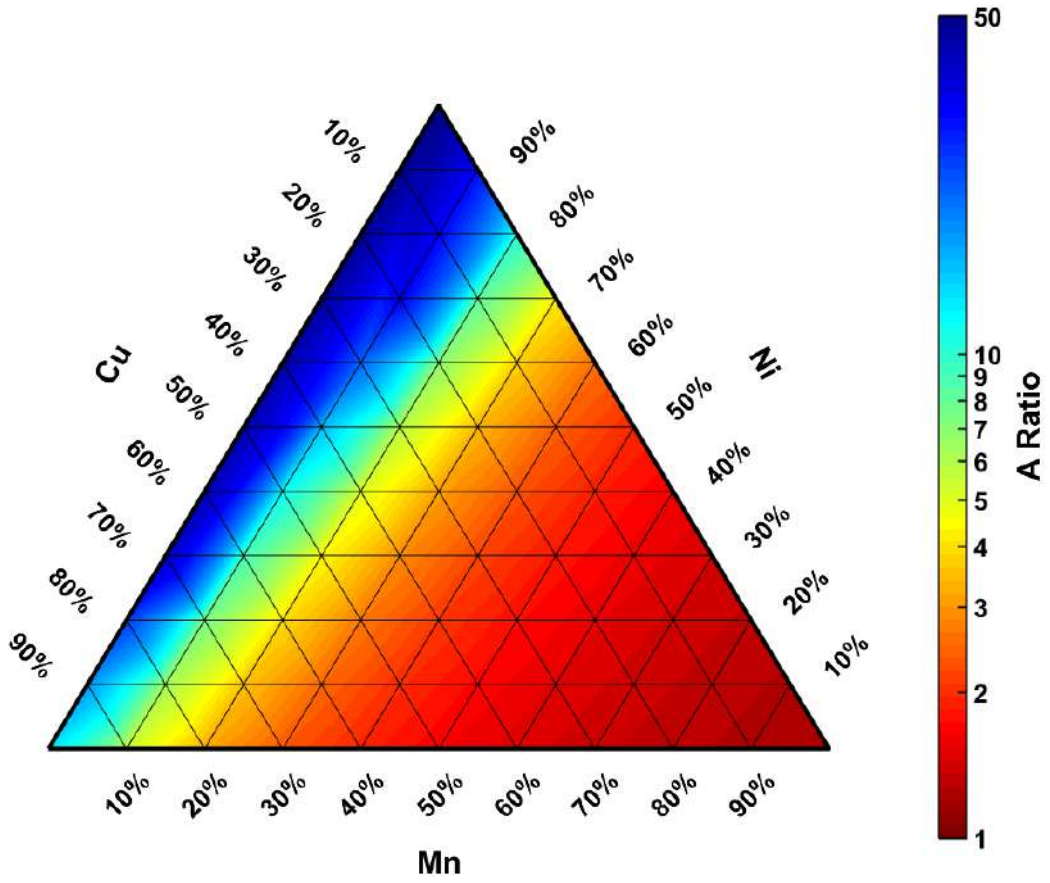

Figure 4.18: Cu - Mn - Ni ternary plot depicting the A ratio dependence on the composition of the precipitates when these are considered to be non-magnetic. The colour scale has been set to logarithmic scale for clarity.

the other to keep a constant A ratio. Increased A ratios could be due to higher Cu (or Ni) content in the clusters. This is also in agreement with reported studies, arguing that samples with high Cu content (> 0.1 wt.%) contain Cu-rich irradiation induced precipitates. SANS studies on Fe0.1Cu, Fe1.2Mn0.7Ni, and Fe1.2Mn0.7Ni0.1Cu model alloys[20] provide A ratio values of 5, 1.5, and about 2 respectively. It is argued that the binary Fe0.1Cu alloy with an A ratio value of 5 contains Cu-vacancy clusters and the Fe1.2Mn0.7Ni alloys should have Mn-Ni-alone clusters. Regarding the Fe1.2Mn0.7Ni0.1Cu alloy the cluster composition is expected to be in between the other two, containing Mn, Ni, and Cu. In specimens as complex as the ones investigated here, being model RPV steels, one should

also make a mass-balance argument and take into account the total solute available for precipitation from the matrix composition of the sample, especially when it comes to precipitation of Mn and Ni in such high-Cu steels.

Earlier it was argued that the scattering features in the size range between 10 and 40 nm are possibly cementite commonly formed after the austenisation stage of steel processing as the temperature drops. A calculated A ratio for such features, under the non-magnetic assumption, is much higher than our experimental values though (> 10). Also regarding the irradiation-induced nano-precipitates, APT studies[33] on similar specimens under similar irradiation conditions, indicate the high content of Ni and Fe in the precipitates. Again this would result in really high A ratio values. As a result, the non-magnetic nature of the scattering features is not necessarily an accurate assumption and their magnetic nature should also be investigated.

4.4.2 Magnetic Clusters

The discussion so far was under the assumption of non-magnetic scattering features but, in most cases, irradiation-induced precipitates contain Ni (depending on the wt.% of Ni in the alloys), Mn and sometimes Fe (evident by some APT measurements[33]). In such cases, precipitates could be partially or fully magnetic. There are a few studies on the magnetic character of solute clusters formed by irradiation but so far there is no clear image on their magnetic properties and there are no extensive, independent studies on identifying the magnetic properties of small clusters.

To find the possible composition of irradiation induced clusters will be even more complicated. If the magnetic contrast decreases, then so must the nuclear contrast to maintain a constant A ratio. J.M. Hyde *et al.*[25] reported that there are numerous possible compositions of scatterers given an A ratio value of 2.5, under the assumption of partially or fully magnetic scattering features (see Fig. 4.19). In our study, the RPV model alloys contain large amounts of Ni (3.5 wt.%) that cannot be excluded and the presence of

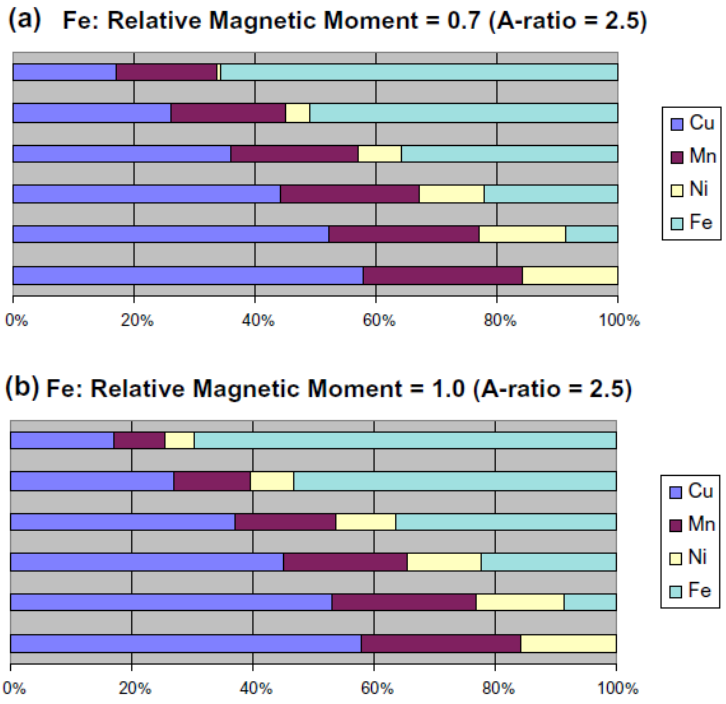

Figure 4.19: Possible compositions of precipitates containing Cu, Mn, Ni, and Fe when they are (a) partially or (b) fully magnetic for a given A ratio value of 2.5.

Fe in the clusters is not conclusive. Thus the SANS data, in isolation, cannot prove or disprove the hypothesis that the scattering features contain Fe, or the hypothesis that the scattering features have magnetic properties. Since neither the nuclear nor the magnetic contrast are fixed for a given A ratio value, the absolute V_f and N_o will depend on the Fe content and the magnetic properties of the scattering features, as discussed earlier.

To be able to further establish the validity of the SANS results a comparison with APT measurements was done. Published works of APT studies performed on high-Cu steels, also containing high levels of Ni, argue that irradiation induced precipitates have a quite high Ni content and possibly Fe. A report by Connolly *et al.*[33] contains results from APT measurements performed on a variety of different RPV alloys. One of their samples (having similar composition with the samples of our study and irradiated under the same conditions) contained irradiation induced precipitates with high levels of Ni and Fe as well as Mn, Si, and Cu (6.9 at.% Cu, 11.2 at.% Mn, 21.3 at.% Ni, 7.3,at.%

Si, 52.7 at.% Fe). To test these results and compare with the results of this study, the precipitates' compositions were put into the A ratio formula, originally taking into account the magnetic scattering length density of the matrix alone. The resulting A ratio

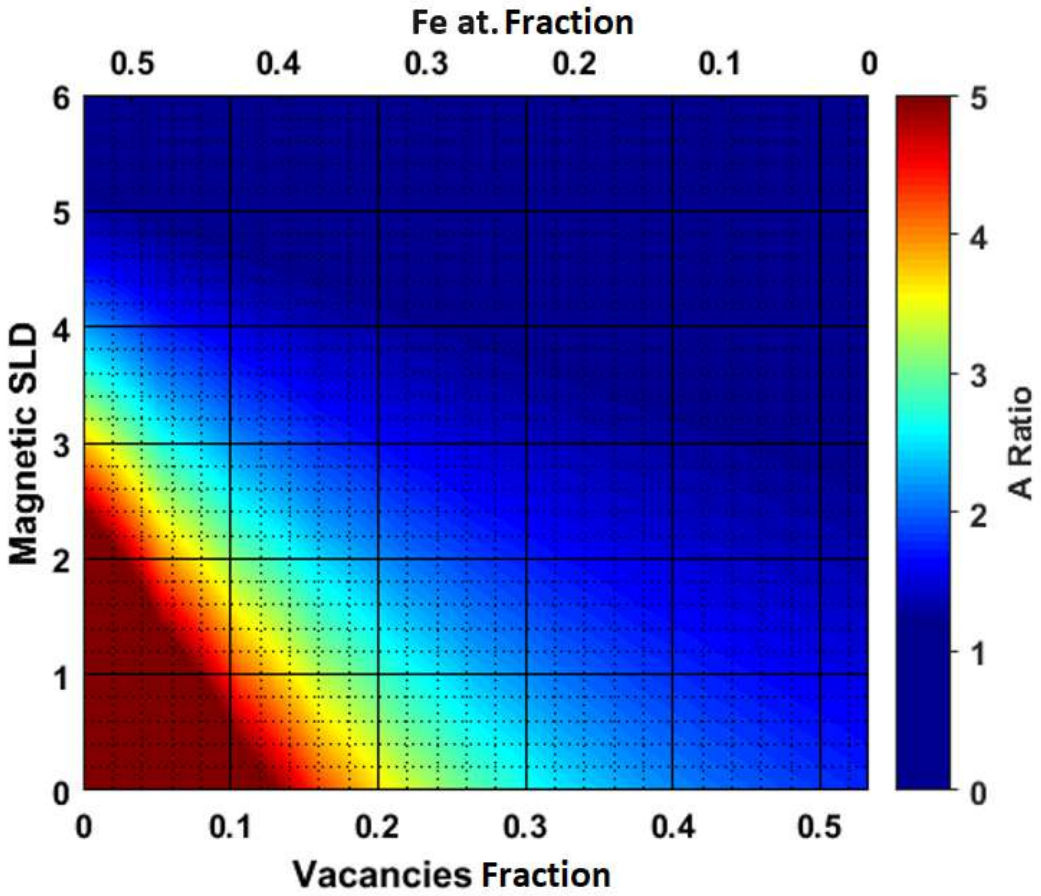

Figure 4.20: Magnetic scattering length density of scattering features for A ratio values between 0 and 5 with respect to the content of vacancies and/or Fe, containing 6.9 at.% Cu, 11.2 at.% Mn, 21.3 at.% Ni, and 7.3 at.% Si. As the A ratio increases so does the magnetic scattering length density for a specific vacancy or Fe content and *vice versa*.

values were indeed much higher than any of our experimental values. For this reason, numerical calculations were performed in order to find possible magnetic scattering length densities for the precipitates that would give A ratio values matching our values. For the calculation, equations 4.8 and 4.9 were used. Because APT is insensitive to vacancies we also assumed that the Fe levels might be overestimated and vacancies might be present, so the levels of Fe and vacancies were used as free parameters. The results can be seen in Fig. 4.20.

From the figure one can see that for a relative low A ratio value (matching our values) and a high Fe content the magnetic scattering length density of the precipitates is considerably high. Even when increasing the vacancy content, while lowering the Fe content, the magnetic scattering length density remains over zero indicating that the precipitates must be at least partially magnetic. This investigation was repeated considering a composition of 6.67% carbon and 93.3% iron by weight (carbides) for the larger scattering features. With this composition at hand and considering magnetic Fe in the scattering features we were able to find that for a given A ratio value of about 1.5 the magnetic moment for Fe is around 2.1 emu/μ_{B}, a value close to the that of bulk fcc-Fe indicating that the cementite particles are magnetic.

4.4.3 Cluster Size, Volume Fraction & Number Density

The cluster size of the scattering features seems to be slightly dependent on temperature, more profoundly that of the irradiation induced precipitates. This is not irregular since increased temperature could affect the precipitation rate due to an increasing in diffusion. In general one would expect to find larger precipitates as the temperature increases due to the enhanced solute mobility through the lattice of the steels. Studies reported in literature[34,35] show a similar trend where the precipitates' radii increase with increasing irradiation temperature while their number density decreases. This indicates that temperature and irradiation have a synergistic role in the formation and development of precipitation. Some irregularities observed in how the size of the scatterers change, mainly between samples HA, HD, and HE, is attributed to smearing effects during the SANS measurements; most of SANS measurements are influenced by resolution effects due to the instrument and when the scattering curves are measured with overlapping $\vec{q}$-ranges the smearing effects can be significant. Such effects can produce systematic errors in the results as well as the derived parameters.

Overall, a coarsening process could be evident of Ostwald ripening; the interfacial

energy between a matrix and the particles distributed in that matrix tends to decrease via matter transport from small to large particles. This shifts the size distribution to larger values and decreases the overall number density. This process is also known as the Gibbs−Thomson effect[36]. Since Ostwald ripening is a thermodynamically-driven process[37], it could be enhanced by increased temperature. This result is further explained by the lower nucleation rate of CRPs at higher temperatures where Cu is more soluble in Fe.

4.5 Conclusion

Proton irradiated (50°C – 400°C) and heat treated (300°C and 400°C) high-Cu RPV model steel alloys were investigated by means of SANS. SEM and Vickers microhardness testing were also employed providing complementary microstructural information.

The results indicate the presence of two general groups of scattering features. One is present before and after irradiation with a size ranging between 10 and 40 nm. These features seem to be carbides that were formed during the original process of the steel as part of its manufacturing. This was verified by performing Thermocalc analysis showing that indeed cementite (iron carbides) do precipitate and exist with a volume fraction of about 0.17. The other group of precipitates appears after irradiation at elevated temperatures, indicating irradiation-induced precipitation, with sizes of 1 to 4 nm. Further compositional analysis of the precipitates was performed by considering A ratio values calculated by separating the nuclear and magnetic scattering signals. For interpretation of the results both non-magnetic and magnetic scatterers were considered separately.

Under the non-magnetic assumption, considering the generally low A ratio values, the scattering features should be of high-Mn content with relatively low Cu and Ni. This contradicts APT studies done on similar samples, containing high Ni, stating that induced precipitates should be Cu-Mn-Ni-enriched with Ni and not Mn or Cu dominating. Also the results for non-magnetic scatterers do not allow the presence of Fe-containing

carbides. The assumption of magnetic scatterers though, provides with results that are well in agreement with literature as well as with the formation of cementite.

A common aspect between RPV steel SANS studies is the confinement of the investigation at the highest $\vec{q}$-range possible since this corresponds to known sizes of irradiation induced precipitates. In the current study a larger $\vec{q}$-range was used extending at lower values. This allowed for a full range investigation and detection of microstructural features such as grain boundaries, carbides as well as irradiation induced clusters. This of course was made possible by the combination of the bimodal log-normal distribution model with the Porod law. The use of fitting processes though is not always fully realistic (as it was discussed earlier) and one should have good prior knowledge of both the samples and the investigative technique, so as to be familiar with what to expect. Different analysis and interpretation approaches can also be taken, e.g. the assumption of magnetic scattering features. Techniques such as APT, SEM, and Vicker's microhardness measurements can also prove to be important to provide with complementary information that can be used as a guide.

References

[1] G. R. Odette. On the dominant mechanism of irradiation embrittlement of reactor pressure vessel steels. *Scripta Metallurgica*, 17(10):1183–1188, 1983.

[2] G. R. Odette and G. E. Lucas. Embrittlement of nuclear reactor pressure vessels. *JOM*, 53(7):18, 2001.

[3] E. Meslin, B. Radiguet, and M. Loyer-Prost. Radiation-induced precipitation in a ferritic model alloy: An experimental and theoretical study. *Acta Materialia*, 61(16):6246–6254, 2013.

[4] P. D. Styman. *Atomic scale studies of thermally aged pressure vessel steels*. PhD thesis, University of Oxford, 2013.

[5] B. L. Bramfitt and A. O. Benscoter. *Metallographer's guide: practice and procedures for irons and steels*. ASM International, 2001.

[6] G. S. Was, J. T. Busby, T. Allen, E. A. Kenik, A. Jensson, S. M. Bruemmer, J. Gan, A. D. Edwards, P. M. Scott, and P. L. Andreson. Emulation of neutron irradiation effects with protons: validation of principle. *Journal of Nuclear Materials*, 300(2):198–216, 2002.

[7] K. J. Stephenson and G. S. Was. Comparison of the microstructure, deformation and crack initiation behavior of austenitic stainless steel irradiated in-reactor or with protons. *Journal of Nuclear Materials*, 456:85–98, 2015.

[8] G. S. Was. Challenges to the use of ion irradiation for emulating reactor irradiation. *Journal of Materials Research*, 30(9):1158–1182, 2015.

[9] J. F. Ziegler, M. D. Ziegler, and J. P. Biersack. *SRIM: the stopping and range of ions in matter*. Cadence Design Systems, 2008.

[10] R. E. Stoller, M. B. Toloczko, G. S. Was, A. G. Certain, S. Dwaraknath, and F. A. Garner. On the use of SRIM for computing radiation damage exposure. *Nuclear Instruments and Methods in Physics Research Section B: Beam Interactions with Materials and Atoms*, 310:75–80, 2013.

[11] M. J. Norgett, M. T. Robinson, and I. M. Torrens. Standard practice for neutron radiation damage simulation by charged-particle irradiation. *Annual Book of ASTM Standards*, 1975.

[12] R. S. Averback, R. Benedek, and K. L. Merkle. Ion-irradiation studies of the damage function of copper and silver. *Physical Review B*, 18(8):4156, 1978.

[13] G. Wallner, M. S. Anand, L. R. Greenwood, M. A. Kirk, W. Mansell, and W. Waschkowski. Defect production rates in metals by reactor neutron irradiation at 4.6 K. *Journal of Nuclear Materials*, 152(2-3):146–153, 1988.

[14] J. Kohlbrecher and W. Wagner. The new SANS instrument at the Swiss Spallation Source SINQ. *Journal of Applied Crystallography*, 33(3):804–806, 2000.

[15] C. D. Dewhurst. D33 — a third small-angle neutron scattering instrument at the Institut Laue-Langevin. *Measurement Science and Technology*, 19(3):034007, 2008.

[16] C. Dewhurst. GRASP: graphical reduction and analysis SANS program for Matlab. *Institut Laue-Langevin (2001–2007) http://www.ill.eu/fileadmin/users_files/Other_Sites/lss-grasp/grasp_main. html*, 2007.

[17] S. R. Kline. Reduction and analysis of SANS and USANS data using Igor Pro. *Journal of Applied Crystallography*, 39(6):895–900, 2006.

[18] J. B. Wiskel, D. G. Ivey, and H. Henein. The effects of finish rolling temperature and cooling interrupt conditions on precipitation in microalloyed steels using small angle neutron scattering. *Metallurgical and Materials Transactions B*, 39(1):116–124, 2008.

[19] P. A. Beaven, F. Frisius, R. Kampmann, and R. Wagner. Analysis of defect microstructures in irradiated ferritic alloys. In *Atomic Transport and Defects in Metals by Neutron Scattering*, pages 228–233. Springer, 1986.

[20] F. Bergner, A. Ulbricht, P. Lindner, U. Keiderling, and L. Malerba. Post-irradiation annealing behavior of neutron-irradiated FeCu, FeMnNi and FeMnNiCu model alloys investigated by means of small-angle neutron scattering. *Journal of Nuclear Materials*, 454(1):22–27, 2014.

[21] F. Bergner, M. Lambrecht, A. Ulbricht, and A. Almazouzi. Comparative small-angle neutron scattering study of neutron-irradiated Fe, Fe-based alloys and a pressure vessel steel. *Journal of Nuclear Materials*, 399(2):129–136, 2010.

[22] F. Bergner, A. Ulbricht, A. Gokhman, and D. Erak. Nature of defect clusters in neutron-irradiated iron-based alloys deduced from small-angle neutron scattering. *Journal of Nuclear Materials*, 373(1):199–205, 2008.

[23] J. Zelenty, G. D. W. Smith, K. Wilford, J. M. Hyde, and M. P. Moody. Secondary precipitation within the cementite phase of reactor pressure vessel steels. *Scripta Materialia*, 115:118–122, 2016.

[24] J.-O. Andersson, T. Helander, L. Höglund, P. Shi, and B. Sundman. Thermo-calc & DICTRA, computational tools for materials science. *Calphad*, 26(2):273–312, 2002.

[25] J. M. Hyde, M. G. Burke, G. D. W. Smith, P. Styman, H. Swan, and K. Wilford. Uncertainties and assumptions associated with APT and SANS characterisation of irradiation damage in RPV steels. *Journal of Nuclear Materials*, 449(1):308–314, 2014.

[26] P. Asoka-Kumar, B. D. Wirth, P. A. Sterne, R. H. Howell, and G. R. Odette. Composition and magnetic character of nanometre-size Cu precipitates in reactor pressure vessel steels: implications for nuclear power plant lifetime extension. *Philosophical Magazine Letters*, 82(11):609–615, 2002.

[27] F. Bergner, C. Pareige, V. Kuksenko, L. Malerba, P. Pareige, A. Ulbricht, and A. Wagner. Critical assessment of Cr-rich precipitates in neutron-irradiated Fe–12 at% Cr: Comparison of SANS and APT. *Journal of Nuclear Materials*, 442(1):463–469, 2013.

[28] A. Morley, G. Sha, S. Hirosawa, A. Cerezo, and G. D. W. Smith. Determining the composition of small features in atom probe: BCC Cu-rich precipitates in an Fe-rich matrix. *Ultramicroscopy*, 109(5):535–540, 2009.

[29] Y. Nagai, Z. Tang, M. Hassegawa, T. Kanai, and M. Saneyasu. Irradiation-induced Cu aggregations in Fe: An origin of embrittlement of reactor pressure vessel steels. *Physical Review B*, 63(13):134110, 2001.

[30] Q. Xu, T. Yoshiie, and K. Sato. Dose dependence of Cu precipitate formation in Fe-Cu model alloys irradiated with fission neutrons. *Physical Review B*, 73(13):134115, 2006.

[31] A. T. Al-Motasem, M. Posselt, F. Bergner, and U. Birkenheuer. Structure, energetics and thermodynamics of copper–vacancy clusters in BCC-Fe: An atomistic study. *Journal of Nuclear Materials*, 414(2):161–168, 2011.

[32] R. Ngayam-Happy, C. S. Becquart, C. Domain, and L. Malerba. Formation and evolution of MnNi clusters in neutron irradiated dilute Fe alloys modelled by a first principle-based AKMC method. *Journal of Nuclear Materials*, 426(1):198–207, 2012.

[33] P. Pareige, D. Parfitt, P. Styman, S. Connolly, J. Hyde and K. Wilford. The effect of irradiation temperature on precipitation in RPV steels.

[34] E. D. Eason, G. R. Odette, R. K. Nanstad, and T. Yamamoto. A physically based correlation of irradiation-induced transition temperature shifts for RPV steels. Technical report, Oak Ridge National Laboratory (ORNL), 2007.

[35] R. B. Jones and C. J. Bolton. Neutron radiation embrittlement studies in support of continued operation, and validation by sampling of MAGNOX reactor steel pressure vessels and components. Technical report, Nuclear Regulatory Commission, Washington, DC (United States). Office of Nuclear Regulatory Research; Brookhaven National Lab., Upton, NY (United States), 1997.

[36] A. D. Brailsford and P. Wynblatt. The dependence of Ostwald ripening kinetics on particle volume fraction. *Acta Metallurgica*, 27(3):489–497, 1979.

[37] Z. Zhang, Z. Wang, S. He, C. Wang, M. Jin, and Y. Yin. REDOX reaction induced Ostwald ripening for size-and shape-focusing of palladium nanocrystals. *Chemical Science*, 6(9):5197–5203, 2015.

CHAPTER 5

INVESTIGATION OF PROTON IRRADIATION EFFECTS ON LOW-COPPER REACTOR PRESSURE VESSEL STEELS

5.1 Introduction

In Chapter 3 materials radiation, radiation damage as well as parameters such as material's composition, that are directly connected with embrittlement were thoroughly discussed. It is understood that precipitation is one of the main causes of embrittlement and more specifically precipitation of Cu-rich clusters is of major concern [1–3]. Precipitation of Cu is a hardening mechanism and can be induced even at low neutron fluences [4]. Despite the fact that Cu is not a solute deliberately added in the steels, it was introduced as an impurity during the welding process. In Chapter 4, the effects of irradiation on high-Cu RPV steels were investigated. The results showed clearly that there were precipitates enriched with Cu, Mn, Ni, Si and possibly Fe/vacancies induced during irradiation.

Modern reactors and RPVs are built with steels containing very low levels of Cu and the levels of impurity traces are well controlled. In such low-Cu steels other types of precipitation seem to play a role in their embrittlement. Mn-Ni-(Si)-rich precipitates (MNPs) are found among precipitation events in steels with Cu not exceeding 0.1 wt. % [5]. It is speculated that they appear in high accumulated fluence [5,6] and for that reason they are also known as late-blooming-phases (LBPs) [7].

In this chapter, SANS, SEM, and Vicker's microhardness measurements on proton-irradiated low-Cu RPV model steels are reported and the effects of the low Cu content, in combination with the proton fluence on the SANS results are discussed. The results provide an insight on the role of fluence on the formation of nanoprecipitates in such low-Cu containing RPV steels. The connection of cementite precipitation with possible increase of hardness is also discussed.

5.2 Experimental Details

5.2.1 Materials & Sample Preparation

The materials investigated and reported in this chapter are low-Cu variants of RPV, about 0.06 wt. % Cu model steel alloys, with varying content of Mn and Ni, a total number of four different steels. They were manufactured by vacuum induction melting. The process followed is the same as for the high-Cu RPV steels presented in Chapter 4; the steel plates were first rolled and then heat treated at 920 °C for 1 h undergoing austenisation followed by an air cool. Next, they were tempered at 600 °C for 5 h followed by a final air cool. The overall chemical composition of the alloys is given in Table 5.1.

Table 5.1: Nominal composition of low-Cu model steel alloys (wt. %). The different steels have been coded as L1, L2, L3, and L4 with L standing for low-Cu.

Steel	C	Mn	P	Si	Ni	Cr	Mo	Cu	Fe
L1	0.21	0.26	0.005	0.21	0.3	0.1	0.49	0.06	98.365
L2	0.27	1.47	0.008	0.22	3.53	0.1	0.48	0.06	93.862
L3	0.22	1.48	0.01	0.23	3.53	0.13	0.53	0.06	93.81
L4	0.22	2.06	0.006	0.19	3.44	0.09	0.52	0.07	93.404

A total number of 19 samples was studied including as received, heat treated, and proton irradiated samples. Proton irradiations were performed using the Scanditronix MC40 cyclotron and the dynamitron accelerator facilities at the University of Birmingham, UK. The facilities offered a good control over irradiation temperature (± 5 °C).

The cyclotron irradiations were performed using a 5.4 MeV proton beam and produced an average damage ranging between about 0.6 and 7 mdpa. The dynamitron irradiations were performed using a 2.8 MeV proton beam and produced an average damage of about 100 mdpa. The lower energy of the proton beam for the dynamitron irradiations was chosen so as to reduce the penetration depth of the proton in the Fe matrix due to the samples being about 100 μm thick. This allowed for the specimens to be irradiated from both sides as the thicker ones. To induce higher damage levels the dynamitron irradiations were performed for longer. Information on the calculations of damage as well as specific irradiation details (fluence, flux, irradiated surface area etc.) for the different samples are provided in the next section.

Table 5.2: Summary of samples' thickness, irradiation conditions and heat treatment (where applicable).

Sample	**Thickness (μm)**	**Damage Level (mdpa)**	**Temperature (°C)**	**Device**	**Energy (MeV)**
L1A	177	No Irradiation/AR	n/a	n/a	n/a
L1B	219	No Irradiation/HT	2.5 h @ 300	n/a	n/a
L1C	221	No Irradiation/HT	2.5 h @ 400	n/a	n/a
L1D	200	6.7	50	Cyclotron	5.4
L1E	190	6.2	300	Cyclotron	5.4
L2A	68	No Irradiation/AR	n/a	n/a	n/a
L2B	280	No Irradiation/HT	2.5 h @ 400	n/a	n/a
L2C	50	7.2	50	Cyclotron	5.4
L2D	40	0.6	400	Cyclotron	5.4
L3A	229	No Irradiation/AR	n/a	n/a	n/a
L3B	200	No Irradiation/HT	2.5 h @ 300	n/a	n/a
L3C	203	No Irradiation/HT	2.5 h @ 400	n/a	n/a
L3D	247	6.7	50	Cyclotron	5.4
L3E	193	6.4	300	Cyclotron	5.4
L3F	118	103	250	Dynamitron	2.8
L4A	187	No Irradiation/AR	n/a	n/a	n/a
L4B	185	No Irradiation/HT	2.5 h @ 300	n/a	n/a
L4C	260	No Irradiation/HT	2.5 h @ 400	n/a	n/a
L4D	120	83	250	Dynamitron	2.8

All the samples were investigated by means of SANS. Complementary SEM and Vicker's microhardness measurements were also performed on steels L1, L2, L3, and L4 as received specimens to receive information on their original microstructure. For the SANS measurements the specimens were polished down to a thickness ranging between about 50 to 300 μm and had a surface area of 10 x 10 mm^2. The samples that were sufficiently

thick, typically over at least 100 μm, were irradiated from both sides to increase total damage. Some of the irradiation details and the exact thickness of each sample are given in Table 5.2 along with the code name for each sample.

5.2.1.1 Damage Calculations

For the calculation of irradiation induced average damage in the samples the software SRIM[8] was used by simulating proton irradiation of a Fe matrix. The choice of Fe was made as it was considered a good approximation to the entire composition of the different samples since they mainly consist of Fe (> 93 wt. %). The experimental irradiation details per sample that were used for the calculations are given in Table 5.3.

Table 5.3: Experimental details of irradiations for the different steel specimens.

Sample	Side	Total Integrated Charge (C)	Irradiated Surface Area (cm^2)	Fluence (10^{17} protons/cm^2)	Flux (10^{11} protons/cm^2·s)	Proton Energy (MeV)
L1A	-	-	-	-	-	-
L1B	-	-	-	-	-	-
L1C	-	-	-	-	-	-
L1D	1	0.051732	1.3273	2.4	4.4	5.4
	2	0.051732	1.3273	2.4	4.4	5.4
L1E	1	0.07	1.96	2.2	5	5.4
	2	0.07	1.96	2.2	4.5	5.4
L2A	-	-	-	-	-	-
L2B	-	-	-	-	-	-
L2C	1	0.12984	1.54	5.3	4.3	5.4
L2D	1	0.0165	1.96	0.5	1	5.4
L3A	-	-	-	-	-	-
L3B	-	-	-	-	-	-
L3C	-	-	-	-	-	-
L3D	1	0.051732	1.3273	2.4	4.4	5.4
	2	0.051732	1.3273	2.4	4.4	5.4
L3E	1	0.072	1.96	2.3	4.3	5.4
	2	0.072	1.96	2.3	4.3	5.4
L3F	1	0.08	0.25	20	-	2.8
	2	0.06954	0.25	17.4	-	2.8
L4A	-	-	-	-	-	-
L4B	-	-	-	-	-	-
L4C	-	-	-	-	-	-
L4D	1	0.07858	0.25	19.6	-	2.8
	2	0.04218	0.25	10.5	-	2.8

For the simulations, following the same process as in Chapter 4, 100,000 protons (H ions) of 5.4 MeV and 2.8 MeV energy, corresponding to cyclotron and dynamitron irradi-

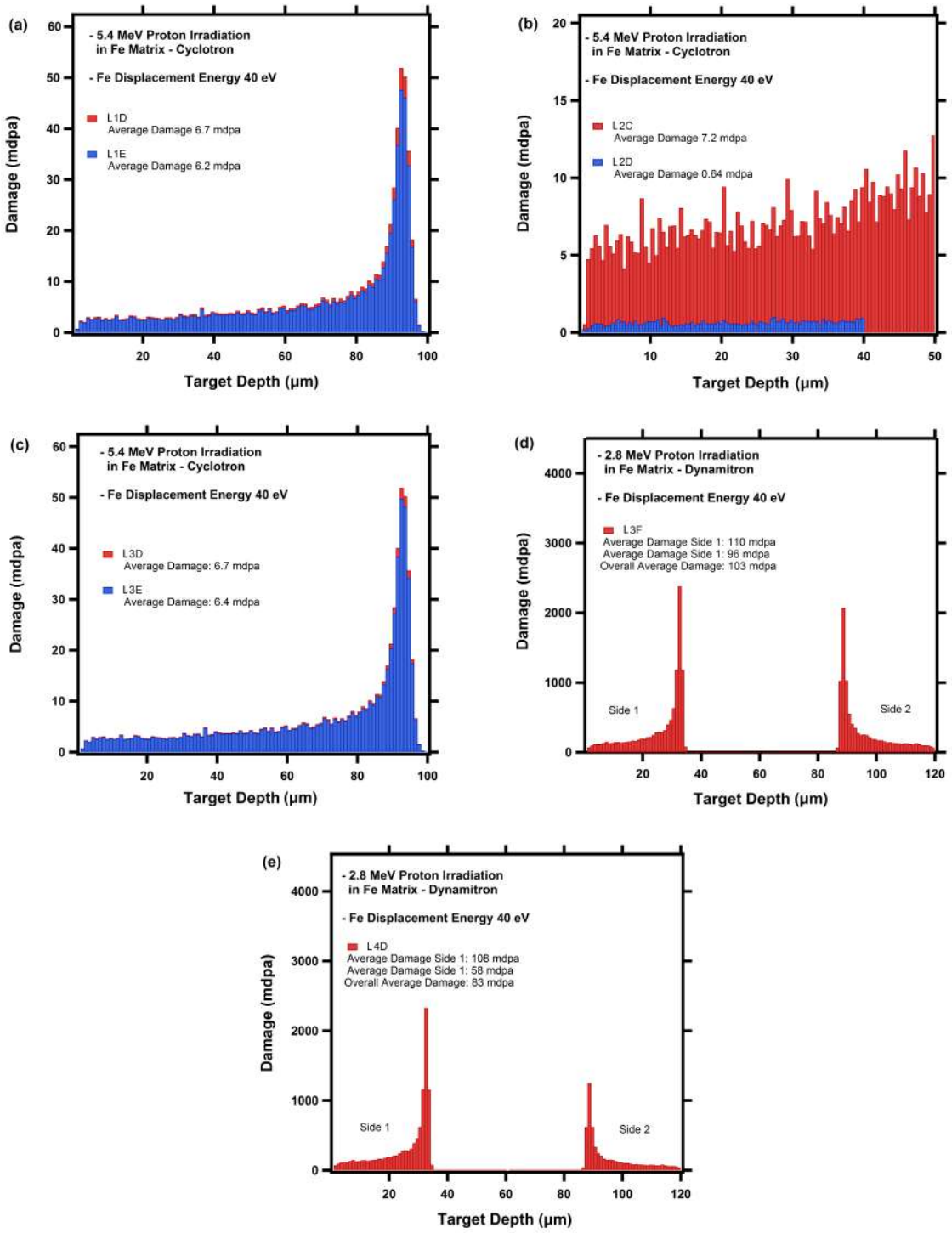

Figure 5.1: Calculated damage profiles for samples (a) L1D, L1E, (b) L1C, L2D, (c) L3D, L3E, (d) L3F, and (e) L4F. The first six samples were irradiated with a proton beam of 5.4 MeV. The last two were irradiated using the dynamitron accelerator with a proton beam of 2.8 MeV and double the fluence producing higher levels of damage. For most of the samples there is a Bragg peak appearing before the protons stop apart for samples L2C and L2D that are very thin and the damage is averaged over the plateau region of the damage profile.

ations respectively, were fired at 100 μm, 50 μm, and 40 μm thick Fe target. The SRIM option "Ion Stopping and Range Tables" was used to calculate the maximum penetration depth of protons in Fe given the energies used. For an energy of 5.4 MeV the maximum penetration depth was found to be 91.35 μm and for an energy of 2.8 MeV it was found to be 31.33 μm. Following the work of R. E. Stoller *et al.*[9] and the ASTM standards (ASTM E521)[10] for "Neutron Radiation Damage Simulation by Charged-Particle Irradiation", the displacement energy for Fe was kept at 40 eV. For the calculations the SRIM option "Ion Distribution and Quick Calculation of Damage" was chosen. To calculate the dpa values the file VACANCY.txt was used providing the number of vacancies produced by both ions and recoils. Summing these up and averaging over the entire penetration depth gave the total number of vacancies per ion. This number was then multiplied with the fluence used for each sample separately and was scaled with the atomic fraction given the corresponding penetration depth for each specimen. The resulting damage profiles are given in Fig. 5.1 where damage is plotted with respect to the target depth. The trajectories of 5.4 MeV protons in 100 μm, 50 μm, and 40 μm thick Fe matrix and of 2.8 MeV protons in 100 μm thick Fe matrix can all be seen in Fig. 5.2. All the calculated damage values are given in Table 5.4.

Table 5.4: Calculated average damage values for each irradiated specimen.

Sample	**Average Damage (mdpa)**
L1D	6.7
L1E	6.2
L2C	7.2
L2D	0.6
L3D	6.7
L3E	6.4
L3F	103
L4D	83

The samples L1D, L1E, L3D, and L3E that were irradiated under similar conditions have taken roughly the same amount of damage, 6.7, 6.2, 6.7, and 6.4 mdpa respectively.

They were irradiated from both sides but only one side was simulated since the irradiation conditions for both sides were exactly the same. The overall damage was calculated by averaging over both sides.

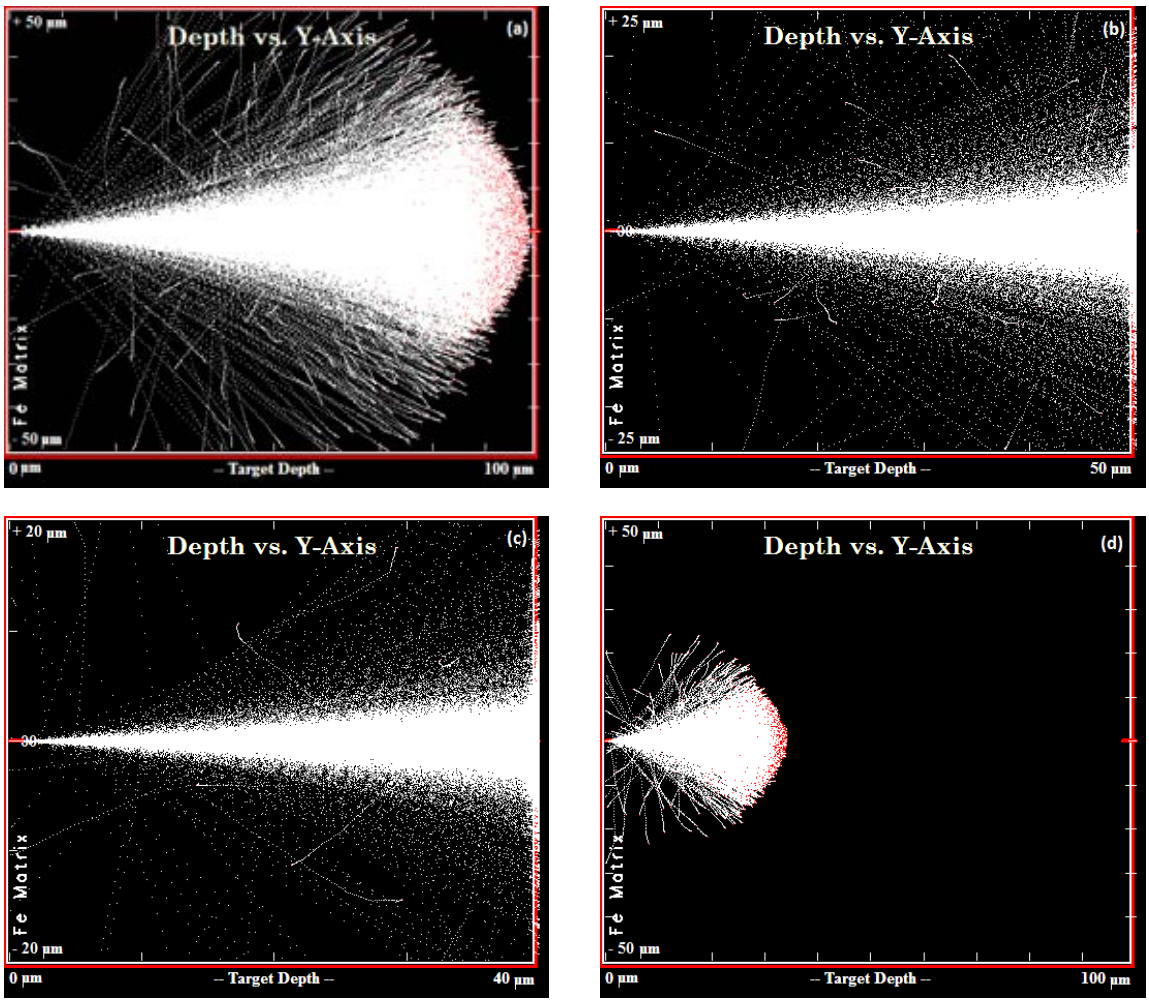

Figure 5.2: Trajectories of (a) 5.4 MeV protons in 100 µm thick Fe matrix, (b) 5.4 MeV protons in 50 µm thick Fe matrix, (c) 5.4 MeV protons in 40 µm thick Fe matrix, and (d) 2.8 MeV protons in 100 µm thick Fe matrix as simulated by SRIM. When the beam energy is sufficiently high and the material is thin the protons travel through the target rather than stopping. The maximum penetration depth seen in (a) and (d) is well in agreement with the calculations made using the "Ion Stopping and Range Tables" of SRIM.

Samples L2C and L2D were irradiated only from one side due to their small thickness. As a result the damage is calculated by averaging over the plateau region of the damage profile, in contrast to the rest of the samples that the Bragg peak, appearing at about 90 µm for 5.4 MeV proton beam energy, is also taken into account. Consequently, to

induce similar damage levels, as for samples L1D, L1E, L3D, and L3E, in sample L2C the irradiation time was almost double (340 mins versus 150 mins) resulting in roughly double the proton fluence. The average damage calculated was 7.2 mdpa. In contrast, the resulting damage of L2D is almost a tenth of that of L2C due to the proton fluence being one order of magnitude smaller. This was due to a larger effective irradiation area. The irradiations performed with the dynamitron produced significantly higher amounts of damage, in the order of about 100 mdpa, due to the high fluences used. For these irradiations the Bragg peak appears at about 30 μm due to the lower proton beam energy (2.8 MeV). In Fig. 5.1(d) and 5.1(e) the damage profiles for samples L3F and L4D appear to have two different Bragg peaks, one for each side of irradiation. This is due to the different fluences used for each side. The overall damage for each sample was calculated by averaging the damage produced over the two sides.

5.2.2 SANS - Configuration, Reduction & Analysis

Small-angle neutron scattering (SANS) measurements were performed at the D33 instrument at HFR-ILL[11], France, and at the CG-2 instrument at HFIR-ORNL, USA. For the experiments sample-to-detector distance (SDD) of 3 to 19 m, with corresponding collimation, was chosen to measure a total scattering vector, $\vec{q}$, ranging from 0.0016 to 0.27 Å^{-1}, where $\vec{q}$ is calculated using $|\vec{q}| = (4\pi/\lambda)\cdot \sin(\theta)$ with θ being half the scattering angle and $\lambda = 4 - 13$ Å the neutron wavelength. Different combinations of collimation, SDD, and wavelength allowed for the aforementioned $\vec{q}$-range to be covered, always depending on each instrument's specifications. For configuration details the reader can refer to Table 5.5.

The counting time per sample varied between 10 min and 4 h depending on the statistics of the data received. This was also dependent on the measured $\vec{q}$-range since typically higher $\vec{q}$-ranges require longer measuring time; the coherent part of the scattering signal drops as $\vec{q}$ increases, resulting in considerably larger errors on the scattering signal. Ad-

ditionally the counting time is dependent on the neutron flux arriving at the instrument. Overall D33 had higher neutron flux than the CG-2 thus the measuring time was significantly shorter.

Table 5.5: Main set-up details of the SANS instruments (CG-2 and D33) used for the measurements.

Instrument	λ **(Å)**	**Collimation (m)**	μ_o**H (T)**
CG-2	4 and 12	3 and 19	1
D33	6 and 13	2.8 and 12.8	1

For the detection of the scattered neutrons two-dimensional area detectors with 128x128 (CG-2 and D33) and 32x128 (D33) pixels were used and correction measurements for electronic noise and background scattering were performed. Saturating magnetic fields $\mu_o\vec{H} = 1$ T were applied perpendicular to the neutron beam to facilitate separation of nuclear and magnetic contribution to the scattering. Circular and square Cd apertures were positioned in front of each sample defining the sample area measured. Raw-data treatment and analysis was performed using the software GRASP[12] and the NCNR analysis pachage[13].

After checking the measured data sets for multiple scattering the differential scattering cross section $d\Sigma/d\Omega$ ($\equiv I(q)$) was derived after scaling of the scattered neutron beam intensity with transmission measurements and correcting for electronic noise and background scattering. In order to separate the magnetic and nuclear contributions a sector averaging, vertically and horizontally, on the 2D scattering image and subtraction of the horizontal from the vertical scattering intensity was performed. Sectors of $\Delta\theta = 35^o$ were chosen due to reduced signal-to-noise ratio.

Following the same analysis method as in Chapter 4, to receive information on the possible composition of the scattering features the A-ratio formula is employed,[14,15]

$$A = \frac{(d\Sigma/d\Omega)_{\perp}}{(d\Sigma/d\Omega)_{\parallel}} = \frac{(d\Sigma/d\Omega)_{mag}}{(d\Sigma/d\Omega)_{nuc}} + 1 = \frac{\Delta\rho^2{}_{nuc} + \Delta\rho^2{}_{mag}}{\Delta\rho^2{}_{nuc}} \tag{5.1}$$

with $\Delta\rho$ given by

$$\Delta\rho = \left(\sum_i x_i^C b_i^C - \sum_i x_i^M b_i^M\right) = \left(\sum_i x_i^C b_i^C - b_{Fe}^M\right) \tag{5.2}$$

where b_i is the nuclear or magnetic scattering length of element i, x_i is the fraction of element i, and C and M refer to cluster and matrix respectively.

5.2.3 Vicker's Microhardness & SEM Imaging

Vicker's microhardness measurements were performed using the Mitutoyo MVK-H1 Hardness Testing Machine at the School of Metallurgy and Materials of the University of Birmingham, UK, on all as received samples. Due to radiation protection policies of the University of Birmingham it was not possible to measure irradiated samples, thus the microhardness tests were restricted to as received specimens alone.

Prior to any measurements the samples were mechanically ground and polished. For the grinding process abrasive SiC grit paper disks with grades 400, 600, and 1200 were used progressing from coarse to fine grit. The grade numbers correspond to the number of grains of SiC per square inch, with increasing number indicating finer grinding. For the polishing procedure soft cloth disks containing diamond particles were used. Disks of 9, 6, 3, and 1 micron were employed progressively. Diamond suspension was simultaneously used for reducing excess friction. The polishing process was performed with repeating steps when necessary resulting in the samples having scratch-free mirror-like surface. The intermediate and final results were examined by means of optical microscopy.

The microhardness measurements were performed with the samples mounted on aluminium stubs ensuring that their surface was flat throughout the measurements for uniformity. Originally the edges of each sample were identified and a focus measurement was performed. Next, 9 - 13 equidistant indentations were performed forming a square

matrix. The bulk hardness value for each specimen was received by averaging over the values of the individual indentations.

SEM measurements were performed on samples L1A, L3A, and L4A. For the preparation of samples the grinding and polishing procedures were again followed. Then, surface etching was performed so as to expose microstructural features, such as grain boundaries, and to chemically enhance contrast between different structural phases of the materials. For the etching process 2% Nital was used as etchant. The samples were dipped in the etchant for a few seconds; sufficient time so as for the specimens not to be under- or over-etched. The final results were examined by means of optical microscopy after the samples were cleaned with acetone. Next, the specimens were mounted on aluminium stubs using conductive adhesive carbon disks. The SEM measurements were performed using the Hitachi S-4000 SEM facility of the School of Metallurgy and Materials of the University of Birmingham, UK. The SEM acceleration voltage used was 15 kV.

5.3 Results

5.3.1 SANS

The resulting nuclear and magnetic differential scattering cross sections for all samples are plotted as a function of the total scattering vector, $\vec{q}$, and are given in Fig. 5.3, 5.4, 5.5, and 5.6. An offset has been applied to all curves for the sake of clearness. The plots contain an inset showing the scattering curves at their original position (no offset applied) overlapping. The original errors on the scattering data were produced using Poisson statistics and subsequent errors were calculated by error propagation. First observations indicate that the scattering signal has a $\vec{q}^{\,-4}$ (Porod law) dependence contributing to the overall scattering signal of the specimens. This contribution is possibly originating from grain boundaries. Removing the Porod law from the scattering signal can facilitate the investigation of any scattering features present within the samples. For this

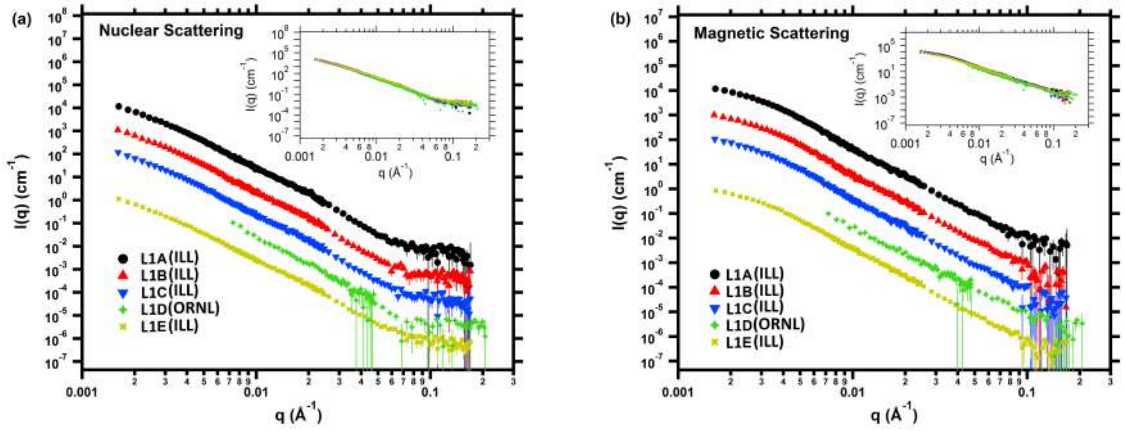

Figure 5.3: (a) Nuclear and (b) magnetic differential scattering cross section as a function of scattering vector, $\vec{q}$, for steel L1. An equidistant offset has been applied to the datasets for the sake of clearness. The insets show the scattering curves at their original positions. Sample L1D was measured at a $\vec{q}$ values limited at high range due to shortage of experimental time.

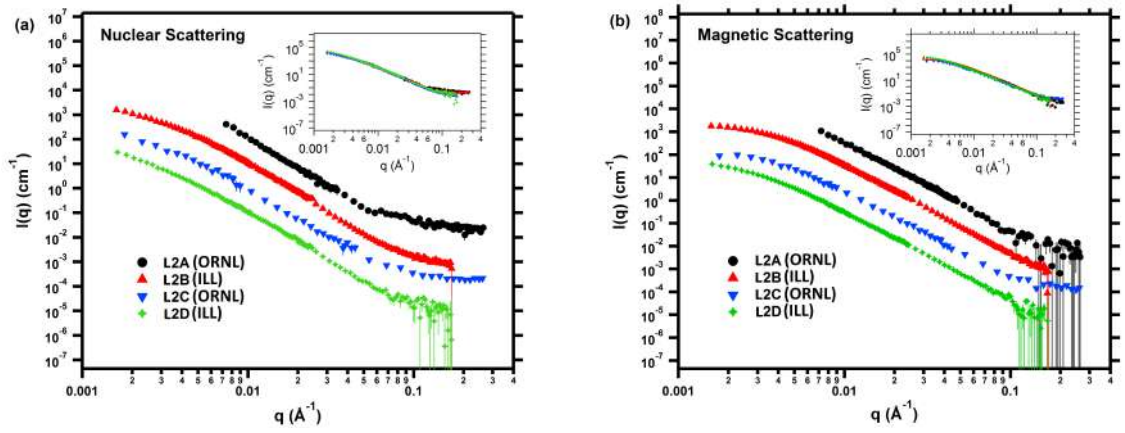

Figure 5.4: (a) Nuclear and (b) magnetic differential scattering cross section as a function of scattering vector, $\vec{q}$, for steel L2. An equidistant offset has been applied to the datasets for the sake of clearness. The insets show the scattering curves at their original positions. Sample L2A was measured at a $\vec{q}$ values limited at high range due to shortage of experimental time.

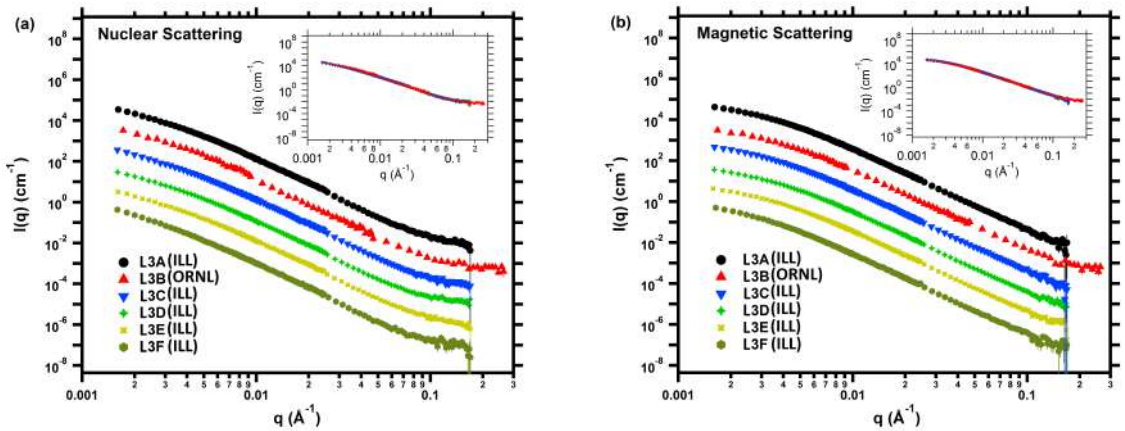

Figure 5.5: (a) Nuclear and (b) magnetic differential scattering cross section as a function of scattering vector, $\vec{q}$, for steel L3. An equidistant offset has been applied to the data-sets for the sake of clearness. The insets show the scattering curves at their original positions.

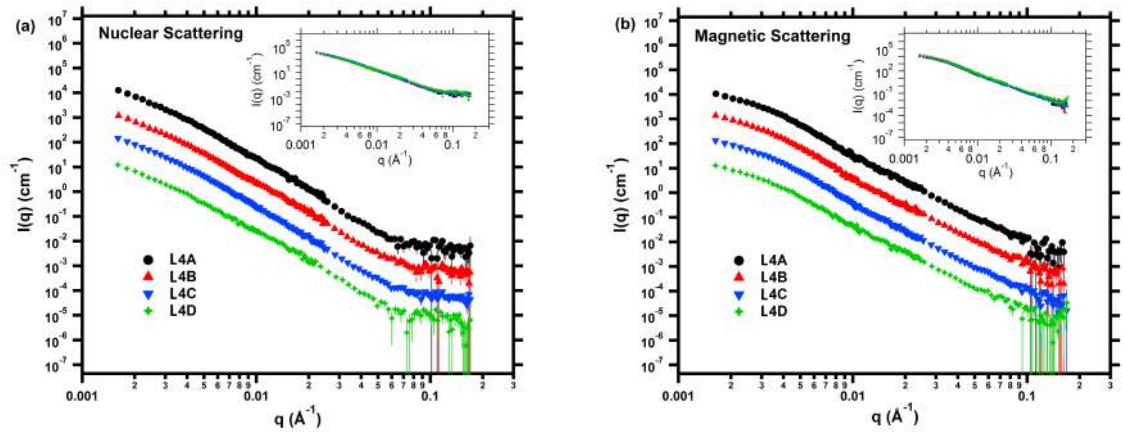

Figure 5.6: (a) Nuclear and (b) magnetic differential scattering cross section as a function of scattering vector, $\vec{q}$, for steel L4. An equidistant offset has been applied to the data-sets for the sake of clearness. The insets show the scattering curves at their original positions.

purpose a power law model was fitted on the scattering data, both nuclear and magnetic. After its removal the resulting scattering curves showed little to no change, that being mainly at the lowest $\vec{q}$ region, indicating that any grain boundary contribution to the total scattering signal is small. As such the removal of the Porod law was deemed unnecessary. An example of scattering curves before and after the removal of the Porod contribution is provided in Fig. 5.7.

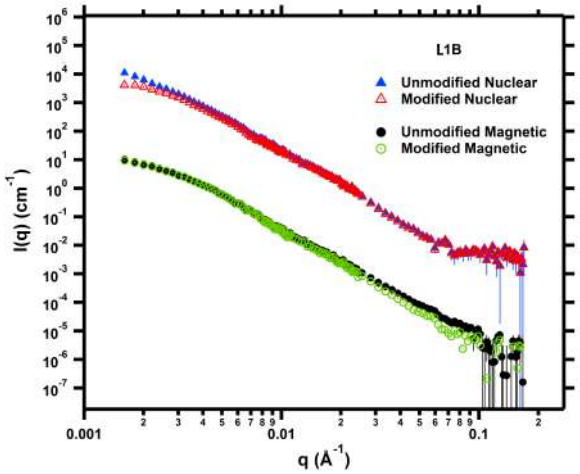

Figure 5.7: Nuclear and magnetic scattering curves of sample L1B before (unmodified) and after (modified) the removal of the Porod law contribution. It is illustrated that removal of the Porod law only slightly affects the shape of the scattering curves. Its removal was deemed unnecessary for the analysis and it was kept as an extra term to the fitting model to account for the minor effects.

Further observations indicate that the overlapping scattering curves show no deviation from each other indicating that there are no irradiation induced features in any of the samples. To verify this quantitatively though, fitting processes are necessary. Overall, for the fitting procedures a unimodal or bimodal log-normal distribution model for spherical features along with a Porod law model was employed by making the assumption that for each sample the nuclear and magnetic contributions are the same, and thus the radius of the precipitates was fixed to the same value. For some curves a Porod law model alone was used as the log-normal distribution failed to fit due to limited $\vec{q}$-range. The resulting fitting curves are plotted along with the corresponding scattering curves and are given in Fig. 5.8, 5.9, 5.10, and 5.11.

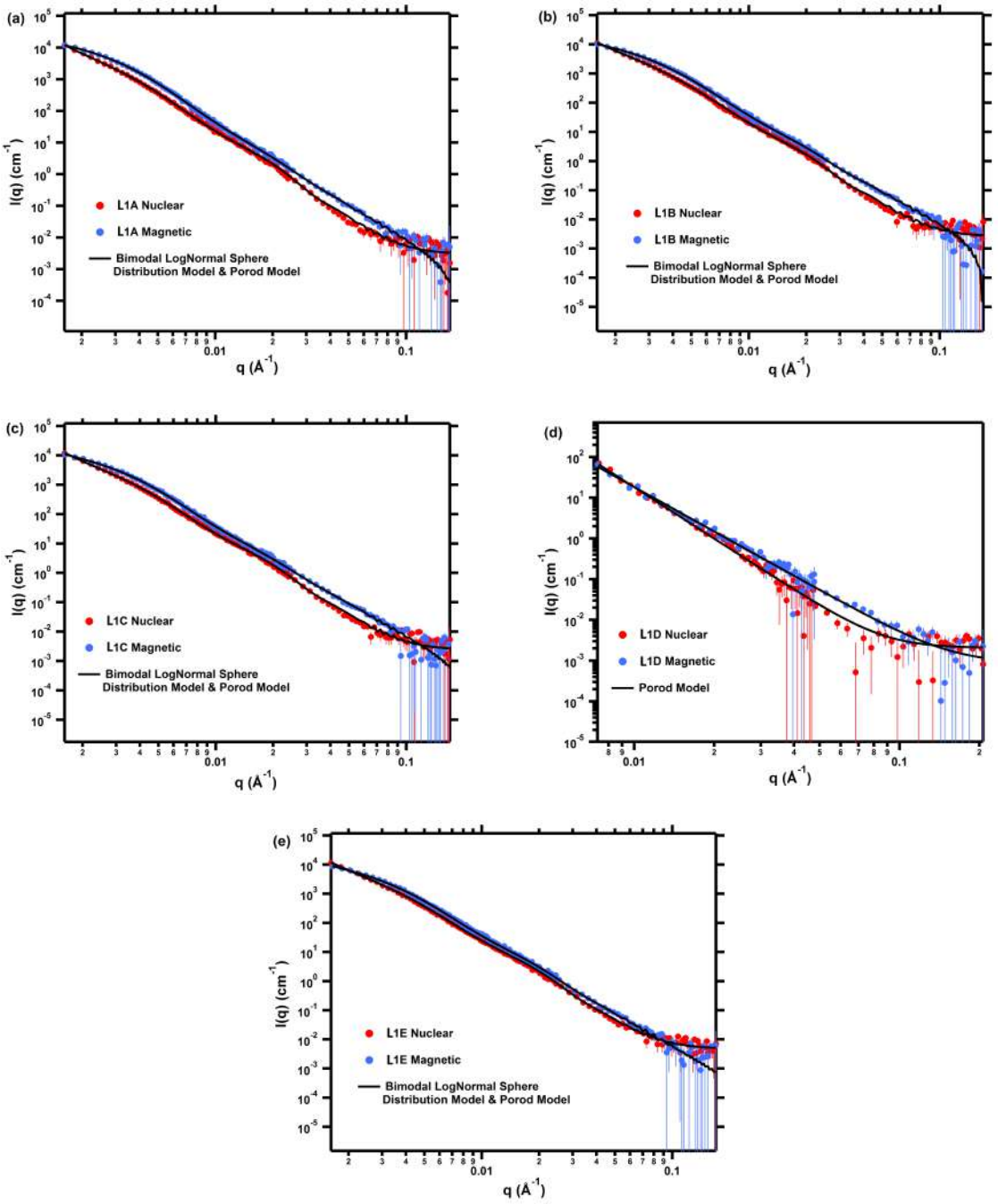

Figure 5.8: Nuclear (red) and magnetic (blue) scattering curves of samples (a) L1A, (b) L1B, (c) L1C, (d) L1D, and (e) L1E. A function consisting of a bimodal lognormal sphere distribution summed with a Porod model (seen as a black solid line) has been fitted to each of the curves. A Porod model alone is used to fit the scattering curves of L1D due to the limited $\vec{q}$-range, where a lognormal distribution fails to fit.

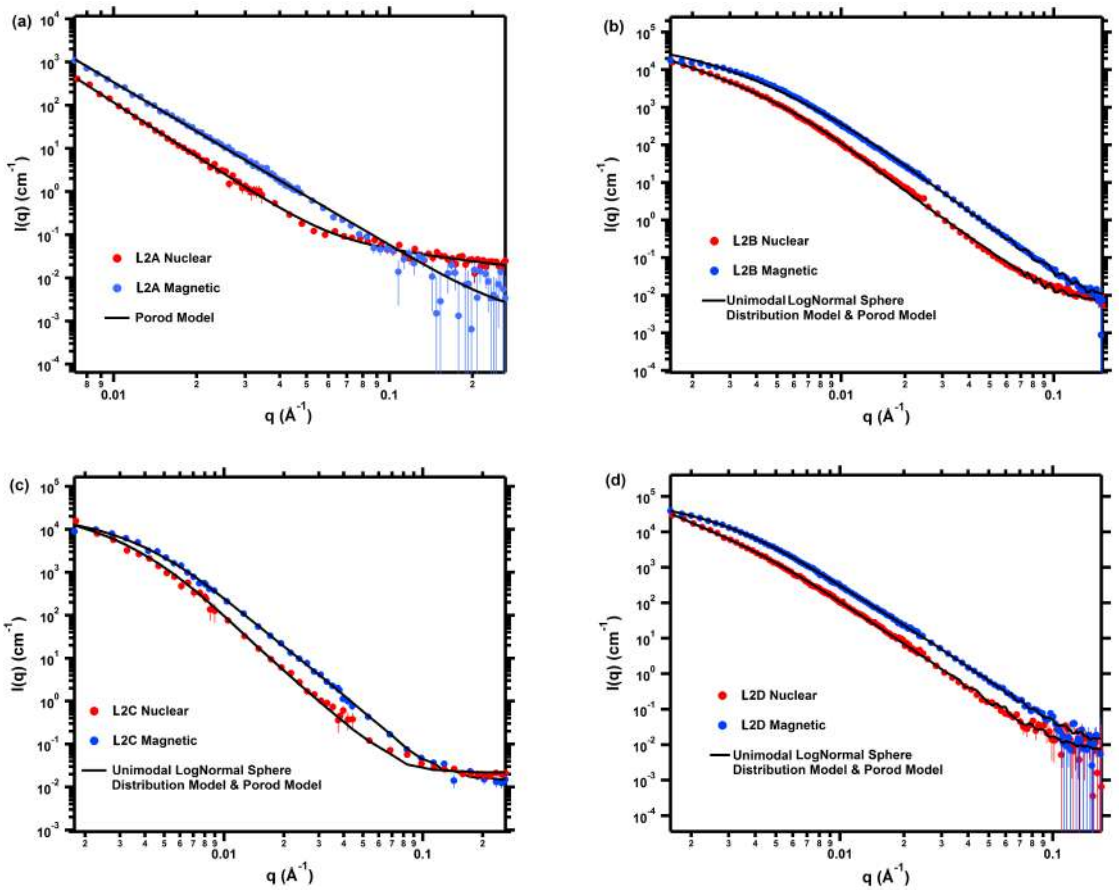

Figure 5.9: Nuclear (red) and magnetic (blue) scattering curves of samples (a) L2A, (b) L2B, (c) L2C, and (d) L1D. A function consisting of a unimodal or bimodal lognormal sphere distribution summed with a Porod model (seen as a black solid line) has been fitted to each of the curves. A Porod model alone is used to fit the scattering curves of L2A due to the limited $\vec{q}$-range, where a log-normal distribution fails to fit.

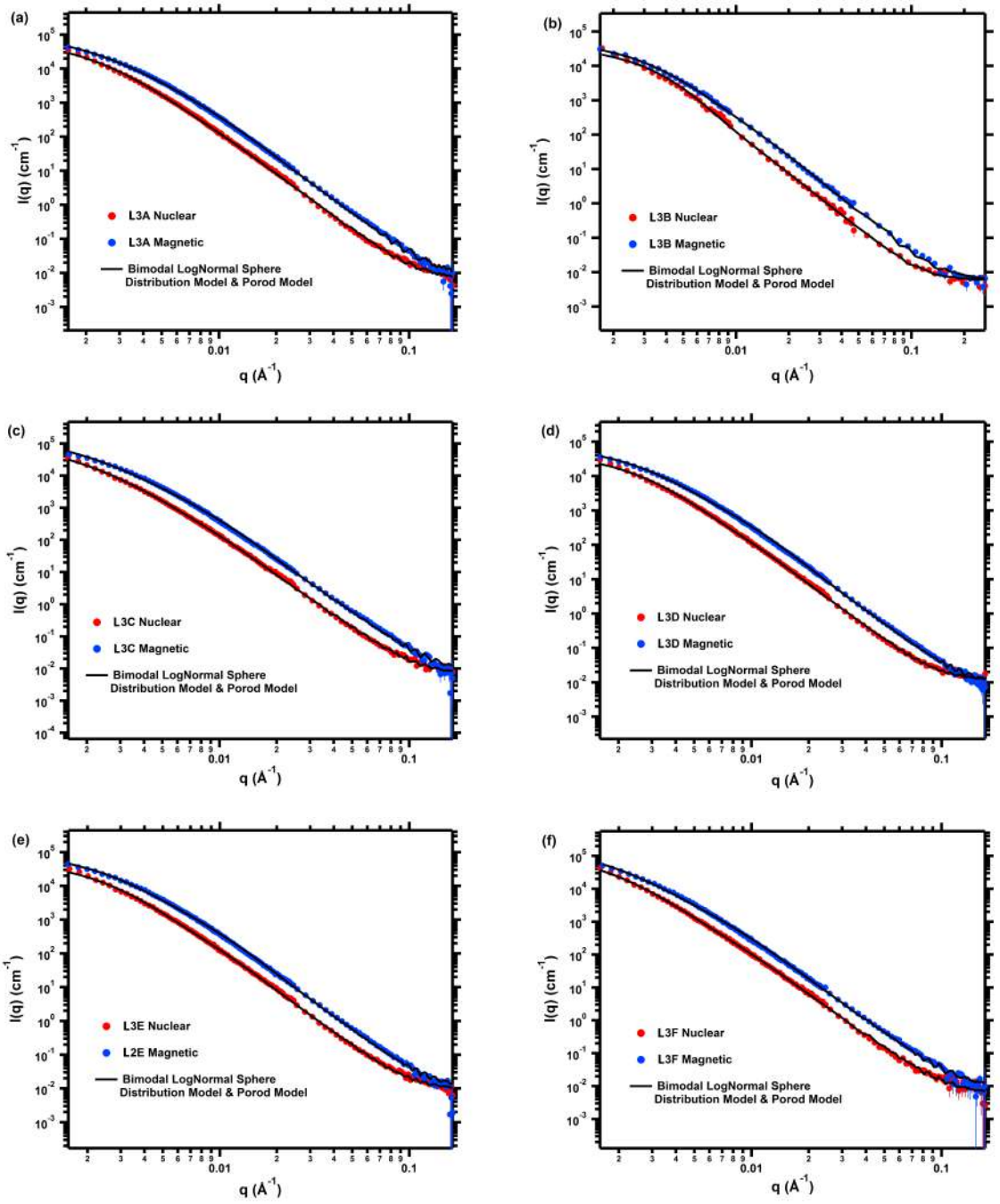

Figure 5.10: Nuclear (red) and magnetic (blue) scattering curves of samples (a) L3A, (b) L3B, (c) L3C, (d) L3D, (e) L3E, and (f) L3F. A function consisting of a bimodal log-normal sphere distribution summed with a Porod model (seen as a black solid line) has been fitted to each of the curves.

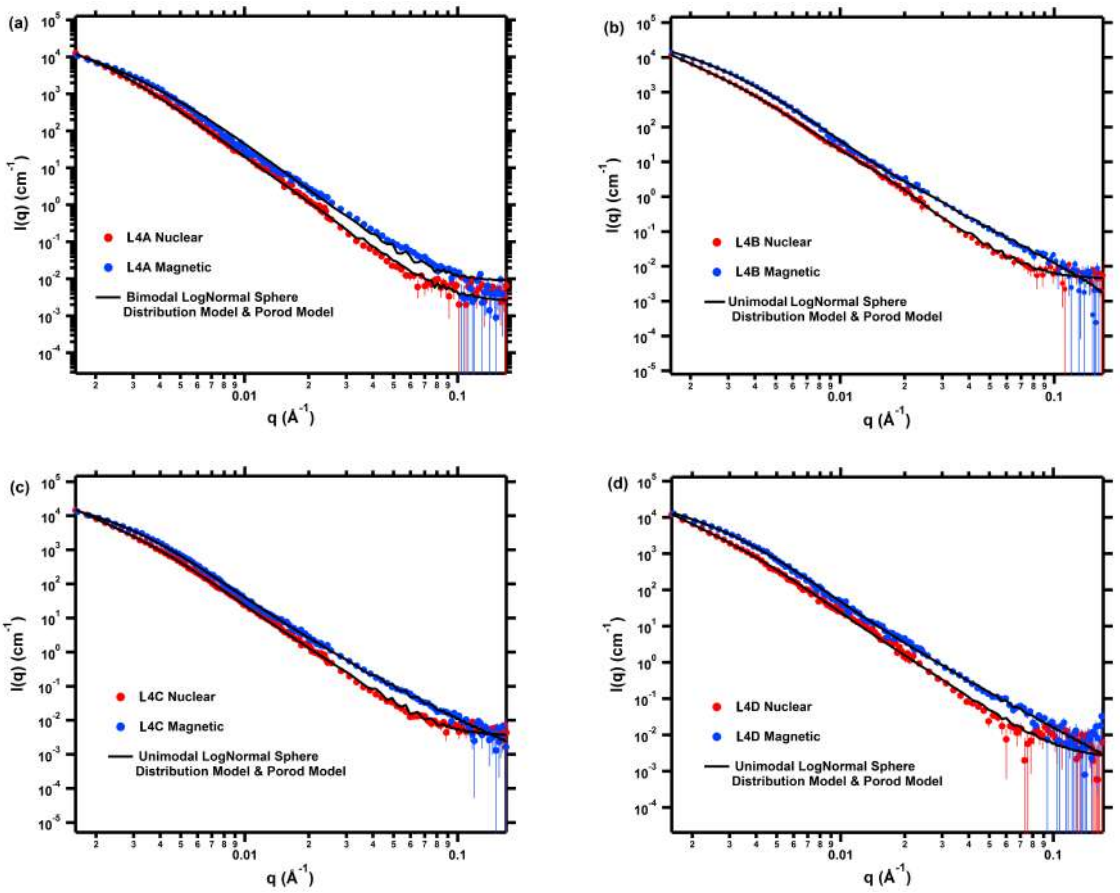

Figure 5.11: Nuclear (red) and magnetic (blue) scattering curves of samples (a) L4A, (b) L4B, (c) L4C, and (d) L4D. A function consisting of a bimodal log-normal sphere distribution summed with a Porod model (seen as a black solid line) has been fitted to each of the curves.

The fitting results indicate that there are no scattering features at the higher $\vec{q}$-range (0.02 - 0.2 Å^{-1}). In real space this would give a radius range between 5 and 0.5 nm. Such sizes would be in well agreement with literature reported irradiation induced or enhanced precipitates being within the first order of the nanometer scale. Following these results along with the fact that the scattering curves of non-irradiated and irradiated specimens overlap throughout the entire $\vec{q}$-range, we reach the conclusion that irradiation had no effects on these samples (always considering the specific irradiation conditions) and irradiation induced precipitation has not occurred. In the lower and middle $\vec{q}$-range (0.0016 – 0.02 Å^{-1}) one or two scattering events were detected, always depending on the overall $\vec{q}$-range available per sample. These scattering features, being in the overall range between about 10 and 50 nm in radius, are present in both irradiated and non-irradiated samples (when the $\vec{q}$-range is sufficient for them to be detected) and seem to have matching size ranges between specimens. This is indicative of microstructural features being present prior to irradiation. Good candidates are cementite particles, Fe_3C, that typically form after the austenisation process during cooling, part of the initial treatment of the steels. Similar features were detected within the high-Cu RPV specimens reported in Chapter 4.

Using the fitting results of the log-normal sphere models we were able to obtain quantitative information of the scattering features, such as precipitation mean radius, R_{mean}, volume fraction, V_f, and number density, N_o. Since the exact cluster composition as well as their magnetic properties are not exactly known, relative instead of absolute V_f and N_o are calculated, as was done in Chapter 4. Experimental values of the A ratio were also calculated so as to have an insight on the precipitates' possible composition. Apart from the radius of precipitates, the scattering contrast was also fixed to an arbitrary number, equal to 4×10^{-12}. As a result the A ratio was calculated by only considering differences in number density and consequently volume fraction. A ratio values between 1.2 and about 3 were calculated. All the calculated quantities and results are given in Tables 5.6 and 5.7. The fitting processes and the resulting quantities are considered valid enough for relative comparisons between specimens. The reader is also referred to Chapter 4 in

Table 5.6: Characteristics of precipitates calculated from unimodal or bimodal log-normal distribution for steels S1 and S2.

Sample	**R_{mean} (Å)**	σ	**Rel. V_f (%)**	**Rel. N_o ($\times 10^{20}$ m^{-3})**	**A Ratio**
L1A	373.6 ± 2.3	0.45 ± 0.01	0.010 ± 0.001	0.25 ± 0.04	1.90 ± 0.01
	121.4 ± 1.9	0.19 ± 0.01	0.0038 ± 0.0001	4.6 ± 0.7	1.23 ± 0.01
L1B	361.7 ± 2.5	0.46 ± 0.01	0.014 ± 0.001	0.38 ± 0.05	1.70 ± 0.01
	126.4 ± 2.0	0.15 ± 0.01	0.0029 ± 0.0001	3.2 ± 0.6	1.34 ± 0.02
L1C	383.9 ± 2.8	0.42 ± 0.01	0.014 ± 0.001	0.35 ± 0.05	1.74 ± 0.01
	123.9 ± 2.0	0.19 ± 0.01	0.0031 ± 0.0001	3.5 ± 0.6	1.20 ± 0.01
L1D	-	-	-	-	-
L1E	358.3 ± 2.3	0.45 ± 0.01	0.016 ± 0.001	0.45 ± 0.08	1.70 ± 0.01
	119.6 ± 1.9	0.22 ± 0.01	0.004 ± 0.001	5.0 ± 0.7	1.45 ± 0.01
L2A	-	-	-	-	-
L2B	160.7 ± 2.4	0.56 ± 0.03	0.04 ± 0.01	8.9 ± 0.4	2.18 ± 0.02
L2C	140.5 ± 2.2	0.60 ± 0.03	0.03 ± 0.01	9.1 ± 0.4	2.25 ± 0.02
L2D	165.2 ± 2.3	0.63 ± 0.03	0.05 ± 0.01	8.4 ± 0.4	2.15 ± 0.02

Table 5.7: Characteristics of precipitates calculated from unimodal or bimodal log-normal distribution for steels S3 and S4.

Sample	**R_{mean} (Å)**	σ	**Rel. V_f (%)**	**Rel. N_o ($\times 10^{20}$ m^{-3})**	**A Ratio**
L3A	417.9 ± 3.0	0.47 ± 0.01	0.068 ± 0.002	1.2 ± 0.1	1.40 ± 0.01
	123.5 ± 1.9	0.62 ± 0.03	0.049 ± 0.002	19 ± 2	2.57 ± 0.21
L3B	373.5 ± 2.5	0.40 ± 0.01	0.07 ± 0.01	2.06 ± 0.2	1.30 ± 0.01
	79.8 ± 1.5	0.73 ± 0.04	0.038 ± 0.001	37 ± 6	2.78 ± 0.21
L3C	367.7 ± 2.3	0.54 ± 0.02	0.08 ± 0.01	1.6 ± 0.1	1.59 ± 0.02
	138.3 ± 2.1	0.55 ± 0.02	0.039 ± 0.001	14 ± 1	2.52 ± 0.19
L3D	434.4 ± 2.8	0.43 ± 0.02	0.057 ± 0.001	0.96 ± 0.02	1.55 ± 0.02
	131.9 ± 2.0	0.54 ± 0.02	0.037 ± 0.001	16 ± 1	2.49 ± 0.19
L3E	449.0 ± 2.8	0.43 ± 0.02	0.061 ± 0.001	0.93 ± 0.02	1.59 ± 0.02
	134.8 ± 2.1	0.54 ± 0.02	0.041 ± 0.001	17 ± 1	2.44 ± 0.18
L3F	504.9 ± 2.9	0.48 ± 0.02	0.063 ± 0.001	0.6 ± 0.1	1.51 ± 0.02
	140.0 ± 2.5	0.59 ± 0.02	0.039 ± 0.001	12 ± 1	2.46 ± 0.19
L4A	487.3 ± 2.8	0.53 ± 0.02	0.017 ± 0.001	0.15 ± 0.02	1.20 ± 0.02
	180.4 ± 2.7	0.65 ± 0.03	0.013 ± 0.001	1.4 ± 0.2	2.80 ± 0.21
L4B	328.1 ± 2.1	0.54 ± 0.02	0.016 ± 0.001	0.44 ± 0.03	1.76 ± 0.03
L4C	324.5 ± 2.0	0.54 ± 0.02	0.018 ± 0.001	0.51 ± 0.02	1.65 ± 0.02
L4D	302.1 ± 2.0	0.54 ± 0.02	0.016 ± 0.001	0.58 ± 0.02	1.98 ± 0.03

which a detailed evaluation of the fits and their results was performed; it was found that precipitation of cementite indeed takes place after the austenisation process, when the system cools down, below 650 °C. After repeating the fitting processes using the Thermocalc results (i.e. cementite exact composition and volume fraction) it was seen that the resulting mean radii were well in agreement with the original fits and indeed the volume fractions were almost the same. Since the exact same processes were followed for the low-Cu specimens presented in this chapter, one can consider the results valid. Overall the volume fraction of cementite found by Thermocacl is overall close to the volume fractions mainly of the larger precipitates ($R > 300$ Å) as given by the fits. The fact that there are also smaller scattering features ($R < 200$ Å) having different number density and volume fractions could be evidence of an extra phase (e.g. G-phase, or different carbides). One needs to keep in mind that small discrepancies between radii of different samples could also be due to smearing effects of the overlapping scattering vector regions. Irradiation induced precipitates were not detected in none of the specimens.

5.3.2 SEM & Hardness

The SEM images taken for the as received samples of steels L1, L3, and L4 are provided in Fig. 5.12 and 5.13. The measured microhardness values for samples L1A, L2A, L3A, and L4A are 168.4 ±6.3 HV, 263.4 ± 3.1 HV, 332.1 ±8.1 HV, and 255.1 ±5.0 HV respectively.

The microstructure of steel L1 seems to be a mixture of ferritic and pearlitic phases. The pearlite can be seen as lamellar structure with alternating layers of ferrite and cementite (seen as white layers). The images indicate that the dominant phase is ferrite. The measured hardness value of 168.35 HV is also indicative of the ferrite-pearlite mix; ferrite is relatively soft with a hardness of about 95 HV while pearlite is harder than ferrite with a value of about 270 HV. A mixture of them results in the measured hardness value. Similar structure can also be seen for steel L4. From the SEM images the fer-

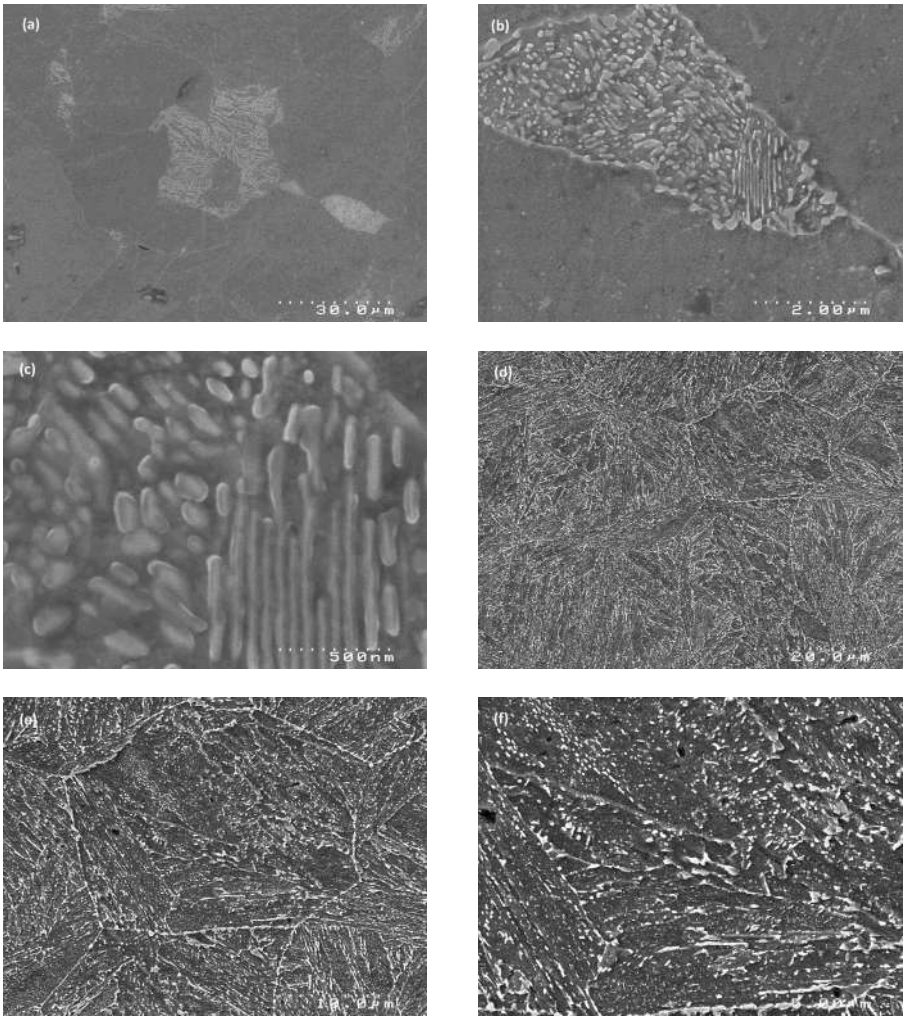

Figure 5.12: SEM images taken for samples (a)(b)(c) L1A and (d)(e)(f) L3A. White spheroidal features are seen on the surface of both specimens. The general microstructure of the two steels is different with sample L1A seemingly being a mixture of ferrite and pearlite seen as lamellar structure in (a), (b), and (c). Sample L3A has a bainitic structure with cementite precipitates distributed throughout.

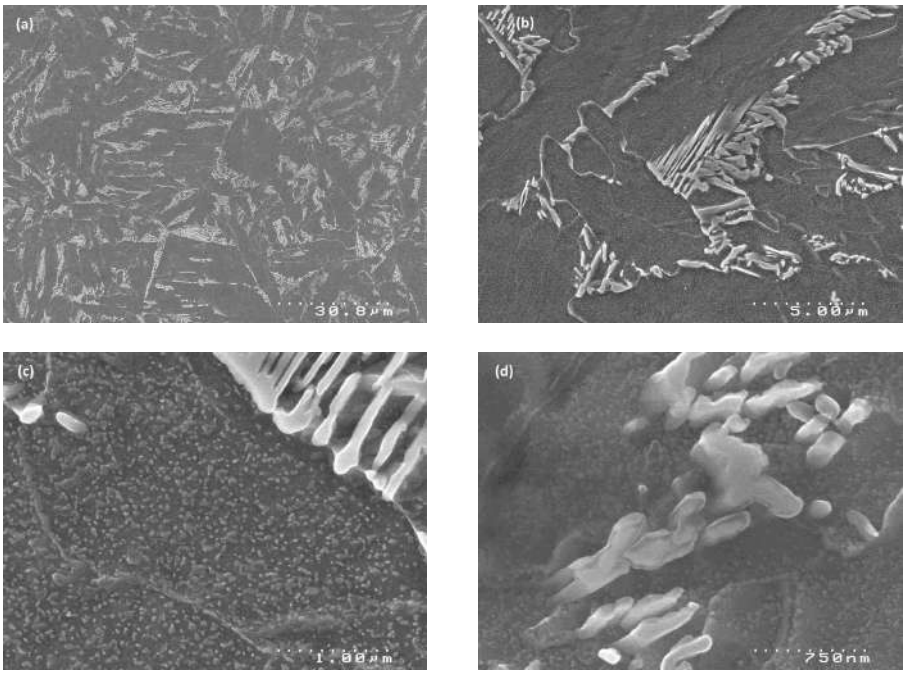

Figure 5.13: SEM images taken for sample L4A. The general microstructure of the sample is seemingly a mixture of ferrite and pearlite seen as lamellar structure with the two phases having roughly a 50:50 ratio. In the ferritic phase cementite particles are distributed throughout.

rite/pearlite ratio seems different than in L1 but in order to evaluate precisely the ratio of ferrite to pearlite in these two steels, SEM images from an extended area of the specimens are required. The hardness value of 255 HV though indicates that pearlite dominates in L4. The thickness of the cementite layers within both samples (L1 and L4), within the pearlitic constituent, was estimated to be roughly between 70 and 100 nm. For both steels spherical particles can be seen residing within the ferritic phase (more profoundly within steel L4). These spherical features are probably residuals from the etching process and not carbide precipitation.

In contrast to steels L1 and L4, steel L3 has a clear bainitic structure with cementite particles uniformly distributed throughout the surface of the sample. The contribution of cementite to the average hardness is made clear due to the increased value (compared to the other samples) of 332.13 HV. The size of the cementite precipitates was estimated to

be roughly between 30 and 200 nm. For measuring the sizes of the different features seen in the SEM images the open software ImageJ was used.

5.4 Discussion

By assessing the results two main points can be drawn. First, no features were induced due to irradiation, at any irradiation temperature or any damage level. Second, the scattering features detected by the SANS measurements are possibly cementite particles that precipitated during the initial processing of the steels.

Regarding the former, it could be mainly due to the following reasons, or a synergy between them:

- low Cu level,
- low accumulated fluence.

It is well known that in high-Cu RPV steels[16,17] as well as in high-Cu model binary, ternary, or quaternary alloys[18,19] irradiation induces precipitation of Cu-rich nanoclusters (1 to 8 nm in diameter) mainly due to supersaturation of Cu in the Fe matrix[20,21]. Cu then acts as nucleation point and elements such as Mn, Ni, and/or Si precipitate forming a shell around Cu clusters (core-shell formation)[22]. Cu-rich precipitates can form even at relatively low doses[22]. This was clear for the high-Cu samples investigated in Chapter 4 where differences between non-irradiated and irradiated samples, mainly at higher irradiation temperatures, indicate the formation of features after irradiation.

In contrast, the low-Cu RPV model alloys reported in this chapter showed no features that could be irradiation induced. This was made clear by the fact that there is no apparent difference between the scattering curves of non-irradiated and irradiated specimens at any irradiation temperature and no increase of scattering intensity at higher q values was observed. This was also supported by the fitting processes. The irradiation conditions of most of the high- and low-Cu specimens were similar and the resulting average damage

was almost the same so at first, the low level of Cu (about 0.06 wt. %) seems to be a key point. Precipitates containing other elements rather than Cu have been reported in low-Cu containing steels though. Indeed Cu is not a major concern in low-Cu RPV steels and instead Mn-Ni-(Si) precipitates (MNPs) seem to play a key role in irradiation induced damage and embrittlement[5,6]. The majority of reported literature on irradiation of low-Cu RPV steels and model alloys shows the formation of MNPs as well as their connection with increase in hardness[23]. Such clusters are also known as late blooming phases[7] due to their late appearance at fluences similar to those accumulated close to the design end-of-life of nuclear reactors[24,25]. It is made clear then that even if the low level of Cu could be the reason why irradiation induced precipitates have not appeared, this alone is not enough to explain why they have not. Other parameters, such as total accumulated fluence, should also be taken into account.

M. K. Miller *et al.*[26] in 2006 published studies performed on low-Cu (0.05 wt. %), high-Ni (1.26 wt. %) RPV steel forgings of a VVER-1000 reactor, measured by means of APT. The specimens were irradiated at a temperature of about 300 °C with a total fluence of 1.38 x 10^{19} n/cm^2 (exact induced damage levels are not provided). The resulting APT maps indicate the formation of MNPs without the presence of Cu with a diameter between 2 and 4 nm. They conclude that their results support the idea of a " strong synergism of nickel and manganese in increasing the radiation sensitivity of RPV steels even for steels with low copper contents"[26]. P. B. Wells *et al.*[27] in 2014 reported studies performed on a series of RPV steels with varying composition (both low- and high-Cu) irradiated at high (1.3 x 10^{20} n/cm^2 and 1.1 x 10^{21} n/cm^2) fluences. The samples were investigated by means of APT and microhardness measurements. Their results indicate the formation of MNPs in the low-Cu steels (0.01 and 0.02 wt. %), at both fluences, with their size, number density, and volume fraction significantly increasing with increasing fluence. Other reported studies also yield similar results; at high fluences, ultrafine Ni-, Mn-, Si-enriched precipitates do form. All this is indicative of the importance of fluence upon the formation of MNPs in low-Cu RPVs, especially when compared to the irradi-

ation details of our study. The overall fluence of protons and that of neutrons though might not be directly comparable and one should probably directly compare damage levels. The fluence used for irradiating the low-Cu specimens reported in this chapter was at least one order of magnitude lower than the values most commonly reported in literature. The calculated damage values were also one to three orders of magnitude smaller. It is safe to conclude then that the amount of Cu along with the total accumulated fluence must have a synergistic role. The effectiveness of proton irradiation against neutron irradiation is also debatable. Differences in the primary knock-on atom (PKA) spectrum, accelerated damage rates, and small penetration depth leading to surface effects and consequently small analysis volume are a few drawbacks of using protons instead of neutrons but evidence have been brought forward to support that proton irradiations, under well controlled conditions, could be a good surrogate to neutron irradiations yielding similar results. For more detailed information the reader is referred back to Chapter 2.

Regarding the scattering features that were detected by the SANS measurements it is believed that they are microstructural features present in the samples prior to any heat treatment or irradiation. The scattering curves show that these features are roughly within the same size range for almost all the samples and they are stable after irradiation. The SEM images support this assumption; small features of spherical (or spheroidal) shape with varying size are seen in all images. It is common during the austenisation of steels (part of their manufacturing process) for carbides to precipitate. Such features were also found in the high-Cu steels investigated and reported in the previous chapter. The size of the features in these high-Cu steels were roughly the same as in the low-Cu steels, they were detected within the as-received samples and remained stable during irradiation indicating that the two types of steels contained the same pre-irradiation features. J. Zelenty *et al.*[28] in 2016 performed measurements on both as received and thermally aged high- and low-Cu RPV steels by means of APT. The samples were prepared in exactly the same way as the ones studied here. Their findings indicate the precipitation of carbides of both as received and aged specimens. The analysis of their APT results

indicated that the carbides are cementite, Fe_3C.

The experimentally calculated A ratio values could also give an insight on the nature of the scattering features. Revisiting equations 5.1 and 5.2 one can calculate the A ratio value using cementite's composition and compare it to the experimental values. First, it is assumed that the particles are non-magnetic. This yields an A ratio value of over 70 which is quite larger than the experimental values. Thus, as a next step the cementite particles are assumed be partially or fully magnetic. Taking into account the high amount of Fe in cementite this is a valid assumption. Published literature also supports the idea that cementite is actually magnetic[29,30]. Considering a magnetic moment of 2.6 emu/μ_B for Fe gives an A ratio value of about 2 which is well in agreement with some of our experimental A ratios. As such, considering the scattering features to be magnetic cementite particles seems valid. The differences seen in the experimental A ratio values between samples or scattering events could be due to solutes, such as Mn or Ni, trapped within the cementite phase[28]. Excess of Mn can decrease the A ratio in contrast to a decrease of the A ratio if Ni content is increased. Of course the precipitation of different types of carbides, such as $M_{23}C_6$ (M for metal), cannot be excluded. This could also account for the relatively wide size range of the scattering features since they can be of two different types. Also the lower A ratio values could also be explained by the presence of $M_{23}C_6$ even by assuming that they are not magnetic since Mn has a negative nuclear scattering length lowering the A ratio.

Despite the fact that hardness-increasing irradiation induced MNPs are not present in our samples, the precipitation of cementite or other carbides could still have implications on the hardness of the steels and probably their consequent embrittlement. Depending on their size and number density, cementite precipitates can act as dislocation pinning points, not allowing dislocations from freely moving through the matrix of the steels. This could significantly increase hardness and lead to subsequent failure of the alloys. Heat treatment though have some effects; thermally induced coarsening could increase the size of cementite particles and decrease their number density resulting in reduced pinning

points for dislocations and decrease of hardness (see Fig. 5.14).

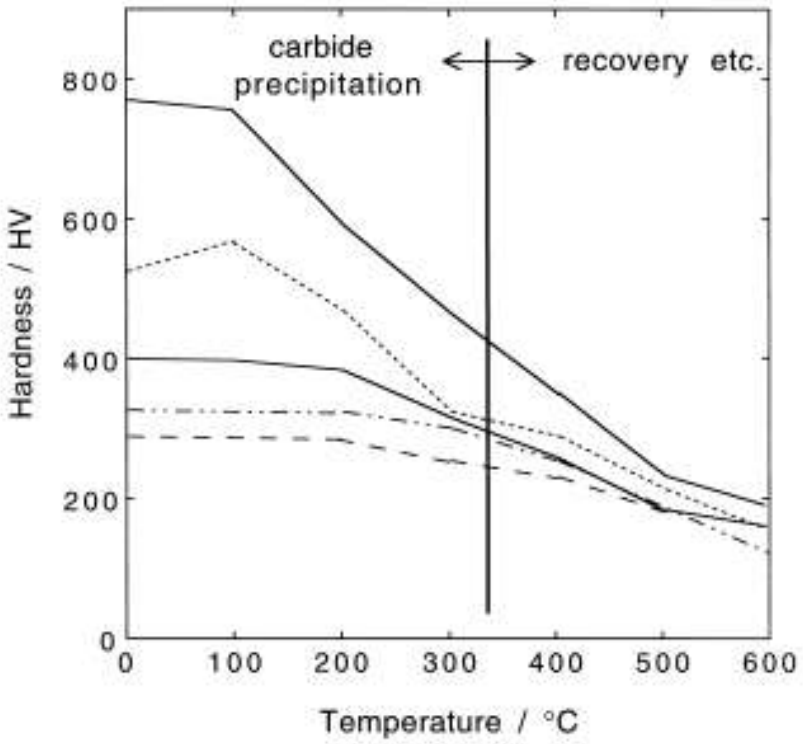

Figure 5.14: Hardness values of different carbon-containing martensitic steels as a function of temperature. Curves with higher hardness at 0 °C correspond to higher carbon content. At lower temperatures carbide precipitation dominates increasing hardness while increasing temperature leads to coarsening and decrease in hardness is observed[31].

5.5 Conclusions

Proton irradiated (50°C – 400°C) and heat treated (300°C and 400°C) low-Cu RPV model steel alloys were investigated by means of SANS. SEM and Vickers microhardness testing were also employed providing complementary microstructural information.

The results indicate that there is no irradiation induced changes to any of the specimens and precipitation due to irradiation has not occurred. This effect, or rather its absence, is attributed to a synergy between the low amount of Cu and the relatively low proton fluences used for the irradiations, along with the low damage levels produced. Despite the low level of Cu, increasing the induced damage by at least one or two orders

of magnitude could possibly induce ultrafine nano-precipitates enriched with Mn, Ni, and possibly Si.

Both SANS and SEM showed the presence of stable spherical features with radii ranging between 10 and 100 nm (10 – 50 nm for SANS due to limited $\vec{q}$-range). Their presence within the as received specimens along with their stability during heat treatment or irradiation indicates their formation during the steels' manufacturing process. Such features are carbides with cementite (Fe_3C) being the one most commonly found among them. Examining the received A ratio values indicates that cementite must be magnetic and the presence of solutes trapped in cementite is not conclusive. Other carbides could also have precipitated accounting for variations in size and A ratio. The precipitation of carbides might have a role in possible increase of hardness of the steels. Heat treatment at temperatures of about 400 °C or higher could lead to coarsening and a decrease in hardness; temperature effects within materials can be significant, even at temperatures and times not considered to be extreme. The heat treatments performed for the scope of this thesis though were not sufficient enough to change the microstructure of the steels (e.g. grain coarsening so as to decrease their contribution on the scattering signal). The minor effect of the Porod law indicates that heat treatment could possibly lead to grain growth but longer time scales and higher temperatures are needed to fully eliminate the effect.

In SANS investigations of RPV steels the use of the log-normal distribution model is generally robust. The majority of SANS experiments though are confined in probing irradiation induced precipitates at the highest $\vec{q}-$ranges often excluding mictrostructural features that could be detected at higher $\vec{q}$ values. The combination of the extended $\vec{q}$-range and the employment of the log-normal distribution models allowed for the detection of the stable scattering features, also supporting the findings from the SEM. It should be pointed out that even if the use of the log-normal model is trivial the interpretation of the results can have various routes as in the case of the A ratio analysis (i.e. magnetic versus non-magnetic features). Familiarity with the under-investigation system is crucial

and comparison with other techniques could be valuable.

References

[1] G. R. Odette. On the dominant mechanism of irradiation embrittlement of reactor pressure vessel steels. *Scripta metallurgica*, 17(10):1183–1188, 1983.

[2] G. R. Odette and G. E. Lucas. Embrittlement of nuclear reactor pressure vessels. *JOM*, 53(7):18, 2001.

[3] E. Meslin, B. Radiguet, and M. Loyer-Prost. Radiation-induced precipitation in a ferritic model alloy: An experimental and theoretical study. *Acta Materialia*, 61(16):6246–6254, 2013.

[4] G. R. Odette and G. E. Lucas. Irradiation embrittlement of reactor pressure vessel steels: mechanisms, models, and data correlations. In *Radiation Embrittlement of Nuclear Reactor Pressure Vessel Steels: An International Review (Second Volume)*. ASTM International, 1986.

[5] P. Pareige, J. C. Van Duysen, and P. Auger. An APFIM study of the microstructure of a ferrite alloy after high fluence neutron irradiation. *Applied Surface Science*, 67(1-4):342–347, 1993.

[6] A. Wagner, A. Ulbricht, F. Bergner, and E. Altstadt. Influence of the copper impurity level on the irradiation response of reactor pressure vessel steels investigated by sans. *Nuclear Instruments and Methods in Physics Research Section B: Beam Interactions with Materials and Atoms*, 280:98–102, 2012.

[7] G. R. Odette. Radiation induced microstructural evolution in reactor pressure vessel steels. *MRS Online Proceedings Library Archive*, 373, 1994.

[8] J. F. Ziegler, M. D. Ziegler, and J. P. Biersack. *SRIM: the stopping and range of ions in matter*. Cadence Design Systems, 2008.

[9] R. E. Stoller, M. B. Toloczko, G. S. Was, A. G. Certain, S. Dwaraknath, and F. A. Garner. On the use of SRIM for computing radiation damage exposure. *Nuclear Instruments and Methods in Physics Research Section B: Beam Interactions with Materials and Atoms*, 310:75–80, 2013.

[10] M. J. Norgett, M. T. Robinson, and I. M. Torrens. Standard practice for neutron radiation damage simulation by charged-particle irradiation. *Annual Book of ASTM Standards*, 1975.

[11] C. D. Dewhurst. D33 — A third small-angle neutron scattering instrument at the institute Laue-Langevin. *Measurement Science and Technology*, 19(3):034007, 2008.

[12] C. D. Dewhurst. GRASP: graphical reduction and analysis sans program for Matlab. *Institut Laue-Langevin (2001–2007) http://www.ill.eu/fileadmin/users_files/Other_Sites/lss-grasp/grasp_main.html*, 2007.

[13] S. R. Kline. Reduction and analysis of SANS and USANS data using Igor Pro. *Journal of Applied Crystallography*, 39(6):895–900, 2006.

[14] P. A. Beaven, F. Frisius, R. Kampmann, and R. Wagner. Analysis of defect microstructures in irradiated ferritic alloys. In *Atomic Transport and Defects in Metals by Neutron Scattering*, pages 228–233. Springer, 1986.

[15] F. Bergner, A. Ulbricht, P. Lindner, U. Keiderling, and L. Malerba. Post-irradiation annealing behavior of neutron-irradiated FeCu, FeMnNi and FeMnNiCu model alloys investigated by means of small-angle neutron scattering. *Journal of Nuclear Materials*, 454(1):22–27, 2014.

[16] P. Pareige and M. K. Miller. Characterization of neutron-induced copper-enriched clusters in pressure vessel steel weld: an APFIM study. *Applied Surface Science*, 94:370–377, 1996.

[17] A. Ulbricht and J. Böhmert. Small angle neutron scattering analysis of the radiation susceptibility of reactor pressure vessel steels. *Physica B: Condensed Matter*, 350(1):E483–E486, 2004.

[18] M. K. Miller, B. D. Wirth, and G. R. Odette. Precipitation in neutron-irradiated Fe–Cu and Fe–Cu–Mn model alloys: a comparison of APT and SANS data. *Materials Science and Engineering: A*, 353(1):133–139, 2003.

[19] E. Meslin, M. Lambrecht, M. Hernández-Mayoral, F. Bergner, L. Malerba, P. Pareige, B. Radiguet, A. Barbu, D. Gómez-Briceño, A. Ulbricht, et al. Characterization of neutron-irradiated ferritic model alloys and a rpv steel from combined APT, SANS, TEM and PAS analyses. *Journal of Nuclear Materials*, 406(1):73–83, 2010.

[20] G. Salje and M. Feller-Kniepmeier. The diffusion and solubility of copper in iron. *Journal of Applied Physics*, 48(5):1833–1839, 1977.

[21] M. Perez, F. Perrard, V. Massardier, X. Kleber, A. Deschamps, H. De Monestrol, P. Pareige, and G. Covarel. Low-temperature solubility of copper in iron: experimental study using thermoelectric power, small angle x-ray scattering and tomographic atom probe. *Philosophical Magazine*, 85(20):2197–2210, 2005.

[22] J. C. van Duysen and G. M. de Bellefon. 60 th anniversary of electricity production from light water reactors: Historical review of the contribution of materials science to the safety of the pressure vessel. *Journal of Nuclear Materials*, 2016.

[23] T. Takeuchi, A. Kuramoto, J. Kameda, T. Toyama, Y. Nagai, M. Hasegawa, T. Ohkubo, T. Yoshiie, Y. Nishiyama, and K. Onizawa. Effects of chemical composition and dose on microstructure evolution and hardening of neutron-irradiated reactor pressure vessel steels. *Journal of Nuclear Materials*, 402(2):93–101, 2010.

[24] J. E. Zelenty. Understanding thermally induced embrittlement in low copper RPV steels utilising atom probe tomography. *Materials Science and Technology*, 31(8):981–988, 2015.

[25] G. R. Odette and G. E. Lucas. Recent progress in understanding reactor pressure vessel steel embrittlement. *Radiation Effects and Defects in Solids*, 144(1-4):189–231, 1998.

[26] M. K. Miller, M. A. Sokolov, R. K. Nanstad, and K. F. Russell. APT characterization of high nickel RPV steels. *Journal of Nuclear Materials*, 351(1):187–196, 2006.

[27] P. B. Wells, T. Yamamoto, B. Miller, T. Milot, J. Cole, Y. Wu, and G. R. Odette. Evolution of manganese–nickel–silicon-dominated phases in highly irradiated reactor pressure vessel steels. *Acta Materialia*, 80:205–219, 2014.

[28] J. Zelenty, G. D. W. Smith, K. Wilford, J. M. Hyde, and M. P. Moody. Secondary precipitation within the cementite phase of reactor pressure vessel steels. *Scripta Materialia*, 115:118–122, 2016.

[29] D. Chaira, B. K. Mishra, and S. Sangal. Magnetic properties of cementite powder produced by reaction milling. *Journal of Alloys and Compounds*, 474(1):396–400, 2009.

[30] H. Choe, T. Terai, T. Fukuda, T. Kakeshita, S. Yamamoto, and M. Yonemura. Easy axis of magnetization of Fe_3C prepared by an electrolytic extraction method. *Journal of Magnetism and Magnetic Materials*, 417:1–5, 2016.

[31] H. K. Dharamshi and H. Bhadeshia. *Bainite in steels: theory and practice*. Maney Publishing, 2015.

CHAPTER 6

PROBING NANO-SCALE HETEROGENEITIES IN FE-GA BINARY ALLOYS

6.1 Introduction

In Chapter 2 it was discussed that pure bcc Fe exhibits quite small magnetostriction, on the order of $\lambda_{100} \sim 20$ $\mu\epsilon$ and $\lambda_{111} \sim 16$ $\mu\epsilon$ at room temperature. If non-magnetic Ga is added, the magnetostriction of $Fe_{100-x}Ga_x$ (Galfenol) system rises up to 400 $\mu\epsilon$ (λ_{100} in excess of 250 $up\mu\epsilon$ for quenched single crystals, with a peak at x $\sim$ 0.2 and a second peak at x $\sim$ 0.29)[1]. The reason of such high magnetostriction of Fe-Ga systems still lacks solid explanation. One theory proposes that the magnetostriction arises from the structural reorientation of Ga-rich, tetragonal nano-precipitates[2,3], and another argues that the magnetostriction might be due to Ga–Ga pairs randomly distributed throughout the solid solution matrix[4]. It is apparent that extensive experimental effort is required towards understanding the magnetostrictive mechanism in Galfenol.

In literature one finds studies on Fe-Ga specimens reporting the presence of nano-scale heterogeneities precipitating out of the matrix of the alloy. To this day though none provides decisive results on their exact composition. In this Chapter anomalous small-angle X-ray scattering (ASAXS) is employed in order to investigate the composition of precipitates in a Fe-Ga specimen containing about 23 at. % Ga. ASAXS is a technique that makes use of the energy dependence of each element close to its respective absorption

edge. Careful measurements can reveal variations in contrast between the matrix and the precipitates which can lead to a direct estimation of their composition. For analysing the experimental data fitting processes using theoretical models that can describe the scattering features is required. Since the exact nature of the precipitates is not *a priori* known one needs to carefully evaluate the fitting results, before reaching conclusions. A comparison between different theoretical models with a simultaneous survey of reported studies is essential.

6.2 Experimental Details

6.2.1 Materials & Sample Preparation

The sample studied and reported in this chapter is a Fe-Ga binary alloy, originally grown as a single crystal, with composition $Fe_{0.765}Ga_{0.235}$. The sample was grown at the Materials Preparation Center, Ames, IA using a Bridgeman furnace. After growth the sample was quenched to ambient temperature to enhance magnetostriction.

The sample was measured by means of small-angle X-ray scattering (SAXS) and anomalous small-angle X-ray scattering (ASAXS). For both the SAXS and ASAXS experiments, and after examining the X-ray attenuation length, λ, at the absorption edges of Fe and Ga, the specimen was polished down to an estimated thickness of about 30 μm in order to achieve suitable X-ray transmission. The exact thickness of the sample was later verified by X-ray transmission/absorption measurements. The polishing process proved to be harsh for the sample and destroyed the single crystal structure ending up as polycrystalline. The bulk composition of the specimen was originally evaluated by means of energy dispersive X-ray spectroscopy (EDS) at the Materials Preparation Centre and then re-evaluated with X-ray transmission/absorption measurements.

A series of polycrystalline $Fe_{1-x}Ga_x$ samples, with $0.1 \leq x \leq 0.25$, were also prepared at the University of Birmingham, UK using the vacuum arc melting method but severe

difficulties with the (A)SAXS instrument did not allow for any full measurements to be taken. As such, this chapter is focused on the first sample alone.

6.2.2 ASAXS - Configuration, Reduction, & Analysis

Small-angle X-ray scattering (SAXS) and anomalous small-angle X-ray scattering (ASAXS) measurements were performed on the I22 instrument at Diamond Light Source, UK. A schematic layout of the beam-line is provided in Fig. 6.1.

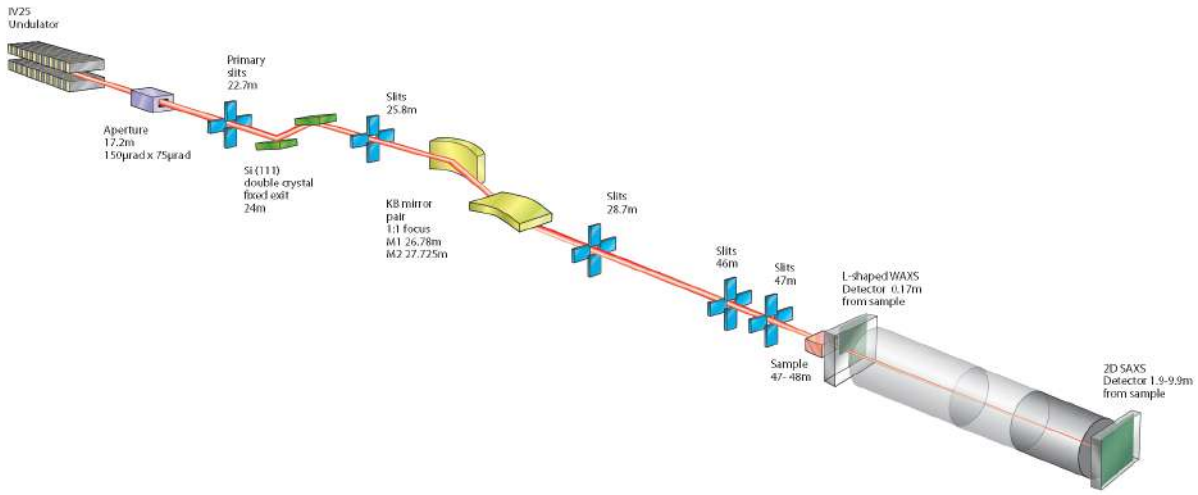

Figure 6.1: Schematic of the small-angle X-ray instrument I22 at Diamond Light Source, UK[5]. The beam-line consists of apertures and slits defining the size and shape of the beam as part of the collimation system along with beam guiding mirrors. A Si (111) crystal is used as monochromator. The WAXS and SAXS detectors are used for the detection of the scattered beam at wide and small angles respectively.

The SAXS measurements were performed at an energy of 7.07 keV, far from the Fe or Ga edges (7.1120 keV and 10.3671 keV respectively), for the purpose of receiving structural information, such as size, shape, and volume fraction, of the heterogeneities within the sample. The ASAXS measurements were performed by choosing several energies close to the absorption edges of Fe and Ga. Evaluating the results of the ASAXS measurements made possible the determination of the composition of the scattering features. For choosing a specific energy value a Si (111) rotating crystal incident to the white X-ray beam was used as monochromator. The energy resolution, $\Delta E/E$, due to the monochromator

was 1.2×10^{-4}. Overall, a total scattering vector, $|\vec{q}| = 0.01 - 0.4$ Å^{-1}, was covered, where $\vec{q}$, as previously defined, is calculated using $|\vec{q}| = (4\pi/\lambda) \cdot \sin(\theta)$ with θ being half the scattering angle and λ the X-ray wavelength.

For the detection of the scattered X-ray beam the silicon hybrid pixel Pilatus P3-2M SAXS and Pilatus P3-2M-DLS-L WAXS detectors were used. The detectors had a total pixel area of 1475 × 1679 (pixel size 172 × 172 μm^2). For detector calibration a silver behenate sample was measured with first known Bragg peak found at $\vec{q} = 1.067$ nm^{-1} (see Fig. 6.2); silver behanate is one of the standard calibrants for determining the $\vec{q}$-scaling as well as for determining the beam centre relative to the detector.

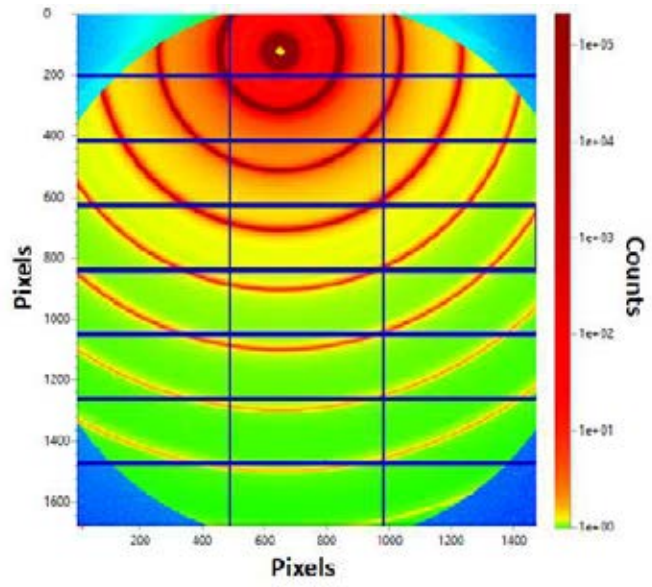

Figure 6.2: Two-dimensional scattering picture of silver behenate. The rings correspond to known Bragg peaks and are used for the determining the q-scale. The dark blue horizontal and perpendicular stripes running through the detector are unused pixels that are, along with dead pixels, masked during processing and reduction.

The data were originally measured and taken as 2D scattering images as taken from the detectors (see Fig. 6.3). For reducing to 1D scattering curves a sector averaging was performed on the corresponding 2D scattering images of all different energy scans after masking dead or unused pixels of the detector (about 8 % of total). For choosing the optimal sector for the averaging process a systematic check was performed with $\Delta\theta$ ranging between 10° and 180° on different parts of the detector image. It was found

that a sector at the left side of the beam centre, as seen in Fig. 6.3, with $\Delta\theta = 20^{o}$ provides the optimal results minimising the reflection effects from grain boundaries and multiple scattering, seen as flairs around the beam centre, or artificial features originating from the detector or the detector's mask. The measured scattering curves were then corrected for electronic noise and background scattering and calibrated with transmission measurements and sample thickness. To probe the transmitted and the incident X-ray beam, photosensitive diodes were used. One was located on the beam stop close to the detector to probe the transmitted beam. A second diode was positioned between the monochromator and the specimen so as to monitor the incident beam intensity at different energies.

Raw-data treatment and analysis was performed using the software DAWN[6,7], the NCNR analysis package[8], as well as MATLAB scripting. The full reduction was done by using the following expression

$$I = \frac{CF}{D}\left(\frac{1}{T}I_S - \frac{I_{oS}}{I_{oE}}I_E\right) \tag{6.1}$$

where I_{S} and I_{E} are the raw data from the sample and an empty measurement, used as the background, respectively. With D we express the sample's thickness and T is the transmission of the sample. Calculations of the transmission and thickness are provided in the next section. I_{oS} and I_{oE} correspond to the total count of the incident beams for the sample and empty measurements respectively. The coefficient CF is a calibration factor used for calibrating the SAXS and ASAXS curves into absolute scattering units. It was calculated by measuring a glassy carbon standard sample and using the following expression

$$CF_{GC} = \left(\frac{\partial\Sigma}{\partial\Omega}\right)_{GC}\frac{d_{GC}T_{GC}}{I_{GC}} = 1.8897 \times 10^{-7} \tag{6.2}$$

where $\left(\frac{\partial\Sigma}{\partial\Omega}\right)_{GC} = 36.63$ cm^{-1} is the X-ray scattering cross section for glassy carbon for $q = 0.06$ Å^{-1}, d_{GC} is the glassy carbon's thickness, T_{GC} its transmission and I_{GC} the

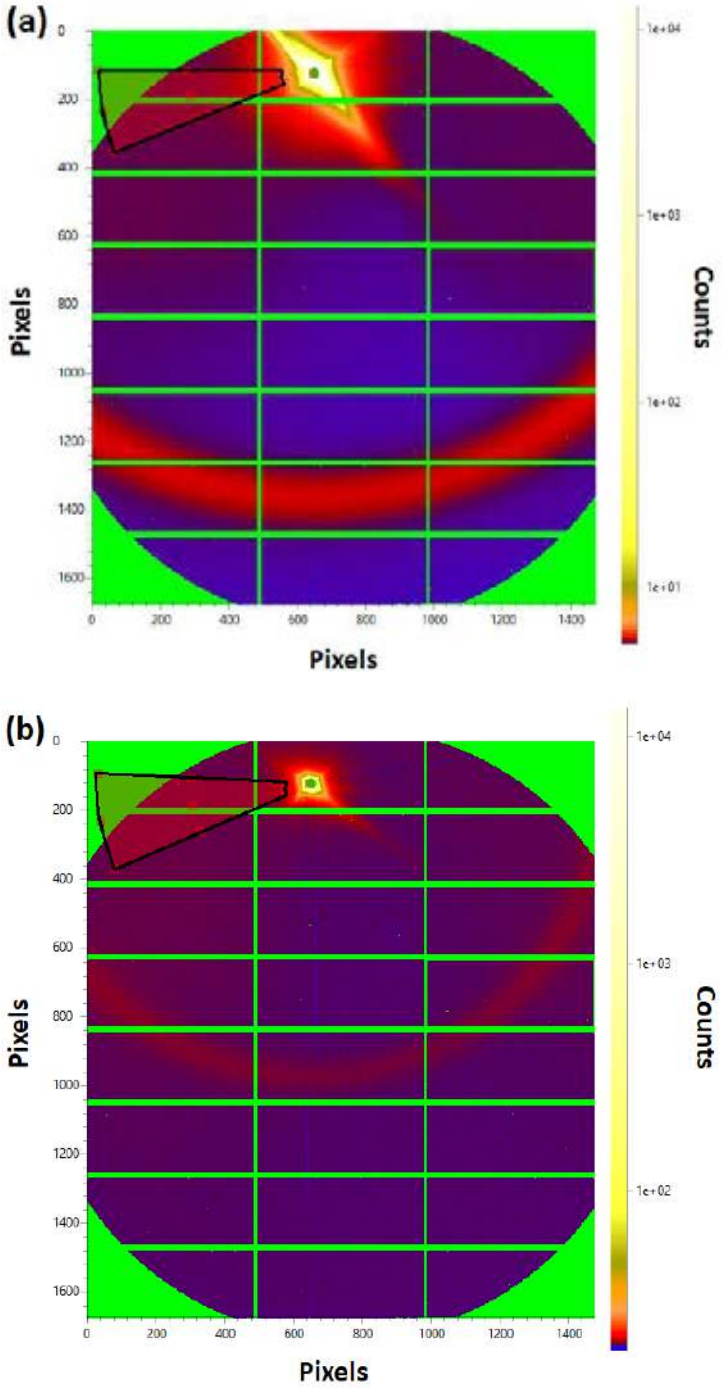

Figure 6.3: Two-dimensional scattering figures of the sample taken close to (a) Fe K absorption edge and (b) close to Ga K absorption edge. The intense ring seen in both 2D images is due to the beam shutter and its contribution is subtracted. The flares around the beam centre are due to reflection effects from the edges of the sample. The choice of sector was done to avoid these effects and reduce contributions to the signal from features on the detector.

measured scattered intensity at $q = 0.06$ Å^{-1}.

In Chapter 1, the theoretical basis of (A)SAXS was presented. Here, a revision of the main aspects of the technique is provided with implementation into the experimental framework and analysis. SAXS probes correlations between scattering densities with the term scattering density here referring to electron density. The differential SAXS cross-section is proportional to the square of the difference between electron densities, i.e. scattering contrast $\Delta\rho^2$, of the different phases of the sample,

$$\frac{\mathrm{d}\sigma}{\mathrm{d}\Omega}(q) \propto \Delta\rho^2 = \Delta\rho(E)\Delta\rho(E)^* \tag{6.3}$$

with $\Delta\rho(E)$ denoting the electron density difference of different phases in the sample and is expressed by

$$\Delta\rho(E) = d_p^{mac}\frac{\sum_i \chi_i f_i(E)}{\sum_i \chi_i M_i} - d_m^{mac}\frac{\sum_j \chi_j f_j(E)}{\sum_j \chi_j M_j} \tag{6.4}$$

The indices i and j correspond to the different elements within the phases with $\mathrm{d_{mac}}$ corresponding to the macroscopic mass density of the corresponding phase (p for particles and m for matrix), and χ to the fraction of each element respectively. M is the molar mass of each element and f(E) is the atomic scattering factor given by

$$f(E) = f_o + f'(E) + if''(E) \tag{6.5}$$

and is energy and composition dependent. The terms f' and f" are element specific anomalous corrections to the atomic scattering factor, they vary significantly when the energy is close to the corresponding X-ray absorption edge and they are connected via Kramers - Kronig relations[9]. Far from the edge the energy variation is small and only f_{o}, being equal to the atomic number Z of the element, is taken into account.

6.3 Results

6.3.1 Transmission, composition, and thickness calculations

In Fig. 6.4 the calculated transmission with respect to X-ray energy, across the Fe and Ga absorption edges, is given where, as expected, a distinct drop is observed when the X-ray energy exceeds each respectful absorption edge. The transmission of the sample is determined by measuring the ratio I_{tS}/I_{oS}, where I_{tS} gives the counts of the beam transmitted through the sample and I_{oS} gives the counts of the beam incident on the sample.

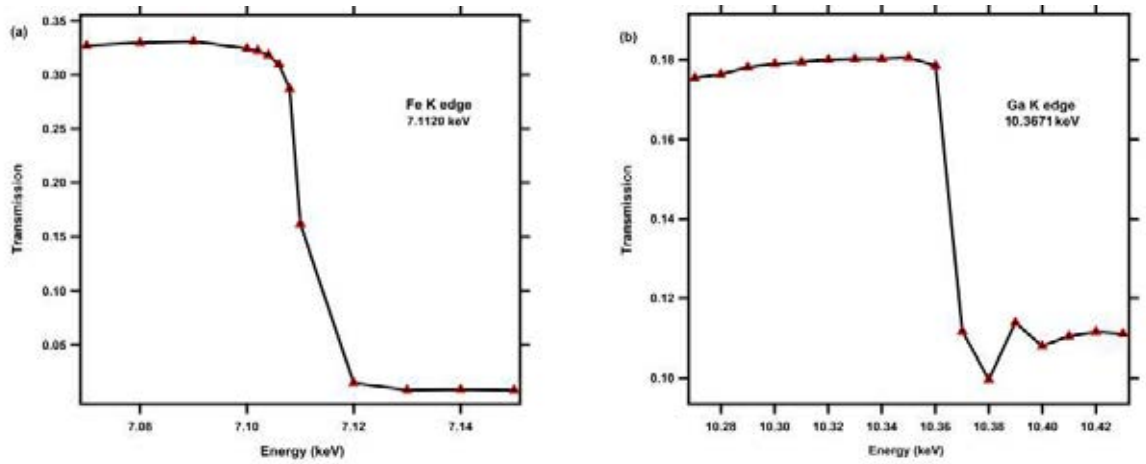

Figure 6.4: Calculated X-Ray transmissions across to the (a) Fe and (b) Ga absorption edges. The transmission drops as the X-ray energy exceeds each respective edge.

Once all the transmission values for each energy, across both absorption edges, is known the bulk composition of the sample can be determined. To do so the relation between the transmission and the attenuation length, λ (not to be confused with the X-ray wavelength), is used

$$T = e^{-D/\lambda} \tag{6.6}$$

where D is the thickness of the sample. The attenuation length is reciprocal to the attenuation coefficient, μ, and is both energy and composition dependent. Since the thickness of the sample is not exactly known at this stage, to determine the composition of the sample a comparative analysis between theoretical values of the attenuation length for different compositions and the experimental values of the transmission was employed. For this purpose equation 6.6 was rearranged to give the following expression

$$\frac{(\lambda_1 - \lambda_2)_{Fe}}{(\lambda_1 - \lambda_2)_{Ga}} = \frac{\left(\frac{lnT_1 - lnT_2}{lnT_1 lnT_2}\right)_{Fe}}{\left(\frac{lnT_1 - lnT_2}{lnT_1 lnT_2}\right)_{Ga}} \tag{6.7}$$

where the indices 1 and 2 refer to values of the attenuation length and transmission just before and right after the absorption edges respectively. The right side of equation 6.7

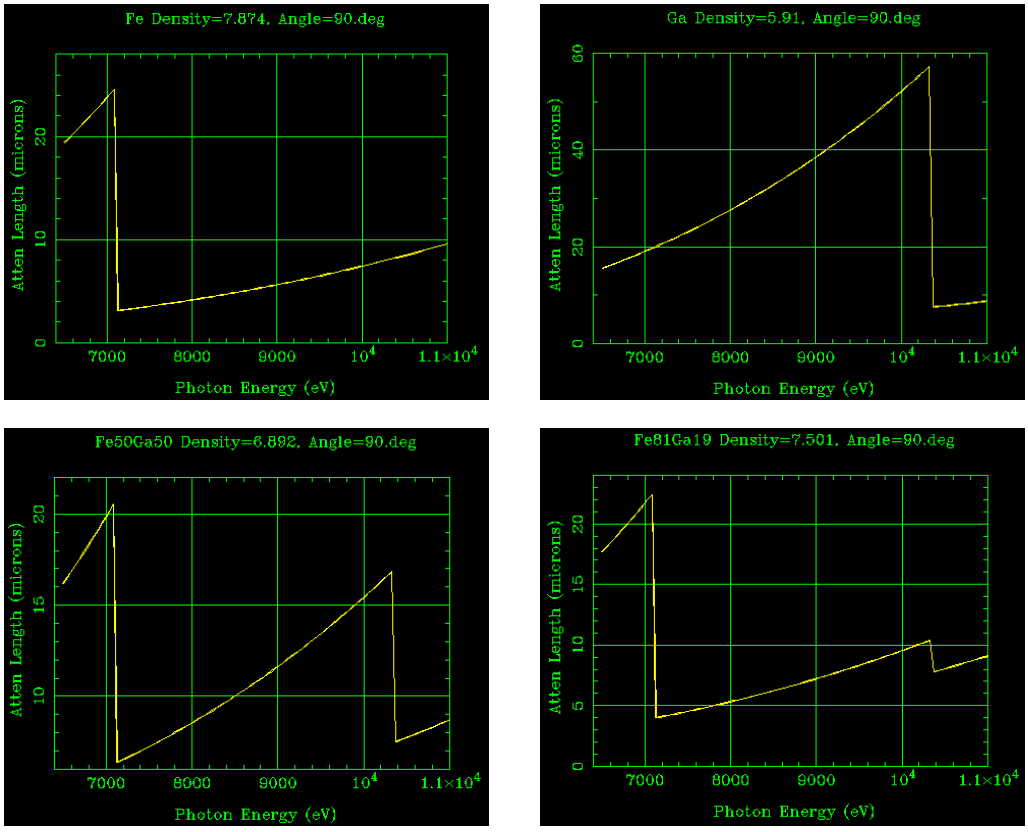

Figure 6.5: Attenuation length with respect to the X-ray energy. (a) (b) Depiction of the attenuation lengths of pure Fe and pure Ga, respectively. (c) Attenuation length of an alloy consisting of equal amounts of the two elements, $Fe_{0.5}Ga_{0.5}$. (d) Attenuation length of $Fe_{0.765}Ga_{0.235}$, which is the calculated bulk composition of the sample.

was calculated from the experimental values of transmission and gave a constant value. The left side was evaluated theoretically for different compositions using known values for the attenuation length always corresponding to the exact same energy values as per transmission measurement. When a matching ratio for the two sides of the equation is found the composition can be determined. The way the attenuation length changes as a function of composition and energy can be seen in Fig. 6.5. From this analysis the bulk composition of the sample was found to be $Fe_{0.765}Ga_{0.235}$, matching the composition originally evaluated at the Ames Laboratory by means of EDS. After the composition of the sample is known the thickness of the sample can be determined by revisiting equation 6.6. An energy preferably far from any absorption edge should be chosen and the corresponding attenuation length should be used. For $Fe_{0.675}Ga_{0.235}$ and an energy of 7.07 keV the attenuation length is 21.9386 μm. The thickness of the sample was calculated to be 25 ±2.1 μm, which is close to the estimated value of 30 μm.

6.3.2 SAXS - ASAXS

The absolute calibrated differential scattering cross sections for both the Fe and Ga K absorption edges are plotted as a function of the scattering vector $\vec{q}$ with varying energy and they are provided in Fig. 6.6. From the plots one can see that at low $\vec{q}$ the intensity decreases as the energy approaches the absorption edges. This is due to the energy dependence of the effective electron density of the Fe or Ga atoms in the vicinity of each absorption edge. In contrast, at higher $\vec{q}$ values the opposite behaviour is observed with the intensity increasing with increasing energy. This is caused by upcoming resonant-Raman scattering which is usually taken as an extra term to the scattering background as well as fluorescence that can also be taken as an extra background term. Fluorescence occurs when the energy approaches the absorption edges and is maximised when it exceeds them. To deal with fluorescence and remove its contribution from the overall scattering signal the WAXS detector is typically employed; the intensity measured at wide angles is

considered to be due to fluorescence alone and as such the scattering profile measured with the WAXS detector can be removed from the data taken at small angles. Unfortunately, the WAXS detector was not working during the beam-time.

The increasing background due to fluorescence is observed for both the Fe and Ga absorption edges but it is more distinct at the Fe edge, reflecting the content of Fe and Ga within the sample. Further observations indicate the presence of a scattering feature seen as a bump on the scattering curves (more clearly seen at the Fe K edge) at a $\vec{q}$ value of about 0.025 Å^{-1}. The scattering data also show a profound $\vec{q}^{\,-4}$ behaviour (Porod law), possibly originating from grain boundaries. To elucidate the scattering feature and to facilitate its analysis a Porod model, $I(q) = Aq^{-m}$, was fitted at the highest $\vec{q}$-range (0.01 – 0.025 Å^{-1}) and then removed from the overall scattering signal. The modified scattering curves at the Fe K edge are given in Fig. 6.7 in which the scattering feature can be clearly seen as a peak at a $\vec{q}$ value between 0.025 Å^{-1} and 0.03 Å^{-1}. By observing the modified curves it is seen that the removal of the Porod law seemingly alters the shape of the curves, mainly at $\vec{q}$ values between 0.03 and 0.1 Å^{-1}, with the effect being more distinct as the energy increases. This might interfere with subsequent analysis and it needs to be taken into consideration. Also, it is apparent that from low to high energy the curves have higher intensity, which is somewhat unexpected. Knowing that the amount of Fe in the specimen is relatively high one expects that as the absorption edge of Fe is approached, the scattering intensity would decrease due to high absorption. This opposite behaviour could be an effect of the Porod law subtraction in combination with upcoming fluorescence and it might require further investigation.

As a first step to the analysis, one of the modified scattering curves was chosen so as to investigate the nature of the scattering feature, starting with structural information. In Fig. 6.8 the curve taken at an energy of 7.07 keV is plotted in linear scale with respect to the scattering vector $\vec{q}$. A Gaussian peak model was originally used to fit the scattering data in the vicinity of the peak. The fitting curve is plotted along with the scattering curve and is also given in Fig. 6.8. From the fit it can be clearly seen that the peak is not

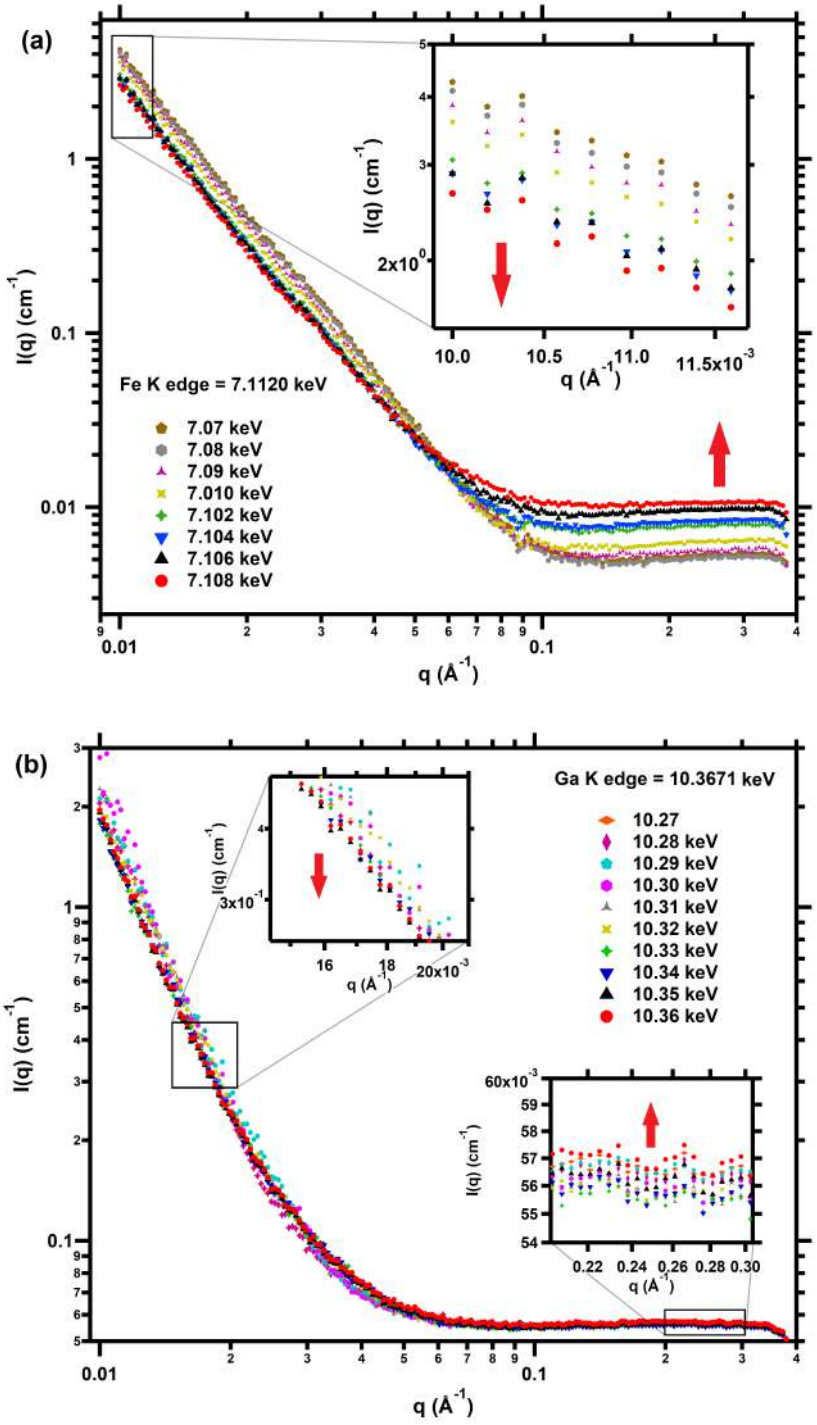

Figure 6.6: Calibrated scattering curves obtained near the (a) Fe and (b) Ga absorption edges. Insets and arrows are used to clarify the behaviour of the scattering curves in the low-$\vec{q}$ and high-$\vec{q}$ regions as the X-ray energy increases. At low $\vec{q}$ the scattering intensity drops as a function of energy, while it increases with increasing energy at high $\vec{q}$.

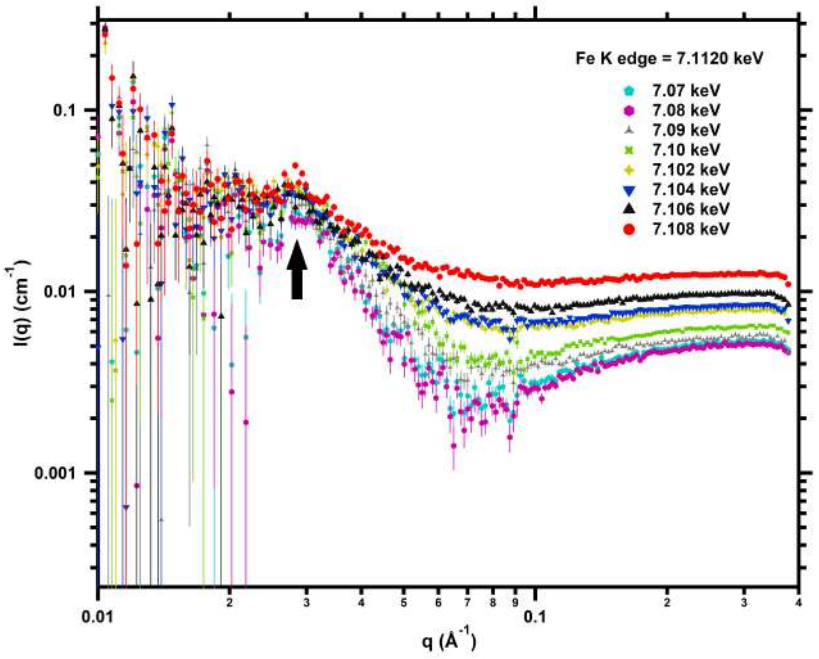

Figure 6.7: Modified scattering curves in the energy region of the Fe K edge. The Porod law contribution has been subtracted from the curves in order to elucidate the scattering feature occurring around 0.025 Å^{-1} (as indicated by the arrow).

fully symmetrical, as a Gaussian peak would be, and the fitted curve is shifted towards the left side of the peak. Similar investigations of the other experimental curves yielded similar results making clear that the use of a Gauss peak model is not appropriate to describe the scattering features.

Simply observing the scattering curves does not clearly point out what model is to be used to describe the scattering objects. An assumption that can be made is that the scattering features within the sample might be non-interacting polydispersed spherical objects. The model most commonly used to describe such scatterers is the log-normal distribution model for spheres. Hence, this model was employed as the next test model. For comparison a model for polydispersed hard interacting spheres was also fitted. The resulting fitting curves are plotted along with the corresponding scattering curve and are given in Fig. 6.9. It can be seen that both models fail to fully fit the data in the vicinity of the peak and the two fitting curves cannot be clearly distinguished. The fitting

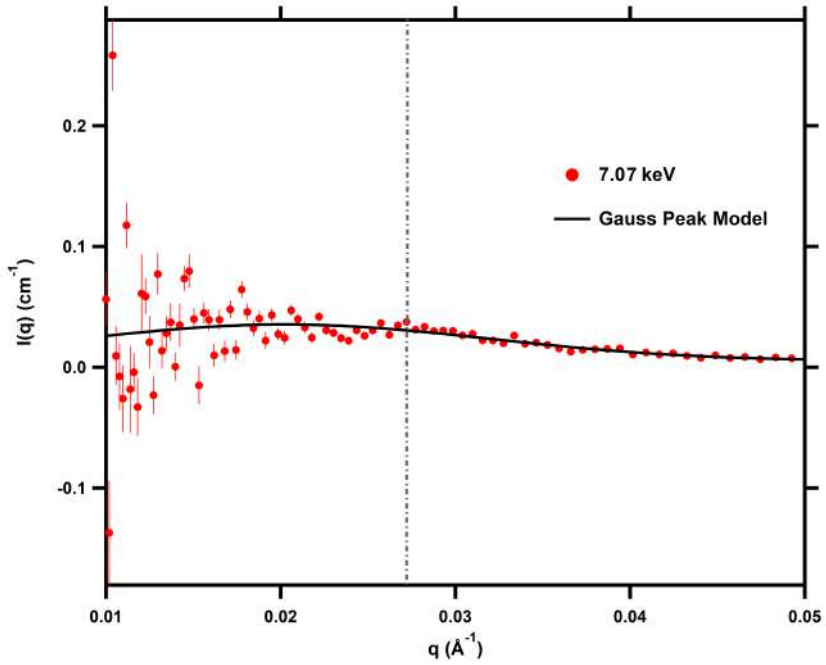

Figure 6.8: A linear-scale plot of a Porod-subtracted curve, measured at an energy of 7.07 keV. A Gaussian peak model is used to highlight the asymmetrical shape of the scattering feature.

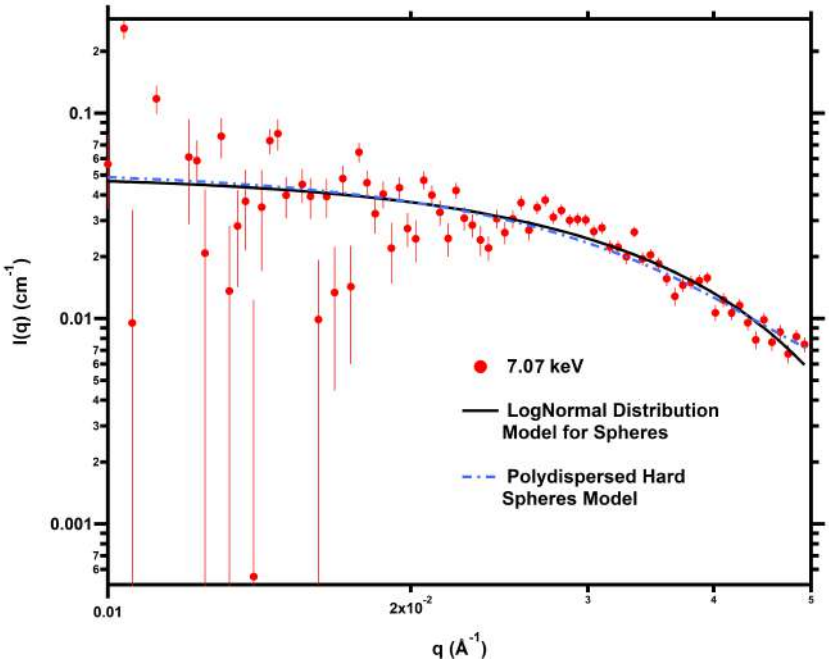

Figure 6.9: Double logarithmic plot of the Porod-subtracted curve at 7.07 keV. A log-normal model for spheres (solid line) and a model for polydispersed hard interacting spheres (dashed lines) have both been used to fit the data.

processes yielded relatively similar results; the log-normal distribution model gave a mean radius of about 60 Å with a polydispersity of 0.09 and a volume fraction of 0.00012. The hard spheres model gave a mean radius of about 64 Å with a polydispersity of 0.02 and a volume fraction of 0.00011. These last two fits were also statistically the same with $\sqrt{\chi^2/N} = 2.17$. At first, the resulting values do not seem off-putting but the errors produced for some of the fitting coefficients were actually larger than the coefficients themselves, indicating that they might be artificial. To check the stability of the results the fitting processes were repeated multiple times with different starting parameters. The results were found to be unstable, often with negative values, and large abnormal errors. Overall, it was concluded that none of these three models used so far can be fully trusted, at least not when fitted on the modified curves since the data are noisy at lower $\vec{q}$ and that could alter the results. It is apparent at this stage that the quality of the data is insufficient to distinguish between the usual specific model functions.

As a next step, the natural logarithm of the differential scattering intensity was plotted with respect to the square of scattering vector and is given in Fig. 6.10. This is the so-called Guinier plot, $ln[I(\vec{q})]$ vs. $\vec{q}^{\,2}$. Within this model the intensity for low-$\vec{q}$ is described by

$$I = I_o e^{-\frac{R_g^2 q^2}{3}} \tag{6.8}$$

and by using the natural logarithm the above equation becomes

$$ln(I) = ln(I_o) - \frac{R_g^2 q^2}{3} \tag{6.9}$$

which is a linear equation with a slope -$R_g{}^2/3$ and an intercept $ln(I_o)$. By performing linear regression one can obtain information on I_o as well as the radius of gyration. For spherical objects the mean radius can then be calculated by $\bar{R} = R_g\sqrt{5/3}$. The linear part of the Guinier plots, $\vec{q}^{\,2} = 0.0007$ - 0.0029 Å^{-2}, was isolated and a linear regression was performed for all different energies. The results are given in Fig. 6.10(b). Assuming that

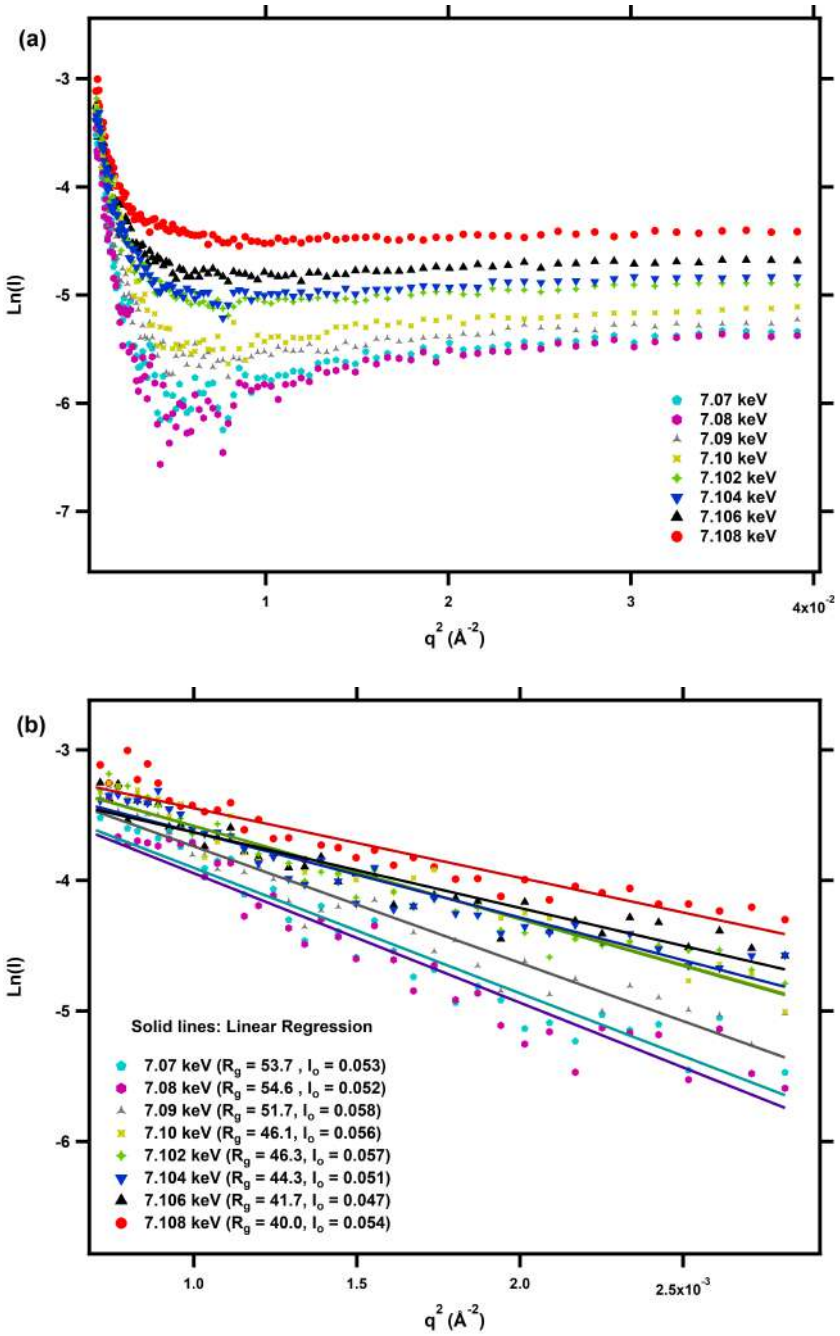

Figure 6.10: Guinier plots of the Fe K edge scattering curves, showing the natural logarithm of the differential scattering intensities as a function of the squared scattering vector. (a) The Guinier plots for the entire $\vec{q}$-range. (b) Linear part of the curves with corresponding linear regression fits showing the variation in slope of the curves.

the structure (size and shape) of the scattering features should be energy independent, i.e. the same for all scattering curves, the linear regression should result in the same radius of gyration. As one can see from the fitted linear regression this is not the case. Of course this is apparent since the linear curves do not have the same slope. This problem, as discussed above, is clearly caused by effects due the removal of the Porod contribution. Hence, for once again the results cannot be trusted to provide useful information, especially regarding changes in the scattering contrast between the scattering features and the matrix. After multiple efforts to find a proper model to describe the scattering features it is made clear that modifying the original scattering curves might not have been the best approach. Analysing the unmodified curves might provide better and more stable results.

The unmodified curves were fitted separately with a summed log-normal spherical distribution - Porod model and a bimodal unified Porod - Guinier model, also known as the two-level Beaucage model. The log-normal model was re-employed to test its validity assuming that the modification of the original curves destabilised the fitting process. First, the structural parameters were extracted using only the 7.07 keV curve and then all curves were globally fitted keeping the structural parameters fixed and using the electron densities (for log-normal) and the Guinier coefficient (for Beaucage) as free fitting parameters. For a third comparison the intensity in the narrow vicinity of the scattering bump ($\vec{q} = 0.025$ - 0.035 Å^{-1}) was numerically integrated assuming that the resulting numbers should be proportional to contrast changes. In Fig. 6.11 fit examples of both models are provided. The scattering curves of only two energies, 7.07 keV and 7.108 keV, far and close to the absorption edge respectively are plotted for clarity.

From the figures one observes that the summed Porod and log-normal models fit the data relatively well at lower $\vec{q}$ values as well as around the area of the scattering feature. As $\vec{q}$ increases though the fit fails to fit the entire high-$\vec{q}$ area with a major mismatch at $\vec{q} = 0.1$ Å^{-1}. It is speculated that this is due to the incoherent background not being entirely flat, especially that of the 7.07 keV curve. Confining the $\vec{q}$-range at lower values improves the fitting but overall there were no significant differences in the fitting

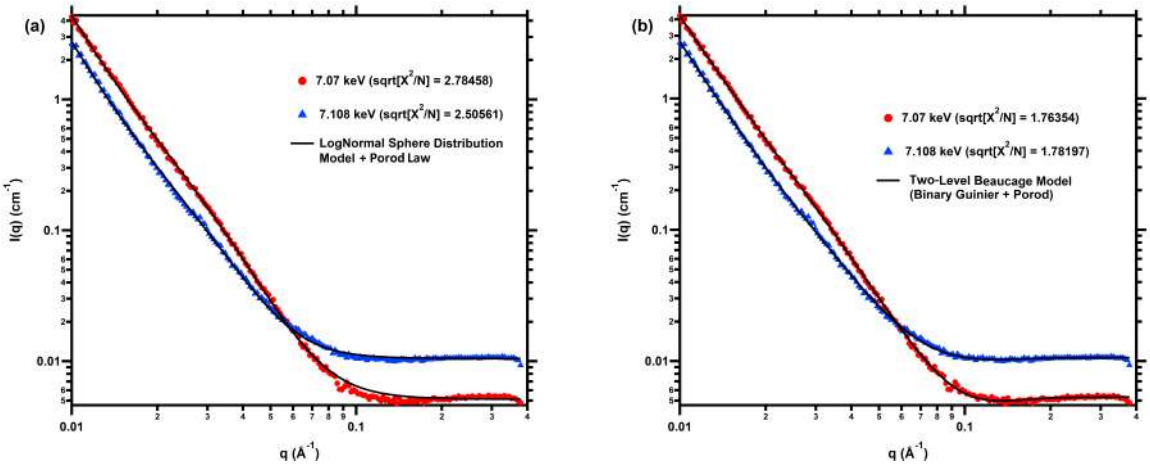

Figure 6.11: Investigation of the suitability of two fit models, using a curve far from and a curve close to the Fe K edge as examples. (a) Fits obtained with the log-normal sphere distribution model and (b) fits obtained with the two-level Beaucage model.

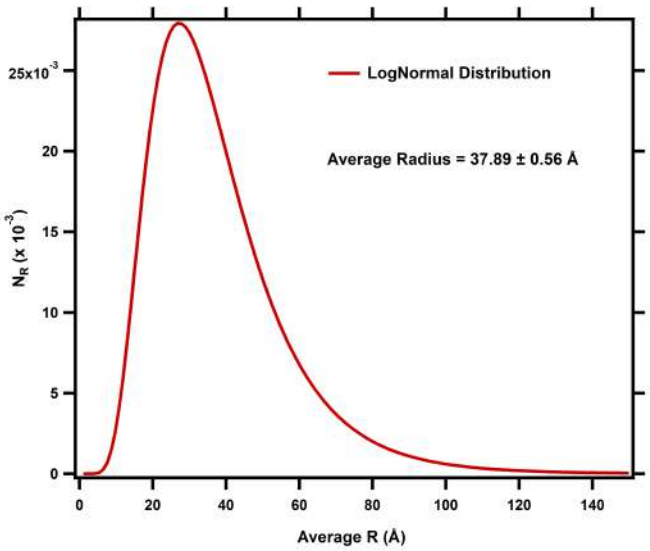

Figure 6.12: Log-normal distribution of the radii of the scattering features. The distribution is based on the fit parameters extracted from the log-normal sphere distribution fit to the 7.07 keV scattering curve, depicted in Fig. 6.11(a).

coefficients, with the χ^2 only slightly decreasing. The log-normal model gave an average radius of the scatterers, $\bar{R} = 37.89 \pm 0.56$ with a volume fraction $V_f = 0.0006 \pm 0.0001$ and a polydispersity $\sigma = 0.47 \pm 0.01$. The log-normal distribution is plotted with respect to the average radius and is given in Fig. 6.12.

The two-level Beaucage model resulted in a better fit with significantly lower χ^2, as seen in Fig. 6.11. This is somewhat expected since the model is bimodal and fits two features on the scattering curve. This includes the $\vec{q} > 0.1$ Å^{-1} region that the log-normal model failed to fully fit. The first level of the model returned a Guinier radius $R_g = 168.1 \pm 0.2$. For spherical objects this is translated in an average radius $\bar{R} = 217.1 \pm 1.2$. This average radius value is quite different than the one extracted by the log-normal model fits and it seems to be out of bounds in the $\vec{q}$-range since such a radius value in reciprocal space would be at $\vec{q} < 0.01$ Å^{-1}. It is safe to speculate then that the Guinier radius is not realistic and it should be discarded. The second level of the model returned negative values for the fitting parameters indicating that a second scattering feature is not present. The resulting values of the Guinier coefficient, as received from the first level, can still be used, assuming they are proportional to the scattering contrast, to be compared against the relative scattering contrast values received from the log-normal fits as well as the integrated intensity values.

The relative experimental contrast values at the Fe K absorption edge as calculated by both fitting processes and the integration procedure are plotted as a function of X-ray energy and are given in Fig. 6.13. No scattering contrasts have been extracted above the absorption edge due to fluorescence effects. It is clear that the relative contrasts calculated with all three different approaches show the same trend with the values calculated from the Beaucage model being slightly lower but still within errors. It needs to be pointed out that the calculated contrast measured for an energy of 7.1 keV seems not to follow the overall trend of smooth descending and is slightly increased compared to the expected one. This was consistent between all three approaches indicating that the original scattering measurement might be anomalous, i.e. the energy failed to set correctly. Contrast values

were not possible to be resolved at the Ga edge due to minimal variation of the scattering curves with varying energy.

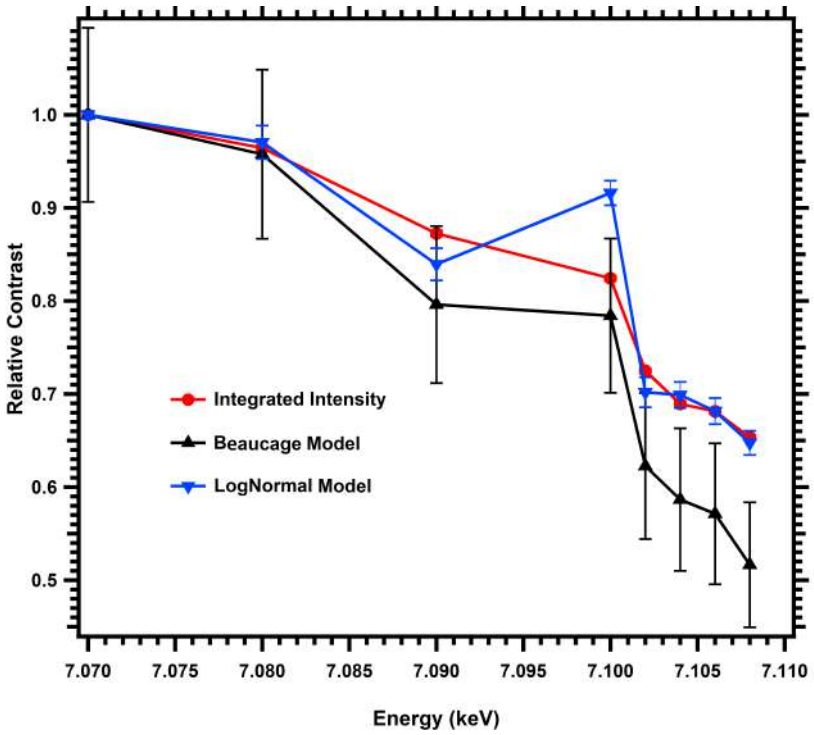

Figure 6.13: Relative experimental scattering contrasts derived from a numerical integration of the scattering feature in the range 0.025 $Å^{-1}$ to 0.035 $Å^{-1}$, from the second level Baucage model, and from the log-normal sphere distribution model. To get the relative contrast changes all values have been normalized with respect to the 7.07 keV value.

6.4 Discussion

In Chapter 2 it was discussed that one of the leading theories trying to explain the significant values of magnetostriction in Fe-Ga argues that magnetostriction is not an intrinsic property of the alloy but rather the result of nano-scale Ga-rich heterogeneities that precipitate out of the bcc A2 matrix reorientating with the application of an external magnetic field. It is theorised that the heterogeneities differ both compositionally and structurally from the A2 phase, originally having a bcc-based ordered $D0_3$ structure that undergoes a transformation into a fct $D0_{22}$ phase[2,3].

The existence of heterogeneities within Fe-Ga alloys has been reported[10–13] but their

exact nature is not exactly known and their connection with magnetostriction is not yet solidly proven. In this study, the analysis of the scattering signal revealed the presence of heterogeneities within the specimen without a solid result on their exact size. Comparing the fitting results and observing the position of the bump on the scattering curves it is safe to assume that the log-normal distribution model is the one that gives the most realistic radius, about 4 nm. Looking in literature one finds studies performed on similar samples supporting the results. In 2010, M. Laver *et al.*[10] performed studies on a $Fe_{0.81}Ga_{0.19}$ single crystal that was grown by the Bridgeman technique. The sample was quenched after growth for enhancing magnetostriction, it was then electron irradiated so as to increase the formation of heterogeneities and it was investigated by means of SANS. Their

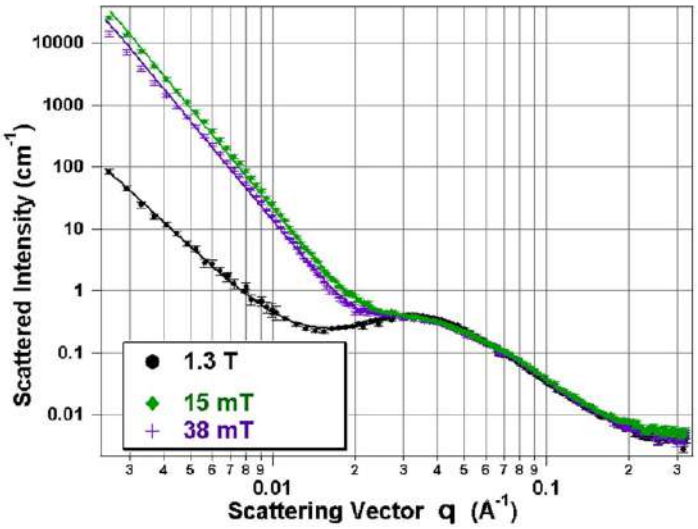

Figure 6.14: SANS curves of a $Fe_{0.81}Ga_{0.19}$ single crystal obtained with different applied magnetic fields. As the field increases the sample reaches saturation that eliminates the contribution of the magnetic domains on the overall signal. The presence of a scattering feature at $\vec{q} = 0.034$ Å^{-1} is apparent. Plot obtained from Ref. 10.

results clearly indicated the presence of heterogeneities within the sample. Looking at the scattering curves, given in Fig. 6.14, a clear bump is seen at $\vec{q} = 0.034$ Å^{-1}. The authors reported that in order to describe this scattering feature they used an ellipsoidal model, i.e. spheroidal form factor, and a non-trivial statistical structure factor that resulted in prolate spheroids with semi-principal axes 15 Å and 51 Å with an average spacing of 147 Å between the scatterers. Observations of their experimental curves and comparison with

the modified scattering curves given in Fig. 6.7 illustrates that the shape of the curves and the peak's position may be similar. The main difference between the two experiments is that in the study of M. Laver *et al.*[10] there was no major Porod contribution from grain boundaries since their sample was a single crystal. Additionally, the sample was saturated under strong magnetic fields thus the Porod contribution from magnetic domains was eliminated too. As such the scattering features where easily detected on the scattering signal. In contrast the sample investigated here was polycrystalline in nature thus a strong Porod contribution was observed due to grain boundaries. Its removal resulted in a somewhat abnormal change in the shape of the scattering curves as well as in increased noise in the data.

Despite the fact that the aforementioned study was able to reveal heterogeneities within Fe-Ga single crystals, elegantly detected by SANS, it was unable to provide direct information on their exact stoichiometry. The purpose of employing the ASAXS method was to reveal specific information on the composition of the scattering features. To attain compositional information equation 6.4 was used to fit the experimental relative contrast values. As it was not possible to resolve differences in contrast from the curves measured at the Ga edge, only the contrast values acquired at the Fe K edge were fitted. The fitting process was performed by assuming an overall starting composition equal to the bulk composition of the sample, $Fe_{0.765}Ga_{0.235}$ (i.e. sum of matrix and precipitates equal to the bulk). The terms f' and f" per energy value for the Fe edge were kept constant. Their values were taken from Ref. 9 and are provided in Table 6.1 along with the corresponding energy values. The way f' and f" vary close to the Fe K edge is depicted in Fig. 6.15. A multitude of fits were then performed with the ratio, y, between Fe and Ga in the precipitates used as a free parameter. The fraction of Fe, x, precipitating out of the matrix varied between fits but was kept fixed during each individual fitting process. This procedure was followed to minimize the number of fitting parameters. More specifically, the amount of Fe in the precipitates is given by $n_{Fe} = x \times 0.765$ (0.765 being the amount of Fe in the bulk), where $0.1 < x < 0.6$. The amount of Ga in the precipitates is given by

Table 6.1: Values of f' and f" used for the theoretical calculation of the scattering contrast. Taken by Ref. 9.

Energy (keV)	**f'**	**f"**
7.07	-4.8337	0.4729
7.08	-5.1493	0.4717
7.09	-5.5259	0.4705
7.10	-6.1509	0.4693
7.102	-6.3359	0.469
7.104	-6.5109	0.4629
7.106	-6.779	0.4686
7.108	-7.1358	0.4689

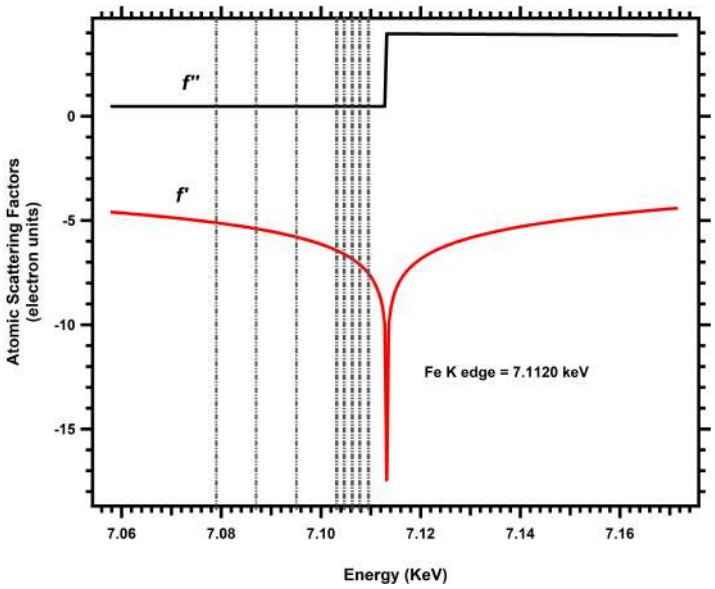

Figure 6.15: Theoretical curves of f' and f" close to the Fe K edge, based on tabulated values from Ref. 9. Vertical dashed lines are used to highlight the energy values at which experimental scattering contrasts have been extracted.

$n_{\mathrm{Ga}} = n_{\mathrm{Fe}}/y$. The matrix composition was then calculated as the difference between the amount of the bulk and that of the precipitates. The resulting fits are given in Fig. 6.16. It is seen that the fitted contrast values between the different models are very similar.

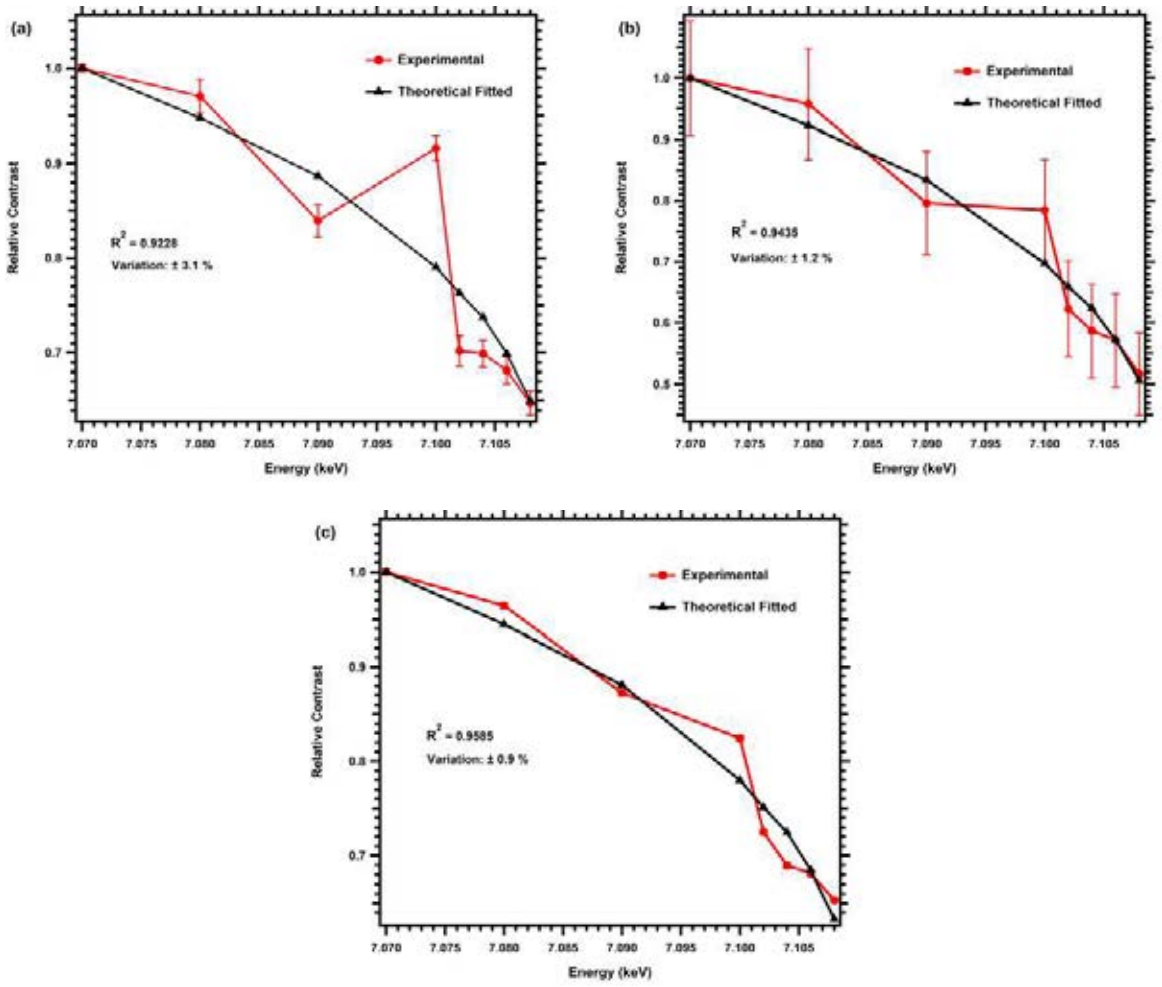

Figure 6.16: Theoretical fits to the normalized experimental scattering contrasts extracted from (a) log-normal spheres distribution model, (b) two-level Beaucage model, and (c) integrated intensity method. The different experimental scattering contrasts result in roughly the same fitting results, leading to the same precipitate compositions.

Evaluating the goodness of fit (R^2) one finds that the integration method produced the best results. Overall the differences were minor indicating that the contrast could be model independent. The fitted curves, for each model, are actually multiple overlapping curves having different combinations of x and y but the same R^2. This clearly indicates that there is not a single stoichiometry for a given series of contrast values. This is due to the dependence of the contrast to the stoichiometry of both the matrix and the precipitates.

Table 6.2: Fitting results of equation 6.4 to the experimental contrast values. The parameter, x, was kept constant per fitting process, while y was a free parameter. Fe_m and Ga_m as well as Fe_p and Ga_p (m for matrix, p for precipitates) have been calculated from these two parameters.

Model	$\mathbf{R^2}$	**x**	**y**	$\mathbf{Fe_m}$	$\mathbf{Ga_m}$	$\mathbf{Fe_p}$	$\mathbf{Ga_p}$
Integration	0.9585	0.42	2.2044	0.83254	0.16746	0.68793	0.31207
		0.43	2.3131	0.82454	0.17546	0.69817	0.30183
		0.44	2.4272	0.81643	0.18357	0.70822	0.29178
		0.45	2.5473	0.80819	0.19181	0.71810	0.28190
		0.46	2.6738	0.79982	0.20018	0.72780	0.27220
		0.47	2.8072	0.79132	0.20868	0.73734	0.26266
		0.48	2.9481	0.78269	0.21731	0.74671	0.25329
		0.51	3.4232	0.75593	0.24407	0.77392	0.22608
		0.52	3.6017	0.74672	0.25328	0.78269	0.21731
		0.53	3.7921	0.73734	0.26266	0.79132	0.20868
Beaucage	0.9435	0.42	2.0610	0.84869	0.15131	0.67331	0.32669
		0.43	2.1772	0.83862	0.16138	0.68526	0.31474
		0.44	2.3009	0.82845	0.17155	0.69705	0.30295
		0.45	2.4331	0.81816	0.18184	0.70872	0.29128
		0.46	2.5745	0.80776	0.19224	0.72024	0.27976
		0.47	2.7261	0.79725	0.20275	0.73162	0.26838
		0.48	2.8892	0.78662	0.21338	0.74288	0.25712
		0.51	3.4617	0.75400	0.24600	0.77587	0.22413
		0.52	3.6865	0.74288	0.25712	0.78662	0.21338
Log-Normal	0.9228	0.42	2.2315	0.82979	0.17021	0.69055	0.30945
		0.43	2.3386	0.82213	0.17787	0.70047	0.29953
		0.44	2.4507	0.81437	0.18563	0.71020	0.28980
		0.45	2.5684	0.80647	0.19353	0.71976	0.28024
		0.46	2.6919	0.79845	0.20155	0.72914	0.27086
		0.47	2.8219	0.79030	0.20970	0.73835	0.26165
		0.48	2.9587	0.78201	0.21799	0.74739	0.25261
		0.51	3.4165	0.75627	0.24373	0.77358	0.22642
		0.52	3.5873	0.74739	0.25261	0.78201	0.21799
		0.53	3.7687	0.73835	0.26165	0.79030	0.20970
		0.54	3.9616	0.72914	0.27086	0.79845	0.20155

For clarity the fitting results for all models are given in Table 6.2 in which only values that provide a realistic fit are shown. For less than 42 % or higher than 53 % of Fe precipitating from the bulk the fitting process fails to provide realistic results. The same stands for about 50 % of Fe. From the results it is indeed made clear that there is a number of combinations of Fe and Ga contents that produce the same relative contrast values that fit the experimental values. Generally, as the amount of Fe in the precipitates increases the amount of Ga decreases, as reflected by an increase in y. Looking at the results more carefully one finds that despite the variance of the values between models they all give approximately the same range for the ratio between Fe and Ga in the precipitates with an average between 2.7 and 2.9. It could be easily argued that the resulting stoichiometry of the nano-precipitates, by average, is close to that reported in literature with Fe and Ga having a 3:1 ratio. This could easily be translated into precipitation of ordered bcc $D0_3$ phase or a lower-symmetry $D0_{22}$ phase with a Fe_3Ga stoichiometry without excluding a $L1_2$ phase, since all three are very similar. Looking at the equilibrium and metastable phase diagrams of Fe-Ga (Fig. 6.17) it is seen that at a 25 at. % of Ga a slow cooled sample will result to the $D0_3$ and the $L1_2$ phases competing with the former dominating. Below 25 at. % of Ga there is a mixture (miscibility gap) of the A2 and $D0_3$ phases. In contrast quenching the sample seemingly suppresses the formation of $D0_3$ and the result is an equilibrium between the A2 and $L1_2$ phases, though precipitation of the $D0_3$ phase distributed throughout the matrix or its possible transformation into a $D0_{22}$ phase is not resolved. The precipitation of a heterogeneous to the A2 matrix $D0_3$ phase has been detected by both neutron diffuse scattering[12] and high-resolution transmission electron microscopy[13] for samples containing 19 at. % of Ga or higher. The lowering of symmetry though, that could directly contribute to enhancement of magnetostriction, is only reported in Ref. 12 and extensive studies on the specific crystal structure of the nano-precipitates is missing. Even if the ASAXS method used in this thesis was able to resolve the stoichiometry of the scattering features, resembling that of the $D0_3$ phase, it is not capable of providing direct crystallographic details, thus a lowering of symmetry

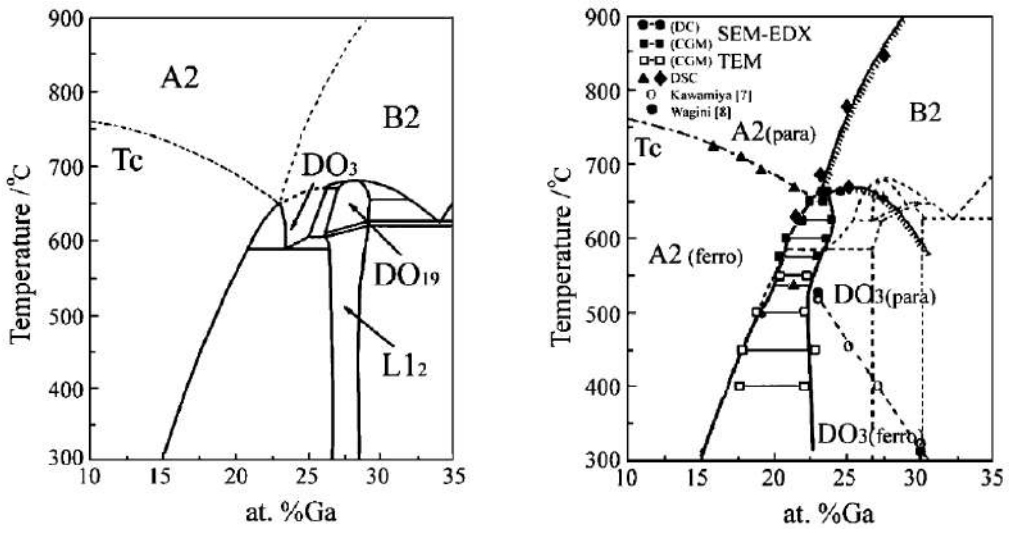

Figure 6.17: (a) Equilibrium phase diagram of Fe-Ga obtained after quenching of the alloy and (b) metastable phase diagram of Fe-Ga for slow cooled samples[14]. In the former the $D0_3$ phases is supressed but at slow cooling rates the phase dominates for Ga exceeding 22 at. In the metastable diagram, between 15 and 22 at. % Ga, the alloy has a mixture of the disordered A2 and ordered $D0_3$ phases.

from cubic to tetragonal cannot be determined. Overall ASAXS is proven to be a valuable tool for determining the exact stoichiometry of the sample as a whole and that of nano-precipitates and the remaining matrix.

6.5 Conclusions

Anomalous small-angle X-ray scattering was used to investigate nano-precipitates in a $Fe_{0.765}Ga_{0.235}$ quenched polycrystal. The technique allows the probing of contrast variations close to the K absorption edges of Fe and Ga, thus providing compositional information (bulk, matrix, and precipitates) for the sample. In general the use of ASAXS proved to be non-trivial since it was the first time it was employed for the investigation of Fe-Ga binary alloys and their nano-structure. This in combination with major experimental difficulties and instrumental instabilities made the analysis and interpretation of results somewhat complicated.

The resulting scattering curves showed the presence of heterogeneities within the sample. Due to minimal variation of the scattering curves at the Ga edge it was easier to resolve the features at the Fe edge. To receive structural and compositional information of the scatterers a variety of different approaches was taken. These include fitting processes of models such as the Gauss peak, log-normal spherical distribution, and two-level Beaucage models as well as integration of the scattering intensity in a narrow region in the vicinity of the scattering bump. Information on the exact size of the scattering features was difficult to extract due to their apparent dependence upon the fitting model. The log-normal model returns the most realistic result with an average precipitate radius of about 38 Å. In contrast, regarding the relative experimental contrast variations all models produced similar results indicating that the contrast is model-independent. Non-linear regression of the contrast values at the Fe K edge gave a precipitation stoichiometry of $Fe_{0.7489}Ga_{0.2511}$ and $Fe_{0.781}Ga_{0.219}$ for the remaining matrix. The stoichiometry of the precipitates matches that of Fe_3Ga $D0_3$ cubic phase or Fe_3Ga tetragonal $D0_{22}$.

In general, the small-angle scattering technique, as in the case of the two previous chapters, was proven to be valuable for the detection of precipitates within the sample and the specific use of ASAXS paved the way for detailed determination of the exact stoichiometry of the scattering features. Of course the main aim of investigating Fe-Ga and its stoichiometry is to make a direct connection with magnetostriction. The work performed for this part of the thesis can be considered as a first step towards this goal.

References

[1] A. E. Clark, K. B. Hathaway, M. Wun-Fogle, J. B. Restorff, T. A. Lograsso, V. M. Keppens, G. Petculescu, and R. A. Taylor. Extraordinary magnetoelasticity and lattice softening in bcc Fe-Ga alloys. *Journal of Applied Physics*, 93(10):8621–8623, 2003.

[2] A. G. Khachaturyan and D. Viehland. Structurally heterogeneous model of extrinsic magnetostriction for Fe-Ga and similar magnetic alloys: Part I. Decomposition and confined displacive transformation. *Metallurgical and Materials Transactions A*, 38(13):2308–2316, 2007.

[3] A. G. Khachaturyan and D. Viehland. Structurally heterogeneous model of extrinsic magnetostriction for Fe-Ga and similar magnetic alloys: Part II. Giant magnetostriction and elastic softening. *Metallurgical and Materials Transactions A*, 38(13):2317–2328, 2007.

[4] J. Cullen, P. Zhao, and M. Wuttig. Anisotropy of crystalline ferromagnets with defects. *Journal of Applied Physics*, 101(12):123922, 2007.

[5] Diamond Light Source. *I22: Small Angle Scattering & Diffraction*. http://www.diamond.ac.uk/Beamlines/Soft-Condensed-Matter/small-angle/I22/layout.html.

[6] M. Basham, J. Filik, M. T. Wharmby, P. C. Y. Chang, B. El Kassaby, M. Gerring, J. Aishima, K. Levik, B. C. A. Pulford, I. Sikharulidze, et al. Data Analysis Workbench (DAWN). *Journal of Synchrotron Radiation*, 22(3):853–858, 2015.

[7] J. Filik, A. W. Ashton, P. C. Y. Chang, P. A. Chater, S. J. Day, M. Drakopoulos, M. W. Gerring, M. L. Hart, O. V. Magdysyuk, S. Michalik, et al. Processing two-dimensional X-ray diffraction and small-angle scattering data in DAWN 2. *Journal of Applied Crystallography*, 50(3), 2017.

[8] S. R. Kline. Reduction and analysis of SANS and USANS data using Igor Pro. *Journal of Applied Crystallography*, 39(6):895–900, 2006.

[9] D. T. Cromer and D. Liberman. Relativistic calculation of anomalous scattering factors for X-rays. *The Journal of Chemical Physics*, 53(5):1891–1898, 1970.

[10] M. Laver, C. Mudivarthi, J. R. Cullen, A. B. Flatau, W.-C. Chen, S. M. Watson, and M. Wuttig. Magnetostriction and magnetic heterogeneities in iron-gallium. *Physical Review Letters*, 105(2):027202, 2010.

[11] C. Mudivarthi, M. Laver, J. Cullen, A. B. Flatau, and M. Wuttig. Origin of magnetostriction in Fe-Ga. *Journal of Applied Physics*, 107(9):09A957, 2010.

[12] H. Cao, P. M. Gehring, C. P. Devreugd, J. A. Rodriguez-Rivera, J. Li, and D. Viehland. Role of nanoscale precipitates on the enhanced magnetostriction of heat-treated Galfenol ($Fe_{1-x}Ga_x$) alloys. *Physical Review Letters*, 102(12):127201, 2009.

[13] S. Bhattacharyya, J. R. Jinschek, A. Khachaturyan, H. Cao, J. F. Li, and D. Viehland. Nanodispersed $D0_3$-phase nanostructures observed in magnetostrictive Fe-19 % Ga Galfenol alloys. *Physical Review B*, 77(10):104107, 2008.

[14] O. Ikeda, R. Kainuma, I. Ohnuma, K. Fukamichi, and K. Ishida. Phase equilibria and stability of ordered bcc phases in the Fe-rich portion of the Fe-Ga system. *Journal of Alloys and Compounds*, 347(1-2):198–205, 2002.

CONCLUSIONS

Two main topics have been tackled for the overall scope of this thesis; the investigation of proton irradiated Fe-based reactor pressure vessel steel alloys and the structural and compositional analysis of a Fe-Ga binary magnetostrictive alloy.

For the first experimental framework small-angle neutron scattering was employed. SANS is one of the main experimental techniques widely used for the detection of irradiation induced features in RPV steels. The overall experimental results indicate the presence of irradiation induced precipitates enriched with Cu, Mn, Ni, and Si within the high-Cu RPV steels. The clusters' size was between ≈ 1 and 4 nm that is a typical size range for irradiation induced nano-clusters. In contrast, no precipitation due to irradiation was detected in the low-Cu alloys. The latter is attributed to the low Cu level within the specimens in combination to the generally low damage levels produced during irradiations. In both types of steels pre-irradiation formed precipitates were found having almost the same size for the two steels. The features remained relatively stable during irradiation with a minor hint of coarsening with increasing temperature. It is theorised that these features are either one or more types of carbides that precipitated during the original treatment of the steels, prior to irradiations. This is supported by Thermocalc analysis. Contribution of grain boundaries from all samples also added up to the overall scattering signal of both high- and low-Cu containing alloys. The experimental approach was trivial with SANS being used for numerous studies of the same type but several different approaches for the the interpretation of the experimental data can be taken. Quite a common approximation for analysing the data and for receiving information on

the possible composition of the scattering features is that the precipitates are generally non-magnetic clusters precipitating out of magnetically saturated Fe matrix. A few studies exist taking into account the possible magnetic nature of the features but still there is no solid proof of such magnetic behaviour. In this thesis the magnetic nature of the precipitates is taken under consideration trying to interpret the experimentally deduced A ratio values. As a guide, reported work from literature utilising APT is consulted. Despite the general difference of the two experimental techniques and the differences in their results, under the magnetic approximation the two methods reconcile making clear that the general discrepancies in their results also lies in the interpretation of data and not necessarily on the techniques.

For the second part of the experimental work the method of choice was anomalous small-angle X-ray scattering. The method in its basis is the same with SANS with the main difference being the energy dependence of the scattering results. ASAXS makes use of the energy dependence of the elements within a specimen when the X-ray energy approaches their respective absorption edges. In the present study utilising the ASAXS method made possible the detection of scattering features, directly comparable with literature, and their stoichiometric analysis with the resulting precipitates having a stoichiometry close to Fe_3Ga resembling the $D0_3$, $D0_{22}$ (or even $L1_1$) phases as predicted from theory, though clear distinction between phases is not possible.

FUTURE WORK

Overall for both sets of materials that were investigated in this thesis (RPV steels and Fe-Ga alloys) there could surely be prospective future work that could lead to improvement of results, and add to general knowledge and literature.

Regarding the RPV steels the main topics that need to be pursued are the further investigation of the synergy of Cu levels and the overall induced damage, the effectiveness of proton irradiation versus neutron irradiation, the effects that temperature might have in the microstructure of the steels as well as different manufacturing processes such as additive manufacturing. Since modern reactors are built with materials containing Cu with less than 0.05 wt. % the research should be mainly focused on low-Cu containing alloys. It is generally known that precipitates enriched in Mn, Ni, and Si are found in steels after high accumulated neutron fluence and induced damage. In this work it was shown that at low damage levels precipitation has not occurred but there is not a clear line as to what is low and what is high damage (always in connection with the appearance of precipitates). For the purpose of clarifying this a detailed investigations is needed with a series of irradiations from low to high damage keeping other parameters (e.g. composition and temperature) constant. Of course one needs to consider safety regulations as there is always the possibility of sample activation. Such a thorough investigation can also provide more clues as to whether protons are as effective as neutrons.

Regarding Fe-Ga alloys the investigations should be turned towards further stoichiometric analysis of the specimens as it seems to be of major importance. The overall microstructure of the alloys along with their thermal history seemingly play an impor-

tant role in the manifestation of magnetostriction. For this purpose high-quality Fe-Ga single crystals should be used, both quenched and slow cooled, of varying Ga content along with detailed magnetostriction measurements. This will allow for a full range of results. ASAXS is certainly a technique that can offer precise information as to whether heterogeneities exist and what their nature is. For future ASAXS experimentation a triple-aspect preparation is required; production of high-quality (single crystal) samples with varying composition; careful preparation of ASAXS experiments and measurements; and accurate modelling of the results. Complementary crystallographic methods, such as X-ray or neutron diffraction, could also be of much help.